FUNDAMENTAL STUDIES AND SPECTRAL SIMULATION OF THE INDUCTIVELY COUPLED ARGON PLASMA

By

LYLE LORRENCE BURTON

B. Sc., University of British Columbia, 1985

A THESIS SUBMITTED IN PARTIAL FULFILMENT OF
THE REQUIREMENTS FOR THE DEGREE OF
DOCTOR OF PHILOSOPHY

in

THE FACULTY OF GRADUATE STUDIES

Department of Chemistry

We accept this thesis as conforming
to the required standard

THE UNIVERSITY OF BRITISH COLUMBIA

December, 1990

In presenting this thesis in partial fulfilment of the requirements for an advanced degree at the University of British Columbia, I agree that the Library shall make it freely available for reference and study. I further agree that permission for extensive copying of this thesis for scholarly purposes may be granted by the head of my department or by his or her representatives. It is understood that copying or publication of this thesis for financial gain shall not be allowed without my written permission.

Department of Chemistry

The University of British Columbia
Vancouver, Canada

Date Dec. 12, 1990

Abstract

The objectives of this work are twofold: firstly, to understand the inductively coupled argon plasma (icp) from a fundamental point of view and, secondly, to attempt to put that knowledge to practical use.

In an effort to realize this first objective, a simple two-level rate model was developed which allows the estimation of the deviations (due to radiative decay) of analyte level populations in the icp from local thermodynamic equilibrium (lte). The results were found to agree very well with experiment for analyte elements (Fe, Cr and Ba) which did not exhibit charge transfer with the argon support gas.

A comprehensive study of magnesium excited-state level populations was performed. It was found that charge transfer between argon ions and ground state magnesium atoms caused ionic magnesium to be overpopulated (with respect to the simple rate model calculations mentioned above). It was also found that, due to appreciable self-absorption, argon itself conforms to an lte model.

Electron temperatures (T_e) were measured in the icp. It was found that, for electron densities greater than about 2×10^{15} cm^{-3}, T_e was within experimental uncertainty of the so-called lte temperature ($T_{e,lte}$ - calculated from the electron density). At lower electron densities, due to the large experimental errors involved, it was difficult to draw definitive conclusions regarding their agreement.

The plasma was also extensively characterized when an extra argon flow was added to the aerosol gas. It was found that at low values of the aerosol gas flow rate, mixing between it and the plasma gas was relatively complete, whereas at higher flow rates there was relatively little mixing. It was also found that the introduction of water into the plasma had a limited effect on sample excitation.

In order to fulfil the second objective, a method was developed to simulate emission spectra from an icp. The method involved the use of a computer program, which worked by combining basic physical data for atomic species, the results of icp fundamental studies, and a realistic instrumental line profile (described in detail). The method was used to simulate a hypothetical silver determination in NBS coal fly ash showing the effects of spectrometer bandpass, silver concentration, and line choice on spectral overlaps.

Table of Contents

	page
Abstract	ii
Table of Contents	iv
List of Tables	viii
List of Figures	x
Acknowledgements	xxiii
List of Symbols	xxiv
Chapter 1 INTRODUCTION	1
1.1 Objectives	1
1.2 Historical	2
1.3 The Inductively Coupled Plasma	3
1.3.1 Development	3
1.3.2 Operation	5
1.4 Collisional and Radiative Processes	8
1.5 Thermodynamic Equilibrium	13
1.6 Electron Density Measurement	18
1.7 Equilibrium in the Inductively Coupled Plasma	20
1.8 The Calculation of Temperature from Electron Density	22
1.9 Overview of Thesis	23

Chapter 2
EXPERIMENTAL 25

2.1 Instrumentation 25

2.2 Data Handling 30

2.3 Sample Preparation 35

2.4 Data Collection 35

2.5 Electron Density Measurement 36

Chapter 3
A SIMPLE METHOD FOR CALCULATING DEVIATIONS FROM LTE IN THE INDUCTIVELY COUPLED PLASMA 38

3.1 Introduction 38

3.2 Theoretical 39

3.3 Experimental 43

3.4 Results 44

3.5 Summary 57

Chapter 4
A STUDY OF MAGNESIUM EXCITED STATE LEVEL POPULATIONS WITH REFERENCE TO CHARGE TRANSFER 59

4.1 Introduction 59

4.2 Experimental 62

4.3 Results 65

4.4 Summary 81

Chapter 5
SOME ELECTRON TEMPERATURE MEASUREMENTS IN THE ICP 83

5.1 Introduction 83

5.2 Theory 85

5.3 Experimental 89

5.4 Results 90

5.5 Summary 99

Chapter 6
THE EFFECT OF A "SHEATHING GAS" ON ANALYTE EXCITATION IN THE ICP 101

6.1 Introduction 101

6.2 Experimental 103

6.3 Results 109

6.3.1 Electron Density 109

6.3.2 Hydrogen and Argon 117

6.3.3 Analyte - Sr, Ca, Mg, Zn, Cd and Ba 121

6.3.4 Results for Aqueous Iron and Ferrocene Vapour 143

6.4 Summary 150

Chapter 7
INFLUENCE OF INSTRUMENTAL BROADENING ON LINESHAPES DETECTED BY PMT AND LPDA DETECTORS 153

7.1 Introduction 153

7.2 Theory 154

7.3 Experimental 158

7.4 Results 159

7.5 Summary 171

Chapter 8
COMPUTER SIMULATION OF SPECTRAL INTERFERENCES IN THE ICP 173

8.1 Introduction 173

8.2 Method 175

8.3 Experimental 182

8.4 Results 183

8.4.1 Simulation of Single Element Spectra - Iron 183

8.4.2 Spectral Simulation of Complex Mixtures - Ag Analysis 187

8.5 Summary 204

Chapter 9
CONCLUSIONS 208

References 214

List of Tables

Table	Description	page
I	Details of the experimental system.	27
II	Electron density (10^{15} cm^{-3}) and (in parentheses) the corresponding lte temperature (K) in the central channel of the icp at various rf powers and heights above the load coil (from reference [35]).	45
III	Species (Mg I or Mg II), wavelengths, upper energy levels, and degeneracy-weighted transition probabilities (gA) for the spectral lines used in the construction of the experimental Boltzmann plots for magnesium.	64
IV	Solution concentrations (C) and ionization energies (E_i) for the elements studied in chapter six along with the corresponding wavelengths (λ), excitation energies (E) and (where relevant) the degeneracy weighted transition probabilities (gA) for the atomic and ionic spectral lines of the elements used.	105
V	Solution concentrations, wavelengths, partition functions, upper energy levels, transition probabilities, and degrees of ionization for the spectral lines occurring in the simulation of the 338.29 nm line of silver in the geochemical matrix.	189
VI	Solution concentrations, wavelengths, partition functions, upper energy levels, transition probabilities, and degrees of ionization for the spectral lines occurring in the simulation of the 338.29 nm line of silver in NBS coal fly ash.	197

Table	Description	page
VII	Solution concentrations, wavelengths, partition functions, upper energy levels, transition probabilities, and degrees of ionization for the spectral lines occurring in the simulation of the 328.07 nm line of silver in NBS coal fly ash.	198

List of Figures

Figure	Description	page
1.1	A schematic diagram of the inductively coupled plasma torch also showing some features of the plasma.	6
1.2	A Boltzmann plot for a system in p-lte (dotted lines); the straight lines of slope $-1/kT_{exc}$ represent the lte situation. E_i represents the ionization potential.	17
1.3	A plot of the lte electron temperature, $T_{e,lte}$, in the inductively coupled plasma as a function of the electron density.	23
2.1	Schematic diagram of inductively coupled plasma - optical emission spectrometer system.	26
2.2	Diagram of sheath gas attachment.	31
2.3	(a) Top view of a cross section of the plasma showing the Abel inversion parameters, (b) a typical lateral emission profile and (c) a typical radial emission profile.	33
3.1	A plot of b_{atom} and $1/b_{ion}$ for iron at 16 mm above the load coil and (a) an rf power of 0.75 kW, (b) 1.00 kW, (c) 1.24 kW, (d) 1.50 kW, and (e) 1.75 kW.	44
3.2	Boltzmann plot for iron at 8 mm above the load coil and an rf power of 1.25 kW. The solid line represents lte, the dotted line was derived from equations (3.10) and (3.11), and the error bars represent experimental points (from reference [131]) with their estimated uncertainties.	47

Figure	Description	page
3.3	Boltzmann plot for iron at 8 mm above the load coil and (a) an rf power of 1.25 kW, (b) 1.75 kW; the solid line represents lte, the dotted line was derived from equations (3.10) and (3.11), and the triangles represent experimental points (from reference [131]).	48
3.4	Boltzmann plot for barium at 16 mm above the load coil and (a) an rf power of 1.25 kW, (b) 1.75 kW; the solid line represents lte, the dotted line was derived from equations (3.10) and (3.11), and the triangles represent experimental points (from reference [130]).	49
3.5	Boltzmann plot for chromium at 16 mm above the load coil and (a) an rf power of 0.75, (b) 1.00, (c) 1.25 kW; the solid line represents lte, the dotted line was derived from eqns. (3.10) and (3.11), and the triangles represent experimental points (from ref. [132]).	50
3.6	Boltzmann plot for chromium at 16 mm above the load coil and (a) an rf power of 1.50 kW, (b) 1.75 kW; the solid line represents lte, the dotted line was derived from equations (3.10) and (3.11), and the triangles represent experimental points (from reference [132]).	51
3.7	The non-equilibrium b parameter for the ground state of iron (b_o) as a function of the electron density; dashed lines are drawn at b_o values of 1 and 10.	55
3.8	The minimum electron density needed for a species to be "close to lte" ($b_0 < 10$) as a function of the ionization energy.	56

Figure	Description	page
4.1	An illustration of the charge transfer process of magnesium with argon. E_i^1 (Mg) is the ionization energy of the magnesium atom, E_i^2 (Mg) of the magnesium ion, and E_i^1 (Ar) of the argon atom. The relevant energy levels are labeled with their term symbols.	60
4.2	Boltzmann plot for Mg at 6 mm alc, a radial position of 2 mm and (a) an rf power of 1.00, (b) 1.25, (c) 1.50 kW; the solid line represents lte, the dotted line the simple rate model, and the triangles experimental points.	66
4.3	Boltzmann plot for Mg at 9 mm alc, a radial position of 2 mm and (a) an rf power of 1.00, (b) 1.25, (c) 1.50 kW; the solid line represents lte, the dotted line the simple rate model, and the triangles experimental points.	67
4.4	Boltzmann plot for Mg at 12 mm alc, a radial position of 2 mm and (a) an rf power of 1.00, (b) 1.25, (c) 1.50 kW; the solid line represents lte, the dotted line the simple rate model, and the triangles experimental points.	68
4.5	Boltzmann plot for Mg at 15 mm alc, a radial position of 2 mm and (a) an rf power of 1.00, (b) 1.25, (c) 1.50 kW; the solid line represents lte, the dotted line the simple rate model, and the triangles experimental points.	69
4.6	Boltzmann plot for Mg at 18 mm alc, a radial position of 2 mm and (a) an rf power of 0.75, (b) 1.00 kW; the solid line represents lte, the dotted line the simple rate model, and the triangles experimental points.	70

Figure	Description	page
4.7	Boltzmann plot for Mg at 18 mm alc, a radial position of 2 mm and (a) an rf power of 1.25, (b) 1.50 kW; the solid line represents lte, the dotted line the simple rate model, and the triangles experimental points.	71
4.8	Boltzmann plot for Mg at 21 mm alc, a radial position of 2 mm and (a) an rf power of 1.00, (b) 1.25, (c) 1.50 kW; the solid line represents lte, the dotted line the simple rate model, and the triangles experimental points.	72
4.9	A plot of $\ln\{b(Mg^+_{ct})\}$ (measured from the data presented in figures 4.2-4.8) versus $\ln\{b(Mg_o)\}$ (calculated from equation (3.10)). The line is a linear regression to the points, the equation for which is shown in the inset box.	76
4.10	A plot of $b(Ar_o)$, calculated using the data presented in figure 4.9 and equation (4.2), as a function of the corresponding electron density.	78
4.11	A plot of $\ln\{b(Mg^+_{hi\ E})\}$ as a function of $\ln\{b(Mg^+_{ct})\}$ for the data presented in figures 4.2-4.8. The line is a linear regression to the points, the equation for which is shown in the inset box.	79
5.1	A plot of the ratio of the intensity of the Ar I 430.01 nm spectral line to the intensity of the adjacent continuum (summed over a 10.0 nm wide range), as a function of the electron temperature.	88
5.2	Plots of the electron temperature, T_e (•), and the lte temperature (calculated from the electron density), $T_{e,lte}$ (o), as a function of radial distance across the plasma at a height of 6 mm above the load coil and (a) an rf power of 0.75 kW, (b) 1.00 kW.	91

Figure	Description	page
5.3	Plots of the electron temperature, T_e (•), and the lte temperature (calculated from the electron density), $T_{e,lte}$ (○), as a function of radial distance across the plasma at a height of 6 mm above the load coil and (a) an rf power of 1.25 kW, (b) 1.50 kW.	92
5.4	Plots of the electron temperature, T_e (•), and the lte temperature (calculated from the electron density), $T_{e,lte}$ (○), as a function of radial distance across the plasma at a height of 12 mm above the load coil and (a) an rf power of 0.75 kW, (b) 1.00 kW.	93
5.5	Plots of the electron temperature, T_e (•), and the lte temperature (calculated from the electron density), $T_{e,lte}$ (○), as a function of radial distance across the plasma at a height of 12 mm above the load coil and (a) an rf power of 1.25 kW, (b) 1.50 kW.	94
5.6	Plots of the electron temperature, T_e (•), and the lte temperature (calculated from the electron density), $T_{e,lte}$ (○), as a function of radial distance across the plasma at a height of 18 mm above the load coil and (a) an rf power of 1.25 kW, (b) 1.50 kW.	95
5.7	Plot of the electron temperature, T_e (•), and the lte temperature, $T_{e,lte}$ (solid line), as a function of the electron density; the error bars on T_e are 10 % of that value. In addition, the data of Huang and Hieftje [68] is shown (□).	98
6.1	A plot of the mass of solvent delivered to the plasma as a function of the sheath gas flow rate.	106
6.2	A schematic diagram showing how iron, in the form of ferrocene vapour, was introduced into the plasma.	107

Figure	Description	page
6.3	Plots showing the lateral (a) and the radial (b) intensity distributions of the 486.13 nm hydrogen line; the height above the load coil was 6 mm and the sheath gas flow rate was 0.2 L/min.	110
6.4	Plots showing the wavelength profiles of the H_β line both before (a) and after (b) the Abel inversion process; the plot also shows the full width at half maximum ($\Delta\lambda_{1/2}$) for the Abel inverted case. The height above the load coil was 6 mm, the sheath gas flow rate was 0.2 L/min, and the radial position was +4 mm.	112
6.5	Plots showing (a) ten replicate measurements of the spatially resolved electron density and (b) the resulting percent relative standard deviation; the height above the load coil was 6 mm and the sheath gas flow rate was 0.0 L/min.	113
6.6	Contour plots of the spatially resolved electron density at sheath gas flow rates of (a) 0.0, (b) 0.2, (c) 0.4 and (d) 0.6 L/min. The contour lines are labeled in units of 10^{15} cm^{-3}.	114
6.7	Contour plots of the spatially resolved intensity of the Ar I 549.59 nm spectral line at sheath gas flow rates of (a) 0.0, (b) 0.2, (c) 0.4 and (d) 0.6 L/min. The contour lines are labeled in arbitrary units.	118
6.8	Contour plots of the spatially resolved intensity of the H_β line (486.13 nm) at sheath gas flow rates of (a) 0.0, (b) 0.2, (c) 0.4 and (d) 0.6 L/min. The contour lines are labeled in arbitrary units.	119

Figure	Description	page
6.9	Contour plots of the spatially resolved intensity of the Sr I 460.7 nm spectral line at sheath gas flow rates of (a) 0.0, (b) 0.2, (c) 0.4 and (d) 0.6 L/min. The contour lines are labeled in arbitrary units (but are consistent with those of figure 6.10).	122
6.10	Contour plots of the spatially resolved intensity of the Sr II 407.8 nm spectral line at sheath gas flow rates of (a) 0.0, (b) 0.2, (c) 0.4 and (d) 0.6 L/min. The contour lines are labeled in arbitrary units (but are consistent with those of figure 6.9).	123
6.11	Contour plots of the spatially resolved ratio of the Sr II 407.8 nm intensity to the Sr I 460.7 nm spectral line intensity at sheath gas flow rates of (a) 0.0, (b) 0.2, (c) 0.4 and (d) 0.6 L/min.	127
6.12	Contour plots of the spatially resolved value of the non-equilibrium parameter, b_r, for the strontium lines listed in Table IV at sheath gas flow rates of (a) 0.0, (b) 0.2, (c) 0.4 and (d) 0.6 L/min.	128
6.13	Contour plots of the spatially resolved intensity of the Ca I 422.7 nm spectral line at sheath gas flow rates of (a) 0.0, (b) 0.2, (c) 0.4 and (d) 0.6 L/min. The contour lines are labeled in arbitrary units (but are consistent with those of figure 6.14).	131
6.14	Contour plots of the spatially resolved intensity of the Ca II 393.6 nm spectral line at sheath gas flow rates of (a) 0.0, (b) 0.2, (c) 0.4 and (d) 0.6 L/min. The contour lines are labeled in arbitrary units (but are consistent with those of figure 6.13).	132

Figure	Description	page
6.15	Contour plots of the spatially resolved value of the non-equilibrium parameter, b_r, for the calcium lines listed in Table IV at sheath gas flow rates of (a) 0.0, (b) 0.2, (c) 0.4 and (d) 0.6 L/min.	133
6.16	Contour plots of the spatially resolved intensity of the Cd I 228.8 nm spectral line at sheath gas flow rates of (a) 0.0, (b) 0.2, (c) 0.4 and (d) 0.6 L/min. The contour lines are labeled in arbitrary units (but are consistent with those of figure 6.17).	136
6.17	Contour plots of the spatially resolved intensity of the Cd II 226.5 nm spectral line at sheath gas flow rates of (a) 0.0, (b) 0.2, (c) 0.4 and (d) 0.6 L/min. The contour lines are labeled in arbitrary units (but are consistent with those of figure 6.16).	137
6.18	Contour plots of the spatially resolved intensity of the Zn I 213.9 nm spectral line at sheath gas flow rates of (a) 0.0, (b) 0.2, (c) 0.4 and (d) 0.6 L/min. The contour lines are labeled in arbitrary units (but are consistent with those of figure 6.19).	138
6.19	Contour plots of the spatially resolved intensity of the Zn II 202.5 nm spectral line at sheath gas flow rates of (a) 0.0, (b) 0.2, (c) 0.4 and (d) 0.6 L/min. The contour lines are labeled in arbitrary units (but are consistent with those of figure 6.18).	139
6.20	Plots of the intensities of the Ba I 553.6 nm and the Ba II 455.4 nm spectral lines (taken at radial positions of 0 mm and a height of 10 mm alc), as a function of the sheath gas flow rate.	142

Figure	Description	page
6.21	Contour plots of the spatially resolved intensity of the Fe I 372.0 nm spectral line using aqueous sample introduction at sheath gas flow rates of (a) 0.0, (b) 0.2, (c) 0.4 and (d) 0.6 L/min. The contour lines are labeled in arbitrary units (but are consistent with those of figures 6.22 to 6.24).	144
6.22	Contour plots of the spatially resolved intensity of the Fe II 275.6 nm spectral line using aqueous sample introduction at sheath gas flow rates of (a) 0.0, (b) 0.2, (c) 0.4 and (d) 0.6 L/min. The contour lines are labeled in arbitrary units (but are consistent with those of figures 6.21, 6.23 and 6.24).	145
6.23	Contour plots of the spatially resolved intensity of the Fe I 372.0 nm spectral line using ferrocene sample introduction at sheath gas flow rates of (a) 0.0, (b) 0.2, (c) 0.4 and (d) 0.6 L/min. The contour lines are labeled in arbitrary units (but are consistent with those of figures 6.21, 6.22 and 6.24).	146
6.24	Contour plots of the spatially resolved intensity of the Fe II 275.6 nm spectral line using ferrocene sample introduction at sheath gas flow rates of (a) 0.0, (b) 0.2, (c) 0.4 and (d) 0.6 L/min. The contour lines are labeled in arbitrary units (but are consistent with those of figures 6.21 to 6.23).	147
7.1	Response function (shown for three adjacent diodes) of the 4096 pixel photodiode array.	156
7.2	Calculated instrumental profile, I(x), for entrance slit widths of (a) 10 μm, (b) 30 μm, and (c) 50 μm.	160

Figure	Description	page
7.3	Calculated scanned pmt response for equal entrance and exit slit widths of (a) 10 μm, (b) 30 μm, and (c) 50 μm.	161
7.4	Calculated scanned pmt response, with an expanded intensity scale, for equal entrance and exit slit widths of (a) 10 μm, (b) 30 μm, and (c) 50 μm.	162
7.5	Calculated lpda response for entrance slit widths of (a) 10 μm, (b) 30 μm, and (c) 50 μm.	163
7.6	Experimental scanned pmt relative response for equal entrance and exit slit widths of (a) 10 μm, (b) 30 μm, and (c) 50 μm.	164
7.7	Experimental lpda relative response for entrance slit widths of (a) 10 μm, (b) 30 μm, and (c) 50 μm.	165
7.8	Effect of translating the calculated instrumental profile across the lpda for an entrance slit width of 10 μm; (a) a translation of 3.75 μm, (b) a translation of 7.5 μm.	167
7.9	Effect of translating the calculated instrumental profile across the lpda for an entrance slit width of 50 μm; (a) a translation of 3.75 μm, (b) a translation of 7.5 μm.	168
7.10	Plot of the percent maximum intensity when the calculated instrumental profile is displaced by one half of the diode width (7.5 μm) as a function of the entrance slit width.	169
8.1	Flowchart showing the logic of the spectral simulation program.	177

Figure	Description	page
8.2	Comparison of Gaussian (a) and diffraction (b) instrumental profiles. The inner plots are with no scale expansion, and the outer ones are with a scale expansion of 10 000 times.	181
8.3	Computer simulated iron emission spectra; (a) over the wavelength range 240 to 280 nm, (b) 360 to 400 nm. Wavelengths are tabulated in nm. Inset from 242 to 255 nm was recorded at five times the gain as the remainder of the spectrum.	185
8.4	A comparison between a simulated iron spectrum over the wavelength range 240 to 280 nm (a) and an experimental spectrum over the same range (b). The insets from 242 to 255 nm were recorded at five times the gain as the remainder of the spectra.	186
8.5	A comparison between a simulated iron spectrum over the wavelength range 360 to 400 nm (a) and an experimental spectrum over the same range (b).	188
8.6	Computer simulation of a multi-element mixture. Wavelength range is 338.0 to 338.6 nm at a spectral bandpass of 0.04 nm; (a) linear scale, (b) logarithmic scale. The spectral lines used are given in Table V.	191
8.7	Computer simulation (a) and experimental spectrum (b) of Ag (o), Co (□), Mo(Δ), and Hf(●) in the wavelength range 338.0 to 338.6 nm. The spectral lines used are given in Table V.	192

Figure	Description	page
8.8	Simulation of the silver 338.92 nm line at a concentration of 10 ppm in a silver rich geochemical matrix showing the effect of instrumental bandpass; (a) with no instrumental broadening, and (b) with a 0.005 nm spectral bandpass. The lines are identified by the letters given in Table V.	194
8.9	Simulation of the silver 338.92 nm line at a concentration of 10 ppm in a silver rich geochemical matrix showing the effect of instrumental bandpass; (a) with a 0.01 nm spectral bandpass, and (b) with a 0.04 nm spectral bandpass.	195
8.10	Simulation of the silver 338.92 nm line in NBS coal fly ash at a 0.01 nm instrumental bandpass showing the effect of the silver concentration; (a) with no instrumental broadening and 10 ppm silver, and (b) with 50 ppm silver. The lines are identified by the letters given in Table VI.	199
8.11	Simulation of the silver 338.92 nm line in NBS coal fly ash at a 0.01 nm instrumental bandpass showing the effect of the silver concentration; (a) with 10 ppm silver, and (b) with 1 ppm silver.	200
8.12	Simulation of the silver 328.07 nm line in NBS coal fly ash at a 0.01 nm instrumental bandpass showing the effect of the silver concentration; (a) with no instrumental broadening and 10 ppm silver, and (b) with 10 ppm silver. The lines are identified by the letters given in Table VII.	202
8.13	Simulation of the silver 328.07 nm line in NBS coal fly ash at a 0.01 nm instrumental bandpass showing the effect of the silver concentration; (a) with 1 ppm silver, and (b) with 0.1 ppm silver.	203

Figure	Description	page
8.14	Simulation of the silver 338.92 nm line in the geochemical matrix at a 0.005 nm instrumental bandpass showing the effect of adding random noise to the spectrum presented in figure 5.8 (b); (a) with a constant background of 0.001 with 1 % random noise, (b) with a constant background of 0.01 with 1 % random noise.	205
9.1	A screen dump of the "Line Data" prompt window of the preliminary spectral simulation program written for the Macintosh computer.	212

Acknowledgements

This work is dedicated both to my parents, Lorrence and June Burton, and to my wife, Lee Smith, for their love, patience and support during the course and preparation of this thesis.

A sincere thank you to my supervisor, Mike Blades, for his invaluable guidance throughout the past five years.

A special thanks to the various members of the research group, both for beneficial discussions and their camaraderie - in particular Bernard Dargle and Peter Blanks.

I would also like to acknowledge the financial support of the Natural Sciences and Engineering Research Council of Canada, as well as of the Analytical Division of the American Chemical Society for a summer fellowship sponsored by the Pittsburgh Conference and Exposition.

List of Symbols

A	spontaneous radiative decay transition probability
AA	atomic absorption
alc	above the load coil
AW	atomic weight
$A_{\infty \rightarrow i}$	hypothetical spontaneous radiative decay transition probability from the hypothetical "∞" energy level to energy level "i"
b	non-lte overpopulation factor
b_{atom}	non-lte overpopulation factor for atoms
b_{ion}	non-lte overpopulation factor for ions
b_r	ratio of an experimental ion-to-atom emission intensity ratio to its lte value
C	concentration; an arbitrary constant
$CD_{\infty \rightarrow i}$	hypothetical collisional decay rate co-efficient (by electron impact) from the hypothetical "∞" energy level to energy level "i"
$CE_{i \rightarrow \infty}$	hypothetical collisional excitation rate co-efficient (by electron impact) from energy level "i" to the hypothetical "∞" energy level
c_n	centre position of n'th diode of photodiode array
CT	charge transfer
cte	complete thermodynamic equilibrium
D	the monochromator aperture width

E	excitation energy
E_i, E_j	excitation energy of atomic energy states
E_{ion}, E_∞	ionization energy
E_p, E_q	excitation energy of ionic energy states
f	focal length of monochromator focusing mirror
f'	focal length of monochromator collimating mirror
g	degeneracy of an atomic or ionic energy level
$<\bar{g}>$	thermally averaged Gaunt factor
h	Planck's constant
H_β	486.13 nm spectral transition of hydrogen
icp-afs	inductively coupled plasma - atomic fluorescence spectrometry
icp-ms	inductively coupled plasma - mass spectrometry
icp-oes	inductively coupled plasma - optical emission spectrometry
$I(r)$	radial intensity across plasma
$I(x)$	lateral intensity across plasma
I_a	intensity of an atomic spectral transition
I_i	intensity of an ionic spectral transition
I_n	intensity detected by n'th diode of photodiode array
k	Boltzmann's constant
lpda	linear photodiode array
lte	local thermodynamic equilibrium

M^{+}_{ct}	charge transfer energy states of an ionic species
m_e	electron mass
N, N'	normalization constants
n	population density of a species
NBS	National Bureau of Standards (USA)
n_e	electron density
n_I	population density of atoms
n_{II}, n_i	population density of ions
n_j	population density of a species in the energy state "j"
$n_{i,exp}$	experimental population density of a species in the energy state "i"
$n_{i,lte}$	equilibrium population density of a species in the energy state "i"
$n_{\infty,exp}$	hypothetical experimental population density of the hypothetical "∞" energy level
$n_{\infty,lte}$	hypothetical equilibrium population density of the hypothetical "∞" energy level
o	subscript referring to the ground state atom or ion energy level
P	pressure
p-lte	partial local thermodynamic equilibrium
pmt	photomultiplier tube
ppm	parts per million
Q(T)	partition function

r	radial position across plasma
R	radius of plasma
$R(x)$	response function of photodiode array
$RD_{\infty \rightarrow i}$	hypothetical spontaneous radiative decay rate co-efficient (by electron impact) from the hypothetical "∞" energy level to energy level "i"
s	monochromator entrance slit width
s'	monochromator exit slit width
T	temperature
T_e	electron temperature
$T_{e,lte}$	equilibrium electron temperature (calculated from the electron density)
T_{exc}	excitation temperature
T_{gas}	gas temperature
T_{ion}	ionization temperature
T_{rad}	radiation temperature
T_{react}	reaction temperature
T_{trans}	translational temperature
x	lateral distance across plasma; distance across photodiode array
$\Delta\lambda_{1/2}$	full width at half-maximum intensity of a spectral line
$\varepsilon_{continuum}$	intensity of the plasma continuum
ε_{line}	intensity of the 430.01 nm argon spectral line

γ	degree of ionization
λ	wavelength
$d\lambda/dx$	reciprocal linear dispersion of monochromator

Chapter 1
Introduction

1.1 Objectives

The design and construction of new plasma sources, along with the improvement of old ones, are clearly amongst the primary objectives of the analytical atomic spectroscopist. In order to help achieve these objectives, research into the various excitation mechanisms and other fundamental characteristics of existing plasma sources is of prime importance. Such "fundamental studies" have as their goal the elucidation of these excitation mechanisms, etc. in terms of parameters such as the temperature and the various particle densities (in particular the electron density). Such knowledge should allow one to make various improvements to existing plasma devices and, ideally, point the way to new ones.

The objectives of this thesis are twofold. Firstly, to understand the inductively coupled plasma (icp) from a fundamental point of view - in particular to understand why and how deviations from equilibrium in the icp come about. To this end the plasma has been characterized in terms of electron density, etc. with an extra argon flow added to the aerosol gas, the effect of charge exchange of magnesium with argon has been studied, and electron temperatures have been determined. A simple rate model has been developed which can accurately predict deviations from equilibrium in the icp (for elements which do not exhibit charge transfer with argon). The second objective was to put fundamental knowledge of the icp to practical use: this was done by writing a computer program capable

of allowing icp emission spectra to be simulated with reasonable accuracy.

1.2 Historical

Although pioneered by scientists such as Fraunhofer, the birth of analytical spectroscopy can perhaps be said to date from 1860 when Kirchhoff and Bunsen [77] demonstrated conclusively that the atoms of a metal vaporized in Bunsen's then recently perfected burner emitted light, in the form of characteristic lines, which could be used to positively identify the metal. These workers soon discovered the elements caesium and rubidium; other workers also soon discovered new elements. Thus, although the method was still qualitative, its power was proven.

It was not until the development of sensitive photographic emulsions that quantitative spectrochemical analysis became practical. In 1925 Gerlach began the development of analytical spectrography using arcs and sparks as excitation sources; in 1928 Lundegårdh did the same using flames, leading to the release of the first commercial flame spectrometer in the mid 1930's. Improvements in photoelectric detection, culminating in the invention of the photomultiplier tube during the Second World War, greatly aided the popularity of spark and flame spectrometry in the succeeding years. Throughout the remainder of the 1940's and the 1950's arcs were often the excitation source of choice because, even though they suffered from interferences and self-absorption, the relatively cool temperature of flames made them unsuitable for emission spectroscopy for many elements.

In 1955 Walsh [133] and Alkemade and Milatz [3, 4] led the way to the introduction of flame atomic absorption spectroscopy with their realization that flames could be used for atomizing the sample and that hollow-cathode lamps or gas discharge tubes could be used as excitation sources. The first commercial instruments appeared in 1959. Throughout the 1960's and early 1970's, due to the low detection limits obtainable with flame atomic absorption (AA), the popularity of this technique increased greatly. Because the flame AA method was inherently a single element technique (i.e. only one element could be determined at a time) arc and spark spectrographs with photographic detection still continued to be used, although mostly for qualitative and semi-qualitative analysis.

Although direct current plasma arc devices were first introduced for solution spectrochemical analysis in 1959, it was not until the early 1970's that improvements allowed them to become commercially successful. However, the latest revolution in spectrochemical analysis was caused by the commercial introduction (in 1975) of the inductively coupled plasma, to which we now turn.

1.3 The Inductively Coupled Plasma

1.3.1 Development

Plasmas* sustained at reduced pressures by induction heating using radio frequency currents have existed since the turn of the

* A plasma can be defined as a macroscopically neutral, "sufficiently" ionized collection of charged and neutral particles; sufficiently ionized implies that the particle motions not be dominated by collisions with neutral species.

century [99], however it was not until 1947 that Babat [7] was able to sustain such a discharge at atmospheric pressure. In the early 1960's Reed [114, 115] described an inductively coupled plasma operating at atmospheric pressure supported by a flow of argon gas. This author's plasma torch consisted of a quartz tube, open at one end, through which a flow of argon was passed. The open end of the tube was surrounded by a five-turn water cooled induction coil (operating at 4 MHz and up to 10 kW) which sustained the plasma.

Greenfield et al. [54] and Wendt and Fassel [136] quickly realized the potential application of this new device to analytical atomic spectroscopy. Over the next ten years or so improvements to the method, made largely in Professor Fassel's laboratory (such as the reduction of radio-frequency interference with the measurement electronics, improvements in techniques for generating aerosols and in their injection into the plasma, and especially the optimization of torch design [46]), led to the release of the first commercial icp system in 1975.

Inductively coupled plasma optical emission spectroscopy (icp-oes) has found application for the determination of elemental composition in a number of diverse sample types such as those of geological, agricultural, clinical, petrochemical, and environmental origin. The growth of the method over the last fifteen years or so has been quite astounding; icp-oes is without doubt the dominant method for multi-element analysis of liquids. As of 1987 there were approximately thirty different manufacturers of icp instruments and more than 6000 units operating [99] (the number today is probably nearer 7500).

The growth of the icp technique is due to a number of factors: when coupled to an appropriate detection system icp-oes is very well suited to multi-element analysis (unlike AA), is relatively free from chemical interferences, has a large linear dynamic range (five to six orders of magnitude) and low detection limits (in the range 1 to 20 ng/mL for many elements). In addition to its use in icp-oes, the icp is currently being marketed as an atom source for atomic fluorescence (icp-afs) and as an ion source for mass spectrometric detection (icp-ms). For a more detailed review on the development of the various icp techniques the reader is referred to reference [46].

1.3.2 Operation

A schematic diagram of the icp torch, along with some features of the plasma itself, is given in figure 1.1. Typical values for the rf power and the various flow rates used in this work are given in the figure. The plasma is sustained by the "plasma" (or "support") gas; this gas is generally argon, although other gases have been used. The plasma gas flows axially through a quartz tube which is surrounded by three or four turns of an induction coil connected to a radio frequency generator (the standard frequency of which is 27.12 or 40.68 MHz in North America). The current flowing in the induction coils generates an oscillating magnetic field parallel to the quartz tube. This induced magnetic field in turn induces an emf (Faraday's law) which causes any free electrons to flow in closed annular paths, known as the eddy current, inside the quartz tube space. Resistive or ohmic heating then occurs, thus resulting in a plasma.

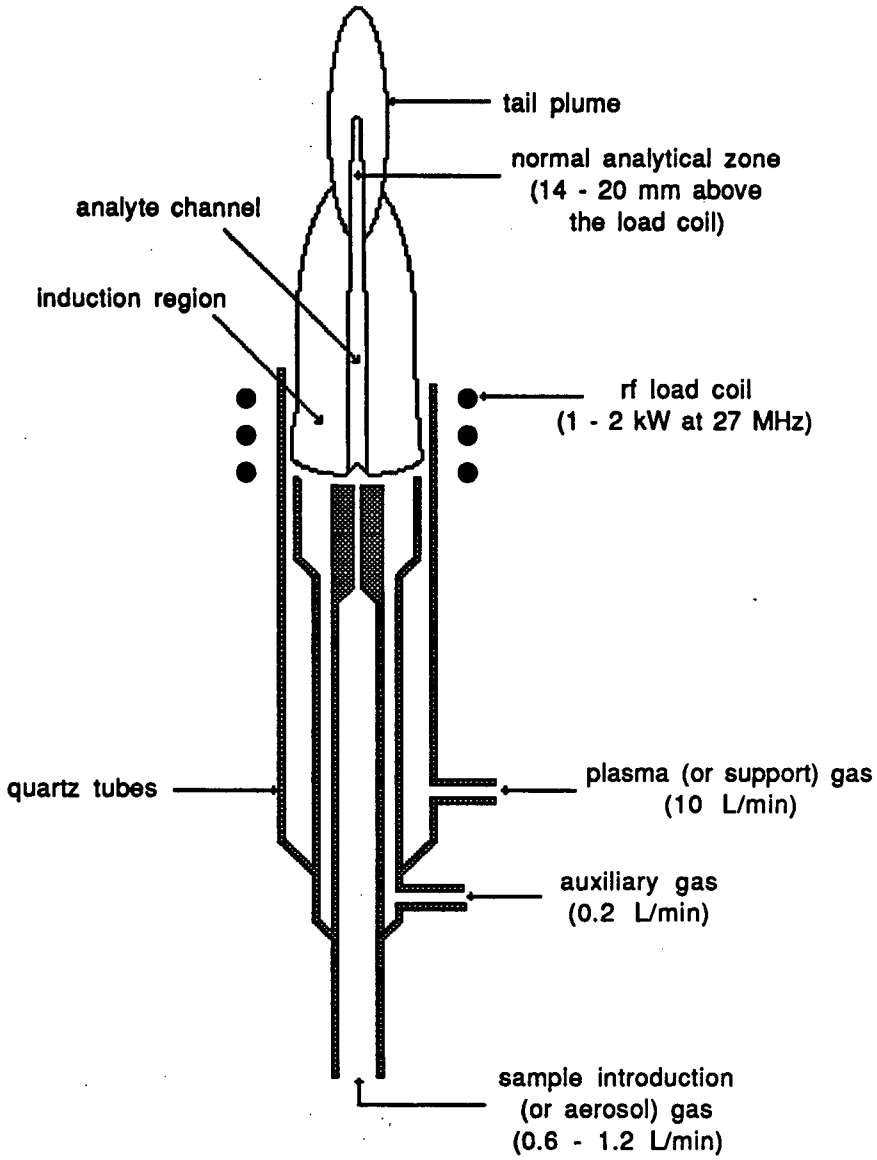

Figure 1.1 A schematic diagram of the inductively coupled plasma torch also showing some features of the plasma.

Since the argon plasma gas is initially neutral, it must be seeded with electrons, usually from a brief Tesla discharge, in order to ignite the plasma - it then becomes self-sustaining. The auxiliary argon gas serves to lift the plasma slightly so that it does not come in contact with the quartz tubes (and thus melt them).

The argon support gas in the inductively coupled plasma is about 0.1 percent ionized, resulting in electron densities of from about $5x10^{14}$ to $5x10^{15}$ cm^{-3} and electron temperatures in the range 7000 to 9000 K. Analyte introduced into the plasma is quickly atomized and ionized (the degree of ionization being between 70 and 99 percent for most elements).

The usual method of introducing samples into the plasma is as aerosols generated using a nebulizer; solid samples must first, therefore, be dissolved (using acid solutions or fusion methods if necessary). The aerosols generated in this way are then passed into a spray chamber which allows only those droplets with diameters less than about 10 µm to be carried through by the argon stream, the rest going to a waste container (this is illustrated schematically in figure 2.1). These droplets are carried into the plasma by the sample introduction gas (see figure 1.1) which causes a channel, known as the "analyte channel", to form running the length of the plasma discharge.

As the aerosol is carried up the channel it mixes with the hot plasma gas and is desolvated, vaporized, dissociated, excited and ionized. Spectral emission from analyte atoms and ions is usually observed at a height of 14 to 20 mm above the top of the load coil (the "normal analytical zone"). Lower down in the plasma there is

intense continuum emission and higher up there will be molecular species starting to form. In commercial icp systems the emitted radiation is detected with either a polychromator (containing a number of photomultiplier tubes) or a sequential slew-scan monochromator to isolate the spectral lines of interest. The emission intensity for each line is then measured and the elemental concentration determined from a calibration curve. For the system in our laboratory radiation was detected using a photodiode array (to be described briefly in the next chapter).

For more details on icp instrumentation in general the reader is referred to the publications by Barnes [9], Boumans [18] and Montaser and Golightly [102]. Before describing the physical properties of the icp discharge in more detail, some general plasma excitation mechanisms will first be discussed, as will the concept of thermodynamic equilibrium (and deviations from it). In addition, the plasma diagnostic method of using the Stark broadening of spectral lines to calculate the electron density will be very briefly described.

1.4 Collisional and Radiative Processes

In order to understand the behaviour of analyte in the icp at a fundamental level, it is necessary that the various mechanisms through which energy is exchanged between analyte atoms and other plasma species be known. Since this thesis is mainly concerned with the behaviour of analyte species, only those collisional and radiative processes believed to play an important role in analyte behaviour in the icp will be described and discussed here.

Collisions can be classified into two basic types: elastic and inelastic. In elastic collisions, the total kinetic energy of the colliding particles is conserved and there is no change in the internal (potential) energies of the individual particles. In general, such collisions serve to establish a Maxwell-Boltzmann velocity distribution of particles. Inelastic collisions, on the other hand, result in changes in the internal energies of the particles. Kinetic energy may be lost to excite or ionize the particles, or it may be gained as the particles are de-excited to lower energy levels. Internal energy may also be lost or gained with the emission or absorption of a photon. The following are the important inelastic processes in the icp:

(i) *Collisional excitation and de-excitation by electrons.*

Analyte atoms (M) or ions (M^+) collide with a free electron (e^-) and undergo a transition in internal energy by giving up (or taking) kinetic energy to (or from) the electron. This process can be written:

$$M_i + e^- \rightleftarrows M_j + e^- \quad \text{where } E_j > E_i \qquad (1.1)$$

$$M_p^+ + e^- \rightleftarrows M_q^+ + e^- \quad \text{where } E_q > E_p \qquad (1.2)$$

where E_i, E_j, E_p and E_q are the excitation energies of the respective levels. For the forward processes the relative kinetic energy must be at least as large as the energy difference between the two energy levels. The rates of collisional excitation and de-excitation by

electron impact will be far larger than for collisions with heavy particles [101, 103]. Thus for plasmas with reasonably high degrees of ionization (such as the icp), it is not generally necessary to consider the collisional excitation and de-excitation of analyte from collisions with heavy particles. The reason for this is the following: the electron is a charged particle with small mass. So the long range interactions (large cross sections) take place with a large rate (large velocity).

(ii) *Collisional ionization and three-body recombination by electrons.*

This process can be written:

$$M_i + e^- \rightleftarrows M^+ + 2e^- . \qquad (1.3)$$

In the forward process (collisional ionization) an atom in a particular state, i, is ionized by impact with a fast moving electron. The kinetic energy of the electron must be at least as large as the binding energy of the electron to the atom in this particular excited state. This process generally leads to the production of analyte ions in their ground state. In the reverse process (three-body recombination) the excess energy released is carried off by the free electron.

(iii) *Charge transfer with argon.*

For argon plasmas (such as most icp's) analyte may be ionized by the transfer of an electron to a ground state argon ion resulting in

the production of an excited analyte ion (and a ground state argon atom):

$$Ar^+ + M_i \rightleftarrows M_p^+ + Ar + \Delta E\,. \qquad (1.4)$$

In order for this process to be favourable the energy difference, ΔE, should be fairly small. This relevance of this process to the icp will be discussed in detail in chapter four.

(iv) *Radiative decay.*

Analyte atoms or ions can decay radiatively from one energy level to a lower one by the emission of a photon:

$$M_j \rightarrow M_i + h\nu_{line} \quad \text{where } E_j > E_i \qquad (1.5)$$

$$M_p^+ \rightarrow M_q^+ + h\nu_{line} \quad \text{where } E_p > E_q\,. \qquad (1.6)$$

This is obviously the process which gives the icp its analytical utility in optical emission spectrometry. The intensity of such a transition is directly proportional to An/λ, where n is the population of the emitting energy level, λ is the wavelength of the transition and A is the transition probability for spontaneous emission between the levels (tabulated in a number of references such as Corliss and Bozman [38]). The reverse process of absorption, along with other processes involving the absorption of a photon (such as stimulated emission), need not be considered for analyte species

(although this is not true for argon) in the icp since analyte lines are generally optically thin for re-absorption.

(v) *Radiative recombination.*

In the last process which will be considered here, analyte ions (often in the ground state) combine with a free electron to give an excited atomic species. The excess energy is carried off by a continuum photon:

$$M^+ + e^- \rightarrow M_i + h\nu_{cont} . \qquad (1.7)$$

This process is most important at low electron densities, whereas three-body recombination becomes dominant at high electron density. The recombination of argon ions with electrons is responsible for the reasonably intense continuum emission seen in regions of high electron density in the icp.

For a more complete description of these processes, as well as for a comprehensive listing of excitation processes (including those which play a limited role in the icp), the reader is referred to references [65] and [101].

Several workers [43, 62-64, 67, 82, 83] have attempted rate model calculations of the icp in which the rate co-efficient for each fundamental process believed to be of importance is calculated for each possible transition in the system (this procedure is necessary

since the icp is not in local thermodynamic equilibrium, as will be described below). In this way it is possible to calculate the population of each energy level. The main difficulty with such calculations is the large uncertainties in the rate coefficients for the various processes. In chapter three it will be seen that it is possible to simplify matters considerably for the icp by assuming that only collisional excitation and de-excitation by electron impact along with radiative decay are important in coupling energy levels within the same ionization stage. The results of such calculations were found (for elements which do not exhibit charge transfer) to agree very well with experiment.

1.5 Thermodynamic Equilibrium

In general, at a given spatial point, plasmas cannot be described by a single temperature; that is to say they are not in equilibrium. For example, in certain glow discharges the translational temperature of atoms and ions is of the order of 1000 K, while that of the electrons is 10 to 1000 times higher [42]. This can be due either to transport effects or to the fact that certain fundamental processes are not balanced by their inverses; for example, radiation may escape the plasma so that emission will not be balanced by absorption. As will be described below and demonstrated in this thesis, this is the reason why the icp, although reasonably close to equilibrium, differs from it.

By far the simplest plasmas to describe, however, are those which are in complete thermodynamic equilibrium (cte). In this case all plasma processes are in detailed balance with their inverses, and

all temperatures in the plasma will be identical. In order to describe the concentrations of the various species in the plasma, a detailed knowledge of the rates of the fundamental processes occurring is not necessary - rather the plasma can be described by the following statistical mechanical distribution functions (which also serve to define the various temperatures).

(i) *Maxwell-Boltzmann velocity distribution.*

If free particles are in equilibrium, their velocities (for all energy levels) will have a Maxwellian distribution. The temperature in the distribution function is referred to as the translational temperature, T_{trans}. In the case of cte this temperature will be the same for all species.

(ii) *Boltzmann distribution.*

The number density, n_i, of atoms (or ions) in a particular state i, with excitation energy E_i, is given by:

$$n_i = \frac{Ng_i}{Q(T)} \exp(-E_i/kT_{exc}) \qquad (1.8)$$

where N is the total atom (or ion) number density, g_i is the statistical weight of the state i, k is Boltzmann's constant, and Q(T) is the partition function (defined as $\sum^{k} g_k \cdot \exp(-E_k/kT)$). The excitation temperature, T_{exc}, will be the same for all species in all energy levels for the case of cte.

(iii) *Saha distribution.*

The Saha equation, a particular statement of the law of mass action, describes how the population density, n_i, of a neutral atomic energy level (of excitation energy E_i) is related to that of the ground state ionic species, n_o^+:

$$\frac{n_e n_o^+}{n_i} = 2\frac{g_o^+}{g_i}\left(\frac{2\pi m_e k T_{ion}}{h^2}\right)^{3/2} \exp\left(-\frac{E_{ion}-E_i}{kT_{ion}}\right) \qquad (1.9)$$

where n_e is the free electron number density, g_o^+ and gi are the statistical weights of the two levels, m_e is the mass of the electron, h is Planck's constant, E_{ion} is the ionization energy of the atomic species, and T_{ion} is the ionization temperature. This equation can be easily generalized to refer to any two adjacent ionization stages.

The Guldberg-Waage law is another statement of the law of mass action for the particular case of molecular reactions. The temperature appearing in the distribution is referred to as the reaction temperature, T_{react}.

(iv) *Planck's law.*

For the case of cte, radiation will obey Planck's law for a blackbody radiator at the temperature T_{rad}, which serves to define the radiation temperature.

The description of a plasma in cte, in which all of the above temperatures will be equal, is relatively simple. However, virtually all analytical plasmas are rarely (if ever) in cte, and are thus usually described in terms of their departures from it.

Local Thermodynamic Equilibrium (lte).

Because photons are more likely to escape from the plasma than other species, Planck's law will virtually always be violated for analytical plasmas (a blackbody radiator would obviously be useless for analytical spectroscopy). However, it is possible for all of the other distribution functions mentioned above to hold at a given temperature for all other species (i.e. for all material particles). In this case the collisional rates which populate the various energy levels will significantly exceed radiative ones. The plasma is said to be in local thermodynamic equilibrium (lte).

Partial-local thermodynamic equilibrium (p-lte).

Due to their small mass it is possible for the free electrons to become "decoupled" from the heavier particles. A two-temperature plasma can be set up, electrons with a Maxwellian distribution at a temperature T_e, and the heavy particles at a different (lower) temperature. Electron collisions are still effective in maintaining equilibrium between species with sufficiently small energy gaps, that is to say excited atomic states near the ionization limit, along with the ground state ion. The free electrons impose their temperature upon these levels, while energy gaps between lower lying levels are too large for retaining Boltzmann equilibrium. This

is illustrated schematically in figure 1.2. The figure presents a Boltzmann plot (a plot of $\ln(n_i/g_i)$ vs. the excitation energy) for a hypothetical system in p-lte (dotted lines). For a system in lte (solid lines) equation (1.8) predicts that the result should be straight lines of slope $-1/kT_e$ for both atomic and ionic species. The "Saha jump" (the difference in ln (n/g) between excited atomic levels at the ionization limit and the ground state ion) can be calculated from equation (1.9). In the p-lte situation the highly excited atomic levels and the ground state ion are in equilibrium with each other (and the free electrons) at the temperature T_e. However, due to radiative decay competing with collisional processes, the lower energy levels are overpopulated with respect to these upper ones. The non-equilibrium parameter, b, shown in the

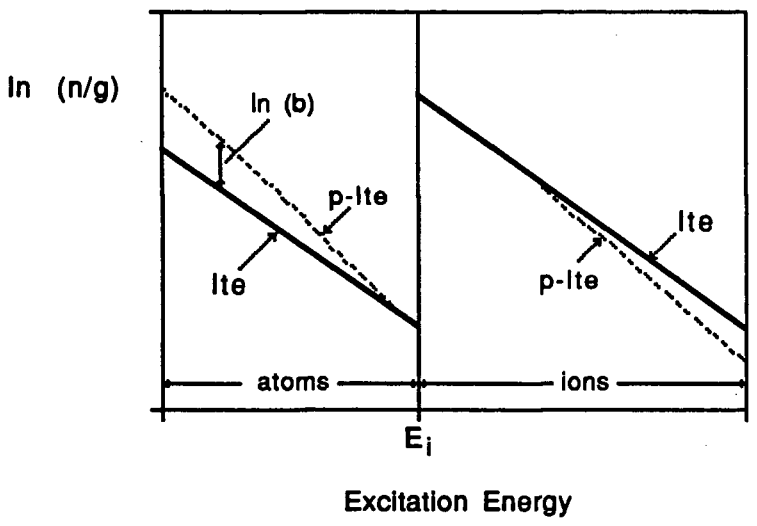

Figure 1.2 A Boltzmann plot for a system in p-lte (dotted lines); the straight lines of slope $-1/kT_{exc}$ represent the lte situation. E_i represents the ionization potential.

figure is defined as:

$$b = \frac{n_{i,exp}}{n_{i,lte}} \qquad (1.10)$$

where $n_{i,exp}$ is the actual experimental population density and $n_{i,lte}$ is the population density which would be expected based on the lte line in the figure. This parameter serves to quantify the deviation from lte.

A number of authors have discussed the lte and p-lte models in detail, and have given validity criteria for determining when it is appropriate to use a particular model [41, 42, 56, 89].

Further deviations from thermodynamic equilibrium.

In plasmas of particularly low electron density (or high electron temperature) further deviations from cte are possible. Since these models are not applicable to the icp they will not be discussed here. However, for those interested, they are described in detail in a number of publications [13, 16, 89, 103, 105, 121].

1.6 Electron Density Measurement

For plasmas which are in lte the simplest method for determining the electron density is to first determine the plasma temperature. This is done by measuring the intensities of several atomic (or ionic) spectral lines and applying equation (1.8). One then measures the intensity of both an atomic and ionic spectral line and applies equation (1.9) to give n_e. In order to do this one makes use of

the fact that the intensity of a spectral transition from one bound level of population n_i to another is directly proportional to $gA \cdot n_i/\lambda$, where λ is the wavelength of the transition and gA is the degeneracy-weighted transition probability for spontaneous emission.

For plasmas which are not in equilibrium (such as the icp) by far the most popular method of determining the electron density is from the Stark broadening of spectral lines, especially those of hydrogen. In general, this method needs to make no assumptions about the state of equilibrium in the plasma. Hydrogen spectral lines are most often used because the theory relating the degree of broadening to the electron density is more accurate for hydrogen than for other species. This method, which was used in this thesis for the measurement of the electron density, will be briefly described below. For a comprehensive treatment the reader is referred to references [55, 56, 137].

The broadening of spectral lines in plasmas is mainly of two types: Doppler broadening and pressure broadening (which is caused by the interaction of the emitters with surrounding particles). Stark broadening is due to interactions with charged particles. In most plasmas which are sufficiently ionized (such as the icp), Stark and Doppler broadening are the only significant broadening mechanisms [137]. Electrons cause broadening to occur by fast impacts which perturb the wave train of light emitted by an atom. During the time of interaction of an emitting atom with a slow moving ion the electric field due to the latter can be considered constant, thus leading to the usual Stark effect.

It is beyond the scope of this work to go into any detail, but Griem has developed a Stark broadening theory which takes into account the influence of both electrons and ions. He has published extensive tabulations of line profiles as a function of the electron density for hydrogen lines and various heavy elements [56-59, 76].

In this work the broadening of the 486.13 nm H_β spectral line (the hydrogen coming from the decomposition of nebulized water) was used for the determination of the electron density. This is the most commonly used line as it is relatively intense, is free from spectral interferences, and, most importantly, is sufficiently broadened (about 0.1 to 0.5 nm in the icp) to allow for precise measurement of the electron density. The full width at half height of the line was measured and compared with the tables of Vidal et al. [128], thus resulting in the electron density. This was then corrected by the numerical factor (1.09) of Baessler and Kock [8]. The next chapter contains a description of the experimental procedure used for the calculation of the electron density.

1.7 Equilibrium in the Inductively Coupled Plasma

Spectroscopic temperatures, electron densities, analyte level populations and other parameters have been measured for the icp by a number of workers in an attempt to determine whether or not the icp is in lte, and if not to what extent it deviates from it. In an important early paper Boumans and DeBoer [20] measured the spectral line emission intensities for both an atomic and an ionic line (of the same element). They found that the ratio of these lines exceeded calculated lte ratios by from one to three orders of

magnitude. Kalnicky et al. [75] calculated electron densities by measuring the intensities of an atomic and ionic analyte spectral line and using the Saha equation. These were found to be from 30 to 50 times less than electron densities determined from the Stark broadening of the H_β line. It thus seemed that the icp was very far from being in lte.

Caughlin and Blades [34, 36] showed that these apparently large deviations from lte were due to the fact that inappropriate analyte excitation temperatures were used in the lte calculations. They found that if a more consistent and logical lte framework (to be described below) based on the electron density were used, deviations from lte would be much less than was previously thought. These authors measured experimental ion-to-atom emission intensity ratios (I_i/I_a) and compared them to expected lte values using the b_r parameter defined as:

$$b_r = \frac{(I_i/I_a)_{exp}}{(I_i/I_a)_{lte}}. \qquad (1.11)$$

They found that this parameter differed from unity by at most a factor of five (not 1000 as had Boumans and DeBoer [20]). It is now fairly well accepted [16, 109, 131] that the icp is "close to lte" and can be accurately described by a partial-lte model. The lte framework upon which this p-lte model is based will now be described.

1.8 The Calculation of Temperature from Electron Density

In order to quantify deviations from lte, it is of course necessary to construct an lte framework to which experimental results can be compared. Since the local electron density is single valued (unlike the temperature) and can be readily measured from the Stark broadening of spectral lines without assuming thermal equilibrium, it is the ideal (if not crucial) parameter upon which to base this lte framework.

As has been previously pointed out [112], it is possible to calculate a temperature from the measured electron density by making the very good approximation that the only species present in the plasma are free electrons, argon atoms and argon ions. One then applies the conditions of local electrical neutrality, the ideal gas law and the Saha equation to result in an lte electron temperature ($T_{e,lte}$). The relation between n_e (in cm^{-3}) and $T_{e,lte}$ (in K) can be written:

$$n_e = 5.95 \times 10^{18} \sqrt{\sqrt{T_{e,lte}}\,(4+2\exp(-2061/T_{e,lte}))\exp(-182900/T_{e,lte})} \quad (1.12)$$

In order to determine $T_{e,lte}$ from the electron density the equation can be solved numerically. This function is plotted in figure 1.3. As will be seen in chapter eight, $T_{e,lte}$ seems to agree quite closely with the actual electron temperature, although its main purpose is simply to set up the lte framework. Once the electron density and $T_{e,lte}$ are known it is possible to calculate equilibrium values of the level populations of the various species in the plasma from the relations given in section 1.5.

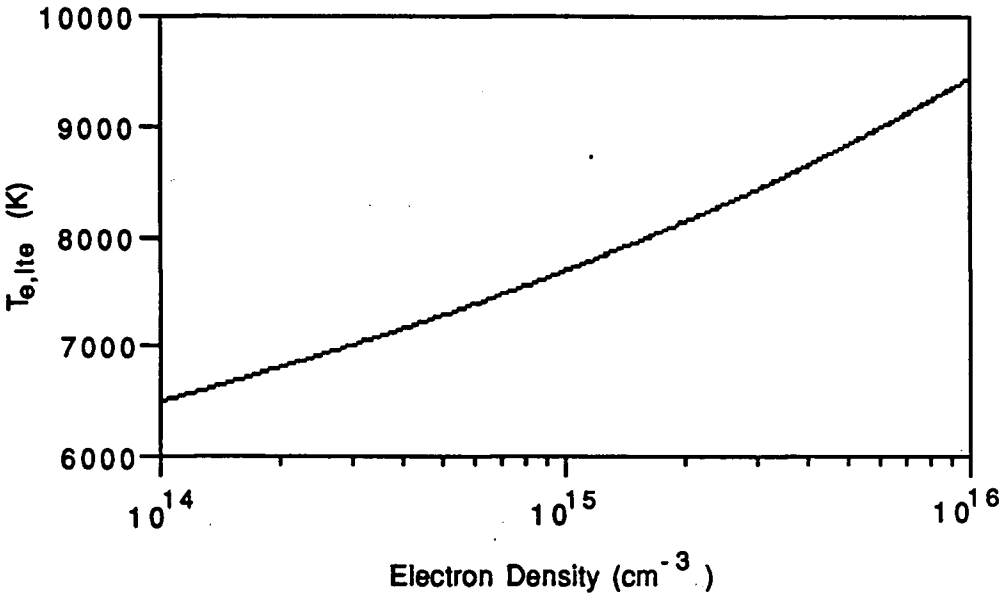

Figure 1.3 A plot of the lte electron temperature, $T_{e,lte}$, in the inductively coupled plasma as a function of the electron density.

Even though it is generally accepted that the icp can be described by a p-lte model, there is still some debate as to the exact cause for the deviation from lte. Some authors suggest that transport processes play a dominant role [109], whereas others feel that radiative decay is primarily responsible for these deviations [2, 16]. In chapter three of this thesis a simple two-level rate model will be developed, showing that significant deviations from lte can be attributed to radiative decay.

1.9 Overview of Thesis

In the next chapter of this thesis, a brief description of the experimental system used will be given. As mentioned above,

chapter three will present a simple two-level rate model of analyte level populations. This model is capable of accurately estimating the departures of analyte level populations from lte, at least for those elements which do not exhibit charge transfer with the argon support gas. Chapter four will present a study of magnesium excited state level populations with particular reference to charge transfer with argon. The main conclusion of this chapter is that charge transfer between argon ions and ground state magnesium atoms causes ionic magnesium energy levels to be overpopulated (with respect to the simple rate model calculations). Chapter five is a study of electron temperatures in the icp. It will be shown that for electron densities greater than about $2x10^{15}$ cm^{-3} the electron temperature is within experimental uncertainty of the lte temperature (as calculated from the electron density). In chapter six an extra argon flow which was added to the aerosol gas will be described. This allowed the effect of the sample introduction gas flow rate on plasma conditions (while keeping the total amounts of both analyte and solvent reaching the plasma constant) to be studied.

The next two chapters will develop a method of generating computer simulated emission spectra for the icp, thus putting the results of icp fundamental studies to practical use. Chapter seven will describe in detail a realistic instrumental profile and the influence of instrumental broadening on the lineshapes detected by pmt and photodiode array detectors. Chapter eight will present the spectral simulation program; it will be seen that the method shows considerable promise as a tool to study the effect of spectral line overlaps, particularly for mixtures having complex composition.

Chapter 2
Experimental

2.1 Instrumentation

A schematic diagram of the icp-oes data collection system used for this work is presented in figure 2.1. Most of the various components have been described in some detail in previous publications from the research group [32, 35, 66, 130, 131], so only a brief summary will be given here. For more details on icp instrumentation in general the reader is referred to the publications by Barnes [9], Boumans [18], and Montaser and Golightly [102].

Specifications for some of the various components used are summarized in Table I. The icp torch was constructed in the UBC glass shop from quartz tubing; the dimensions of the outer tube were: o.d. = 20 mm, i.d. = 17 mm, of the intermediate tube: o.d. = 15 mm, i.d. = 13 mm, and of the aerosol tube: o.d. = 6 mm, i.d. = 1.5 mm.

For most of the work done the nebulizer and spray chamber combination listed in Table I were used, whereas for some (to be noted where appropriate) a Meinhard (Santa Ana, CA) model TR-30-A3 concentric glass nebulizer and a Plasma-Therm (Kresson, NJ) Scott type spray chamber were used. When fitted to an argon regulator at 200 psi the Sherrit-Gordon nebulizer had an uptake rate of 1.7 mL/min and a resulting argon flow rate of 0.60 L/min. For the Plasma-Therm nebulizer fitted to an argon regulator at 32 psi the free uptake rate was found to be 3.2 mL/min and the argon flow rate 1.00 L/min.

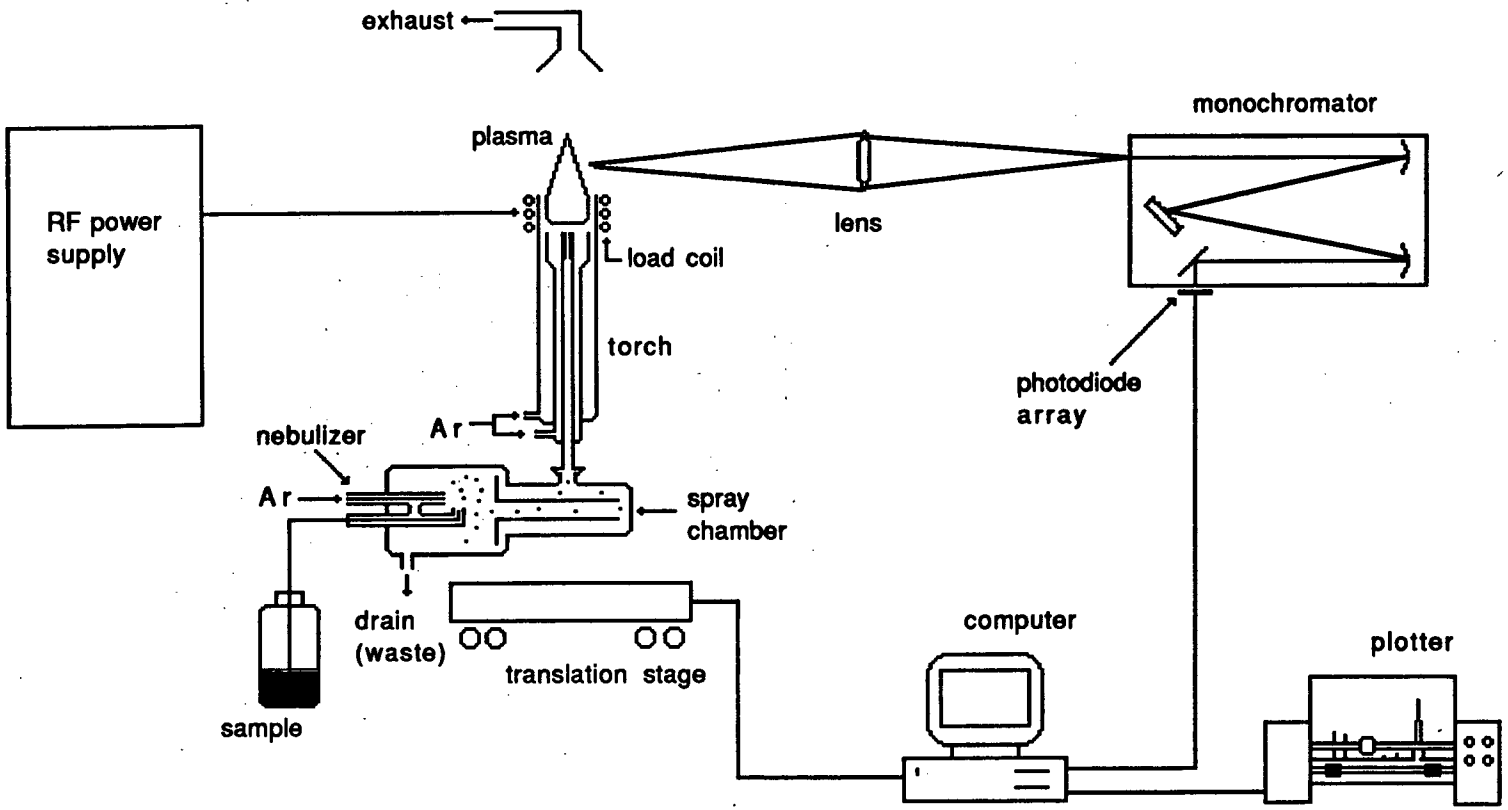

Figure 2.1 Schematic diagram of inductively coupled plasma - optical emission spectrometer system.

Table I: Details of the experimental system

icp system	Plasma-Therm (Kresson, NJ) HFP-2500 rf generator, AMN-2500E automatic matching network, APCS-1 automatic power control unit. The operating frequency was 27.12 MHz and the maximum output power to the load coil was approximately 2.5 kW.
monochromator	Schoeffel-McPherson (Acton, MA) model 270 Czerny-Turner. The focal length was 1.0 m.
grating	Schoeffel-McPherson (Acton, MA) model AH-3264 holographic grating with 1200 lines/mm; this resulted in a reciprocal linear dispersion of 0.83 nm/mm.
detector	Reticon (Sunnyvale, CA) model RL-4096/20: a 4096 pixel photodiode array with their accompanying evaluation board.
thermoelectric cooler	A Melcor (Trenton, NJ) model CP14-71-10L thermoelectric cooler allowed the array to be cooled to -15 °C.
translation stage	Daedal (Harrison, PA) model 4979 stepper motor driven linear translation stage.
nebulizer and spray chamber	Sherrit-Gordon (Fort Saskatchewan, AB) cross-flow type nebulizer (MAK) and spray chamber combination.
computer	Telex (Tulsa, OK) model 1280 IBM AT compatible computer with 1 MByte RAM, a 20 MByte hard disk drive and dual floppy drives.
data acquisition	RC electronics (Santa Barbara, CA) model ISC-16 analog-to-digital converter card.
programming language	Borland International (Scotts Valley, CA) Turbo Pascal, version 3.01A.

The detector was a 4096 element linear photodiode array (lpda) (described in more detail in reference [130]), the use of which greatly facilitated data collection. It was possible to simultaneously monitor 4096 discrete wavelength positions across an approximately 40 nm wide spectral "window". The dimensions of the light sensing area were 0.5 mm in height by 61.4 mm in length, the pixels being 7 μm wide mounted on 15 μm centres. For most of the work presented in this thesis the detector used was that described in Table I. However for some later work a Reticon (Sunnyvale, CA) model RL-2048S with model RC-1020 evaluation board was used - this was a 2048 element linear photodiode array. This photodiode array had a light sensing area of 0.5 mm in height by 51.2 mm in length, the pixels being 12 μm wide mounted on 25 μm centres. When using an entrance slit width on the monochromator of 60 μm, the full width at half maximum of a spectral line due to instrumental broadening was determined to be approximately 0.056 nm (or about 2.9 diodes for the 2048 pixel array). Space considerations do not make it possible to describe the various features of linear photodiode arrays in this thesis; for reasonably comprehensive reviews of their characteristics the reader is referred to references [73, 74, 126].

When it was necessary to directly compare the intensities of various spectral lines of different wavelength a correction was made to compensate for the spectral response of the system (which was quite flat from 400 nm to 800 nm, but decreased rapidly below 400 nm). The calibration was accomplished using an Electro Optics

Associates (Palo Alta, CA) model L-10 quartz-iodine, tungsten filament standard lamp [125].

To aid in the reduction of dark current (the signal read out by the array when no light is falling on it due to thermionic emission of electrons), and thus allow the use of longer integration times, the photodiode array was cooled to -15 °C using a thermoelectric cooler. To prevent ice from forming on the protective quartz covering of the photodiode array, a steady stream of nitrogen was passed over the face of the array when the thermoelectric cooler was in operation.

The entire icp torch enclosure box was mounted on a stepper-motor driven linear translation stage. This allowed the plasma to be translated horizontally in precise steps of 1.27×10^{-3} cm. This was necessary for the implementation of the Abel inversion procedure to be discussed below. Both the readout of the photodiode array and the control of this linear translation stage were supervised by an IBM AT compatible computer. The readout was accomplished using a 1 MHz, 12 bit analog-to-digital converter card which plugged into the Telex computer. Details of the data acquisition system can be found in reference [40].

The plasma was focussed with one-to-one imaging onto the entrance slit of the monochromator using an Oriel (Stratford, CT) model 41775 plano-convex fused silica lens with a focal length of 150 mm and a diameter of 50 mm. The imaging distance (the distance from either the plasma to the lens or from the lens to the entrance slit) was adjusted to account for the achromatic response of the lens using the following empirical equation:

$$\text{Imaging Distance (in cm)} = 16.3 + 6.71\times10^{-2}\,\lambda - 1.04\times10^{-4}\,\lambda^2 + 5.30\times10^{-8}\,\lambda^3 \qquad (2.1)$$

where λ is the wavelength (in nm). The viewing height in the plasma was generally adjusted by moving the lens vertically.

For some of the work described in this thesis an extra argon flow was introduced immediately after the spray chamber using an attachment (shown in figure 2.2) constructed in the UBC glass shop. This extra argon flow, first described in the literature by Mermet et al. [98], is known as the "sheath gas" flow. It was named by Mermet in the belief that this argon flow formed a sheath around the sample droplets emerging from the spray chamber - even if this is not actually the case the name "sheath gas" will still be used. The sheath gas proved to be very valuable in manipulating the plasma conditions, as will be discussed in chapter six.

Parameters such as the various argon flow rates, the rf power supplied to the plasma, etc. spanned a range of settings and will be given in the appropriate results chapters.

2.2 Data Handling

For fundamental studies of the inductively coupled plasma it is, of course, crucial to have a knowledge of the various important plasma parameters (such as temperature, electron density etc.) at a variety of spatial positions in the plasma. A problem arises due to the fact that the icp is a spatially inhomogeneous source - if one attempts to measure the intensity of a particular spectral line using

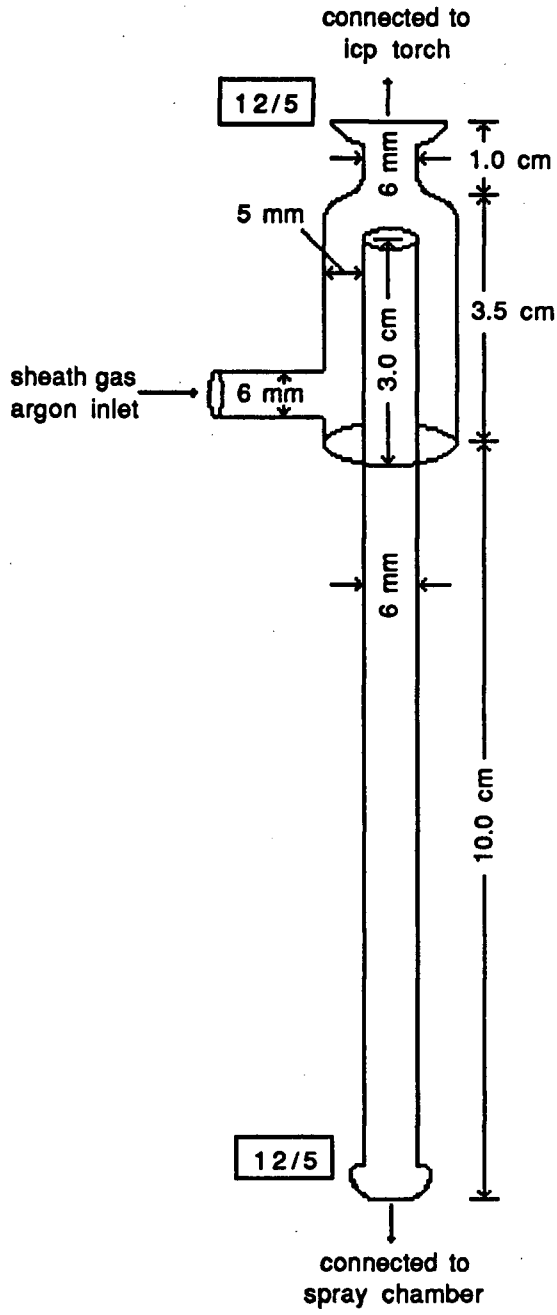

Figure 2.2 Diagram of sheath gas attachment.

the standard configuration of side-on-viewing, one will in fact be integrating the light over the thickness of the plasma, and not measuring it at a unique spatial point. This can be seen in figure 2.3 (a). To understand this figure one must imagine that one is looking down at a thin slice of the plasma from above; at a particular lateral location, x, the intensity measured will consist of the emission from the entire shaded region.

To overcome this a technique known as Abel inversion is used: for a cylindrically symmetrical source such as the icp it is possible to measure the integrated intensity at a number of lateral locations across the plasma (I(x) as a function of x, in the figure) and then to mathematically convert this to the desired radial values (I(r) as a function of r, where r is the distance from the centre of the plasma). It can be shown [39] that I(r) can be determined from I(x) using the following equation:

$$I(r) = \frac{-1}{\pi} \int_{r}^{R} \frac{I'(x)}{\sqrt{x^2-r^2}} dx \qquad (2.2)$$

where R (a constant) is the radius of the plasma and I'(x) is the first derivative of I(x) with respect to x. Figure 2.3 also shows examples of the general form of the lateral (b) and radial (c) profiles.

For this work, thanks to the computer control of the linear translation stage, I(x) was measured at a large number of equally spaced lateral locations (generally 200) across the plasma, for a total scan distance of from about 10 to 20 mm. By assuming that

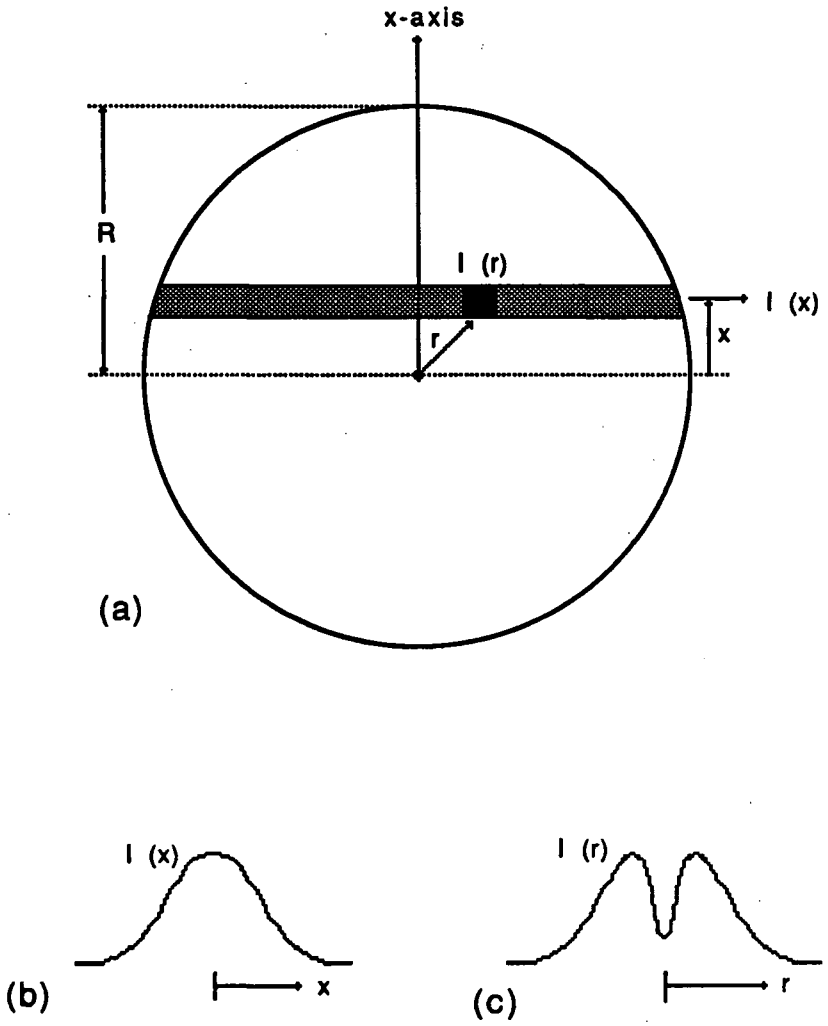

Figure 2.3 (a) Top view of a cross section of the plasma showing the Abel inversion parameters, (b) a typical lateral emission profile and (c) a typical radial emission profile.

I'(x) is constant over each small interval Nestor and Olsen [108] have derived a relatively simple numerical method for calculating I(r) from the above equation. The technique used in this work for determining I(r) is based on a slight modification of the Nestor and Olsen method described by Blades [14]. This method, which makes an attempt to compensate for slight deviations from perfect cylindrical symmetry of the plasma, will not be described here - the reader is referred to the publication by Blades.

In order for this Abel inversion technique to be used it is necessary that the depth of field of the optical system extend over the entire plasma, that any deviations from perfect cylindrical symmetry be small, and that there be negligible self absorption for the spectral lines of interest. These conditions were all met for the data presented in this work. Even so the Abel inversion technique will likely introduce errors of the order of from five to fifteen percent [32].

When performing an Abel inversion any noise (which may initially be roughly equal for all lateral intensity locations) tends to cluster near the centre of the radial profile. In order to minimize the resulting noise in the Abel inverted radial emission profiles, it was necessary to first smooth the lateral profiles, I(x), using a Savitzky-Golay smoothing operation [118]. In most cases a 25 point smoothing function was applied, while for those cases in which the noise level was lower a five point smoothing operation was used.

2.3 Sample Preparation

With the exception of iron, all sample solutions were prepared in deionized water from reagent grade chemicals. The iron solution (made from $FeSO_4 \cdot H_2O$) was prepared in 0.1 M HCl to prevent the formation of iron oxides. The concentrations (the exact values of which will be given in the results chapters) were all in the range of 50-5000 parts per million (by weight). These concentrations were used to obtain reasonable intensity measurements from high excitation energy spectral lines. Analyte concentrations were chosen such that there was negligible self absorption for the spectral lines of interest.

2.4 Data Collection

Unless otherwise noted, the following procedure was used for the collection of the various emission intensities presented in the following chapters. Once the desired analyte solution was aspirated into the plasma, the monochromator was set such that the spectral line(s) of interest fell on the photodiode array (a wavelength range of approximately 40 nm). The integration time (the time the photodiode array is allowed to integrate signal before being read out) was adjusted so that the intensity of the most intense spectral line being measured was as large as possible without saturating the photodiode array. In the case that there were both weak and intense lines of interest in the same wavelength window, it was often necessary to collect two or more separate scans, each at a different integration times, so that the weaker line would not contain excessive noise. Depending upon the exact integration time used, a

number of successive scans (one to fifty) were averaged in order to reduce noise.

Each spectral intensity was acquired at 200 equally spaced positions across the width of the plasma (using the linear translation stage). The resulting lateral emission intensity profile (I(x) vs. x) was generally then background corrected by subtracting the intensity (at each of the 200 points) observed when a deionized water blank was aspirated into the plasma; in some cases the intensity to be subtracted was interpolated from measurements made on each side of the analytical line of interest.

Using this same computer program the resulting lateral emission intensity profiles were subjected to a Savitzky-Golay smoothing operation before being Abel inverted to give the desired radial emission profiles (I(r) vs. r). When desired these radial profiles could then be corrected for the wavelength response of the collection system.

2.5 Electron Density Measurement

For a full description of the method by which spatially resolved electron density measurements were obtained the reader is referred to reference [32]; however, the procedure will be summarized here. Using the photodiode array the intensity of the hydrogen Balmer line at 486.13 nm (H_β) was simultaneously measured at 50 equally spaced wavelength positions across the width of this spectral line (the hydrogen coming from the decomposition of water). This was done for each of the 200 spatial locations across the width of the plasma. Each of the resulting 50 lateral emission intensity profiles

was then background corrected, smoothed, and subjected to an Abel inversion as described above - the result was a spatially resolved wavelength profile of the H_β line at 200 different radial positions.

The full width at half maximum of the H_β line was then calculated from these profiles, resulting in measurements of the half width at 200 spatial positions in the plasma; these values were then corrected to remove the influence of instrumental broadening from the half widths. As described in the introduction to this thesis, it is possible, using the tabulation of Vidal et al. [128], to convert this half width into an electron density (with units of cm^{-3}). However there is one difficulty: in order to use the tables one must know the electron temperature. To overcome this difficulty a temperature of 6000 K was assumed and the electron density calculated. From this electron density a new temperature ($T_{e,lte}$) was calculated as described in the introduction to this thesis. Using this temperature a new electron density was then calculated. This procedure was repeated iteratively until the electron density converged; since the temperature dependence of the broadening is weak the convergence was rapid. Spatially resolved electron density thus resulted. A discussion of the accuracy of the electron density determination can be found in chapter six.

Chapter 3
A Simple Method for Calculating Deviations from LTE in the Inductively Coupled Plasma

3.1 Introduction

As mentioned in the introduction to this thesis, a spectroscopic source is said to be in local thermodynamic equilibrium (lte) when the various distribution functions (Boltzmann, Saha, Maxwell, etc.) hold at a unique temperature for all species (other than photons) in the source. Much effort has gone into testing the state of equilibrium in the inductively coupled plasma [2, 13, 16, 20, 36, 72, 78, 96, 97, 131], the result being clear that the icp is not in lte - the reason for this lack of lte is still uncertain and is presently the subject of discussion. Some authors suggest that the populations of low-lying energy levels can be perturbed from equilibrium by transport processes [109], whereas others believe that radiative decay is primarily responsible for these deviations [2, 16].

Initially it was thought that the icp was very far from lte - experimental ion-to-atom emission ratios were found to be less than calculated values by a factor of 10^1 to 10^3 [20]. However, it is now generally accepted that if a consistent set of electron density (n_e) and temperature (T) is used in the calculations the plasma is "close to lte", and can be accurately described by a partial-local thermodynamic equilibrium (p-lte) model [16, 109, 131].

In the p-lte view, highly excited atomic levels (and also the ground state ion, as a result of its close coupling to them) are in equilibrium with the surrounding electron gas; this is due to the

small energy gaps between levels, and the resulting large rate constants for collisional excitation, collisional de-excitation, ionization, and recombination. Due to its unambiguous nature, the lte framework is best based on the electron density, rather than the temperature. As shown in the introduction to this thesis, it has been previously pointed out [36, 112, 119] that for an argon plasma at a given pressure (1 atm for the icp), the electron temperature can be calculated from the electron density by using charge neutrality, the Saha distribution, and the fact that the total pressure is fixed.

In this chapter evidence is presented to support the view that deviations from lte in the icp are due to radiative decay not being balanced by its inverse process of photo-absorption (as the plasma is optically thin). Using a simple two level rate model, which incorporates the collisional and radiative rate constants, expressions for the non-equilibrium "b" parameter (defined as the ratio of the actual to calculated lte level populations) are presented for atomic and ionic levels. From these values the actual populations can be calculated, allowing theoretical Boltzmann plots to be constructed; these were found to agree very well with previously collected experimental data*. The material in this chapter has been previously published in reference [28].

3.2 Theoretical

For a particular atomic energy level i, the non-equilibrium "b" parameter, b^i_{atom}, can be defined as follows [112]:

---

* The author extends his sincere thanks to Zane H. Walker who collected the experimental data reproduced in this chapter.

$$b^i_{atom} = \frac{n_{i,exp}}{n_{i,lte}} \tag{3.1}$$

where $n_{i,exp}$ is the actual population of the level i, and $n_{i,lte}$ is the expected equilibrium population (in our case, based on the electron density, as described in the introduction).

Introducing a hypothetical bound energy level arbitrarily close to the ionization limit of the atom ($i = \infty$), allows b^i_{atom} to be written (by dividing and multiplying by both $n_{\infty,exp}$ and $n_{\infty,lte}$):

$$b^i_{atom} = \frac{n_{\infty,lte}/n_{i,lte}}{n_{\infty,exp}/n_{i,exp}} \cdot \frac{n_{\infty,exp}}{n_{\infty,lte}} \tag{3.2}$$

$$= \frac{n_{\infty,lte}/n_{i,lte}}{n_{\infty,exp}/n_{i,exp}} \tag{3.3}$$

where $n_{\infty,exp}$ is the limit of the actual population as $i \to \infty$ and $n_{\infty,lte}$ is the limit of the expected lte population as $i \to \infty$. The second equality follows from the fact that for a plasma in p-lte the highly excited atomic levels have b-values near unity, and thus $b^\infty_{atom} = n_{\infty,exp}/n_{\infty,lte} = 1$.

We now introduce the approximation that the only important processes which couple two levels in the same ionization stage are collisional excitation by electron impact (CE), collisional de-excitation by electron impact (CD), and spontaneous radiative decay (RD). Lovett [83] has shown that this is likely a reasonable approximation to make for the icp. These rate constants are defined as follows (where M is the species of interest): the rate for the

process ($M_i + e^- \rightarrow M_\infty + e^-$) is $CE_{i\rightarrow\infty}\cdot n_e\cdot n_{i,exp}$; for the process ($M_\infty + e^- \rightarrow M_i + e^-$) it is $CD_{\infty\rightarrow i}\cdot n_e\cdot n_{\infty,exp}$; and for the process ($M_\infty \rightarrow M_i + h\nu$) it is $RD_{\infty\rightarrow i}\cdot n_{\infty,exp}$. At equilibrium the ratio of any two level populations is related only to the processes coupling them directly. Even though the icp is not in equilibrium, we make the simplifying approximation that this will be true for the level i coupled to the hypothetical level with i=∞, viz:

$$\frac{n_{\infty,exp}}{n_{i,exp}} = \frac{CE_{i\rightarrow\infty}\cdot n_e}{CD_{\infty\rightarrow i}\cdot n_e + RD_{\infty\rightarrow i}} . \qquad (3.4)$$

This is likely a reasonable approximation to make for the icp since atomic levels are largely populated by the recombination of an electron with a ground state ion (which is in equilibrium with the highly excited atomic levels.) By dividing the top and bottom of the above equation by $CD_{\infty\rightarrow i}\cdot n_e$ one obtains:

$$\frac{n_{\infty,exp}}{n_{i,exp}} = \frac{CE_{i\rightarrow\infty}/CD_{\infty\rightarrow i}}{1 + RD_{\infty\rightarrow i}/(CD_{\infty\rightarrow i}\cdot n_e)} . \qquad (3.5)$$

Since for a system in lte $n_{\infty,exp}/n_{i,exp} = n_{\infty,lte}/n_{i,lte} = CE_{i\rightarrow\infty}/CD_{\infty\rightarrow i}$ (this follows by setting $RD_{\infty\rightarrow i} = 0$ in the above equation whence all remaining processes (CE and CD) will balance each other, resulting in lte):

$$\frac{n_{\infty,exp}}{n_{i,exp}} = \frac{n_{\infty,lte}/n_{i,lte}}{1 + RD_{\infty\rightarrow i}/(CD_{\infty\rightarrow i}\cdot n_e)} . \qquad (3.6)$$

One notices from equation (3.6) that in a collisionally dominated plasma ($RD_{\infty\rightarrow i} << CD_{\infty\rightarrow i}\cdot n_e$), $n_{\infty,exp}/n_{i,exp} \approx n_{\infty,lte}/n_{i,lte}$, and the plasma is in lte. Substituting equation (3.6) for $n_{\infty,exp}/n_{i,exp}$ into equation (3.3) gives:

$$b^i_{atom} = 1 + \frac{A_{\infty\rightarrow i}}{CD_{\infty\rightarrow i}\cdot n_e} \qquad (3.7)$$

where it was recognized that the radiative rate constant, $RD_{\infty\rightarrow i}$, is simply the hypothetical transition probability, $A_{\infty\rightarrow i}$. This value will later drop out of the final expressions and is introduced solely for convenience.

The collisional decay rate coefficient (in cm^3/s) can be calculated from a formula given by Seaton [120] as:

$$CD = \frac{3.64x10^{-13} <\bar{g}> A}{E\ (\Delta E)^2\ (kT)^{1/2}} \qquad (3.8)$$

where E is the excitation energy (eV) of the upper level of the transition, ΔE is the energy difference between the two levels (eV), T is expressed in Kelvin, k is Boltzmann's constant (eV/K), A is the transition probability (s^{-1}), and $<\bar{g}>$ is the thermally averaged effective Gaunt factor. $<\bar{g}>$ can be evaluated graphically from Van Regemorter [116]; if $10^{-1} < \Delta E/kT < 10^2$ (which is the case for the results presented in this thesis), $<\bar{g}>$ can be approximated well for neutral atoms by:

$$\langle \bar{g} \rangle = 0.114 \left\{ \frac{\Delta E}{kT} \right\}^{-0.607} . \qquad (3.9)$$

If equation (3.9) is substituted into (3.8) and the result into equation (3.7) the following is obtained (dropping the superscript i):

$$\boxed{b_{atom} = 1 + \frac{6.55 \times 10^{13} \, E_\infty \, (E_\infty - E)^{2.607}}{n_e \, T^{0.107}}} \qquad (3.10)$$

where E_∞ is the ionization energy (eV), and n_e is expressed in cm^{-3}.

An analogous expression can be derived for the ion by coupling an arbitrary ion level to the ion ground state (which has a b-value of unity for a plasma in p-lte), and using the approximation $\langle \bar{g} \rangle = 0.2$ [116] for ions to give the non-equilibrium parameter, b_{ion}:

$$\boxed{\frac{1}{b_{ion}} = 1 + \frac{1.27 \times 10^{11} \, E^3 \, T^{1/2}}{n_e}} \qquad (3.11)$$

where E (in eV) is measured with respect to the ion ground state. The coupling was done to the ion ground state, rather than to, say, the highly excited ionic levels to be consistent with the definition of the underlying p-lte framework (which uses the ion ground state as its reference equilibrium position).

3.3 Experimental

The experimental data presented in this chapter have been previously published by Walker [130] or by Walker and Blades [131, 132]; listings of the wavelengths and energy levels for the spectral

lines used in the construction of the experimental Boltzmann plots can be found in those publications. The electron densities were taken from reference [35]. Details of the experimental system can be found in chapter two of this thesis. The argon flow rates used were: plasma gas - 11 L/min; aerosol gas - 0.9 L/min; no auxiliary gas was used. All data were either Abel inverted or checked to ensure that a lack of Abel inversion would introduce no more than five percent total error in the spectral line intensities.

3.4 Results

In figure 3.1 b_{atom} and $1/b_{ion}$ for iron are plotted as a function of excitation energy at rf powers of 0.75, 1.00, 1.25, 1.50, and 1.75 kW and a height of 16 mm above the load coil (the measured

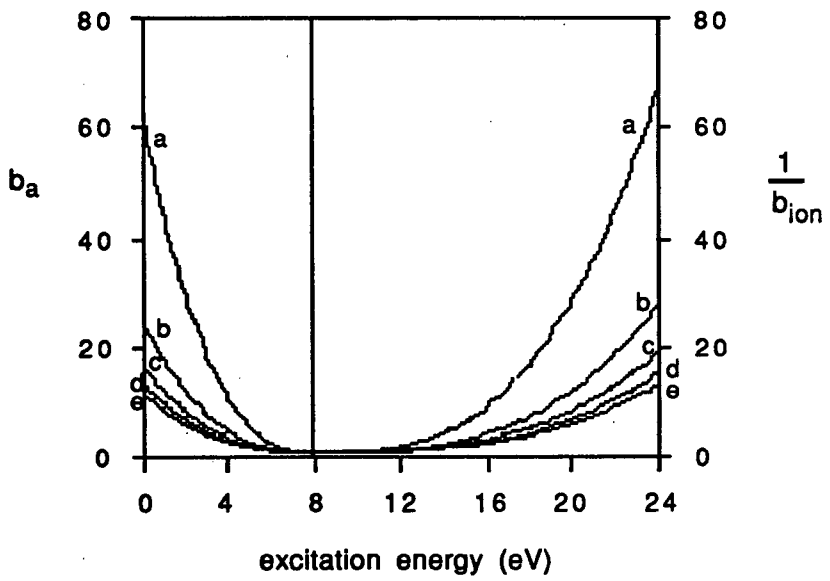

Figure 3.1 A plot of b_{atom} and $1/b_{ion}$ for iron at 16 mm above the load coil and (a) an rf power of 0.75 kW, (b) 1.00 kW, (c) 1.24 kW, (d) 1.50 kW, and (e) 1.75 kW.

Table II: Electron density (10^{15} cm^{-3}) and (in parentheses) the corresponding lte temperature (K) in the central channel of the icp at various rf powers and heights above the load coil (from reference [35]).

Height alc (mm)	Power (kW)				
	0.75	1.00	1.25	1.50	1.75
8	-	-	1.4 (7970)	-	3.0 (8540)
16	0.71 (7550)	1.8 (8160)	2.7 (8460)	3.4 (8630)	4.0 (8760)

electron densities and the corresponding lte temperatures used are shown in Table II). Note that the plot only refers to iron through the value of the ionization energy used in the calculations - any element with a similar ionization energy would behave the same.

The plot shows that ground state Fe I is (in theory) overpopulated by a factor of up to 60, whereas the energy levels near the ionization energy of Fe II at 24.05 eV (with respect to the atom ground state) are underpopulated by a factor of up to about 65 (note that $1/b_{ion}$ is plotted, not b_{ion} itself). As one would expect, the predicted deviations are larger the smaller the electron density. These are the deviations from lte which can be expected due solely to the fact that radiative decay is not balanced by its inverse process of absorption. As is required for a plasma in p-lte the highly excited atomic levels and the ion ground state have b-values of unity.

In figures 3.2-3.6 Boltzmann plots are presented for iron, barium, and chromium; the solid lines refer to lte, the dotted lines to results obtained from the theory presented in this chapter, and the triangles to the experimental points. These plots were constructed as follows: (1) the lte line for the ion was drawn in with a slope of -1/kT, in accord with the Boltzmann distribution; (2) from the Saha equation the Saha jump, ln $(4.83 \times 10^{15} T^{3/2}/n_e)$ (where T is in Kelvin, and n_e in cm^{-3}), was calculated; (3) the lte line for the atom was drawn with a slope of -1/kT such that the difference between the ground state ion and the highly excited atomic levels was equal to the Saha jump; (4) rearranging equation (3.1) to give $n_{exp}/g = n_{lte}/g \cdot b$ (where g is the degeneracy of the level in question)

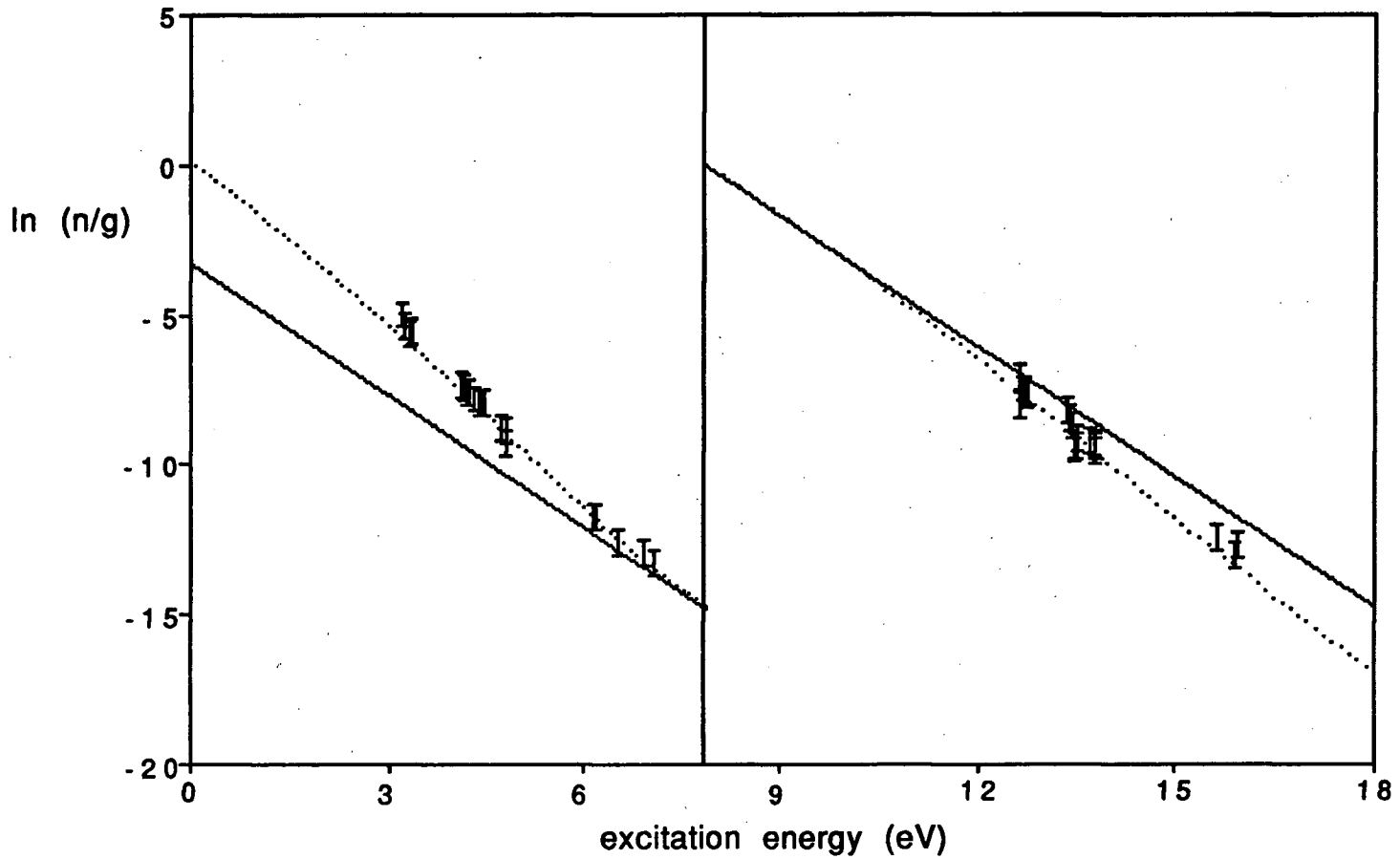

Figure 3.2 Boltzmann plot for iron at 8 mm above the load coil and an rf power of 1.25 kW. The solid line represents lte, the dotted line was derived from equations (3.10) and (3.11), and the error bars represent experimental points (from reference [131]) with their estimated uncertainties.

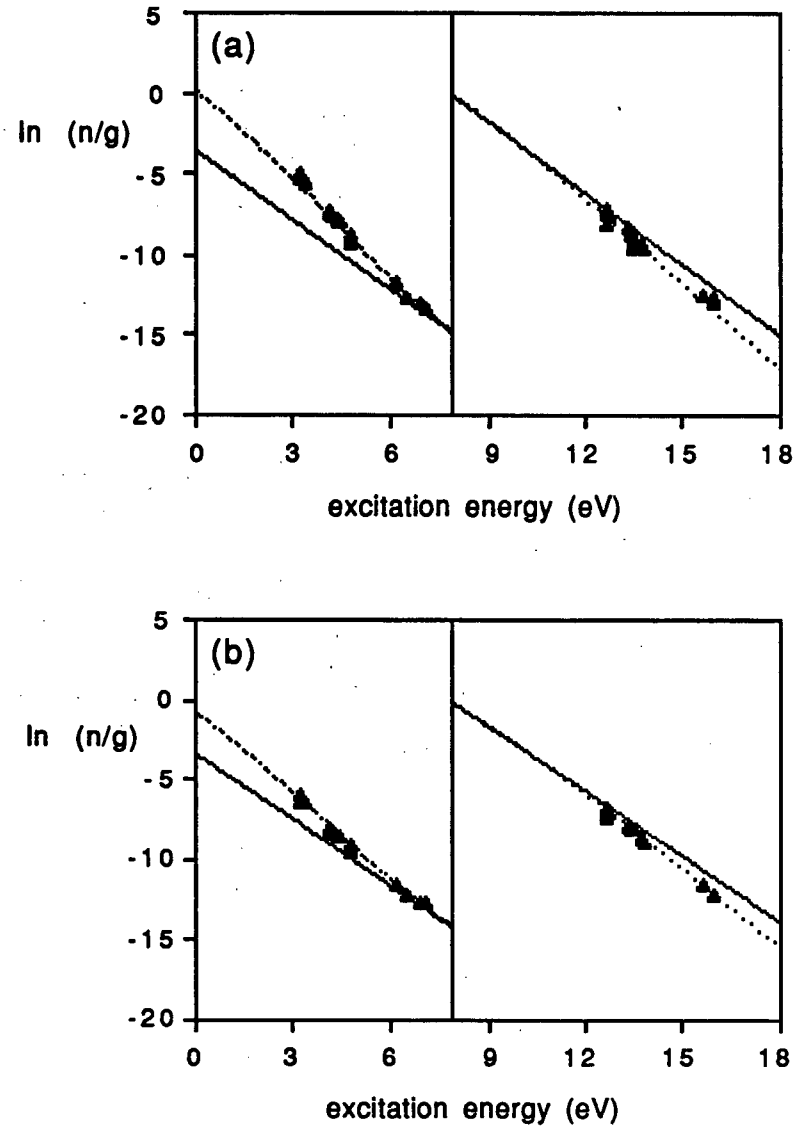

Figure 3.3 Boltzmann plot for iron at 8 mm above the load coil and (a) an rf power of 1.25 kW, (b) 1.75 kW; the solid line represents lte, the dotted line was derived from equations (3.10) and (3.11), and the triangles represent experimental points (from reference [131]).

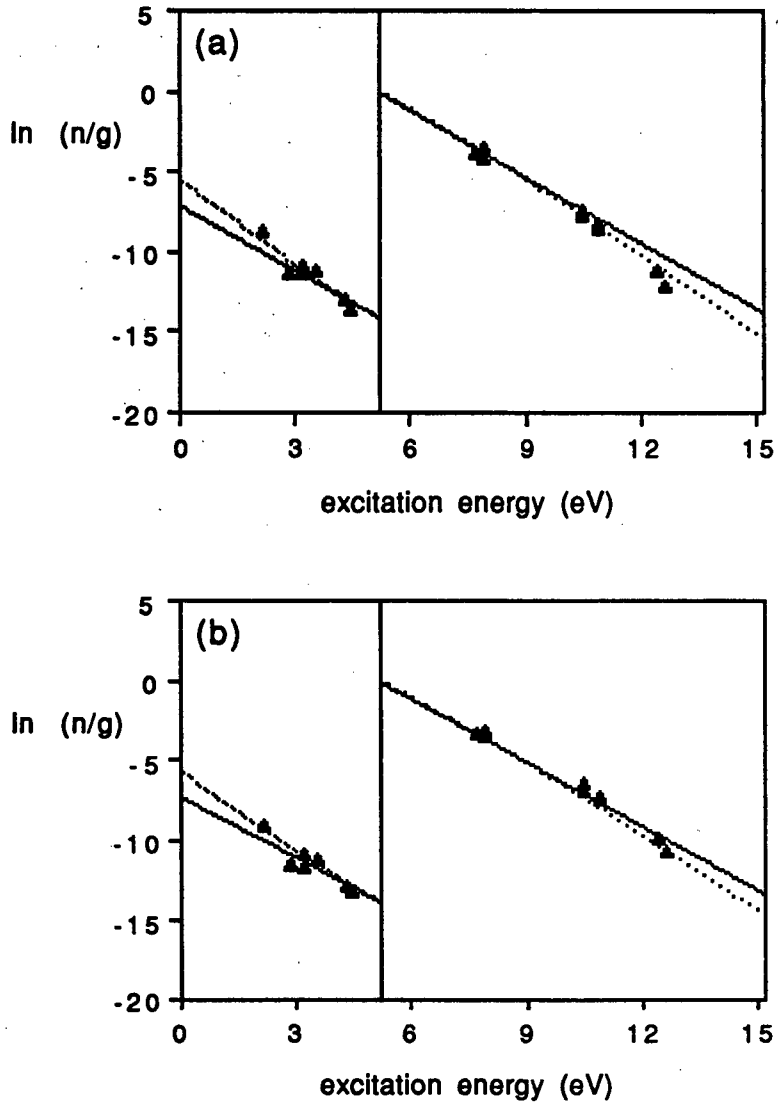

Figure 3.4 Boltzmann plot for barium at 16 mm above the load coil and (a) an rf power of 1.25 kW, (b) 1.75 kW; the solid line represents lte, the dotted line was derived from equations (3.10) and (3.11), and the triangles represent experimental points (from reference [130]).

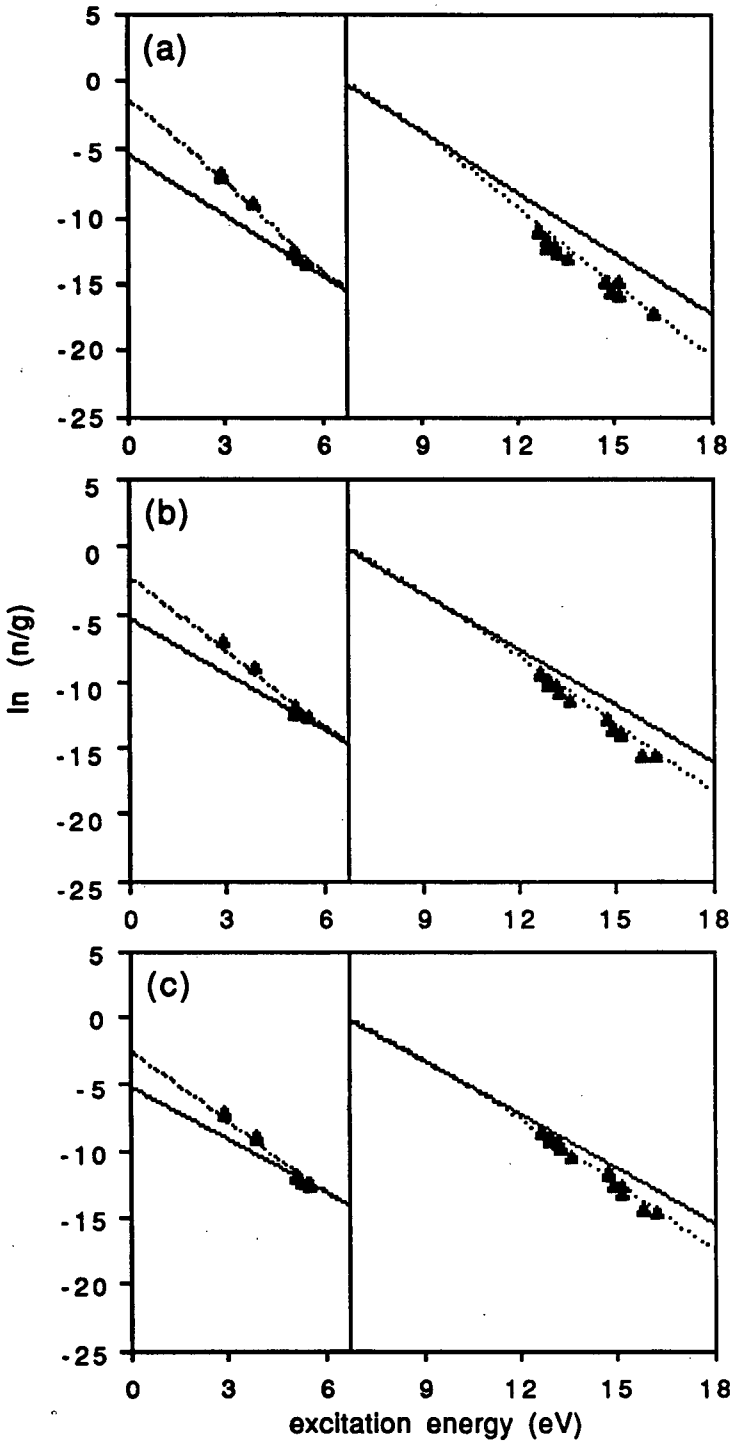

Figure 3.5 Boltzmann plot for chromium at 16 mm above the load coil and (a) an rf power of 0.75, (b) 1.00, (c) 1.25 kW; the solid line represents lte, the dotted line was derived from eqns. (3.10) and (3.11), and the triangles represent experimental points (from ref. [132]).

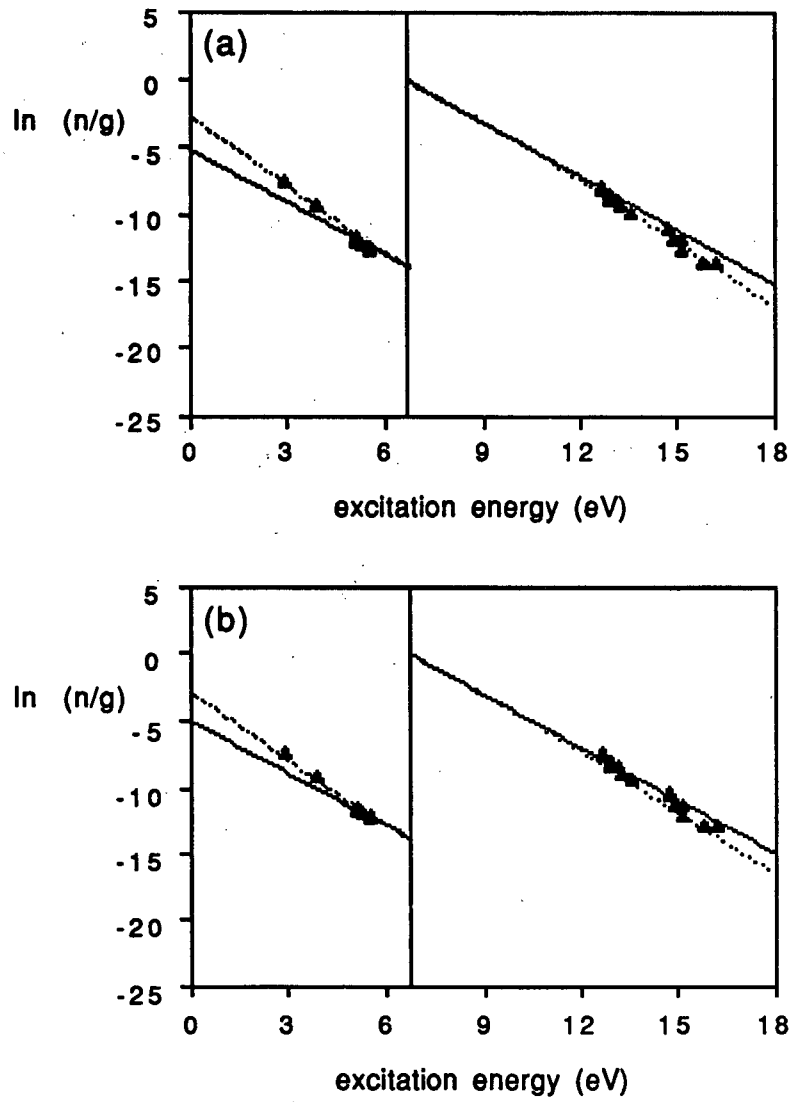

Figure 3.6 Boltzmann plot for chromium at 16 mm above the load coil and (a) an rf power of 1.50 kW, (b) 1.75 kW; the solid line represents lte, the dotted line was derived from equations (3.10) and (3.11), and the triangles represent experimental points (from reference [132]).

allowed the level populations to be calculated from the expressions for b_{atom} and b_{ion} given in equations (3.10) and (3.11) respectively. The experimental populations (n/g) were calculated as $I\lambda/gA$ (in arbitrary units) where I is the intensity of a spectral transition originating from the level in question, λ is its wavelength, and gA is the degeneracy weighted transition probability for the transition. Because both the experimental and calculated populations were relative it was necessary to normalize them to one another; this was done by multiplying all of the experimental points, as a whole, by a constant until the highly excited atomic levels fell on the lte line, in accord with p-lte.

In these plots the uncertainty in the placing of the lte lines due to the experimental uncertainty in the measured electron density is negligible - when lte lines of minimum and maximum deviation were plotted they lay directly on top of one another. This is so because the slope of the lines is determined by the temperature (calculated from the electron density), which is quite an insensitive function of the electron density.

Figure 3.2 is a Boltzmann plot for iron at 8 mm above the load coil (alc) and an rf power of 1.25 kW. The purpose of this figure is to show the maximum uncertainties associated with the experimental points. The plotted error bars correspond to uncertainties in population of ±40 percent. The estimated uncertainties in the intensities of the spectral lines are ±15 percent (due mainly to the Abel inversion technique), while the maximum errors in the transition probabilities are ±25 percent. In practice the uncertainties will be less than those shown for two reasons.

Firstly, with the exception of the barium transitions, the published uncertainties in the transition probabilities are generally of the order of ±10 percent. Secondly, these uncertainties are absolute - the relative uncertainties (which are of interest here) will be smaller. Thus the actual uncertainties in the experimental points will likely be of the order of, perhaps, one third of those shown in figure 3.2. In the subsequent Boltzmann plots presented in this chapter (and in chapter four of this work) the size of the triangles used to represent the experimental points corresponds roughly to their estimated uncertainty range.

Figure 3.3 shows Boltzmann plots for iron at 8 mm above the load coil; figure 3.3(a) refers to an rf power of 1.25 kW, and figure 3.3(b) to a power of 1.75 kW. It can be seen that the agreement between experiment and the theory presented here is very good - within the estimated experimental uncertainly. From these plots one can see how previous researchers [20] were led to the conclusion that analyte is underpopulated with respect to lte. If a straight line is fitted to the experimental atomic levels a temperature much lower than that used for the lte line shown would be obtained. If a line of this slope were then drawn through an arbitrary ion level the ion ground state would seem to be much more highly populated, making it appear as if all of the atomic levels were drastically underpopulated with respect to the ion.

Figure 3.4 is a plot for barium at 16 mm above the load coil; figure 3.4(a) refers to an rf power of 1.25 kW, and figure 3.4(b) to a power of 1.75 kW. The calculated line certainly agrees with the experimental points within their rather large uncertainty (due

mainly to uncertainties in the transition probabilities). Once again the same trend is observed: an overpopulation of the atomic levels with respect to lte, and an underpopulation of the high-energy ionic levels.

Figures 3.5 and 3.6 present Boltzmann plots for chromium at 16 mm above the load coil; figures 3.5(a), 3.5(b), 3.5(c), 3.6(a), and 3.6(b) refer to rf powers of 0.75, 1.00, 1.25, 1.50, and 1.75 kW respectively. Again the calculated lines agree very well with the experimental points.

Deviations from lte are caused by radiative de-excitation competing with collisional de-excitation; since the radiative de-excitation rate is independent of electron density, and the collisional de-excitation rate is directly proportional to it, one would expect deviations from lte to be smaller at higher values of the electron density (i.e. higher rf powers). This can be seen in figures 3.5 and 3.6 - as the rf power is increased both the calculated and experimental points move closer to the lte lines.

As defined in reference [109], in order for a given species to be considered to be "close to lte" it is necessary that the non-equilibrium b parameter for the ground state atom of that species (b_o) satisfy $0.1 < b_o < 10$. Substituting E = 0 eV (for the ground state atom) into equation (3.10) and recognizing that the resulting expression for b_o will always be greater than unity one obtains:

$$b_o = 1 + \frac{6.55 \times 10^{13} (E_\infty)^{3.607}}{n_e \, T^{0.107}} < 10 \qquad (3.12)$$

for the condition which must be satisfied for the species to be close to lte. Because the lte temperature, as calculated from the electron density, is such a slowly varying function of the electron density, $T^{0.107}$ is virtually constant at 2.6 ± 0.1 over the electron density range of interest in the icp. This allows the above equation to be simplified to:

$$n_e > 2.8 \times 10^{12} (E_\infty)^{3.607} \qquad (3.13)$$

where n_e is in cm^{-3} and E_∞ is in electron volts. This provides a very convenient method of determining whether or not a species of a particular ionization energy will be close to lte at a particular electron density. Other authors [42, 56] have also provided validity criteria; however their expressions are more complex as they are of a more general nature, and not tailored to the icp.

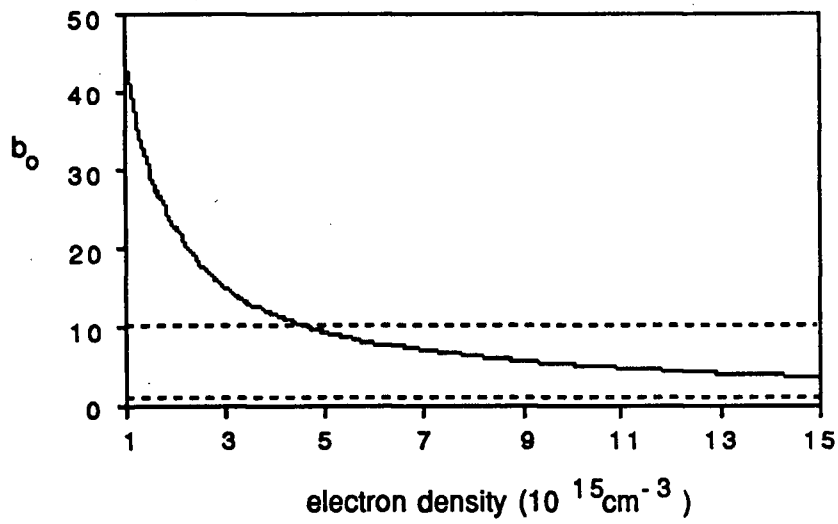

Figure 3.7 The non-equilibrium b parameter for the ground state of iron (b_0) as a function of the electron density; dashed lines are drawn at b_0 values of 1 and 10.

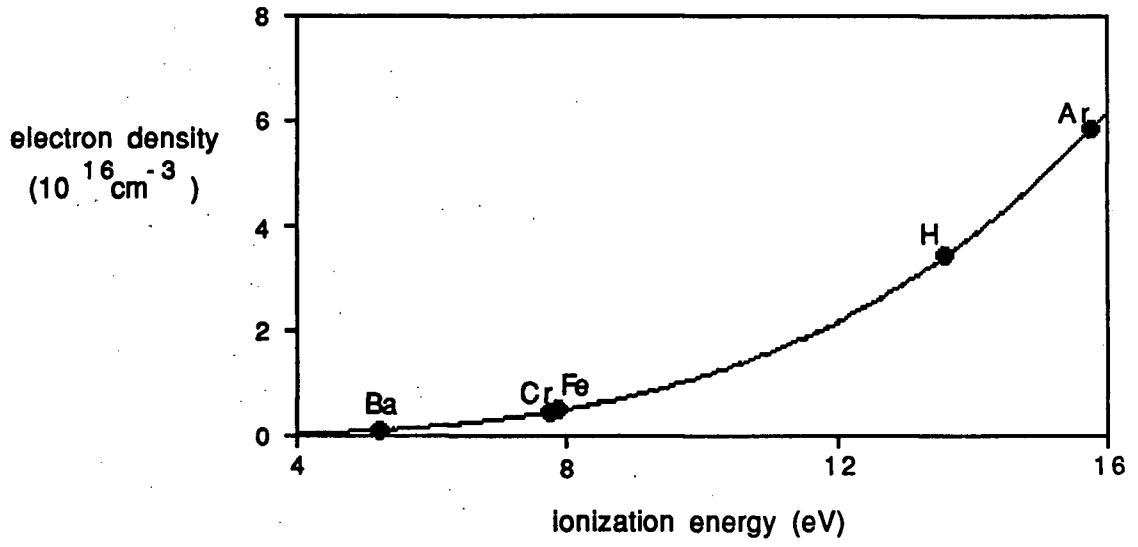

Figure 3.8 The minimum electron density needed for a species to be "close to lte" ($b_0 < 10$) as a function of the ionization energy.

In figure 3.7 b_o is plotted as a function of the electron density for iron. It can be seen that for iron to be close to lte ($b_o < 10$) it is necessary that the electron density be greater than about $5x10^{15}$ cm^{-3}. It can also be seen that, as expected, as the electron density increases b_o approaches a value of unity.

In figure 3.8 the minimum electron density needed for a species to be close to lte (as calculated from equation (3.13)) is plotted as a function of the ionization energy; circles denote the values corresponding to the ionization energies of barium, chromium, iron, hydrogen, and argon, as indicated in the figure. One can see that for the species for which experimental data were presented in this chapter (Ba, Cr, and Fe), an electron density of at least $5x10^{15}$ cm^{-3} is needed for the concept of close to lte to apply; these values of the

electron density are readily realizable in the icp. According to equation (3.13), for species with high ionization energies such as hydrogen and the argon support gas, the electron density needed for the close to lte concept to apply is considerably greater than any likely to be found in the icp - although, as will be seen in the next chapter, this will not be the case for argon as self absorption must be taken into account.

3.5 Summary

It has been shown that in the icp significant departures from lte can be attributed to the fact that radiative decay is not balanced by its inverse process of absorption, and thus competes with collisional de-excitation by electrons. In addition, using a simple two-level rate model approach, these deviations can be calculated essentially within experimental error; some deviations can be expected in the theoretical curve due solely to the fact that equation (3.8) for the collisional de-excitation rate is probably accurate only to within a factor of two [116, 120].

As described in chapter eight of this work and in references [29] and [30], the possibility of using computer-simulated icp emission spectra to aid in the selection of spectral lines for analysis has been explored. One of the limitations of that method (along with the limited accuracies of transition probabilities) was the lack of quantitative understanding of how level populations deviate from their lte values as a function of species and electron density.

As will be seen in the next chapter, the theory presented here is not accurate for species which can undergo charge transfer

(described in the introduction to this thesis) with the argon support gas. However, owing to its simplicity - the only fundamental parameter needed is the electron density (the temperature being calculated from it) - the method presented here is ideal for incorporation into a spectral simulation program for those elements which do not undergo such a charge transfer reaction with argon.

Chapter 4
A Study of Magnesium Excited State Level Populations with Reference to Charge Transfer

4.1 Introduction

In the previous chapter a simple rate model for calculating deviations from lte in the inductively coupled plasma was described. For the initial set of elements investigated (iron, barium, and chromium) the agreement between experiment and theory was shown to be very good. However, as will be seen in the present chapter, the assumption made in the derivation of the expressions for b_{atom} and b_{ion} that an arbitrary atomic (or ionic) energy level can be closely coupled to the ground state ion (and thus also to the highly excited atomic energy levels), causes the method to break down for elements which can undergo a charge transfer (CT) process with the argon support gas.

The charge transfer process of an arbitrary analyte, M, with argon can be written as:

$$M_o + Ar_o^+ \rightarrow M_{ct}^+ + Ar_o \quad + \Delta E \qquad (4.1)$$

where the subscript "o" indicates the ground state and the subscript "ct" indicates any excited state of the M ion which can undergo charge transfer. In order for the reaction to occur at a significant rate it is necessary that the energy difference, ΔE, be small [13,

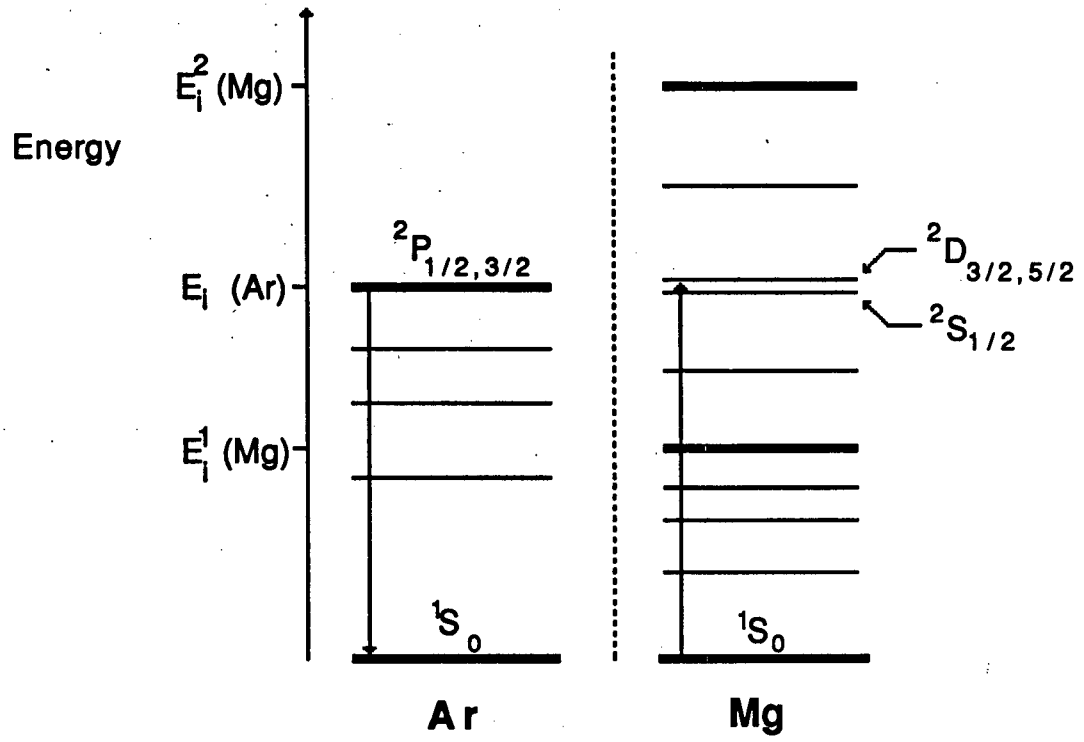

Figure 4.1 An illustration of the charge transfer process of magnesium with argon. E_i^1 (Mg) is the ionization energy of the magnesium atom, E_i^2 (Mg) of the magnesium ion, and E_i^1 (Ar) of the argon atom. The relevant energy levels are labeled with their term symbols.

44, 61]. This charge transfer process is illustrated in figure 4.1 for the particular case of magnesium. For magnesium there are two ionic levels which lie near the ionization energy of argon (15.76 eV), and can thus potentially undergo charge transfer with argon.

The importance of the charge transfer reaction in the inductively coupled plasma is presently a matter of some debate. In a relatively recent paper Hasegawa and Haraguchi [62] have carried out an

extensive rate model calculation for the determination of magnesium level populations. They included a large number of possible reactions, including charge transfer. Their conclusion was that even if the charge transfer reaction were omitted from the calculations, "the population densities would change by only less than 0.3%" - this was in agreement with their experimental observation that the energy levels of the magnesium ion near the 15.76 eV ionization energy of argon were not overpopulated with respect to the other ionic levels.

In the previous chapter of this thesis the results of a simple rate model calculation ignoring charge transfer were found to agree with experiment for both iron and chromium, elements which have ionic energy levels near the ionization energy of argon (and thus would be expected to undergo charge transfer).

Van der Mullen et al. [104] observed that in a standard icp the potential charge transfer energy levels of magnesium were consistently overpopulated with respect to other magnesium ionic energy levels. In addition, using a very simple model (to be discussed briefly in the results section below), they were able to correlate this overpopulation with the overpopulation of the ground state magnesium atom due to spontaneous radiative decay (as discussed in the previous chapter).

Mermet and co-workers [51, 90] have noticed that both copper and manganese ionic energy levels slightly above the ionization energy of argon seem to be excited by different processes from those of relatively nearby energy levels slightly below this limit. A plot of the ratio of the spectral intensities originating from two

energy levels above 15.76 eV, as a function of height above the load coil, behaved quite differently from the situation in which one of the energy levels was slightly below the ionization energy of argon. In our own laboratory we have repeated these experiments of Mermet's for copper, but found that there was no difference in behaviour for spectral lines originating from energy levels slightly above and slightly below the 15.76 eV limit.

In an effort to try to resolve some of the discrepancies involving the charge transfer process in the inductively coupled plasma, this chapter will present the results of a comprehensive study of magnesium excited-state level populations. Over the power range of 0.75 to 1.50 kW and at several vertical heights above the load coil, experimental Boltzmann plots were obtained for both magnesium atomic and ionic species. By comparing the results of this study to the simple rate model calculations described in the previous chapter, it is possible to ascertain the effect of charge transfer alone, separated from the effects of radiative decay (which is accounted for by the simple rate model). It will be shown that the overpopulation of the charge transfer energy levels of magnesium, combined with the results of the simple rate model, seem to confirm the mechanism postulated by van der Mullen et al. [104].

4.2 Experimental

Full details of the experimental system are given in chapter two of this thesis. The detector used was the 2048 pixel linear photodiode array (lpda) and the sample was introduced into the plasma using the Meinhard nebulizer/spray chamber, all of which are

described in the experimental chapter. For the results presented in this chapter the plasma argon flow rate was held constant at 10.0 L/min and the auxiliary argon flow rate was held at 0.2 L/min. The entrance slit width on the monochromator was set to 70 μm when viewing spectral emission from magnesium and to 40 μm when viewing the 486.13 nm spectral line of hydrogen (H_β), used for the determination of the electron density (as described in the introduction to this thesis). The values of the rf power supplied to the plasma were 0.75, 1.00, 1.25, and 1.50 kW and the plasma was observed at the following heights above the load coil: 6, 9, 12, 15, 18, and 21 mm.

The magnesium solution aspirated into the plasma was prepared by dissolving a suitable quantity of $MgCl_2 \cdot 6H_2O$ in deionized water to give a magnesium concentration of five thousand parts per million (ppm) by weight. The 285.21 nm resonance line of the magnesium atom was used to construct a working curve (a plot of spectral intensity versus solution concentration); the linearity of this plot up to 5000 ppm indicated that there was negligible self-absorption by magnesium.

The spectral lines used in the construction of the experimental Boltzmann plots for magnesium are listed in Table III; the table indicates to which species (Mg I or Mg II) the given spectral transition refers, the wavelength of the transition, the energy of the level from which it originates, and the degeneracy-weighted transition probability (gA). These data were taken from reference [138].

Table III: Species (Mg I or Mg II), wavelengths, upper energy levels, and degeneracy-weighted transition probabilities (gA) for the spectral lines used in the construction of the experimental Boltzmann plots for magnesium.

Species	Wavelength (nm)	Excitation Energy (eV)	gA (10^8 s^{-1})
Mg I	277.98	7.173	46.8
	285.21	4.346	15.9
	332.99	6.431	0.099
	333.22	6.431	0.291
	333.67	6.431	0.48
	516.73	5.107	0.348
	517.27	5.107	1.038
	518.36	5.107	1.725
Mg II	279.08	8.863	16.0
	279.55	4.434	10.4
	280.27	4.434	5.2
	292.88	8.654	2.4
	293.65	8.654	4.6
	448.12	11.629	31.22

The criteria used in the selection of the spectral lines in this set was that they be free of spectral overlaps, that their excitation energies span as large a range as possible, that the lines be of sufficient intensity, and that they be clustered in one of several wavelength "windows" (the 40 nm wide viewing region of the photodiode array). At each value of the rf power and height above the load coil a spatial scan of the plasma (as described in chapter two) was carried out for each of five different spectral windows centred at 517, 448, 333, 285, and 486 nm (this last being used for the collection of the 486.13 nm line of hydrogen). The plasma was scanned twice when the monochromator was centred at 285 nm, using two different integration times, so that weak spectral lines would have a reasonable signal-to-noise ratio without saturating stronger ones. The experimental populations (n/g) were then calculated as $I\lambda/gA$ (in arbitrary units) where I is the intensity of a spectral transition originating from the level in question, and λ is its wavelength.

4.3 Results

Figures 4.2-4.8 show some of the resulting Boltzmann plots for magnesium. All of these particular plots correspond to a radial position of 2 mm from the centre of the plasma; this position was chosen because nearer to the plasma centre the noise from the Abel inversion becomes excessive, and yet there is still sufficient magnesium at this position to give intense spectral lines. In figures 4.2, 4.3, 4.4, 4.5, and 4.8, corresponding to heights above the load coil of 6, 9, 12, 15, and 21 mm respectively, the (a) corresponds to

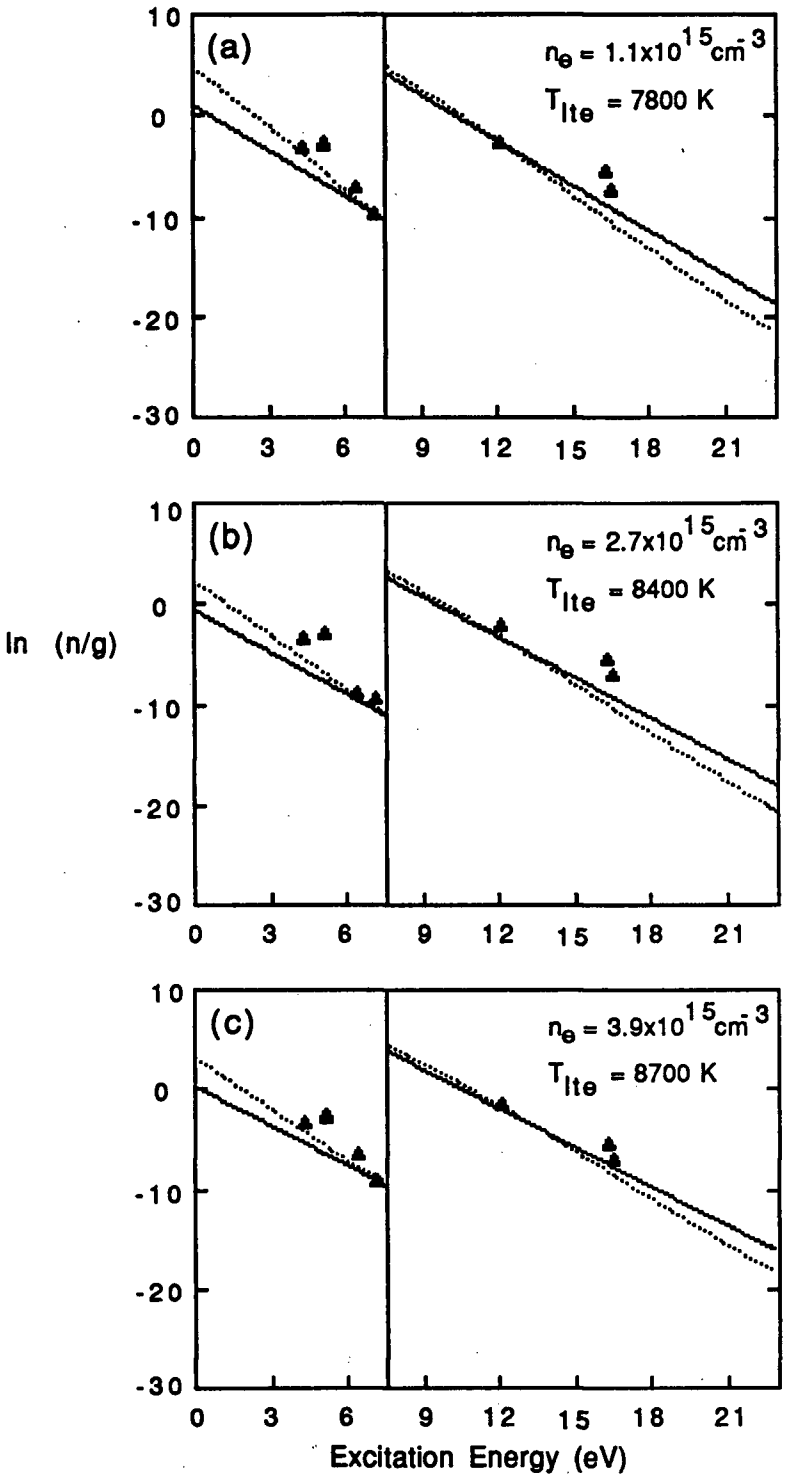

Figure 4.2 Boltzmann plot for Mg at 6 mm alc, a radial position of 2 mm and (a) an rf power of 1.00, (b) 1.25, (c) 1.50 kW; the solid line represents lte, the dotted line the simple rate model, and the triangles experimental points.

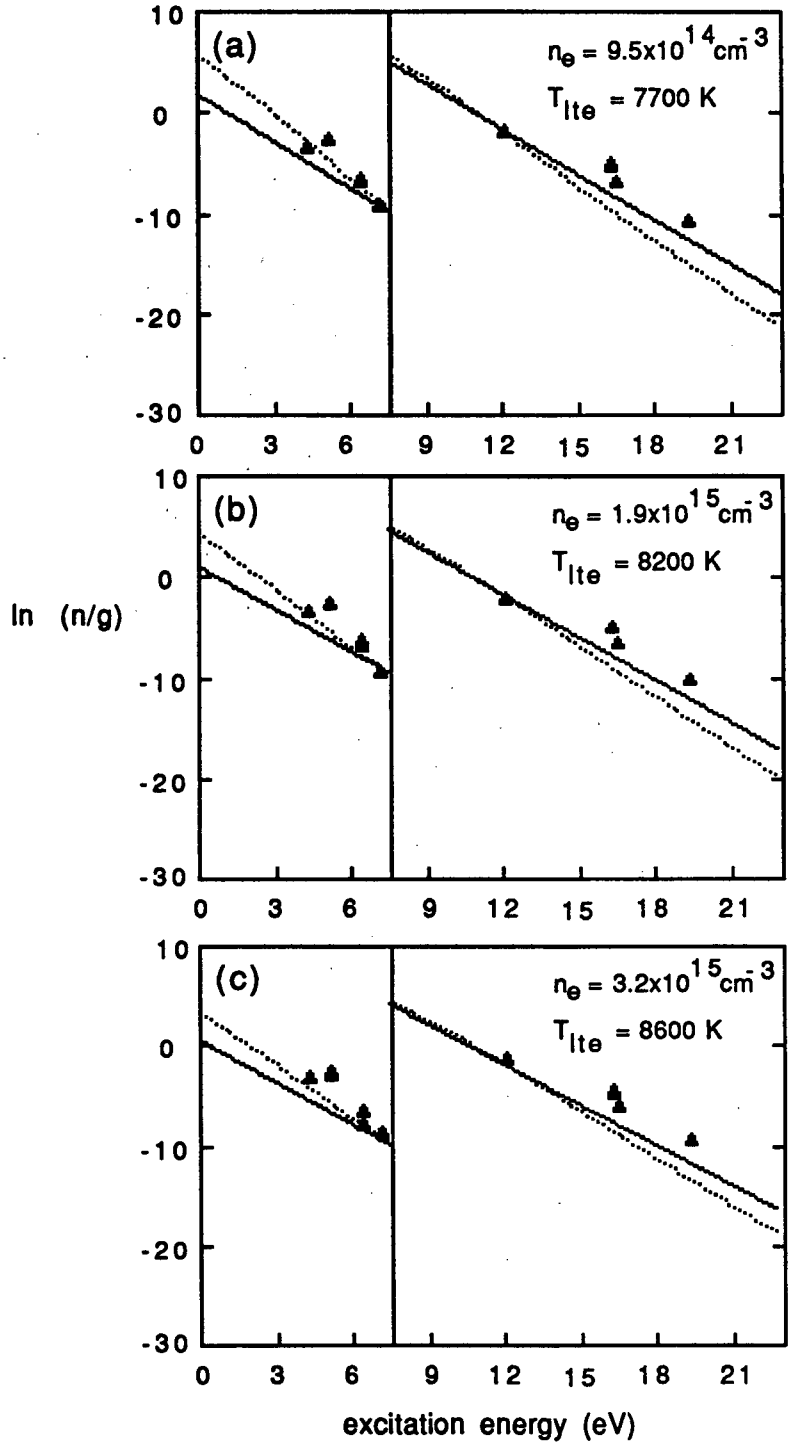

Figure 4.3 Boltzmann plot for Mg at 9 mm alc, a radial position of 2 mm and (a) an rf power of 1.00, (b) 1.25, (c) 1.50 kW; the solid line represents lte, the dotted line the simple rate model, and the triangles experimental points.

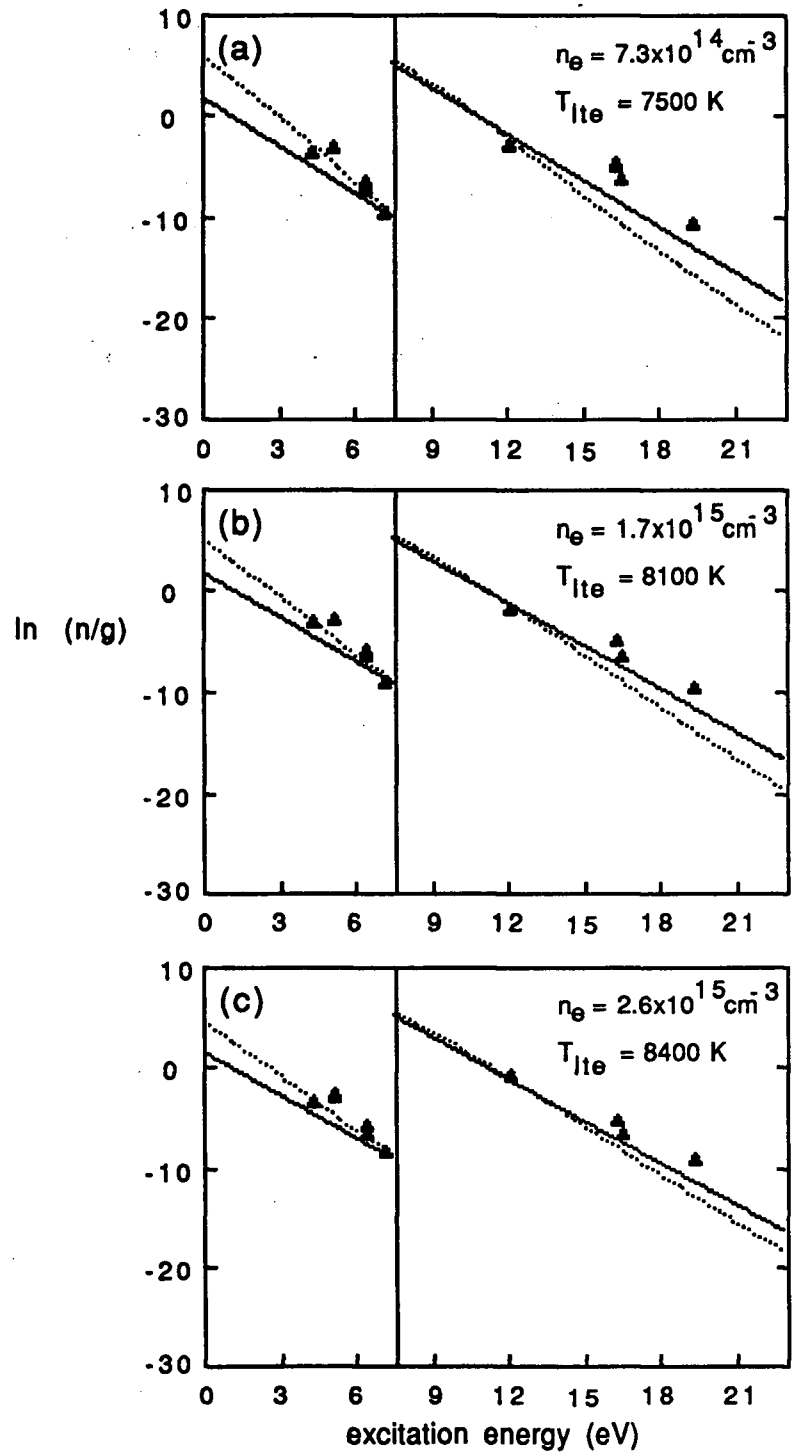

Figure 4.4 Boltzmann plot for Mg at 12 mm alc, a radial position of 2 mm and (a) an rf power of 1.00, (b) 1.25, (c) 1.50 kW; the solid line represents lte, the dotted line the simple rate model, and the triangles experimental points.

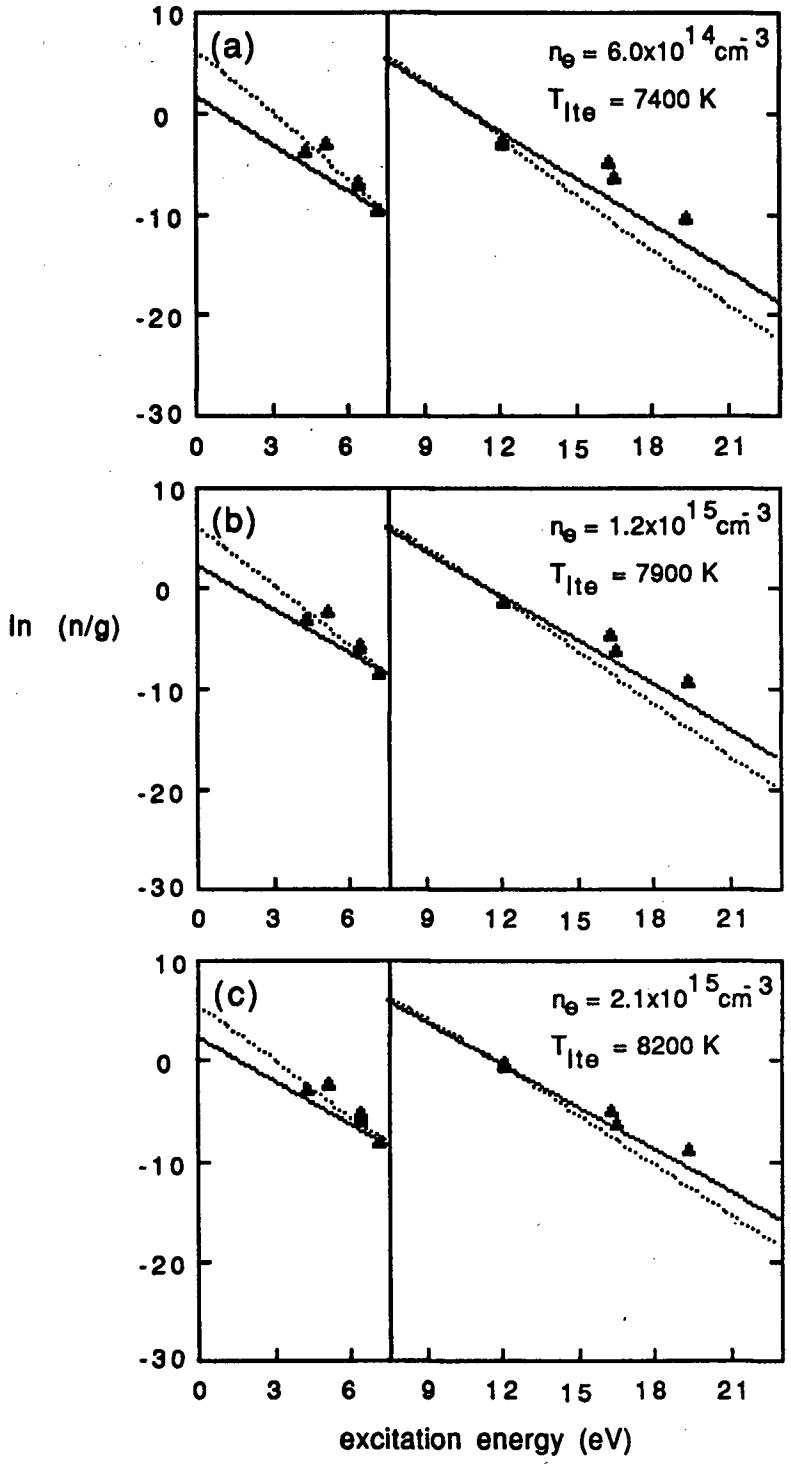

Figure 4.5 Boltzmann plot for Mg at 15 mm alc, a radial position of 2 mm and (a) an rf power of 1.00, (b) 1.25, (c) 1.50 kW; the solid line represents lte, the dotted line the simple rate model, and the triangles experimental points.

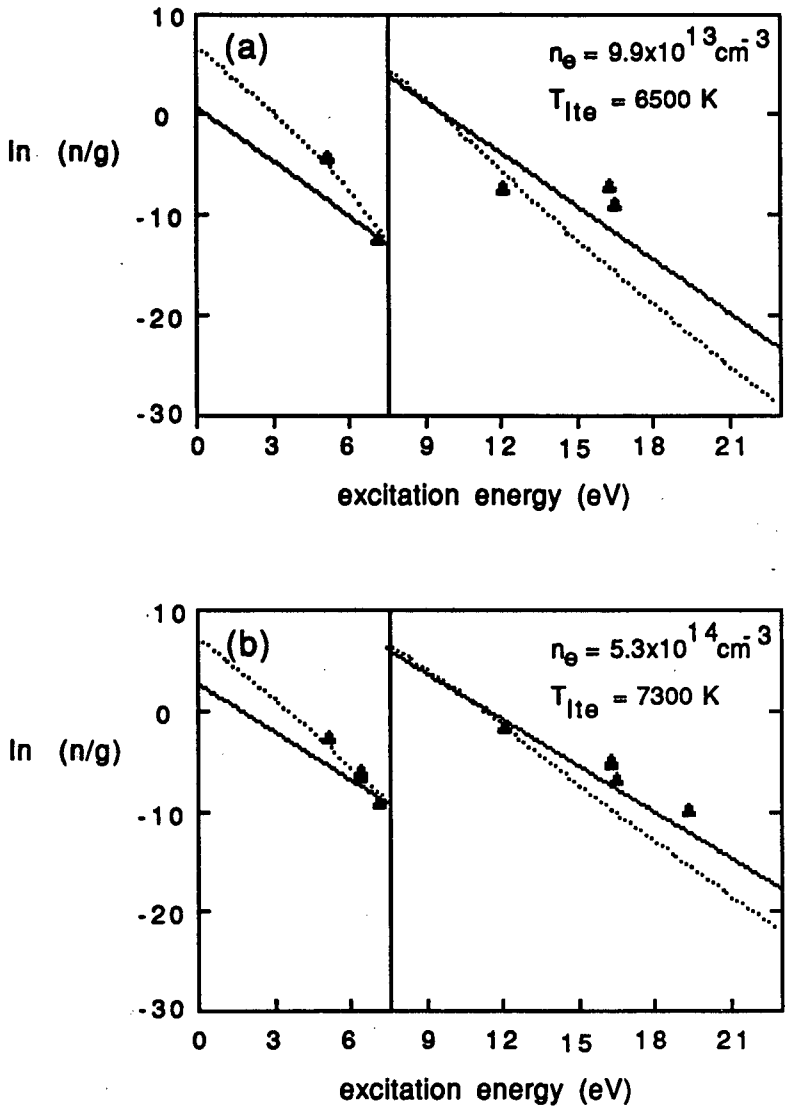

Figure 4.6 Boltzmann plot for Mg at 18 mm alc, a radial position of 2 mm and (a) an rf power of 0.75, (b) 1.00 kW; the solid line represents lte, the dotted line the simple rate model, and the triangles experimental points.

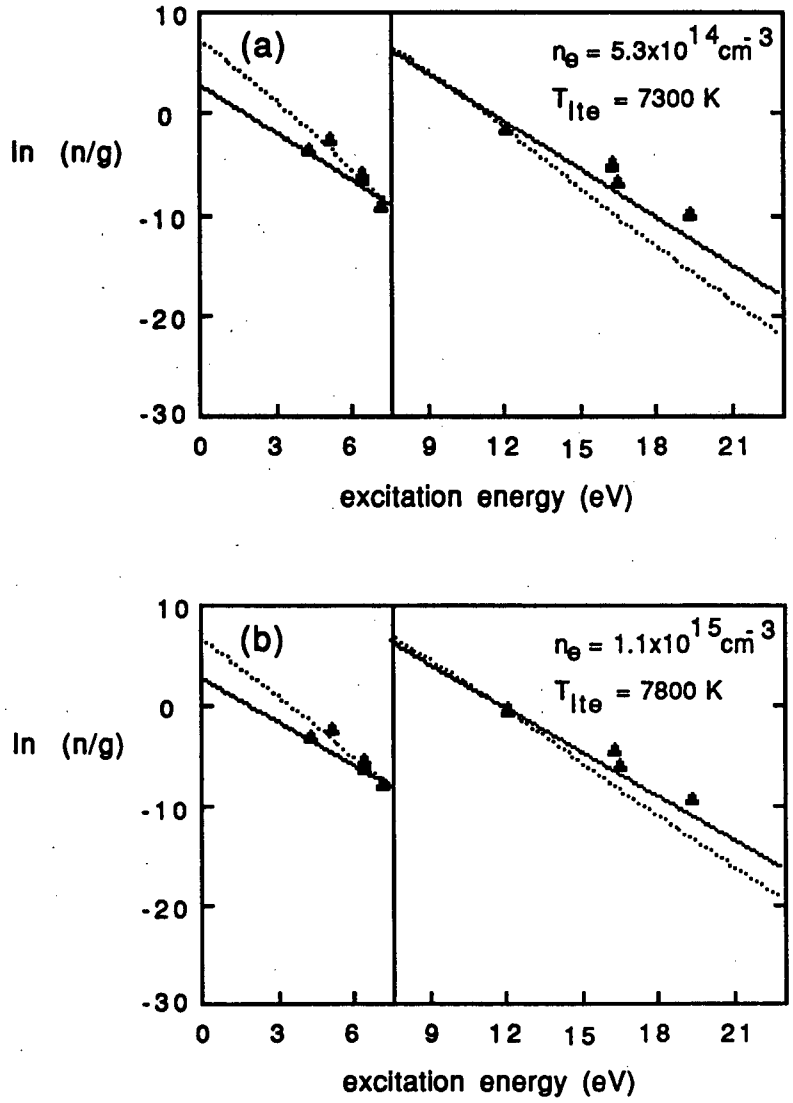

Figure 4.7 Boltzmann plot for Mg at 18 mm alc, a radial position of 2 mm and (a) an rf power of 1.25, (b) 1.50 kW; the solid line represents lte, the dotted line the simple rate model, and the triangles experimental points.

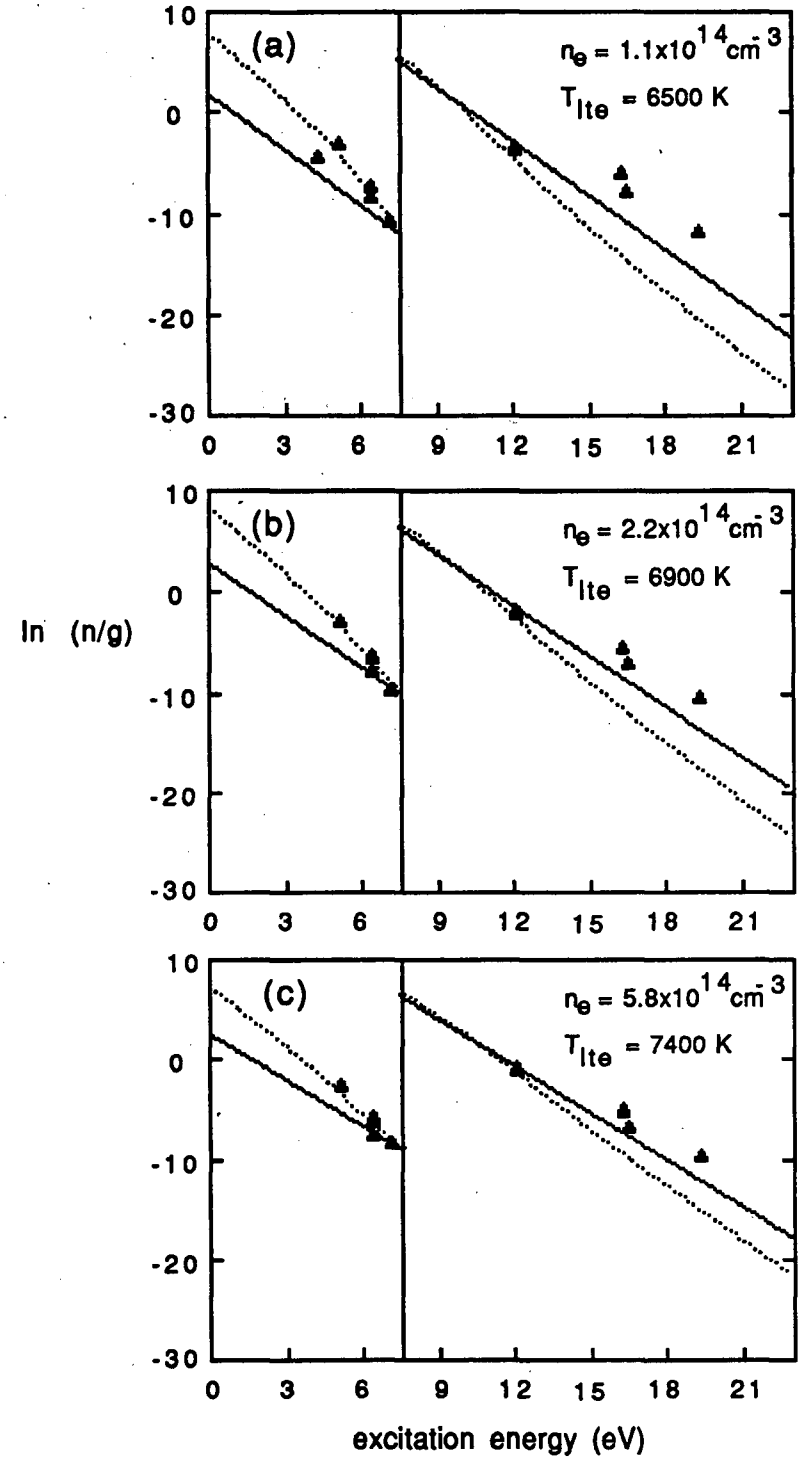

Figure 4.8 Boltzmann plot for Mg at 21 mm alc, a radial position of 2 mm and (a) an rf power of 1.00, (b) 1.25, (c) 1.50 kW; the solid line represents lte, the dotted line the simple rate model, and the triangles experimental points.

an rf power of 1.00 kW, the (b) to 1.25 kW, and the (c) to 1.50 kW. The data in figures 4.6 and 4.7 were collected at a height of 18 mm above the load coil and rf powers of 0.75 kW [4.6(a)], 1.00 kW [4.6(b)], 1.25 kW [4.7(a)], and 1.50 kW [4.7(b)]. In these plots the triangles correspond to the experimental points, the solid line to the expected lte populations (based on the measured electron density), and the dotted line to the results of the simple rate model presented in the previous chapter (i.e. to the populations which would be expected taking radiative decay, but not charge transfer with argon, into account).

As was discussed in the previous chapter, in these plots the uncertainty in the placing of the lte lines due to the experimental uncertainty in the measured electron density is negligible. For a discussion of the experimental errors in the measured level populations the reader is referred to that chapter. In the Boltzmann plots the size of the triangles used to represent the experimental points corresponds roughly to their estimated uncertainty range.

The most immediately striking feature of these plots is the overpopulation of the energy levels of the magnesium ion amenable to charge transfer (around 16.5 eV) with respect to the simple rate model calculations (dotted line). In addition, the ion energy level at 19.28 eV (with respect to the ground state atom) is also overpopulated compared to the rate model predictions*. In every plot, the ion energy level at 12.08 eV, which lies well below the ionization energy of argon (15.76 eV) (and thus would not be

* Due to its low intensity, it was not possible to measure the spectral line originating from this level at 6 mm above the load coil.

expected to undergo charge transfer with argon), argees very well with the rate model calculations, and is not overpopulated at all.

At heights of 12, 15, 18, and 21 mm above the load coil (figures 4.4 to 4.8), although there is some scatter in the experimental points for the lower lying atomic energy levels, it appears that the simple rate model agrees reasonably well with experiment for the atomic magnesium species. At the heights of 6 and 9 mm above the load coil (figures 4.2 and 4.3) these lower lying atomic energy levels appear to be somewhat overpopulated, the effect being more pronounced at higher rf powers.

These observations can be explained using the following tentative argument. Charge transfer between argon ions and ground state magnesium atoms causes the charge transfer levels of the magnesium ion to be overpopulated. The more highly energetic ionic levels are excited by electron impact from the charge transfer levels, and are thus also overpopulated, whereas the lower energy ionic levels are excited by electron impact from the ground state ion, and are thus not overpopulated. The lower energy states of the atom seem to only be overpopulated when the electron density is reasonably high (i.e. low heights above the load coil and high rf powers) and are thus likely populated, at least partially, by the recombination of the charge transfer levels with an electron. This rationale will now be more fully elaborated.

In a relatively recent paper van der Mullen et al. [104] have derived the following expression for the overpopulation of the charge transfer levels of magnesium:

$$b(Mg^{+}_{ct}) = \frac{b(Mg_o)}{b(Ar_o)} \qquad (4.2)$$

where it is recalled that the b-values for the various species are defined as the ratio of the actual population to the expected equilibrium population and $b(Mg^{+}_{ct})$ is the overpopulation due only to charge transfer, not also to radiative decay. This expression follows easily from the charge transfer reaction, $Mg_o + Ar^{+}_o \rightarrow Mg^{+}_{ct} + Ar_o$, realizing that for a system in partial-lte the b-value of the ground state ion must be unity (so $b(Ar^{+}_o) = 1$) and making the approximation that the rate of the charge transfer reaction is significantly larger than that of any other populating or de-populating mechanism of the charge transfer levels of magnesium. Van der Mullen et al. have shown that, under most operating conditions, this is a reasonable approximation to make for the icp.

It is worth pointing out, as it is sometimes misunderstood, that charge transfer can cause a significant overpopulation of the appropriate ionic levels of magnesium even though the reverse process is also occurring. Radiative decay of the excited levels of the magnesium atom to the ground state ($Mg^{*} \rightarrow Mg_o + h\nu$), which is not balanced by the inverse process of absorption, causes the ground state atom to be overpopulated. Using a simple Le Chatlier's principle argument, the reaction $Mg_o + Ar^{+}_o \rightleftarrows Mg^{+}_{ct} + Ar_o + \Delta E$ will have its equilibrium shifted to the right. This is so because, as will be seen below, the ground state argon atom will not be significantly overpopulated (due to radiative decay) since the very high argon concentration is sufficient that self-absorption ($Ar_o + h\nu \rightarrow Ar^{*}$)

will occur to a very appreciable extent, negating the effect of radiative decay.

From the simple rate model presented in the previous chapter it is a simple matter to calculate the overpopulation of the ground state magnesium atom due to radiative decay, $b(Mg_o)$, as a function of electron density; from equation (3.10) this is simply equal to $1 + const/n_e T^{0.107}$. From equation (4.2), one can see that a plot of $\ln\{b(Mg^+_{ct})\}$ versus $\ln\{b(Mg_o)\}$ should yield a straight line with a slope of unity and an intercept of $-\ln\{b(Ar_o)\}$ if this latter value is approximately constant over the electron density range for which data was acquired. If self absorption for argon were relatively complete, this value would be zero. Such a plot is presented in figure 4.9. The procedure for the construction of the plot was as

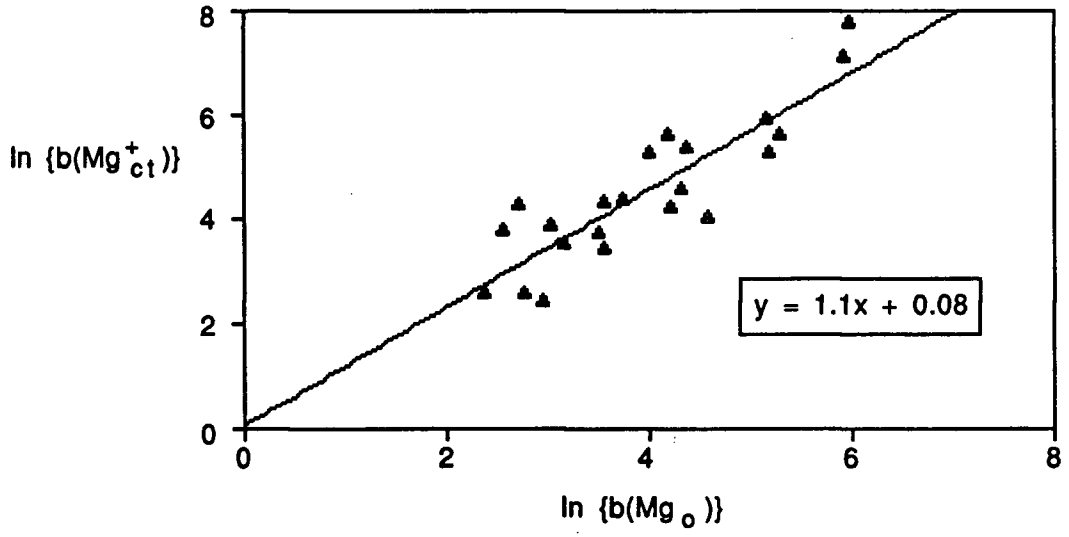

Figure 4.9 A plot of $\ln\{b(Mg^+_{ct})\}$ (measured from the data presented in figures 4.2-4.8) versus $\ln\{b(Mg_o)\}$ (calculated from equation (3.10)). The line is a linear regression to the points, the equation for which is shown in the inset box.

follows: for each of the plots in figures 4.2 to 4.8 for which the population of the charge transfer levels of the magnesium ion was obtained (also including data from an rf power of 0.75 kW, not shown in all the figures), $\ln\{b(Mg^{+}_{ct})\}$ was calculated by taking the average of the distance of the charge transfer levels of magnesium from the population which would be expected from the results of the simple rate model (i.e. the overpopulation due only to charge transfer, not also to radiative decay). Using the corresponding measured electron density $\ln\{b(Mg_o)\}$ was calculated from this model.

Even though there is a fair amount of scatter in the plot the slope is, as expected, quite close to unity; considering the distance which must be extrapolated to determine the y-intercept, this value is quite close to the predicted value of zero. This lends credence to the belief that the ground state of the argon atom is not overpopulated due to radiative decay ($b(Ar_o) \approx 1$) - the high concentration of argon in the plasma leads to relatively complete self-absorption for argon.

Using the data presented in the previous plot it is possible to use equation (4.2) to calculate a value for $b(Ar_o)$; this has been done, the result being plotted as a function of the electron density in figure 4.10. Although it is far from conclusive, it would seem that $b(Ar_o) \approx 1$; it seems unreasonable that $b(Ar_o)$ would vary in such a seemingly random fashion with the electron density, and that therefore the scatter in the plot probably represents the experimental error.

In figure 4.11 the logarithm of the overpopulation factor for the high excitation energy level of magnesium, $\ln\{b(Mg^{+}_{hi\ E})\}$, is plotted

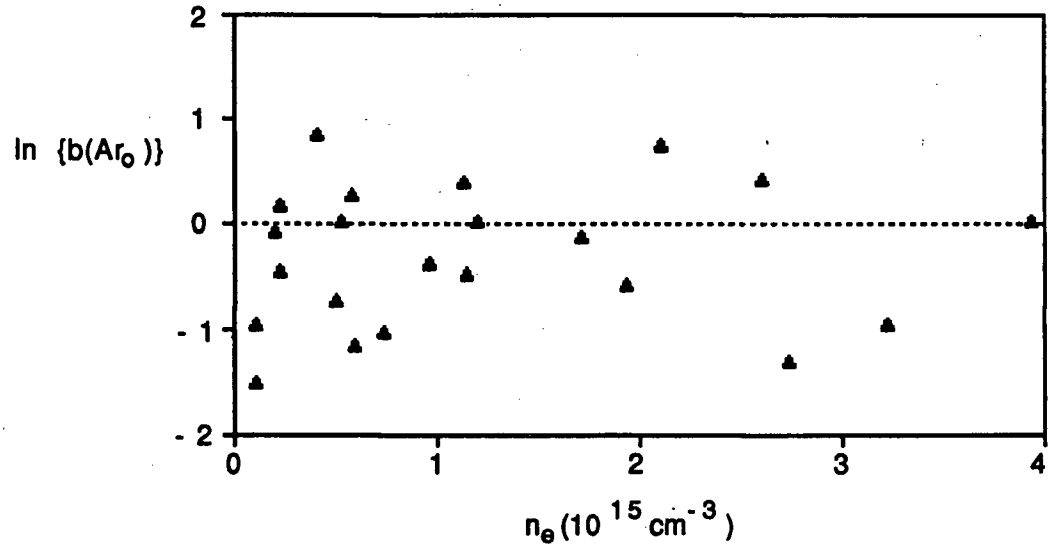

Figure 4.10 A plot of $b(Ar_o)$, calculated using the data presented in figure 4.9 and equation (4.2), as a function of the corresponding electron density.

as a function of $\ln\{b(Mg^+_{ct})\}$. It is fairly clear from the plot that the overpopulation of the highly excited level of the magnesium ion increases roughly linearly with the overpopulation of the charge transfer levels. This lends evidence to the theory that these high excitation energy levels of the ion are populated mainly by electron collisions from lower lying levels, such as the charge transfer ones, as opposed to direct excitation from the magnesium ion ground state. This is so because, as can be seen in figures 4.2 to 4.8, the ionic energy levels lying below the charge transfer levels are not overpopulated at all.

As mentioned previously, the atomic magnesium states seem to be overpopulated (with respect to the simple rate model calculations) only when the electron density is reasonably high. A possible reason for this could be the contribution of the three-body recombination

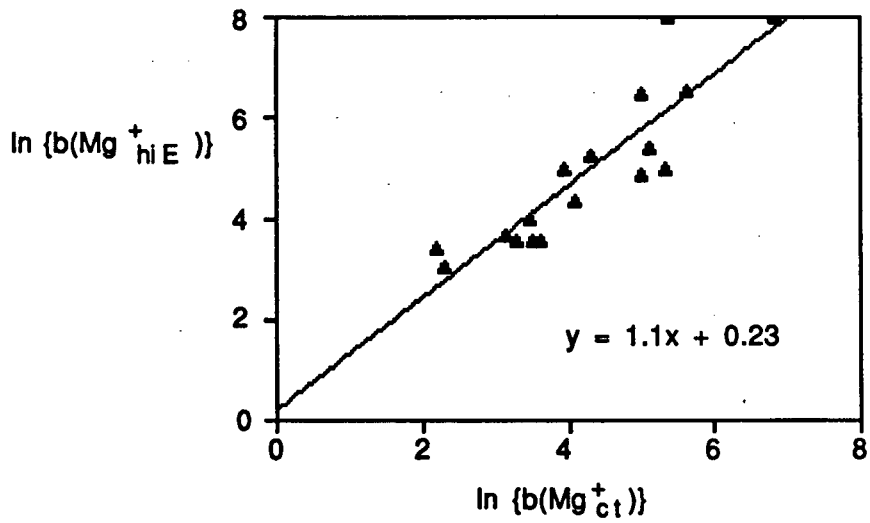

Figure 4.11 A plot of $\ln\{b(Mg^+_{hi\ E})\}$ as a function of $\ln\{b(Mg^+_{ct})\}$ for the data presented in figures 4.2-4.8. The line is a linear regression to the points, the equation for which is shown in the inset box.

process to these atomic levels (Mg^*): $Mg^+_{ct} + 2e^- \rightarrow Mg^* + e^-$. Since the rate of this process scales as the square of the electron density, it would be expected to be significant only at high values of the electron density, as observed.

It is still somewhat unclear as to why Hasegawa and Haraguchi [62] saw no evidence of charge transfer in either their experimental Boltzmann plots or in their theoretical calculations (although their calculations did use the classical theory of Gryzinski [60] for the calculation of the cross section of the charge transfer process of magnesium with argon, which is likely to be quite inaccurate [65]). The reason they saw no experimental evidence for charge transfer is probably due to the fact that their rate model calculations underestimate the extent of deviations from lte in the plasma due to

radiative decay (resulting from their over-estimating the collisional rate constants [84]). Unlike the results presented in this and the previous chapter, their lte prediction is almost the same as their rate model prediction for the ionic species. By examining, for example, figure 4.3(a) one can see that the deviations from prediction due to charge transfer really only become apparent when one compares to the results of the simple model predictions, not to the lte ones.

The reason that, in the previous chapter, no evidence for the existence of charge transfer was found for either chromium or iron (even though they both have energy levels near the ionization energy of argon, and thus would be expected to be amenable to charge transfer) is still uncertain. Hasted [65] and other authors [53, 93] have pointed out that in order for charge transfer to take place between two atoms A and B, the potential energy curves formed by the pseudo-molecule A^+B must cross those formed by AB^+ at large values of the internuclear separation. These authors have also pointed out that only detailed theoretical calculations can determine whether or not such a crossing will occur. It is possible, although in light of the large number of energy levels of both ionic iron and chromium, unlikely that such a crossing does not occur for the pseudo-molecules formed by these species with argon. The most likely explanation for this observation is perhaps that since ionic iron and chromium both have a great many different energy levels, the effect of charge transfer to a few particular ones is very quickly "smeared out" (by electron impact excitation) over all of these levels, and is thus not noticeable. Magnesium, on the contrary, has

relatively few different energy levels by comparison, and thus the effect of charge transfer will likely be much more noticeable.

4.4 Summary

The data presented in this chapter have shed light on the nature of excitation processes in the inductively coupled plasma. It has been shown that charge transfer between argon and ground state magnesium atoms causes the ionic magnesium to be overpopulated (with respect to the simple rate model calculations). It seems that the more highly energetic ionic levels are excited by electron impact from the charge transfer levels (and are thus overpopulated), whereas the lower energy ionic levels are excited by electron impact from the ground state ion (and are not overpopulated). It has also been shown that three body recombination of magnesium ions with electrons is likely of major importance at high electron densities, but not at lower ones.

In addition, it seems that due to the high density of argon atoms in the icp ($>10^{18}$ cm^{-3}) self-absorption for argon is likely very appreciable so that, for argon, radiative decay is balanced by its inverse process of absorption, resulting in no overpopulation of the ground state atom ($b(Ar_o) \approx 1$).

Tentative explanations for some of the apparent contradictions involving charge transfer have been offered. However, there is still considerable work to be done before the nature of charge transfer in the inductively coupled plasma is fully understood and all contradictions (such as why Mermet's research group observed the

existence of charge transfer for copper, whereas our's did not) are resolved.

Chapter 5
Some Electron Temperature Measurements In the ICP

5.1 Introduction

It is generally recognized that in addition to the electron density one of the key parameters needed for a complete description and understanding of the icp is the electron temperature (T_e) [70]. The electron temperature is particularly important since electron collisions are believed to be mainly responsible for analyte excitation and ionization. For a plasma which is far from equilibrium, the electrons may not follow a Maxwell-Boltzmann (MB) velocity distribution, thus making the electron temperature difficult or impossible to define. However, due to their small mass, the time for electrons to reach an equilibrium velocity distribution is extremely short, and thus they should conform to a MB velocity distribution [63, 103]. Hieftje's research group [70] has recently experimentally verified that electrons do indeed seem to possess a MB velocity distribution. The prevailing opinion is that electrons have a MB velocity distribution with a temperature of T_e, while heavier particles also have an equilibrium velocity distribution, but at a different (lower) temperature (T_{gas}) [91].

In chapter three of this thesis it was shown that, for elements which do not exhibit charge transfer with argon, it is possible to use a simple rate model based upon the electron density (which uses the temperature $T_{e,lte}$ calculated from it) to accurately predict excited-state level populations. This is strong evidence for the assertion

that the actual electron temperature does not differ significantly from $T_{e,lte}$. If it did, the fit of the theoretical rate model to the high energy atomic levels would be poor, since, as was pointed out in chapter three, the close spacing of these energy levels causes them to be in equilibrium with the surrounding electron gas.

Very few authors have simultaneously reported radially resolved measurements of both the electron temperature and the electron density, due mainly to the difficulty of determining the electron temperature. Hasegawa and Haraguchi [63] have reported both electron densities and electron temperatures (using the method of absolute continuum intensity measurements). In general their value of T_e is about 200 to 500 K greater than the corresponding $T_{e,lte}$ (calculated from their n_e) - very close considering the errors involved. From the results of Batal et al. [11] T_e is 1000 to 3000 K greater than the corresponding $T_{e,lte}$; this is very difficult to believe and leads one to suspect a systematic error in the measurement [63]. In addition, the electron density in their plasma was quite low ($< 5x10^{14}cm^{-3}$), making the measurement of both T_e and n_e very difficult. More recently, Huang and Hieftje [68] have measured both T_e and n_e using Thomson scattering; they found that T_e was about 1500 K less than the corresponding $T_{e,lte}$ value. Due to experimental difficulties with the Thomson scattering technique it is not clear what the accuracy of these results is.

In this chapter radially resolved values of both $T_{e,lte}$ (calculated from the electron density) and the actual electron temperature itself (determined from the ratio of the emission intensity of the 430 nm line of argon to that of the adjacent recombination

continuum) are reported for rf powers of 0.75, 1.00, 1.25, and 1.50 kW at several heights above the load coil. The motivation for this study was to see how good an approximation $T_{e,lte}$ is to the actual electron temperature. The results indicate that, at least for electron densities greater than about $2x10^{15}$ cm^{-3}, it is a very good approximation. Below this value, due to the large experimental errors involved, it is difficult to draw definitive conclusions regarding the agreement between T_e and $T_{e,lte}$.

5.2 Theory

As described in the introduction to this thesis, it is possible to generate accurate, radially resolved electron densities for the icp from the measurement of radially resolved (i.e. Abel inverted) scans of the profile of the 486.13 nm H_β line of hydrogen [16, 32, 75]. It was also shown how it is possible to use this value of the electron density to calculate an "lte electron temperature", $T_{e,lte}$. Since this method of calculating the electron density is, in general, both convenient (at least when using a photodiode array spectrometer) and more accurate than other methods [12, 75, 137], the resulting $T_{e,lte}$ is also both accurate and conveniently calculated.

The electron temperature itself (T_e), on the other hand, is relatively difficult to measure directly for plasmas which are not in lte [12, 95]. As was pointed out in reference [95], because the intensity of the argon recombination continuum is such an insensitive function of temperature, it cannot be used for the calculation of T_e. The Thomson scattering method used by Hieftje's research group [68-70, 91] is, in theory, quite accurate.

Unfortunately, in practice the necessary equipment is both complex and expensive; in addition the experimental complexity can cause the method to give results less accurate than expected [110].

The method chosen for the calculation of T_e for this work is based upon the measurement of the ratio of the intensity of the 430.01 nm line of argon to that of the adjacent continuum (from the radiative recombination of argon ions with electrons). The method has been described elsewhere [10, 12], so only a brief description will be given here. As was outlined in reference [10], the intensity of the recombination continuum as a function of wavelength (λ) can be written:

$$\varepsilon_{continuum}(\lambda) = (const.)\ \frac{n_e \cdot n_i}{\lambda^2 \cdot \sqrt{T_e}}\ \zeta(T_e) \qquad (5.1)$$

where n_i is the total ion density and ζ is a "correction factor" to account for deviations from classical behaviour. The emission intensity of an argon atom line (of wavelength λ) can be written (using the Saha equation):

$$\varepsilon_{line}(\lambda) = (const.)\cdot\frac{gA}{\lambda \cdot Q_i(T_e)} \cdot n_e \cdot n_i \cdot T_e^{-3/2} \cdot exp\left\{\frac{E_i}{kT_e} - \frac{E}{kT_{exc}}\right\} \qquad (5.2)$$

where gA is the degeneracy weighted transition probability for the transition, Q_i is the partition function for ionic argon, E_i is the ionization energy of argon, E is the energy of the level from which the transition originates, T_{exc} is the excitation temperature, and k is

Boltzmann's constant. In the derivation of the above equation it is assumed that the density of argon ions is equal to n_i (the total ion density).

Dividing equation (5.2) by (5.1) and substituting all the numerical values for the 430.01 nm line of argon gives [10]:

$$\frac{\varepsilon_{line}}{\varepsilon_{continuum}} = \frac{742 \cdot \exp(14330\ K/T_e)}{(T_e/K) \cdot Q_i(T_e)} \quad . \qquad (5.3)$$

For the above equation to apply the continuum should be summed over a 10.0 nm wide spectral range near 430 nm. In deriving the above equation it was assumed that ζ is constant over the temperature range of interest (a very good approximation [95]) and that for this particular argon line, with its excitation energy lying very close to the ionization energy, $T_{exc} \approx T_e$ (again, a very good approximation, especially since argon is "close to lte" {as shown in the previous chapter}). To a very good approximation, $Q_i(T)$ can be set equal to $(4 + 2\exp(-2061K/T))$ (by summing over the two lowest energy levels of the argon ion). In figure 5.1 this intensity ratio is plotted as a function of the electron temperature. It can be seen that this function is relatively sensitive to changes in the electron temperature.

In the derivation of equation (5.3) there is one approximation which may not be reasonable for an icp which has water introduced into it (necessary so that there is sufficient hydrogen in the plasma to determine the electron density from the Stark broadening of the H_β spectral line) - namely the approximation that the total ion

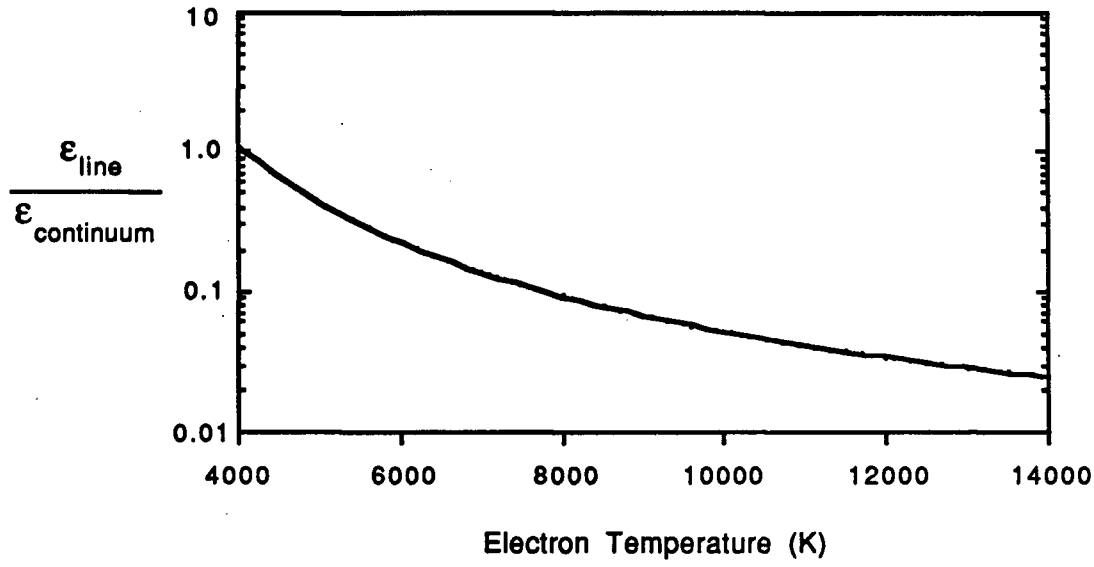

Figure 5.1 A plot of the ratio of the intensity of the Ar I 430.01 nm spectral line to the intensity of the adjacent continuum (summed over a 10.0 nm wide range), as a function of the electron temperature.

density is equal to the argon ion density (that coming from hydrogen and oxygen being negligible). For an icp operating under typical conditions of $T_{e,lte}$ = 7500 K and n_e = 6.6×10^{14} cm^{-3} argon will be about 0.07 % ionized, hydrogen about 0.15 % ionized, and oxygen about 0.3 % ionized. From the total flow rate of argon into the plasma and the total uptake rate of water (assuming a nebulizer efficiency of 1 %), the ratio of argon to water entering the plasma can be easily calculated to be of the order of 900. Assuming that the water is fully dissociated this leads to a ratio of argon ions to other ions (hydrogen and oxygen) of about 100.

At this ratio of argon ions to other ions, equation (5.3) should give reasonably accurate electron temperatures. However, in actual

fact, the water will not be evenly distributed throughout the plasma but will be confined mostly to the aerosol channel. Thus one can expect that at radial positions less than about ±1.5 mm the method may give inaccurate results, whereas at positions further off axis (where the ratio of argon ions to other ions will be considerably greater than 100) the method should give quite accurate results (within 10 % [10]).

5.3 Experimental

Full details of the experimental system are given in chapter two of this thesis. The detector used was the 2048 element linear photodiode array. Deionized water was introduced into the plasma using the Meinhard nebulizer/spray chamber assembly (described in the experimental chapter). For the results presented in this chapter, the plasma argon flow rate was held constant at 10.0 L/min, the auxiliary flow rate was held at 0.2 L/min, and the entrance slit width on the monochromator was held at 40 μm. The values of the rf power supplied to the plasma were 0.75, 1.00, 1.25, and 1.50 kW and the plasma was observed at 6, 9, 12, 15, and 18 mm above the load coil (although at the higher heights and lower powers it was not possible to collect data due to the weakness of either the argon recombination continuum or the 430.01 nm line of argon, or both).

The procedure for collecting and processing the data was as follows. At each value of the rf power and height above the load coil, the wavelength profile of the H_β line of hydrogen was acquired across the width of the plasma, from which the spatially resolved electron density was calculated (as described in chapter two). From

the electron density, $T_{e,lte}$ was then calculated. Subsequently, the intensity of the 430.01 nm line of argon was acquired across the width of the plasma (along with the background ±1 nm on each side of this line for later background correction) at eleven diodes across the wavelength profile of the line. From this data, after Abel inversion, the background corrected intensity of the argon line, integrated across the linewidth (ε_{line}), could be easily calculated. At the same time 38 diodes measuring the continuum background at positions in the wavelength range 415 to 445 nm were acquired. These background continuum intensities were then Abel inverted, averaged, and multiplied by a scaling factor to give the equivalent intensity of the continuum background integrated across 10 nm ($\varepsilon_{continuum}$).

A simple computer program was written which accepted these values of ε_{line} and $\varepsilon_{continuum}$ as input and iteratively calculated the spatially resolved electron temperature at each of the 200 radial locations across the width of the plasma (for each value of the rf power and observation height). The resulting T_e and $T_{e,lte}$ data was then transferred from the Telex computer to an Apple (Cupertino, CA) Macintosh+ computer and plotted using Cricket Software's (Malvern, PA) "Cricket Graph" - a data analysis and plotting program.

5.4 Results

Figures 5.2 to 5.6 are plots of some of the resulting $T_{e,lte}$ (o) and T_e (•) data graphed as a function of radial position; figures 5.2 and 5.3 refer to 6 mm above the load coil (alc), figures 5.4 and 5.5 to

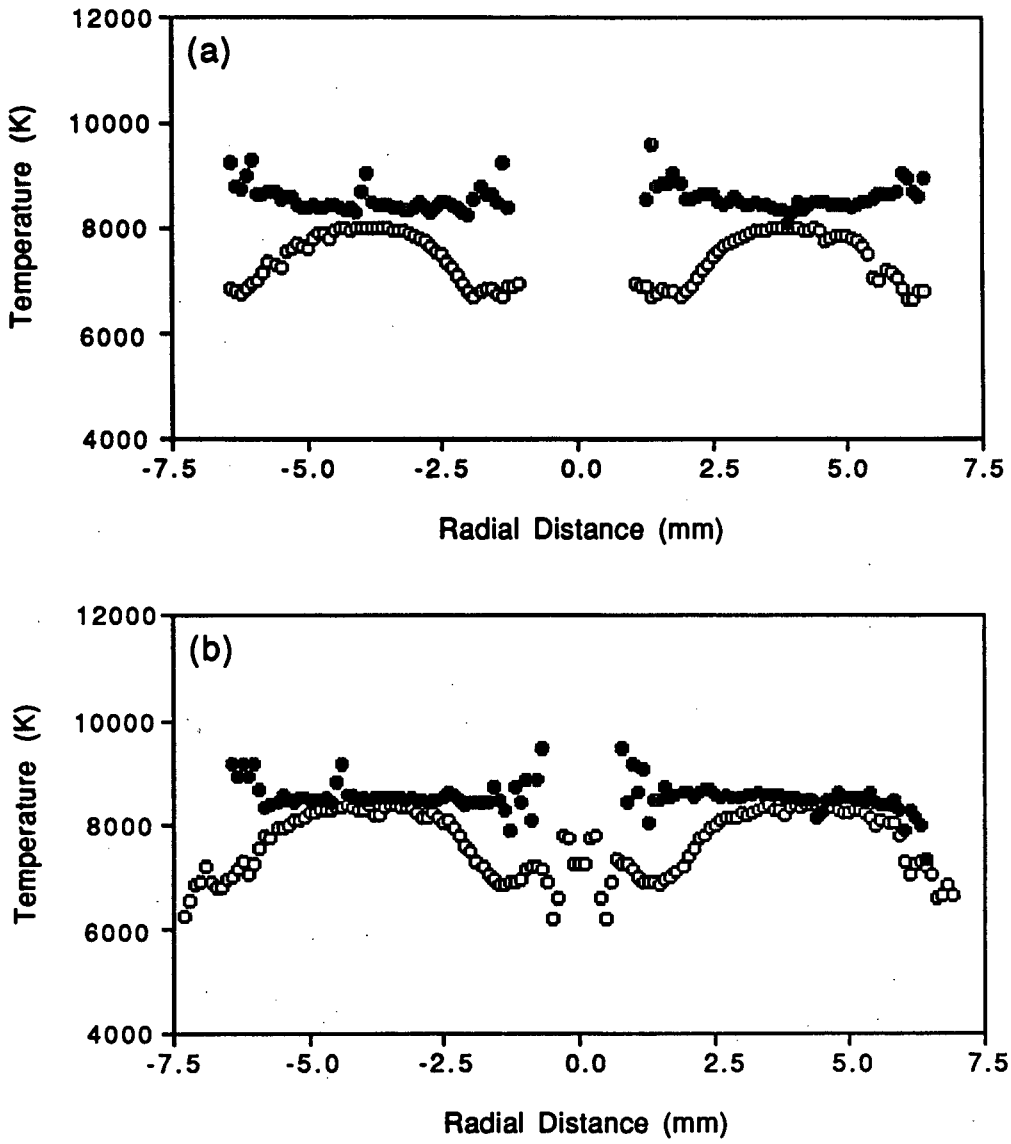

Figure 5.2 Plots of the electron temperature, T_e (•), and the lte temperature (calculated from the electron density), $T_{e,lte}$ (o), as a function of radial distance across the plasma at a height of 6 mm above the load coil and (a) an rf power of 0.75 kW, (b) 1.00 kW.

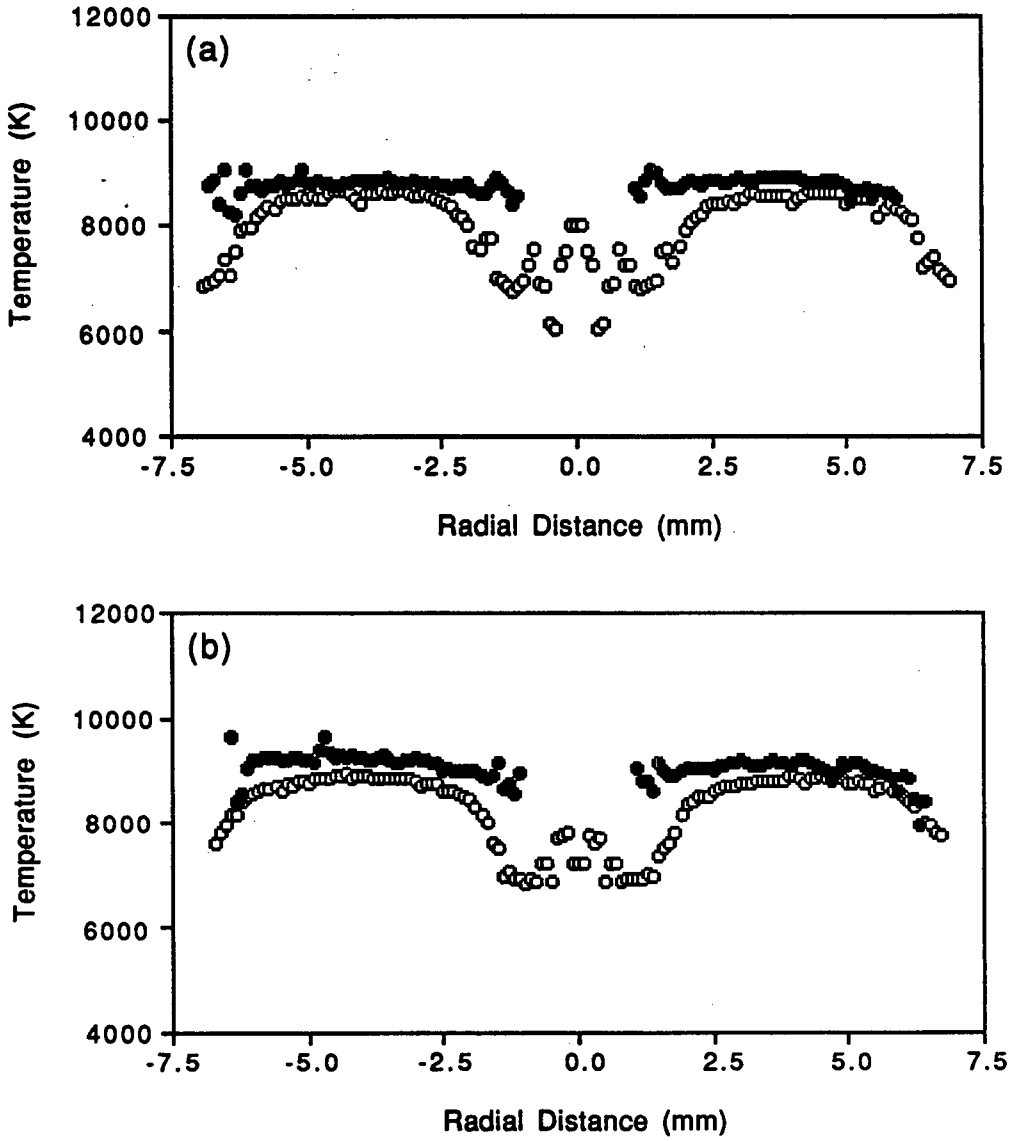

Figure 5.3 Plots of the electron temperature, T_e (•), and the lte temperature (calculated from the electron density), $T_{e,lte}$ (o), as a function of radial distance across the plasma at a height of 6 mm above the load coil and (a) an rf power of 1.25 kW, (b) 1.50 kW.

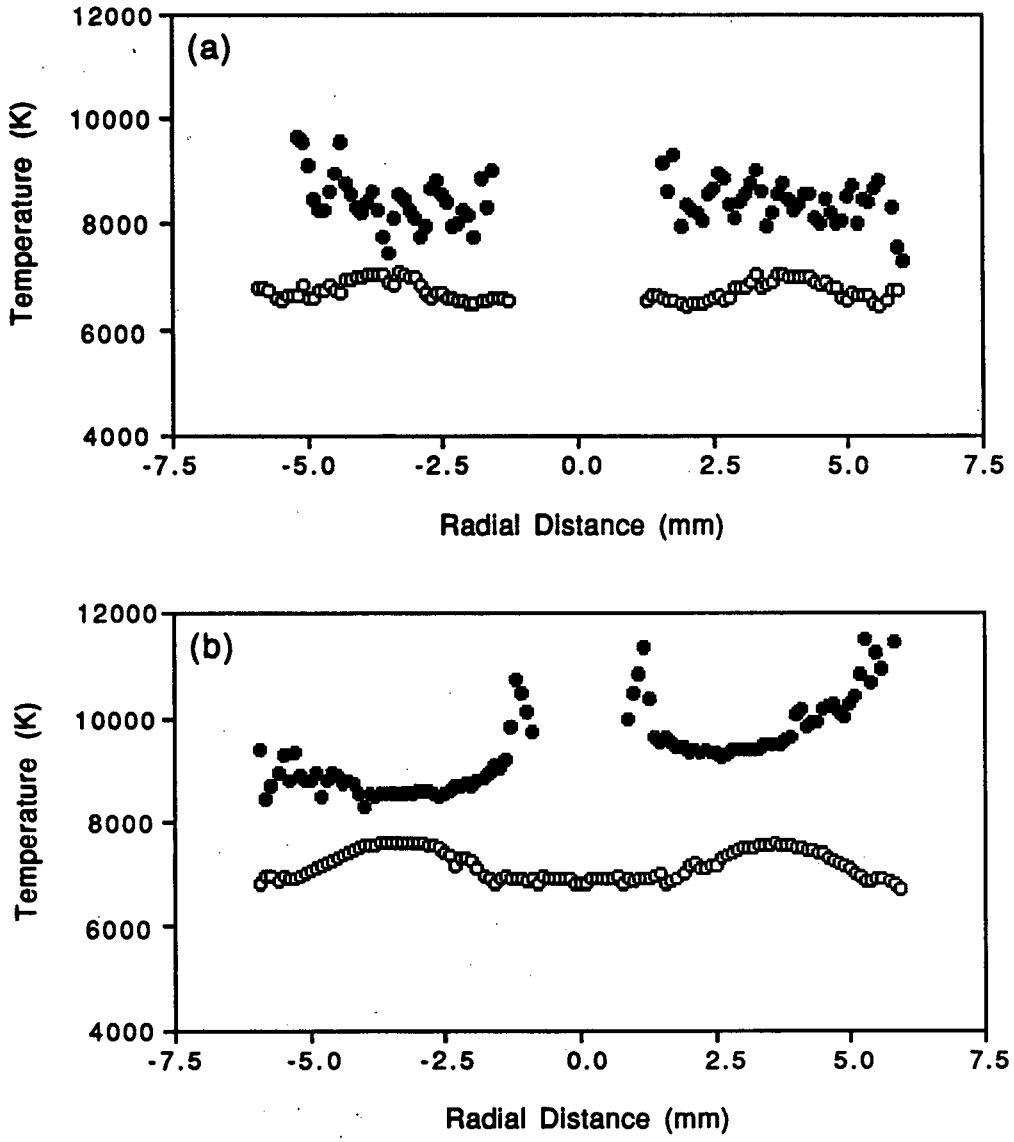

Figure 5.4 Plots of the electron temperature, T_e (•), and the lte temperature (calculated from the electron density), $T_{e,lte}$ (○), as a function of radial distance across the plasma at a height of 12 mm above the load coil and (a) an rf power of 0.75 kW, (b) 1.00 kW.

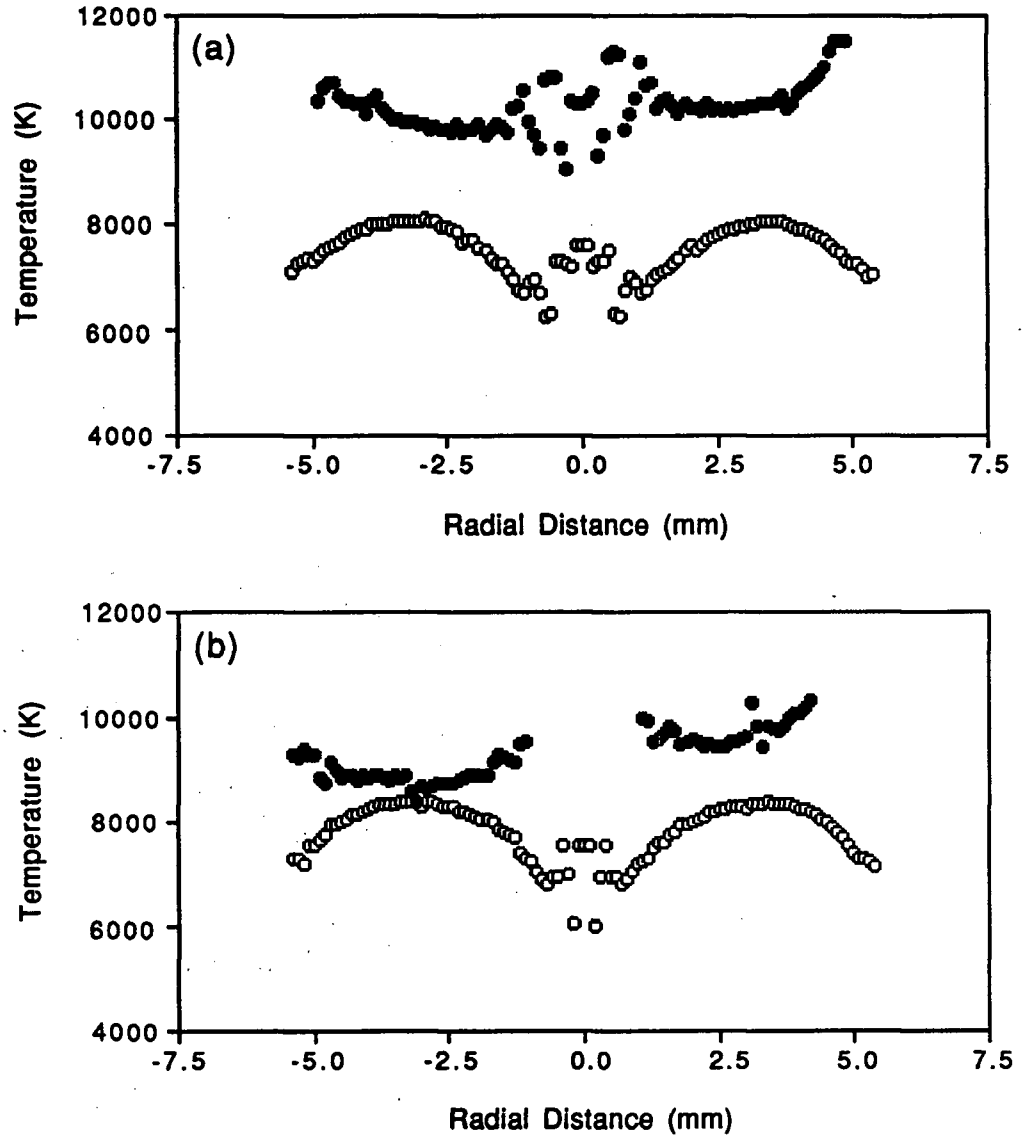

Figure 5.5 Plots of the electron temperature, T_e (•), and the lte temperature (calculated from the electron density), $T_{e,lte}$ (o), as a function of radial distance across the plasma at a height of 12 mm above the load coil and (a) an rf power of 1.25 kW, (b) 1.50 kW.

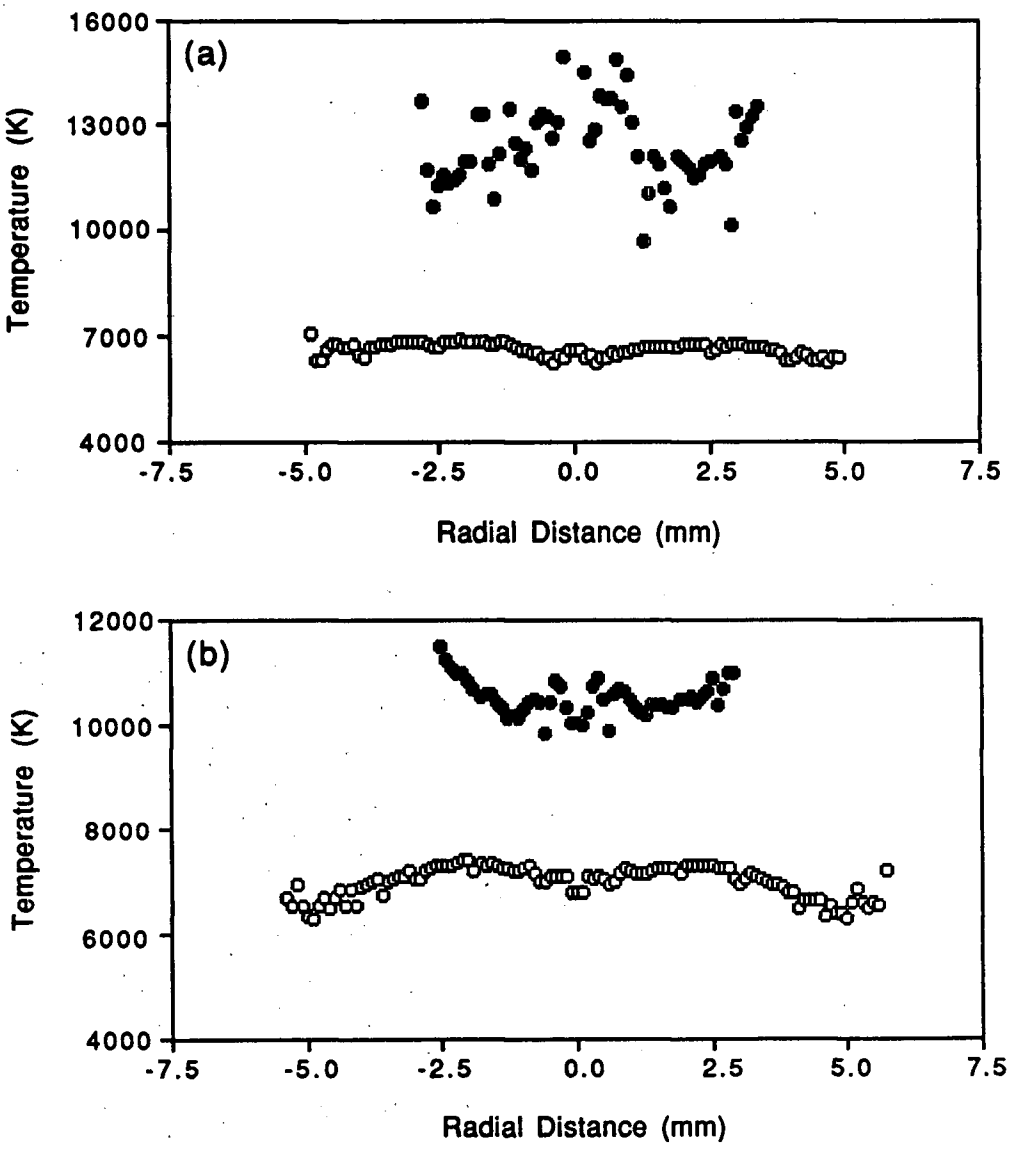

Figure 5.6 Plots of the electron temperature, T_e (•), and the lte temperature (calculated from the electron density), $T_{e,lte}$ (o), as a function of radial distance across the plasma at a height of 18 mm above the load coil and (a) an rf power of 1.25 kW, (b) 1.50 kW.

12 mm, and figure 5.6 to 18 mm. At the extremely low continuum intensities which exist at a height of 18 mm and rf powers below 1.25 kW, it was not possible to determine the electron temperature below this power. Data were also collected at a height of 9 mm alc (for rf powers of 0.75, 1.00, 1.25, and 1.50 kW) and 15 mm alc (for rf powers of 1.25 and 1.50 kW). Due to the low electron density which exists in the central channel of the icp (and also near the plasma edges), the intensity of the argon recombination continuum is very low; for this reason it was generally not possible to compute the electron temperature in this region.

From the data presented for 6 mm above the load coil (figures 5.2 and 5.3) one can see that the electron temperature itself seems to agree quite well with the value of $T_{e,lte}$ (keeping in mind the estimated uncertainty of 10 % in the T_e measurement); this is especially the case at higher values of the rf power. The data for 9 mm alc (not shown) was quite similar to that for 6 mm; the two temperatures were in agreement within about 4 % for all rf powers, with the exception of 0.75 kW (where the difference was approximately 8 %).

For the data at 12 mm alc (figures 5.4 and 5.5) the electron temperature is higher than $T_{e,lte}$ by anywhere from 500 to almost 2000 K. For this height the electron density ranged from about $4x10^{14}$ cm^{-3} (at 0.75 kW) to about $1.5x10^{15}$ cm^{-3} (at 1.50 kW). Unfortunately, at electron densities below about $1\text{-}2x10^{15}$ cm^{-3}, the intensity of the argon recombination continuum was so low that the accuracy of the electron temperature measurements is unclear. The

data for 15 mm above the load coil (not shown) was quite similar to that for 12 mm.

It has been postulated [48] that electrons created in the induction region of the plasma (up to about 6 mm alc or so) retain their kinetic energy for some time as they move upwards by both ambipolar diffusion (the simultaneous drift of both electrons and ions) and the upward flow of the incoming argon gas. If this were the case, by the time they reached 12 mm alc they would have diffused into the larger volume of the plasma at this height, thus having a lower electron density (and resulting $T_{e,lte}$), while still retaining a relatively high value of T_e. However this seems very unlikely. From reference [104], the time required for the electrons to travel 1 cm by ambipolar diffusion can be estimated to be about 5 ms, while the time required for the electrons to be carried 1 cm by the flow of the argon gas is, at the very least, 1 ms. From reference [37], the collision frequency of electrons with argon ions can be estimated to be about 10^{10} collisions/s; thus in 1 ms there would be about 10^7 collisions. In reference [101] it is estimated that an electron will loose about $3x10^{-3}$ % of its kinetic energy in a collision with an argon atom or ion; thus in 1 ms there will be far more than enough electron-heavy particle collisions for the electron velocity distribution to reach equilibrium with the heavy particles. Thus the reason for the apparent high value of T_e at 12 mm alc is likely due only to the experimental error caused by the low electron densities.

Figure 5.6 is a plot of T_e and $T_{e,lte}$ at 18 mm above the load coil (at rf powers of 1.25 and 1.50 kW). The electron temperature (as

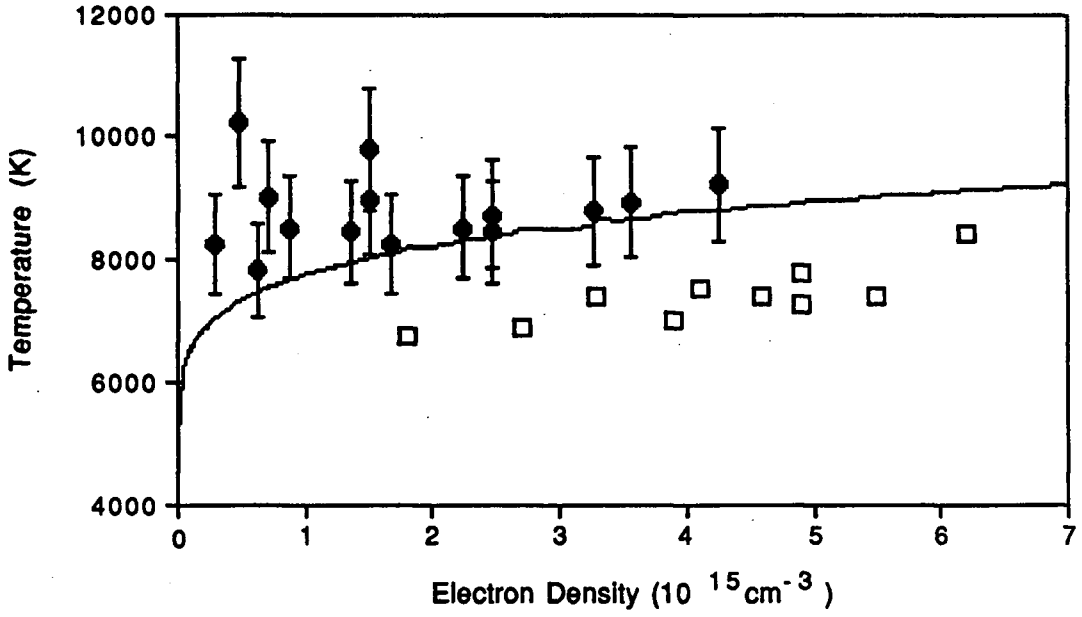

Figure 5.7 Plot of the electron temperature, T_e (•), and the lte temperature, $T_{e,lte}$ (solid line), as a function of the electron density; the error bars on T_e are 10 % of that value. In addition, the data of Huang and Hieftje [68] is shown (□).

calculated) is up to 5000 K larger than $T_{e,lte}$; again, this large discrepancy is most likely due to the error in calculating T_e at these low electron densities (of about $4x10^{14}$ cm^{-3}).

In figure 5.7 the electron temperature as measured here (filled circles) is plotted as a function of the electron density for a radial position of 3 mm from the plasma centre for each value of the vertical height and rf power used; error bars of 10 % of that value are shown. The solid line in figure 5.7 refers to $T_{e,lte}$, as calculated from the electron density; in addition, the results of Huang and Hieftje [68] (open squares) are shown. One can see that at all values

of the electron density greater than about 1.7×10^{15} cm^{-3} the electron temperature (as calculated here) differs from $T_{e,lte}$ by well less than the estimated 10 % uncertainty. At electron densities below this value, however, the difference can be up to 3000 K. Unfortunately, it is not clear if this difference is due only to the fact that the method of calculating T_e used here is inaccurate for values of n_e less than about $1\text{-}2 \times 10^{15}$ cm^{-3}, or if the electron temperature is at least somewhat larger than $T_{e,lte}$ in this electron density range (although the former seems more probable).

It can also be seen from the figure that the electron temperatures of Huang and Hieftje [68] are systematically lower than $T_{e,lte}$ by about 1500 K. Although it is not clear from that reference what the likely uncertainty in their T_e values may be, these results do not appear to be entirely reasonable; one would certainly expect that as the electron density increased (especially for values above about 5×10^{15} cm^{-3}) that the plasma would move closer to equilibrium, whereas their T_e values are consistently lower by an approximately constant factor.

5.5 Summary

It has been shown that for electron densities greater than about 2×10^{15} cm^{-3} the electron temperature (calculated from the ratio of the 430.01 nm line of argon to the adjacent continuum) is within the estimated experimental uncertainty of the lte temperature, $T_{e,lte}$ (as calculated from the electron density, measured by the Stark broadening of the H_β line of hydrogen). At lower electron densities the calculated value of T_e is higher than $T_{e,lte}$; unfortunately the

accuracy of the T_e determination (at these low electron densities) does not allow one to conclude whether or not the electron temperature is indeed actually higher. The implication is that model calculations assuming a p-lte model should be fairly accurate, at least for electron densities above about $2x10^{15}$ cm^{-3}.

From the excellent agreement of the results of the simple rate model (presented in chapter three of this thesis) with experiment (where the electron density ranged down to about $7x10^{14}$ cm^{-3}) one would expect the actual electron temperature to be within experimental uncertainty of $T_{e,lte}$ for these values of the electron density; if it was not, the agreement between the rate model calculations and experiment would certainly have been poorer.

Chapter 6
The Effect of a "Sheathing Gas" on Analyte Excitation in the ICP

6.1 Introduction

In this chapter the effect of a sheathing gas on analyte excitation in the inductively coupled plasma is examined. The "sheathing" or "sheath" gas is an extra argon flow which is added immediately after the nebulizer/spray chamber assembly combination, but before the plasma torch. A schematic diagram of the glass attachment used to introduce this flow is given in figure 2.2. The original purpose of this extra argon flow, first used by Mermet et al. [98], was to prevent the aerosol introduction tube of the plasma torch from becoming blocked when using high salt content samples. It was found that the addition of this extra gas prevented this; it also reduced memory effects associated with the deposition of sample on this aerosol introduction tube.

This extra argon flow was given the appellation "sheathing gas" [98] in the belief that both it and the nebulizer gas (carrying the aerosol) were laminar flows and thus did not mix - the nebulizer gas thus being surrounded by a "sheath" of gas. It turns out, at least for our experimental system, that this is not the case; the "sheath gas" flow is not laminar and thus mixes with the nebulizer gas. Nonetheless, in this work, this flow will still be referred to as the "sheath gas" flow. The gas passed through the nebulizer will be referred to as the nebulizer gas flow, and their combination, after

mixing, will be referred to as the total sample introduction gas flow.

The sheath gas has also found other uses: Borsier and Labarraque [17] found that when using high salt concentration samples that, not only does the sheath gas prevent blocking of the plasma torch, but also that it is possible to vary its flow rate to compensate for inevitable fluctuations in the nebulizer gas flow rate (so that the total sample introduction gas flow rate remains constant). In this way noise was reduced. Murillo and Mermet [106] used a sheathing gas to introduce a small amount of hydrogen into the central channel of the plasma - they found that this considerably increased excitation temperatures.

One of the features of the sheath gas is that it makes it possible to vary the total sample introduction flow rate, while keeping the amount of both analyte and solvent reaching the plasma constant - this makes it an excellent tool for studying the effect of the sample introduction flow on analyte excitation. To date very limited use has been made of this: Murillo and Mermet [107] investigated the effect of the sheath gas flow rate on a number of analytical lines as a function of height above the load coil. They found that the variation in signal intensity was most sensitive for atomic lines with excitation energies above 5 eV and for ionic lines between 11.5 and 12.5 eV (taking the ground state atom as 0 eV). However their results were not spatially resolved (i.e. Abel inverted), and as such are difficult to interpret. In addition (as was pointed out in the introduction to this thesis), what is really needed in order to

understand the behaviour of analyte in the icp is spatially resolved electron density.

This chapter will present, at each of four different sheath gas flow rates, spatially resolved contour maps of the electron density, the Ar I 549.59 nm and the H I 486.13 nm spectral lines, as well as of an atomic and an ionic spectral line for each of strontium, calcium, cadmium and zinc. Magnesium and barium will also be discussed. In order to determine the effect of the water which is delivered to the plasma when using standard nebulization of an aqueous sample, contour maps are also presented (at the same four sheath gas flow rates) of the Fe I 372.0 nm and the Fe II 275.6 nm spectral lines with iron introduced into the plasma in two different ways: as a standard aerosol and directly as a vapour (from the vapour pressure of ferrocene).

6.2 Experimental

For a complete description of the experimental set-up the reader is referred to chapter two. For some of the results in this chapter the 4096 pixel photodiode array was used, whereas for others the more sensitive 2048 pixel array was used. Sample was introduced into the plasma using the Sherrit-Gordon nebulizer/spray chamber combination. For the results presented in this chapter the value of the rf power supplied to the plasma was held at 1.0 kW, the plasma argon flow rate was held at 10.0 L/min and the auxiliary argon flow rate was held at 0.2 L/min. When measuring the intensity of the 486.13 nm H_β line of hydrogen (from which the electron density was determined, as described in the introduction to this thesis) the

entrance slit width on the monochromator was set to 40 μm; when measuring other lines it was set to 50 μm when using the 4096 element photodiode array, and to 70μm when using the 2048 element array. Data was collected at heights above the load coil of 6, 9, 12, 15, 18, and 21 mm.

Analyte solutions were prepared by dissolving suitable quantities of water soluble salts in deionized water to give the solution concentrations (in parts per million by weight) shown in Table IV. These concentrations were chosen to be sufficiently low to avoid both self-absorption and the saturation of the photodiode array detector, and high enough to ensure good signal-to-noise ratios. The table also shows the ionization energies of the elements (from reference [134]) and the wavelengths of the atomic and ionic spectral lines used for each element, along with the excitation energies of the levels from which the transitions originate and the degeneracy weighted transition probabilities (all from ref. [138]).

As described in chapter two, the T-shaped sheath gas attachment (shown in figure 2.2) was connected between the spray chamber and the icp torch, allowing the introduction of an extra argon flow (the "sheath gas flow"); in general, data were collected at sheath gas flow rates of 0.0, 0.2, 0.4 and 0.6 L/min. Combined with the nebulizer flow rate of 0.6 L/min the total sample introduction flow rate thus ranged between 0.6 and 1.2 L/min.

In order to determine whether or not the sheath gas flow rate had an effect on the amount of sample reaching the plasma, a small glass column, filled with approximately 5 g of self-indicating silica gel, was fitted over the icp torch. With the nebulizer turned

Table IV: Solution concentrations (C) and ionization energies (E_i) for the elements studied in this chapter along with the corresponding wavelengths (λ), excitation energies (E) and (where relevant) the degeneracy weighted transition probabilities (gA) for the atomic and ionic spectral lines of the elements.

	Sr	Ca	Mg	Ba	Zn	Cd	Fe
C (ppm)	50	50	250	50	1500	1500	5000
E_i (eV)	5.69	6.11	7.64	5.21	9.39	8.99	7.87
λ_{atom} (nm)	460.7	422.7	285.2	553.6	213.9	228.8	372.0
λ_{ion} (nm)	407.8	393.6	279.5	455.4	202.5	226.5	275.6
E_{atom} (eV)	2.69	2.94	4.35	2.24	5.80	5.43	3.34
E_{ion} (eV)	3.04	3.15	4.43	2.72	6.13	5.48	5.49
gA_{atom} $(\frac{10^8}{s})$	6.03	6.54					
gA_{ion} $(\frac{10^8}{s})$	5.68	5.88					

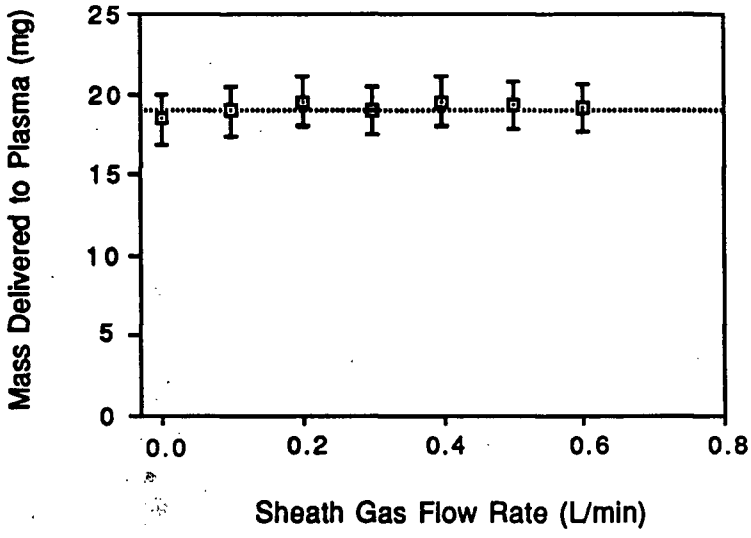

Figure 6.1 A plot of the mass of solvent delivered to the plasma as a function of the sheath gas flow rate.

on the amount of solvent reaching the column was measured as a function of the sheath gas flow rate. The results are presented in figure 6.1. As can be seen there is virtually no difference in the amount of sample reaching the plasma at the different sheath gas flow rates.

In an effort to elucidate the effect of water on analyte excitation iron was introduced into the plasma in two different ways: firstly as an aerosol using conventional nebulization, and secondly directly as a vapour (using the vapour pressure of ferrocene). Figure 6.2 shows a schematic diagram of this second method of introducing iron into the plasma. A large test tube with a side arm was connected to the bottom of the sheath gas attachment. Ferrocene was placed in the bottom of this test tube and warmed to

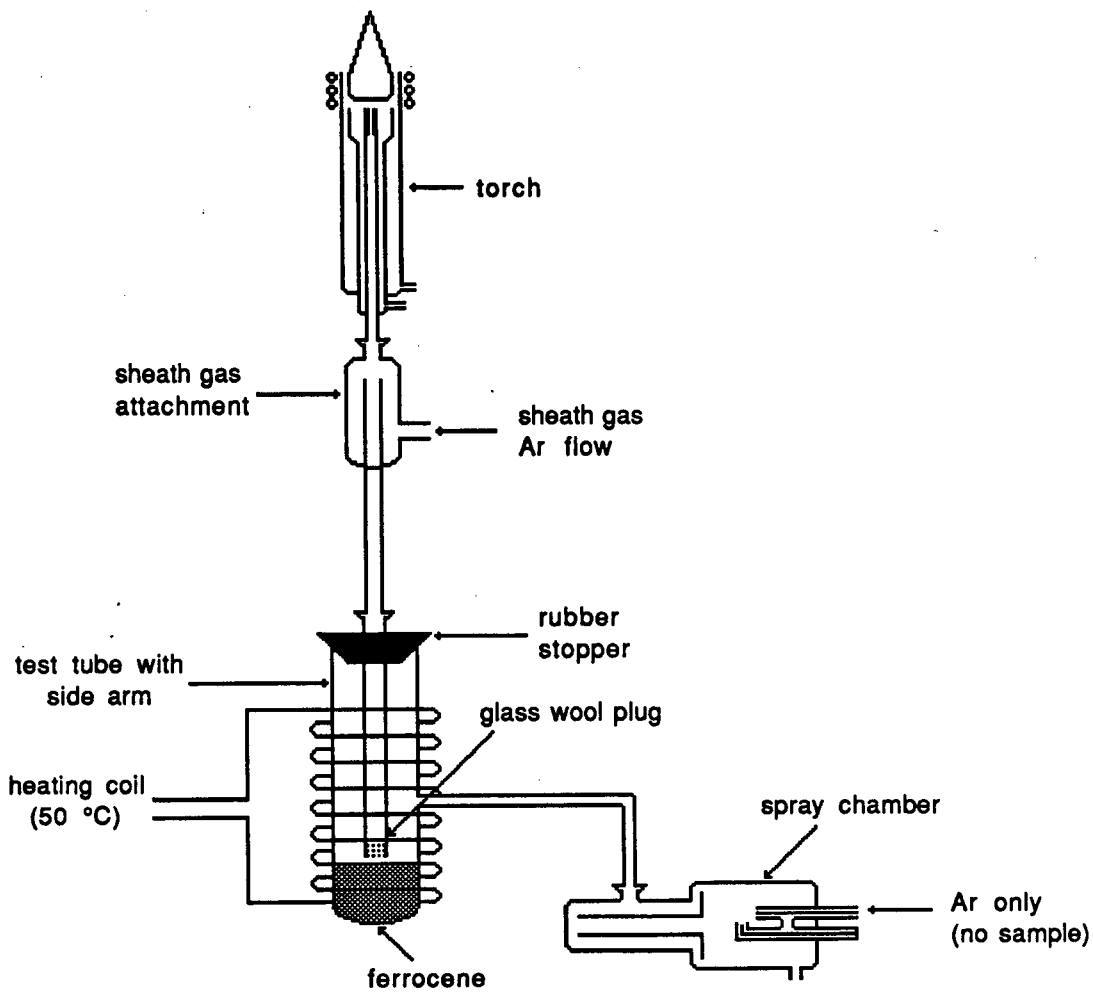

Figure 6.2 A schematic diagram showing how iron, in the form of ferrocene vapour, was introduced into the plasma.

approximately 50 °C using heating tape wrapped around it. With the sample inlet tube blocked (so that no sample (or air) was entering the spray chamber), the usual 0.6 L/min argon flow was allowed to pass through the nebulizer and spray chamber into the test tube and over the ferrocene; this flow then carried the ferrocene vapour through a wad of glass wool (to avoid having solid particles of ferrocene enter the plasma), through the sheath gas attachment, and into the plasma. The sheath gas flow rate was then varied over its usual range of 0.0 to 0.6 L/min. A similar method of introducing ferrocene vapour into the icp has been described in reference [124].

The procedure for the collection of the data presented in this chapter was as follows. For each spectral line of interest, under a given set of experimental conditions, a spatial scan of the plasma (as described in chapter two) was acquired. After smoothing, Abel inversion, and correction for the spectral response of the system, this resulted in a radially resolved intensity as a function of radial distance. When both the atomic and ionic lines of interest for the same species had intensities of the same order of magnitude, and were sufficiently near to one another in wavelength (Ca, Mg, Zn, and Cd), they were both collected during the same scan.

In order to present this spatially resolved data in as concise a format as possible contour maps of the plasma were generated. In these plots the y-axis represents height above the load coil and the x-axis radial distance across the plasma (thus forming a 2-D image of the plasma); contour lines then represent the value of the parameter being plotted. For all of the data presented in this chapter (except that for iron, zinc and cadmium) these contour plots

were generated using Golden Software's (Golden, CO) "Surfer" - a data manipulation and plotting program. For iron, zinc and cadmium the data were first transferred to an Apple (Cupertino, CA) Macintosh+ computer; using a computer program based on an algorithm by Simons [123] contour maps were generated. These were plotted using Cricket Software's (Malvern, PA) "Cricket Graph" and edited using Silicon Beach Software's "Superpaint" (to fill in the broken contour lines generated by Simons' algorithm).

6.3 Results

6.3.1 Electron Density

Before describing the results of the electron density measurements, some typical lateral and radial profiles (both spatial and wavelength) of the hydrogen line used for the calculation of the electron density will be given, along with a discussion of the precision. Figure 6.3 shows a lateral (a) and a radial (b) profile of the 486.13 nm line of hydrogen (H_β) taken at the line centre at a height of 6 mm above the load coil and a sheath gas flow rate of 0.2 L/min (all other conditions are as described in section 6.2). The figure shows the effect of the Abel inversion process (described in chapter two). It can be seen that, for example, in the central channel of the plasma (where the Abel inverted profile dips down) there is less excited hydrogen than at a radial positions of 3 to 4 mm. This cannot be seen from figure 6.3 (a) where the intensity at a lateral position of 0 mm represents, not the intensity of the H_β line at the centre of the plasma, but rather a superposition of intensity along the line of sight passing through the plasma centre.

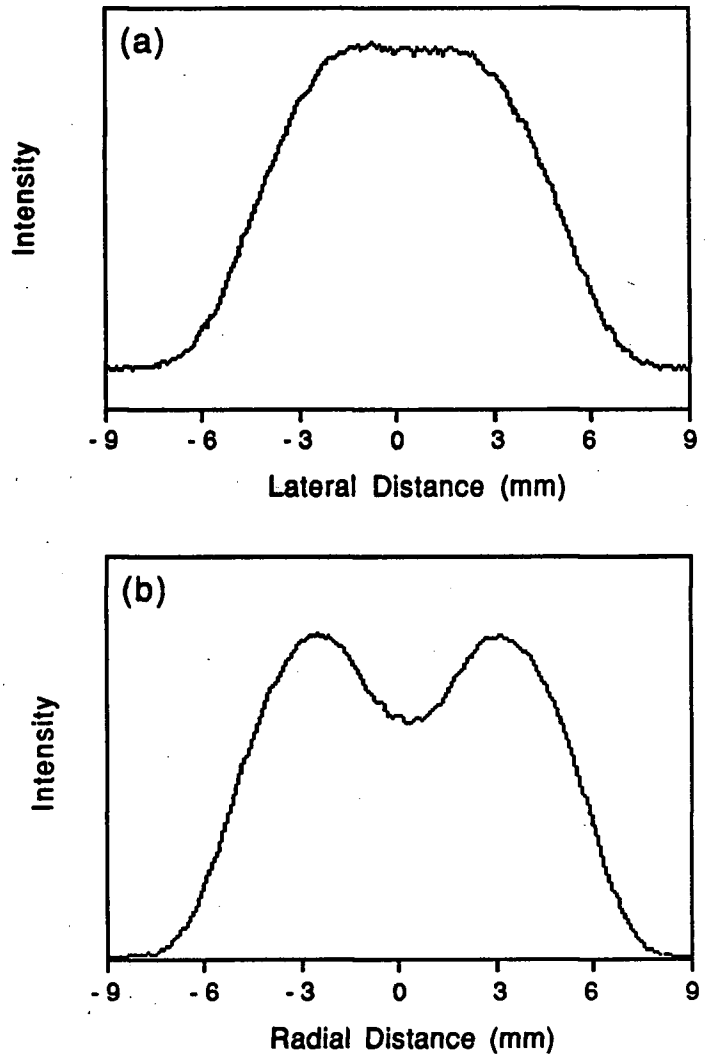

Figure 6.3 Plots showing the lateral (a) and the radial (b) intensity distributions of the 486.13 nm hydrogen line; the height above the load coil was 6 mm and the sheath gas flow rate was 0.2 L/min.

Figure 6.4 shows the wavelength profiles of the H_β line both before the Abel inversion process (a) and after it (b) taken at a spatial position of +4 mm from the plasma centre; the experimental conditions were the same as for figure 6.3. Figure 6.4 (a) represents the superposition of the wavelength profiles integrated along the line of sight at a lateral position of 4 mm. In figure 6.4 (b) the full width at half maximum ($\Delta\lambda_{1/2}$) is shown (about 0.40 nm at this position). As described in the introduction to this thesis, this half-width can be used to calculate the electron density (at each of the 200 radial positions).

Figure 6.5 (a) shows a plot of ten replicate measurements of the electron density (taken at the same experimental conditions as for figure 6.3). After each spatial scan of the plasma the icp was turned off, the various flow meters etc. were turned to zero, and the plasma was then started again for the next scan. Figure 6.5 (b) shows the percent relative standard deviation of the ten measurements. One can see that the precision of the measurements is very good - for radial positions less than about 6 mm the percent standard deviation is mostly below about 2 percent, rising no higher than 4 percent near the plasma centre (due to the accumulative effect of noise associated with the Abel inversion process). At radial positions somewhat greater than 6 mm, the intensity of the H_β spectral line is sufficiently low that the electron density cannot be measured with reasonable accuracy.

Figure 6.6 presents contour maps of the spatially resolved electron density in the icp; figures 6.6 (a), (b), (c) and (d) refer to sheath gas flow rates of 0.0, 0.2, 0.4 and 0.6 L/min (respectively).

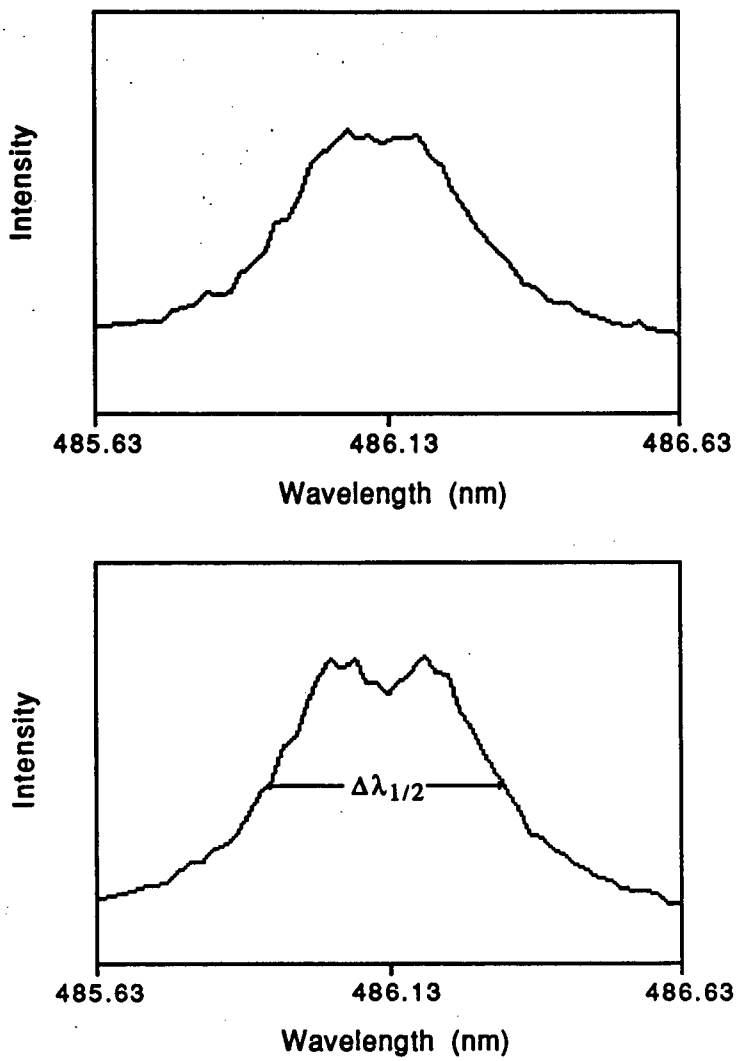

Figure 6.4 Plots showing the wavelength profiles of the H_β line both before (a) and after (b) the Abel inversion process; the plot also shows the full width at half maximum ($\Delta\lambda_{1/2}$) for the Abel inverted case. The height above the load coil was 6 mm, the sheath gas flow rate was 0.2 L/min, and the radial position was +4 mm.

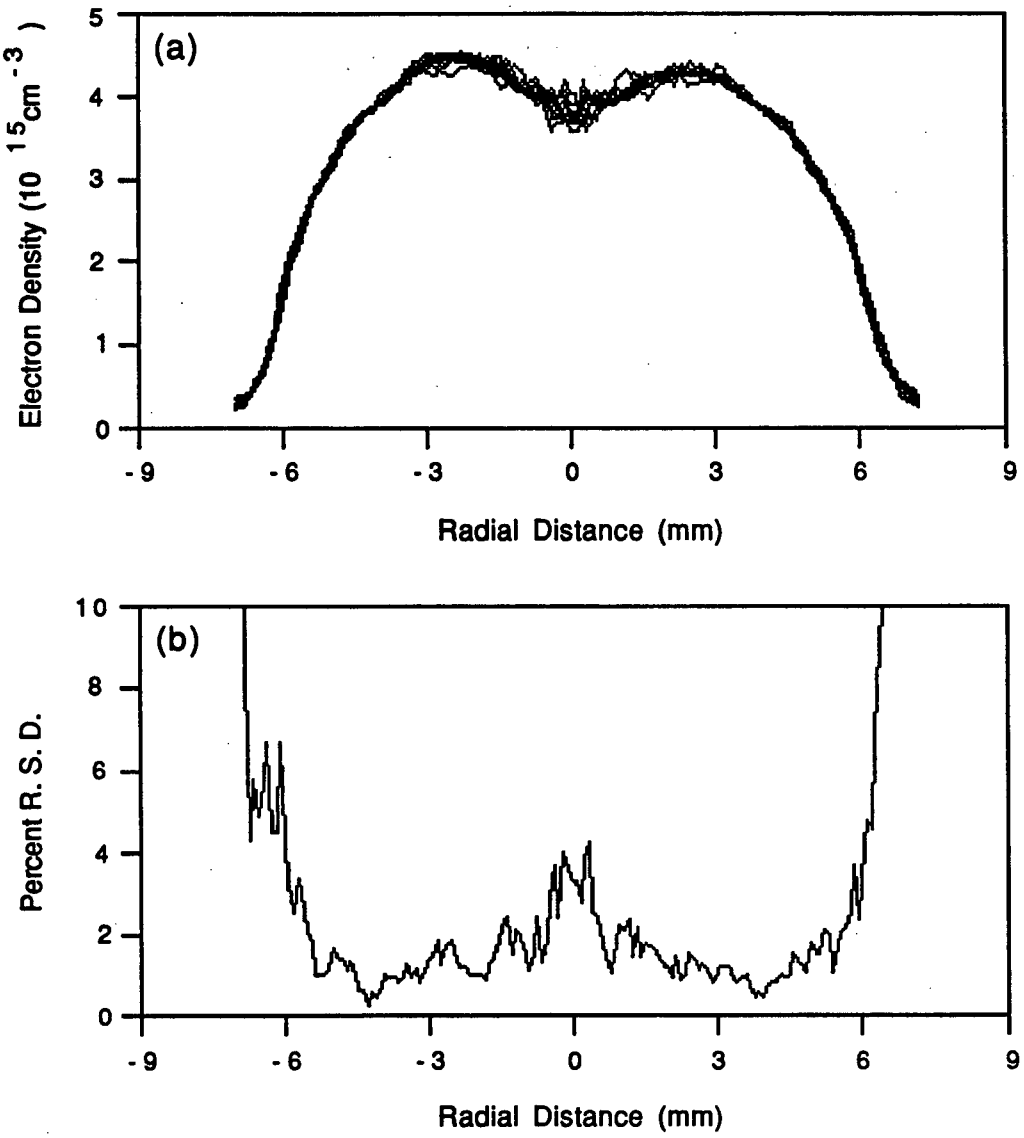

Figure 6.5 Plots showing (a) ten replicate measurements of the spatially resolved electron density and (b) the resulting percent relative standard deviation; the height above the load coil was 6 mm and the sheath gas flow rate was 0.0 L/min.

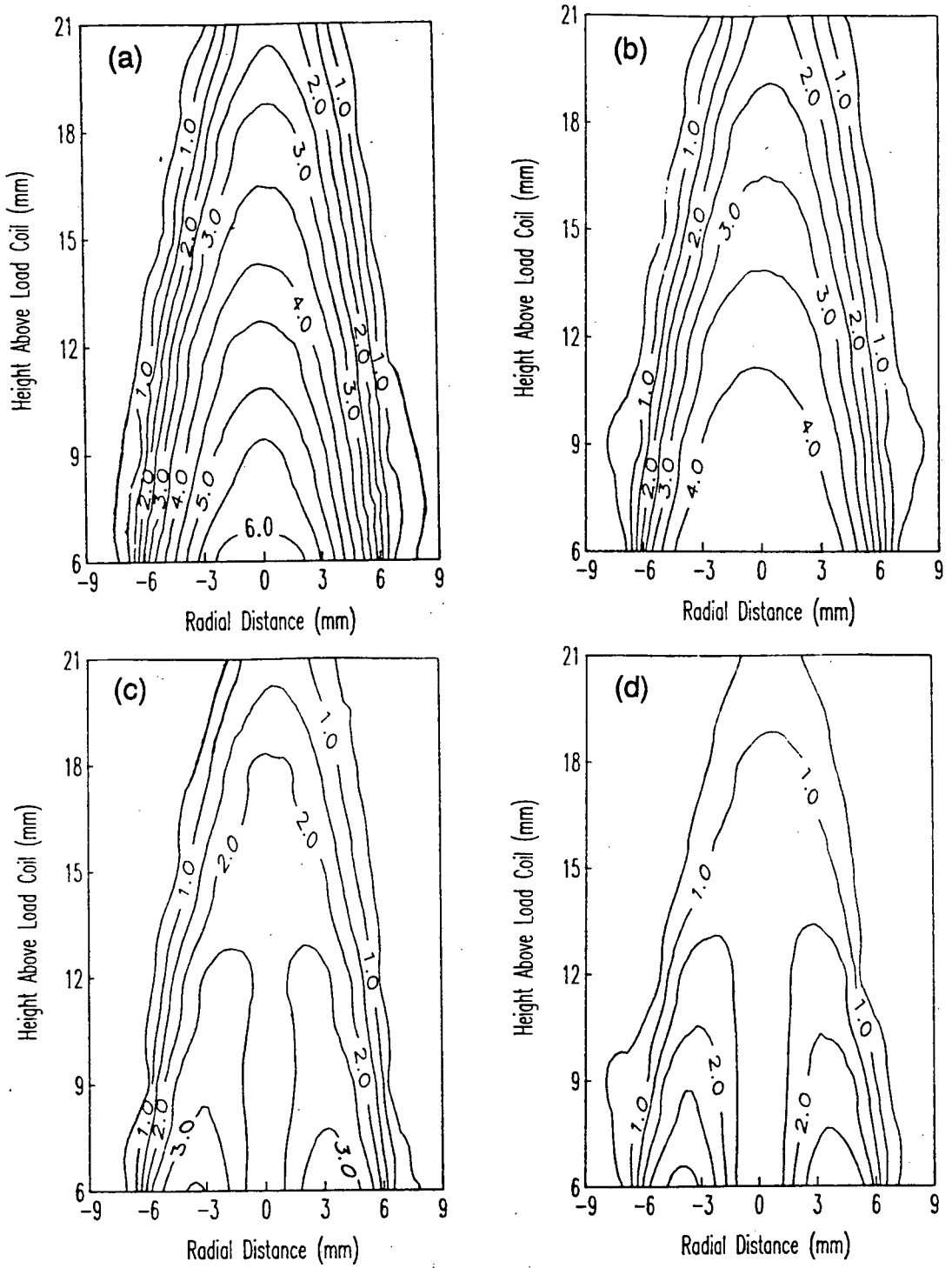

Figure 6.6 Contour plots of the spatially resolved electron density at sheath gas flow rates of (a) 0.0, (b) 0.2, (c) 0.4 and (d) 0.6 L/min. The contour lines are labeled in units of 10^{15} cm^{-3}.

As mentioned in section 6.2, deionized water was introduced through the nebulizer (with an argon flow rate of 0.6 L/min). By far the most obvious influence of the sheath gas is to cause a general decrease in the electron density. At a height of 12 mm above the load coil, for example, the maximum electron density decreases from about 4.5 to 3.5 to 2.5 to 1.5 $x10^{15}$ cm^{-3} as the sheath gas flow rate is increased from 0.0 to 0.6 L/min. This decrease in the electron density is particularly marked in the central channel of the plasma.

With no sheath gas the total sample introduction rate is 0.6 L/min (from the nebulizer flow); at this low value the mixing between the sample introduction gas and the plasma gas is probably reasonably complete (i.e. turbulent mixing can be said to occur). Since the linear velocity of the sample gas is about 570 cm/s (at a flow rate of 0.6 L/min) and the plasma gas emerges from the torch with a linear velocity of only about 42 cm/s, it will experience a much longer residence time in the induction region of the plasma (inside the load coils). Because of this the electron density of the plasma gas in the region below the load coils will be much greater than that of the sample introduction gas and should be independent of the sample gas flow rate [1, 34]. The mixing of this high electron density plasma gas with the sample introduction gas explains the high values of the electron density in the central channel of the icp when there is no sheath gas flow.

At a sheath gas flow rate of 0.6 L/min, for example, the total sample introduction rate is 1.2 L/min. This corresponds to a linear velocity of 1130 cm/s; at this high value the sample gas is able to

"punch a hole" through the plasma gas and thus undergoes relatively little mixing (i.e. laminar flow exists). This can easily be seen visually - with no sheath gas flow the central channel is quite hard to discern, whereas at a sheath gas flow of 0.6 L/min it can be clearly seen to exist up to 15 mm above the load coil. This explains the low values of the electron density in the central channel of the plasma for the sheath gas flow rate of 0.6 L/min.

By comparing figure 6.6 (a) with 6.6 (d) it can easily be seen that if one were to integrate the electron density over the volume of the plasma one would calculate a much greater total number of electrons for the case with no sheath gas flow as compared to that with a flow of 0.6 L/min. This is not explained by the above argument, but can be explained by the following very simplistic calculations.

Consider the spatial position at a height of 6 mm above the load coil and a radial distance of -4 mm. The electron density at this position is about 5.0×10^{15} cm^{-3} (corresponding to an lte temperature, as described in the introduction to this thesis, of 8950 K). At sheath gas flow rates of 0.2, 0.4 and 0.6 L/min the ratios of the total volume of argon entering the plasma to the volumes from the sheath gas flows are 54, 27 and 18, respectively. Considering only the kinetic energy of the plasma, and assuming that the sample introduction gas has a temperature much lower than that of the plasma gas, the temperature of the resulting plasma gas/sample introduction gas would be 54/55, 27/28 and 18/19 that of 8950 K (8780, 8630 and 8480 K) for sheath gas flow rates of 0.2, 0.4 and 0.6 L/min. The lte electron densities corresponding to

these temperatures are 4.1, 3.4 and 2.8 $x10^{15}$ cm^{-3}. These agree well with the values of 4.0, 3.5 and 3.0 $x10^{15}$ cm^{-3} from the data in figure 6.6. Considering the extreme simplicity of the calculation the agreement may be somewhat fortuitous; nonetheless it can be seen that even a relatively small excess volume of high velocity (and thus cool) sample introduction gas can significantly alter the electron density.

The above discussion points out the merit of the sheath gas flow - if the total aerosol flow rate were varied (as in reference [34]) it would be difficult to separate the effect of the increased flow rate from the resulting larger value of the solvent loading to the plasma. In a similar vein some workers are exploring the possibility of passing the sample gas through a condenser to independently vary the solvent loading and the sample gas flow rate [79, 80, 135].

6.3.2 Hydrogen and Argon

Figures 6.7 and 6.8 present contour plots of spatially resolved Ar I 549.59 nm intensity and H_β intensity (respectively); in these plots the (a) refers to a sheath gas flow rate of 0.0 L/min, (b) to 0.2 L/min, (c) to 0.4 L/min and (d) to 0.6 L/min. By comparing figure 6.7 to figure 6.6 one can see, from the similar placement of the respective contour lines, that there is a very strong correlation between the electron density and the population of excited argon. Since the concentration of atomic argon is far greater than that of any other species in the plasma, its density (n) can be calculated from the ideal gas law ($P = nkT$) as 1atm/kT. From the Boltzmann

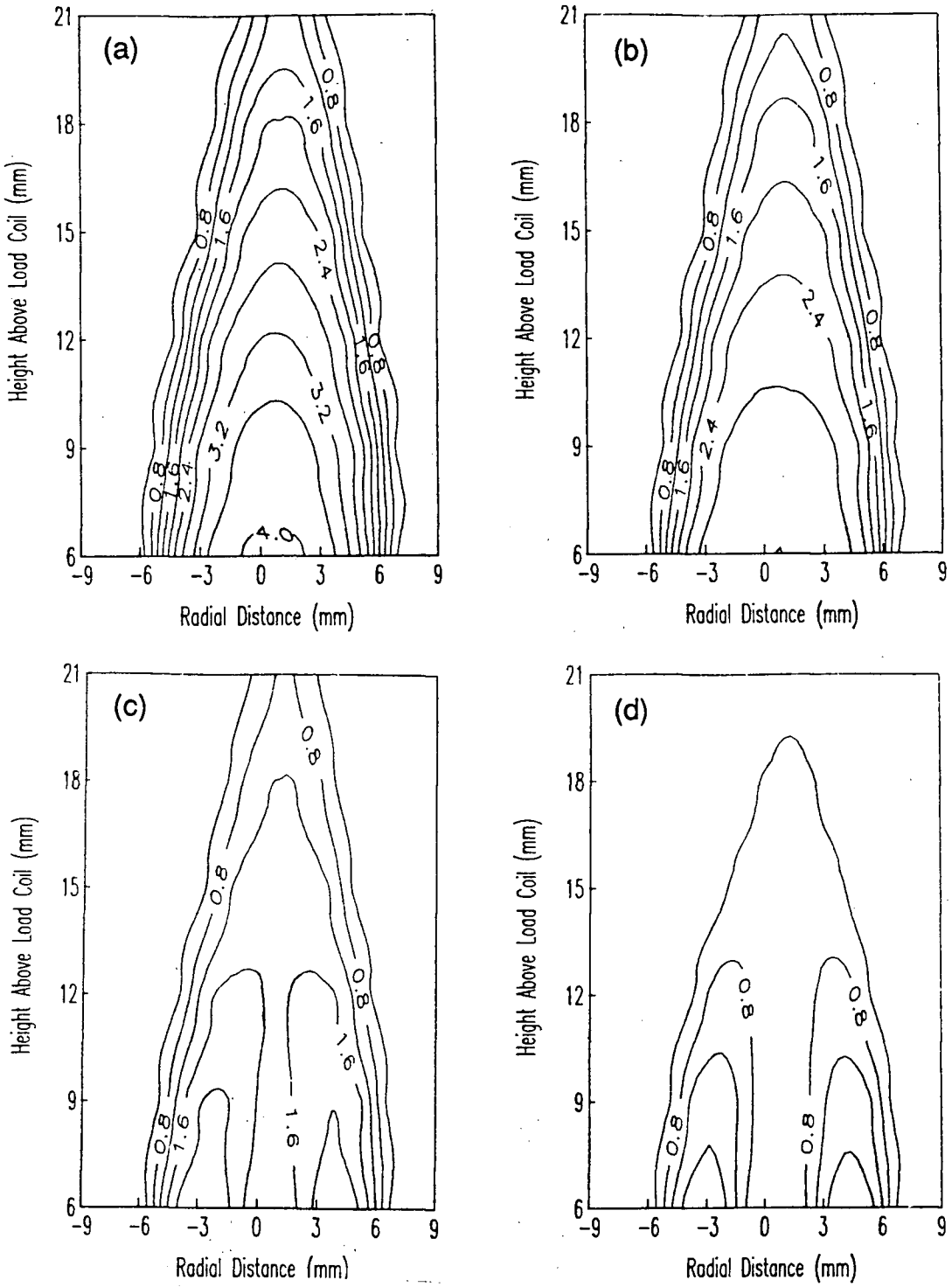

Figure 6.7 Contour plots of the spatially resolved intensity of the Ar I 549.59 nm spectral line at sheath gas flow rates of (a) 0.0, (b) 0.2, (c) 0.4 and (d) 0.6 L/min. The contour lines are labeled in arbitrary units.

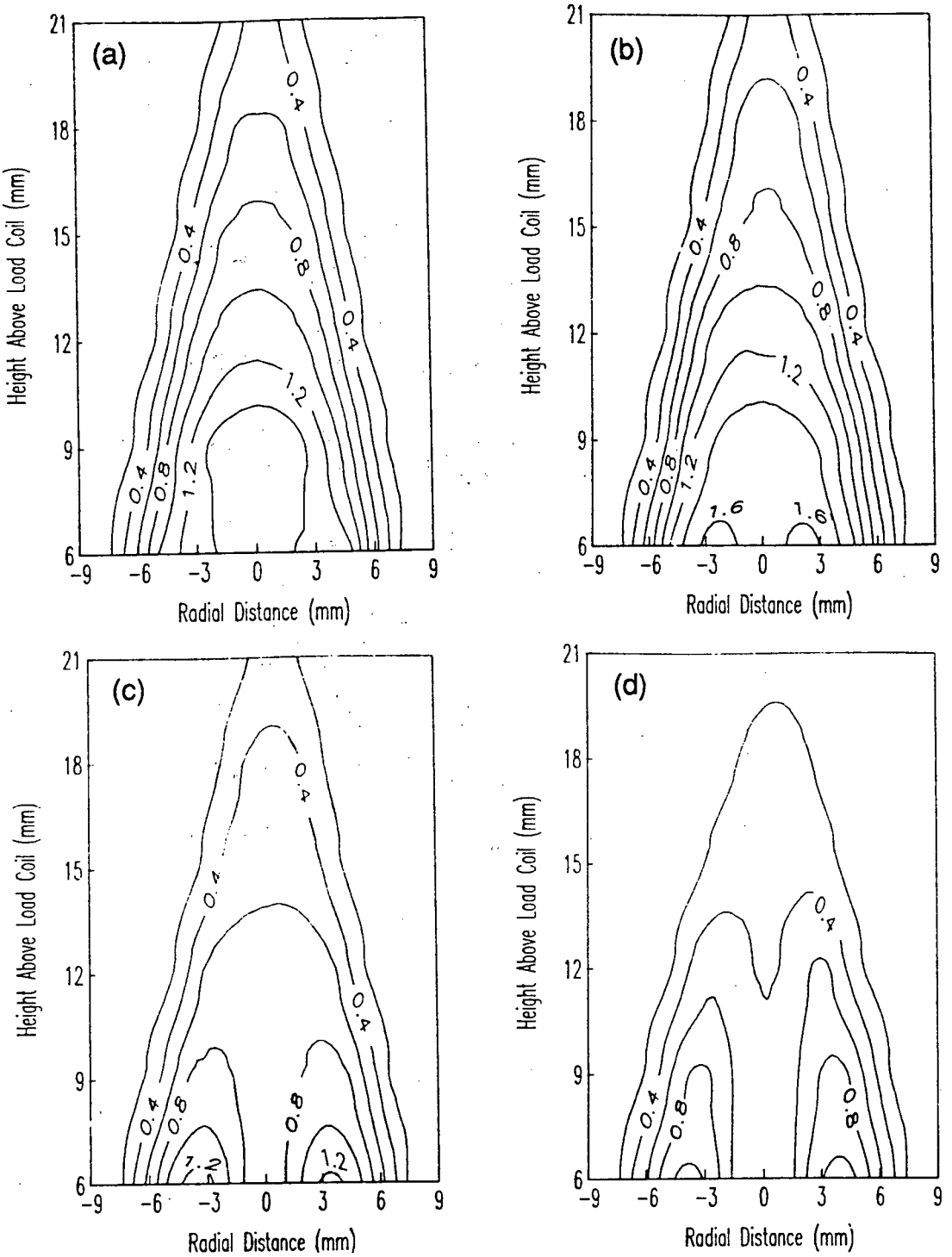

Figure 6.8 Contour plots of the spatially resolved intensity of the H_β line (486.13 nm) at sheath gas flow rates of (a) 0.0, (b) 0.2, (c) 0.4 and (d) 0.6 L/min. The contour lines are labeled in arbitrary units.

distribution the population of an excited state (of excitation energy E) of argon (and hence the intensity of a spectral line originating from it) is proportional to $n \cdot \exp(-E/kT)$ or $\exp(-E/kT) \cdot 1/T$. Since the lte temperature is related to the electron density, and argon itself (as opposed to analyte) is quite close to lte (as was shown in chapter four), the intensity of an argon line should be a direct function of the electron density. Thus the spatial distribution of the 549.59 nm line of argon can be explained by the same reasoning as that for the electron density.

This is not the case for the spatial distribution of the H_β line - its intensity will depend not only upon the local values of the temperature and the electron density, but also upon the local concentration of hydrogen. As will be seen in the next section, analyte is mostly confined to the central channel of the icp. Keeping this in mind when comparing figure 6.8 to 6.6 it can be seen that the spatial distribution of the intensity of the H_β line does not differ all that significantly from that of the electron density. This is perhaps surprising since the hydrogen comes from water introduced with the sample introduction gas. There are two possible reasons for this observation: firstly, and most importantly, with its high excitation energy of 12.1 eV (as compared to 2.2 to 6.1 eV for the analytes studied in this work) the effect of the temperature on its intensity (via the Boltzmann distribution) will be much more important than for analyte species. The intensity will thus tend to peak where the electron density is high. Secondly, due to its light mass, atomic hydrogen is able to diffuse throughout the volume of the plasma

much more easily than the heavy analyte atoms (diffusion coefficients being proportional to the reciprocal of the mass).

6.3.3 Analyte - Sr, Ca, Mg, Zn, Cd and Ba

In this section spatial contour maps for strontium, calcium, zinc and cadmium will be presented; magnesium and barium will also be discussed. These particular elements were chosen so that the effect of ionization energy on analyte excitation could be conveniently studied - all of these elements lie in either group IIa or IIb of the periodic table, and thus have similar ground state electronic configurations of either ns^2 or $ns^2 (n-1)d^{10}$. In addition, all of the spectral transitions studied (listed in Table IV) originated from the first excited states (of either the atom or the ion) which thus have similar term symbols.

Figures 6.9 and 6.10 are spatially resolved contour maps of the intensities of Sr I 460.7 nm and Sr II 407.8 nm; in these plots the (a), (b), (c) and (d) refer to sheath gas flow rates of 0.0, 0.2, 0.4 and 0.6 L/min, respectively. The excitation energies, etc. for the lines used can be found in Table IV. Note that the values of the contours used in figures 6.9 (a) and (b) differ from those of figures 6.9 (c) and (d). Perhaps the most obvious feature of these plots is the confinement of both the strontium atomic and ionic emission intensity to the aerosol channel - as discussed above this differs from the behaviour of hydrogen and (of course) argon. As one would expect, this confinement becomes more marked as the sheath gas flow rate is increased; the high velocity sample introduction gas is unable to mix as effectively with the surrounding plasma gas.

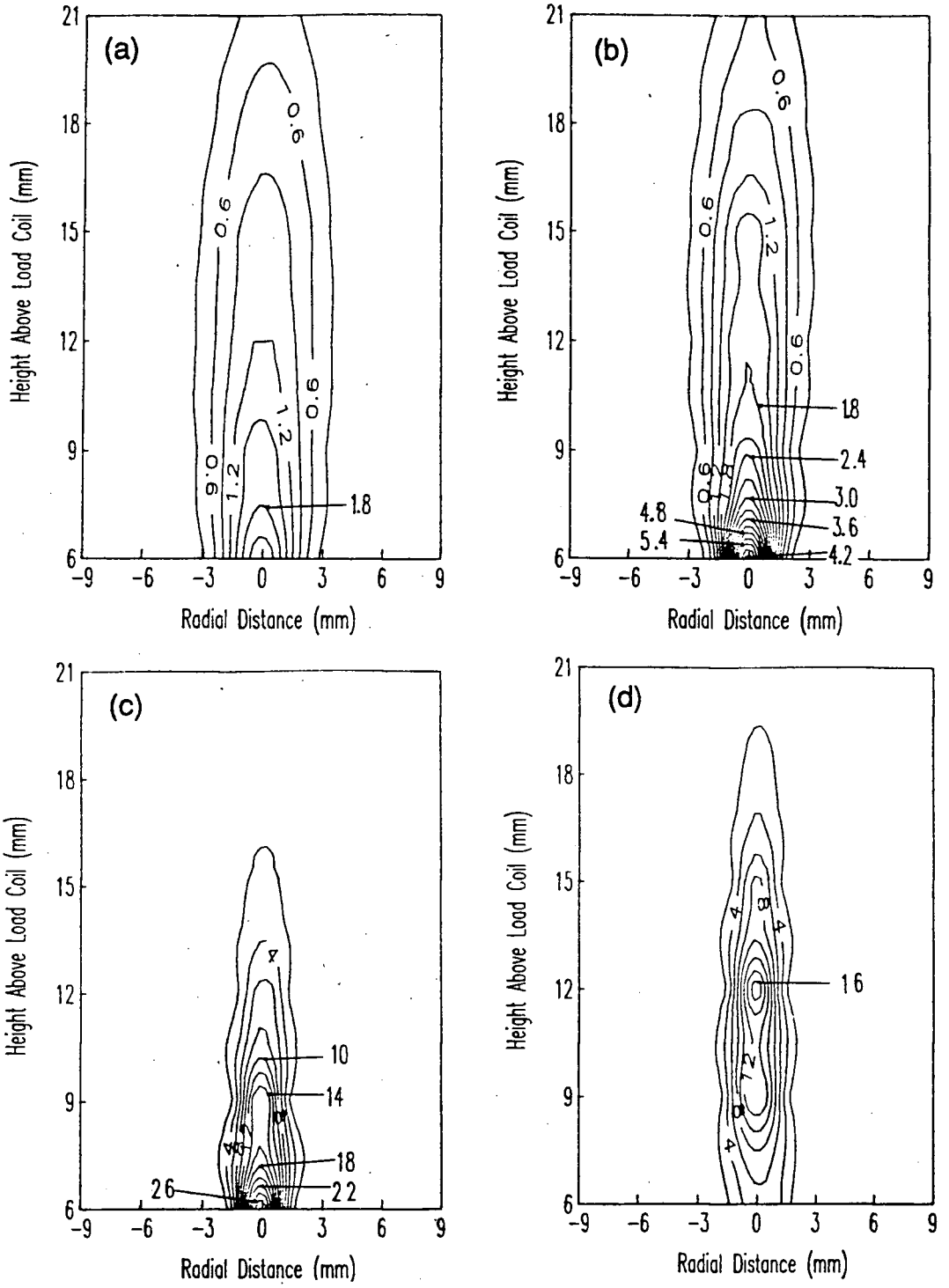

Figure 6.9 Contour plots of the spatially resolved intensity of the Sr I 460.7 nm spectral line at sheath gas flow rates of (a) 0.0, (b) 0.2, (c) 0.4 and (d) 0.6 L/min. The contour lines are labeled in arbitrary units (but are consistent with those of figure 6.10).

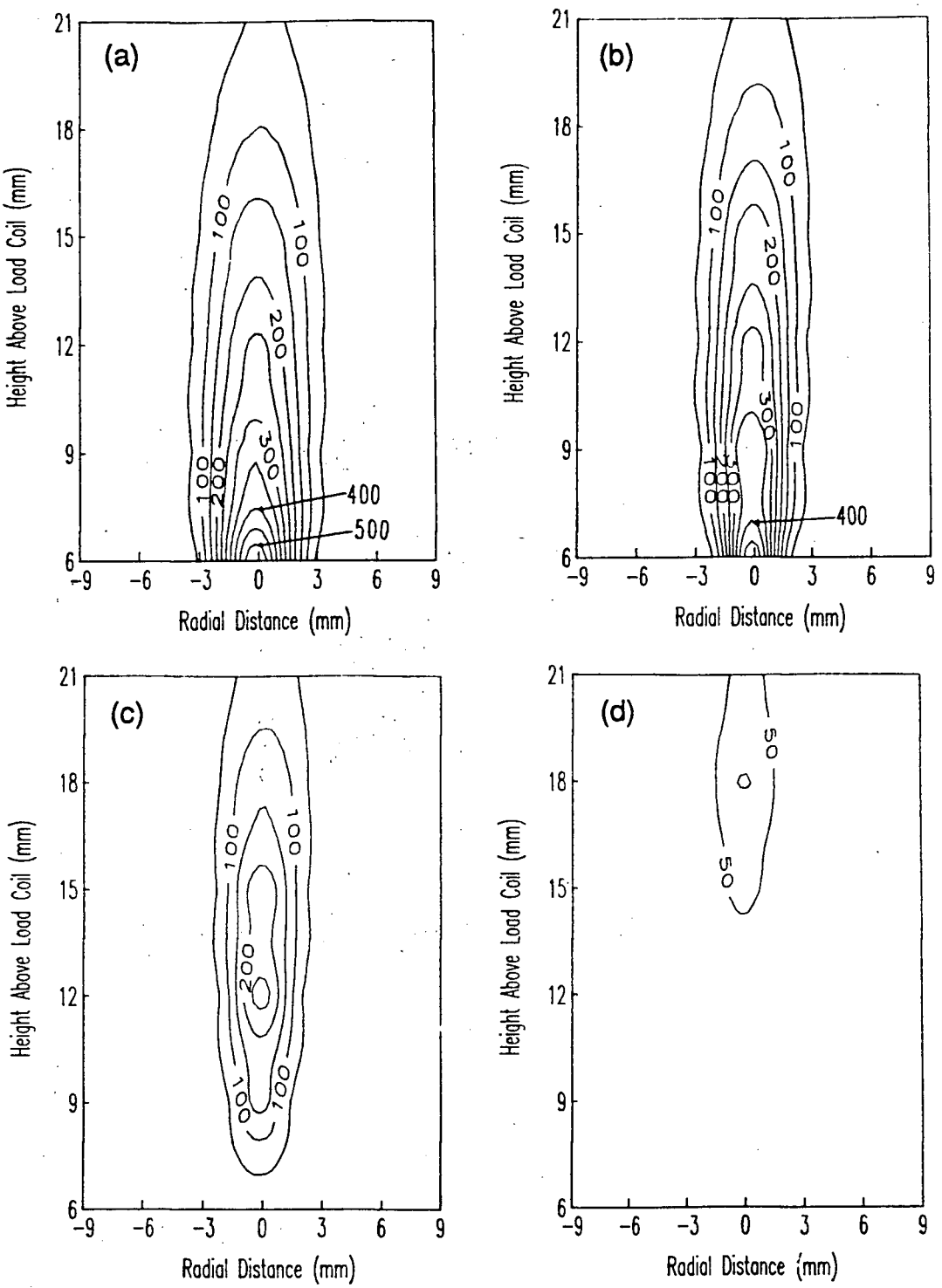

Figure 6.10 Contour plots of the spatially resolved intensity of the Sr II 407.8 nm spectral line at sheath gas flow rates of (a) 0.0, (b) 0.2, (c) 0.4 and (d) 0.6 L/min. The contour lines are labeled in arbitrary units (but are consistent with those of figure 6.9).

The maximum intensity of the strontium atom line increases with an increase in sheath gas flow rate from 0.0 to 0.2 L/min and again (more dramatically) from 0.2 to 0.4 L/min; it then drops somewhat (and the position of maximum intensity shifts from 6 mm above the load coil to 12 mm) when the flow rate is increased to 0.6 L/min. The maximum intensity of the strontium ionic emission, on the other hand, decreases steadily with an increase in the sheath gas flow rate. The position of maximum intensity occurs at 6 mm above the load coil for flow rates of 0.0 and 0.2 L/min, at 12 mm alc for 0.4 L/min and at 18 mm alc for 0.6 L/min. Unlike hydrogen and argon the maximum intensity for any given height for both strontium atomic and ionic emission occurs at a radial position of 0 mm.

These observations can be explained as follows. As can be seen by referring back to its contour maps, the value of the electron density (and thus also the temperature) in the central channel of the icp falls steadily with an increase in the sheath gas flow rate. This will have two effects on strontium excitation: firstly, it will cause a general decrease in the total number of strontium ions (with a corresponding increase in the number of atoms). From the data in reference [34], with an decrease in electron density from 4.0×10^{15} cm^{-3} to 7.1×10^{14} cm^{-3} the degree of ionization for strontium drops from about 0.9988 to 0.9940. This drop would have a negligible effect on the number of strontium ions, but would have a considerable effect on the number of strontium atoms (an increase of about five times). Secondly, as the temperature drops the

fraction of both excited strontium atomic and ionic species will drop (i.e. the ground states will become more populated).

From the above discussion one would thus expect the intensity of the strontium ionic emission to decrease with an increase in the sheath gas flow rate, as is observed. One would also expect that the position of maximum emission intensity would increase from its value of 6 mm above the load coil (at flow rates of 0.0 and 0.2 L/min) with a further increase in the flow rate because the position of maximum electron density in the aerosol channel (where the strontium is more or less confined) also does. This is because with these large linear velocities of the sample introduction gas it is not until higher up in the plasma that the strontium is able to effectively mix somewhat with the higher electron density plasma gas.

The behaviour of atomic strontium can also be explained by the above discussion. As the sheath gas flow rate is increased (and the electron density decreases) the relatively large increase in the total number of neutral strontium atoms outweighs the effect of the decreased amount of excitation, at least up to a flow rate of 0.4 L/min. At a flow rate of 0.6 L/min the electron density is sufficiently low so that the effect of decreased excitation is more important than the effect of decreasing degree of ionization. There is also another important factor to consider: the reason why, for flow rates of 0.0 and 0.2 L/min (for example), the maximum atomic emission observed occurs at a height of 6 mm above the load coil (where the electron density is high, and thus one might expect the reverse) is that the excited level from which the emission

originates is populated by the recombination of a strontium ion with an electron. The excited species formed in this way then decays radiatively.

Figures 6.11 and 6.12 present contour plots of spatially resolved strontium ion-to-atom emission intensity ratios and the value of the non-equilibrium b_r parameter (respectively). The values of the sheath gas flow rates are indicated in the figure captions. As described in the introduction to this thesis, the b_r parameter was calculated by dividing (at each spatial position) the value of the experimental ion-to-atom ratio by the expected lte value of this expression using the spatially resolved electron density (and its corresponding lte temperature) as input.

As can be seen from figure 6.11 the maximum value of the ion-to-atom ratio for the sheath gas flow of 0.0 L/min occurs where the ion intensity is a maximum. This is also more or less the case, albeit with more noise from experimental uncertainty, for the flow rate of 0.2 L/min. At the higher flow rates of 0.4 and 0.6 L/min the position of maximum ion-to-atom intensity ratio occurs at a radial distance of about ±3 mm or so. This is so because, even though the ionic emission peaks in the centre of the discharge, the atomic emission also peaks there and the ionic emission profiles are wider than the atomic ones. It should be pointed out that since the intensity of the ionic spectral line is much larger than that of the atomic one, dividing by this latter value to form the ion-to-atom intensity ratio introduces a fair amount of noise in the result.

The values of b_r are more interesting and revealing. The most obvious feature of these plots is the fact that b_r is less than unity

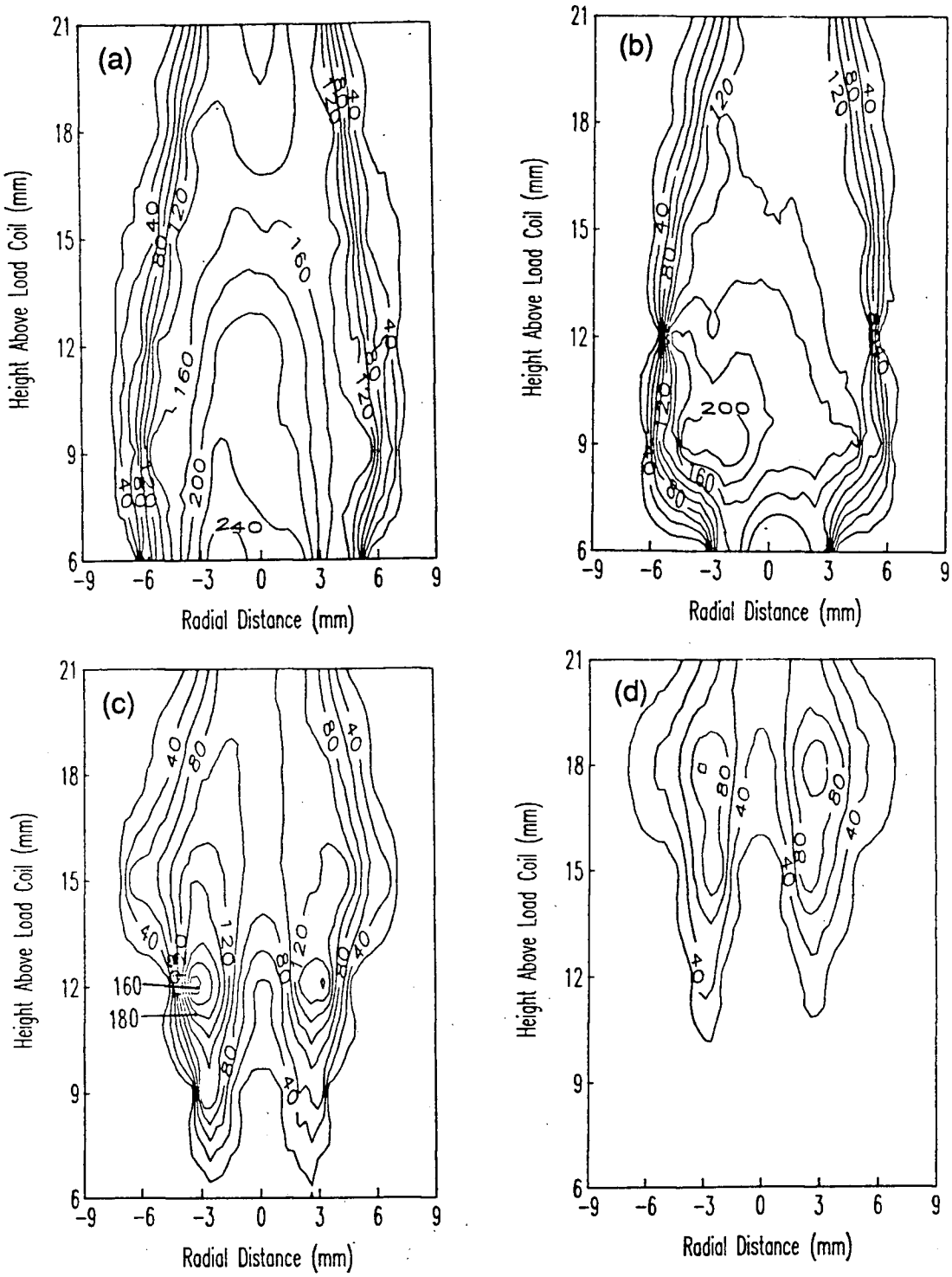

Figure 6.11 Contour plots of the spatially resolved ratio of the Sr II 407.8 nm intensity to the Sr I 460.7 nm spectral line intensity at sheath gas flow rates of (a) 0.0, (b) 0.2, (c) 0.4 and (d) 0.6 L/min.

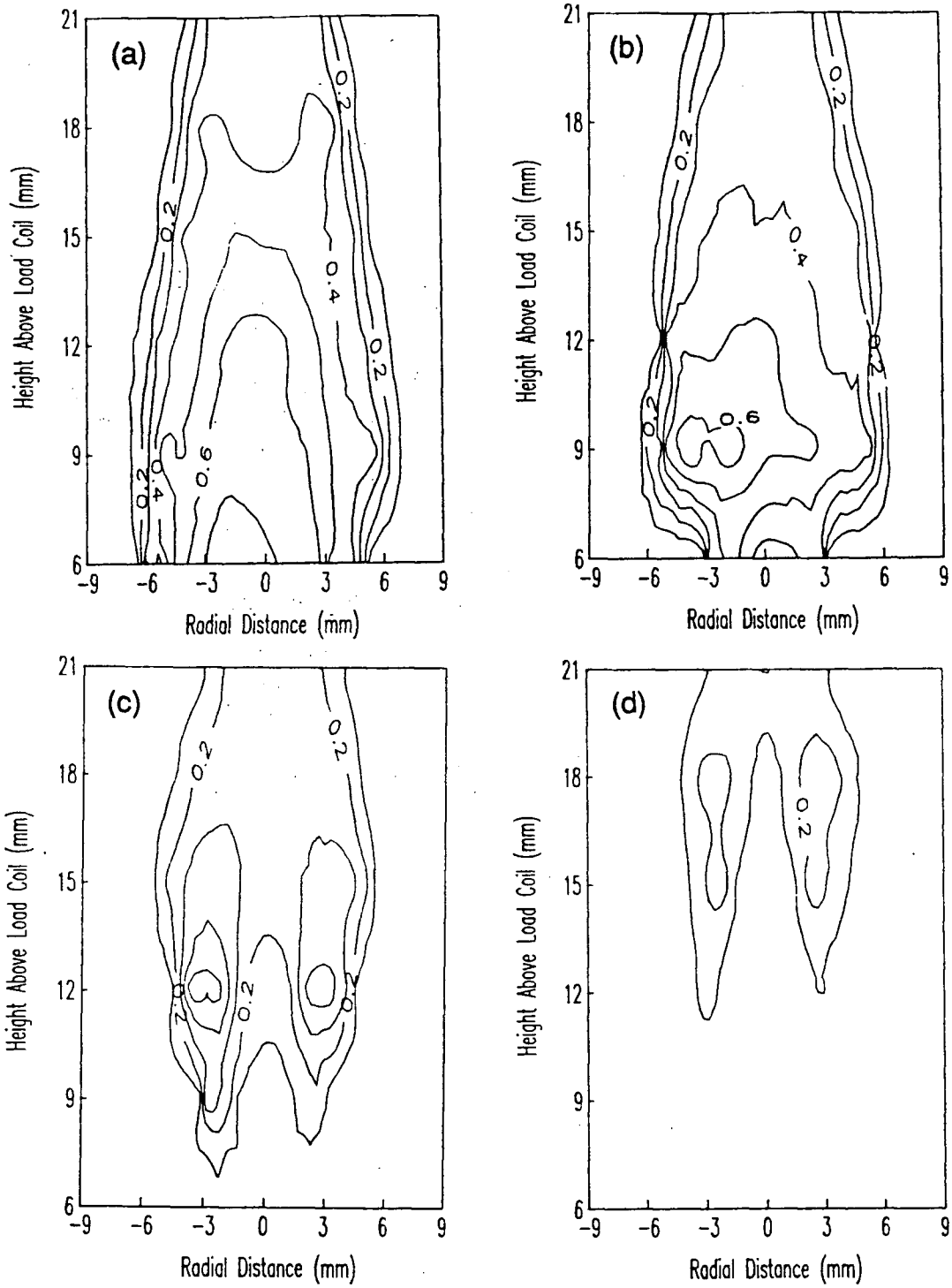

Figure 6.12 Contour plots of the spatially resolved value of the non-equilibrium parameter, b_r, for the strontium lines listed in Table IV at sheath gas flow rates of (a) 0.0, (b) 0.2, (c) 0.4 and (d) 0.6 L/min.

at all spatial positions for all sheath gas flow rates - the plasma is thus clearly not in local thermodynamic equilibrium. As pointed out in the introduction to this thesis, this can be explained by the fact that radiative decay from excited energy states is not balanced by its inverse process of absorption. This leads to a situation in which, taking the most highly excited atomic energy levels as a reference position, the rest of the atomic levels are overpopulated and all of the ionic energy levels (with the exception of the ground state) are overpopulated with respect to the lte values (based on this reference position). The deviations from lte (and thus of b_r from unity) are expected to be more pronounced the lower is the electron density. This situation is now fairly well understood and was discussed in detail in chapter three, where a simple theoretical model capable of predicting deviations of analyte populations from equilibrium (with very good accuracy) was developed. It will suffice here, therefore, to make only a few brief remarks about the spatial b_r distribution.

It should be pointed out that in order for a particular value of b_r to be accurate it is necessary that both the atomic and ionic emission lines used in the calculation of the ion-to-atom emission ratio be reasonably intense; thus one should not expect b_r to be accurate outside of the aerosol channel. At the maximum electron density observed (6.0×10^{15} cm^{-3}) at a radial distance of 0 mm, a height of 6 mm above the load coil and with no sheath gas flow, the value of b_r is about 0.7. This value is really very close to unity; it was initially thought (using an erroneous temperature) that b_r values varied between 10 and 1000 [20]. In fact, as was pointed out

in reference [34] and confirmed here, they are in the range 0.1 to 1.0 for virtually all spatial positions in the plasma (this is the case for all analytes studied). Analyte in the icp can thus be considered to be "close to lte" [109].

It can be seen by comparing figure 6.12 with 6.6 (of the electron density distribution) that, in general, the b_r values are farthest from unity where the electron density is low. As was pointed out in chapter one, and as was seen in detail in chapter three, this is expected: as the electron density decreases, the contribution of radiative decay to the excitation processes occurring in the plasma becomes relatively more important as electron impact processes decrease in magnitude.

In figures 6.13, 6.14, and 6.15 spatial contour maps are presented for the emission intensity of the 422.7 nm spectral line of Ca I, the 393.6 nm line of Ca II, and the resulting value of b_r (calculated using the intensities of these two lines, along with the spatial electron density). In these plots the (a), (b), (c) and (d) refer to sheath gas flow rates of 0.0, 0.2, 0.4, and 0.6 L/min, respectively. By comparing these plots to the corresponding ones for strontium one can see immediately that the behaviour of these two elements is almost identical (this is also the case for the plot of the ion-to-atom emission intensity ratios, which is not shown here for calcium). This is not at all surprising: calcium and strontium lie one above the other in the same group of the periodic table and thus have an analogous atomic structure. In addition, as can be seen from Table IV, their ionization energies differ by only 0.42 eV; also both the atomic spectral lines of calcium and

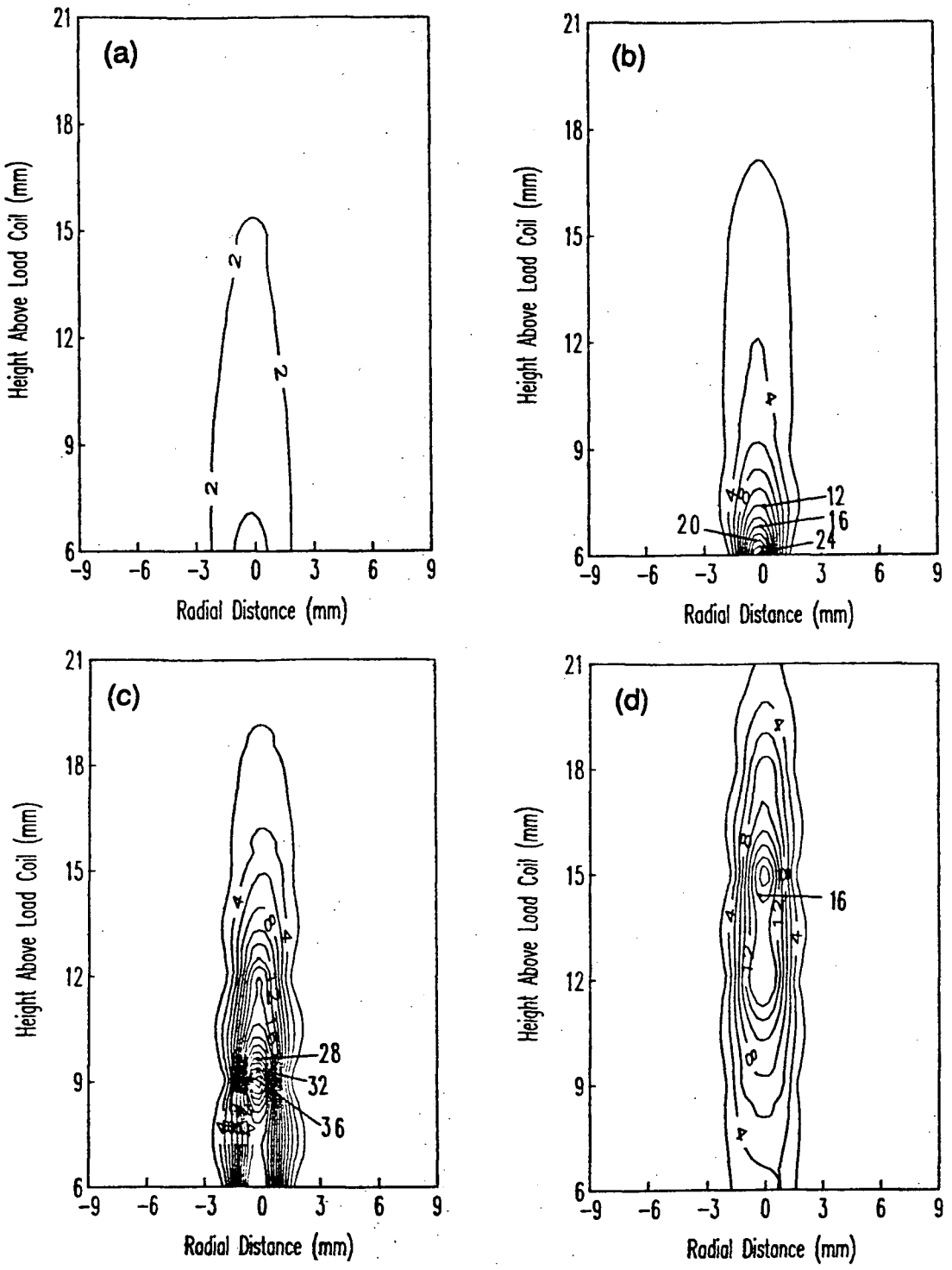

Figure 6.13 Contour plots of the spatially resolved intensity of the Ca I 422.7 nm spectral line at sheath gas flow rates of (a) 0.0, (b) 0.2, (c) 0.4 and (d) 0.6 L/min. The contour lines are labeled in arbitrary units (but are consistent with those of figure 6.14).

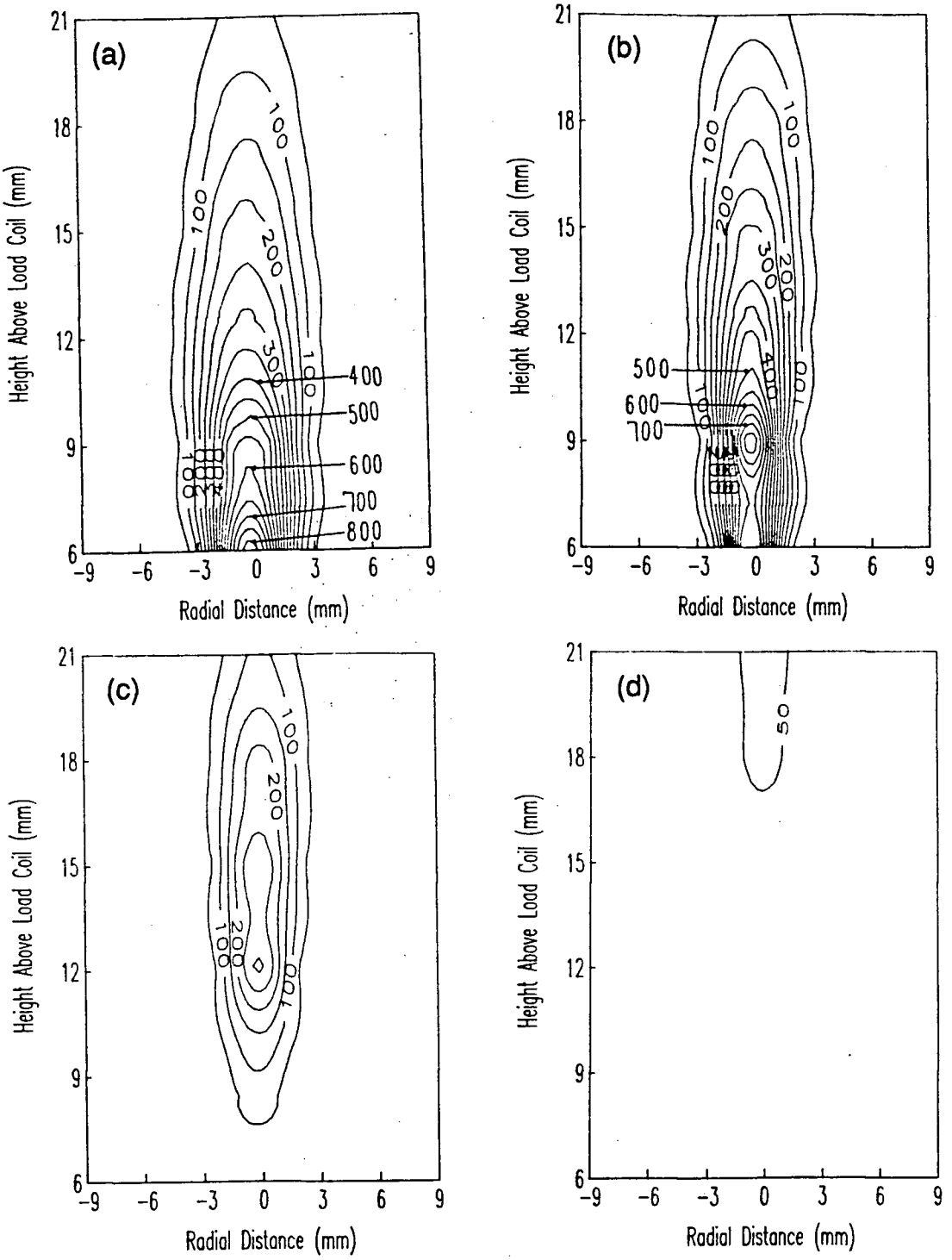

Figure 6.14 Contour plots of the spatially resolved intensity of the Ca II 393.6 nm spectral line at sheath gas flow rates of (a) 0.0, (b) 0.2, (c) 0.4 and (d) 0.6 L/min. The contour lines are labeled in arbitrary units (but are consistent with those of figure 6.13).

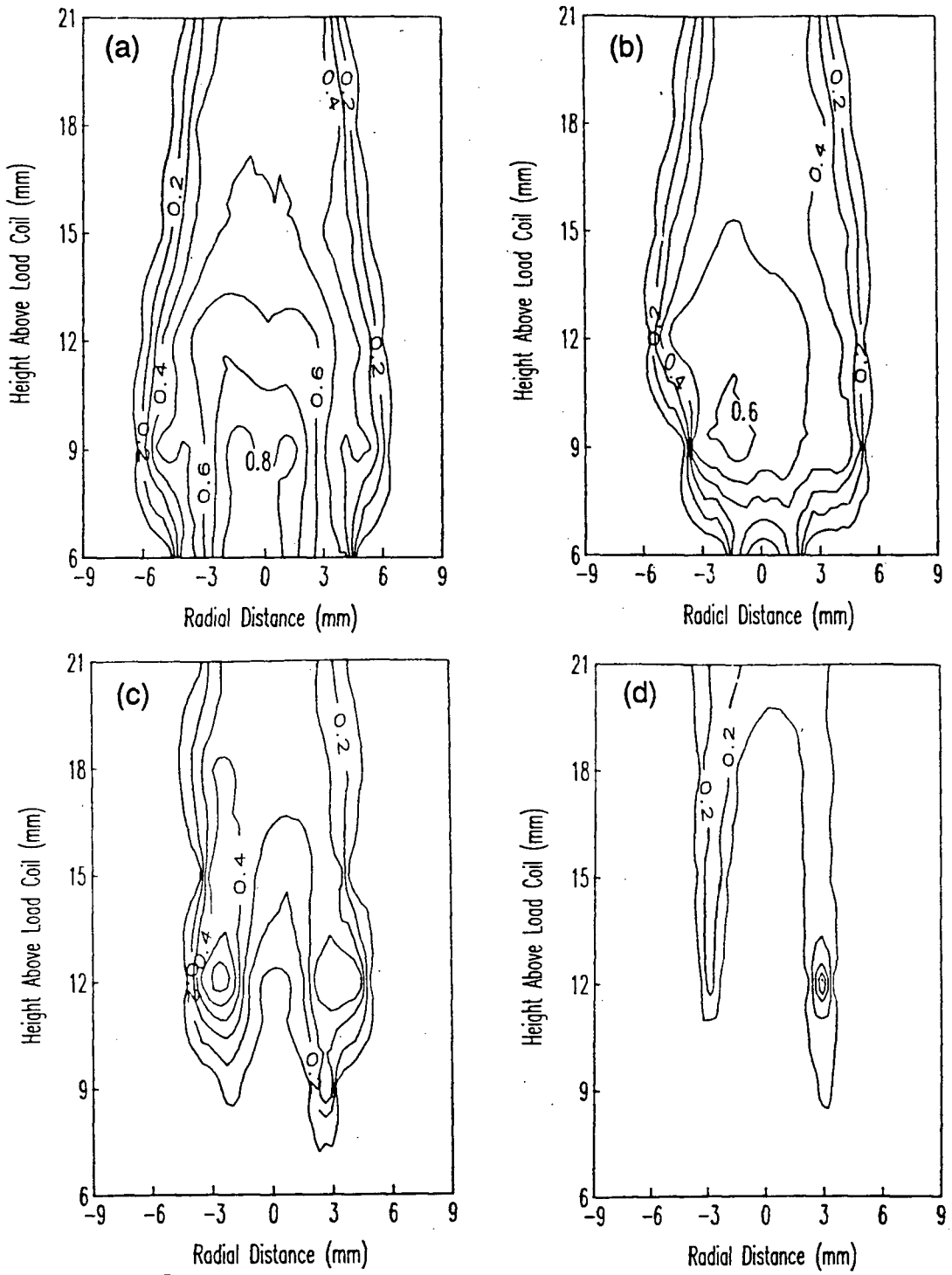

Figure 6.15 Contour plots of the spatially resolved value of the non-equilibrium parameter, b_r, for the calcium lines listed in Table IV at sheath gas flow rates of (a) 0.0, (b) 0.2, (c) 0.4 and (d) 0.6 L/min.

strontium chosen for this study originate from analogous energy levels (and terminate in the ground state), as do the ionic spectral lines. In light of this extreme similarity in behaviour, calcium will not be commented upon, except to note that its b_r values are slightly closer to unity than those of strontium.

Spatial contour maps of the intensities of the Mg I 285.2 nm spectral line and the Mg II 279.5 nm line were also constructed at the usual values of the sheath gas flow rate of 0.0, 0.2, 0.4, and 0.6 L/min. Since magnesium lies in the same group as both strontium and calcium (and spectral transitions originating from analogous energy levels were studied for all the elements) one would expect that it too would show similar behaviour to strontium and calcium. In fact this turned out to be the case - due to this similarity these plots will not be presented here. The only noticeable difference was that, for sheath gas flow rates of 0.4 and 0.6 L/min, significant magnesium ionic emission extended to somewhat larger radial distances than for strontium and calcium. This was simply due to the fact that the spectral transition for Mg II originated from a state with a higher total energy than for the corresponding states of strontium and calcium, due both to the higher ionization energy of magnesium and to the higher excitation energy (with respect to the ionic ground state) of the magnesium spectral line studied. Since the electron density peaks off axis (for these sheath gas flow rates) this relatively difficult-to-excite Mg II line will show significant intensity off axis, even though the total magnesium concentration is not as high as it is in the central channel. Unfortunately the ion-to-atom emission intensity ratios

for magnesium were too noisy to permit the construction of contour maps of b_r.

Figures 6.16, 6.17, 6.18 and 6.19 present spatial contour maps of the Cd I 228.8 nm, the Cd II 226.5 nm, the Zn I 213.9 nm and the Zn II 202.5 nm spectral lines (respectively). In all four of these plots the (a), (b), (c) and (d) correspond to sheath gas flow rates of 0.0, 0.2, 0.4 and 0.6 L/min. The most immediately noticeable feature of the plots, with respect to those for strontium and calcium, is the fact that significant intensity exists for both the atomic and ionic lines of cadmium and (especially) zinc at larger radial distances than for strontium and calcium.

For example, at a sheath gas flow rate of 0.0 L/min, a height above the load coil of 6 mm, and a radial position as large as ±9 mm the intensity of the zinc atom line is still about 5 % that of its maximum intensity (at a radial position of 0 mm). Even at a flow rate of 0.6 L/min, for the height of 9 mm alc, the zinc atom line at a radial position of ±6 mm is still about 12.5 % as intense as it is at a radial position of 0 mm. The behaviour at the flow rate of 0.6 L/min seems relatively easy to understand: because the electron density peaks off axis for this flow rate one would expect that the difficult-to-excite zinc line (due to the high excitation energy of the level from which it originates) would tend to still have reasonable intensity where the electron density is high. The behaviour at a flow rate of 0.0 L/min, on the contrary, is very surprising, and is difficult to understand.

For this flow rate at a height of 6 mm alc the electron density decreases steadily with increasing radial position (figure 6.6). From

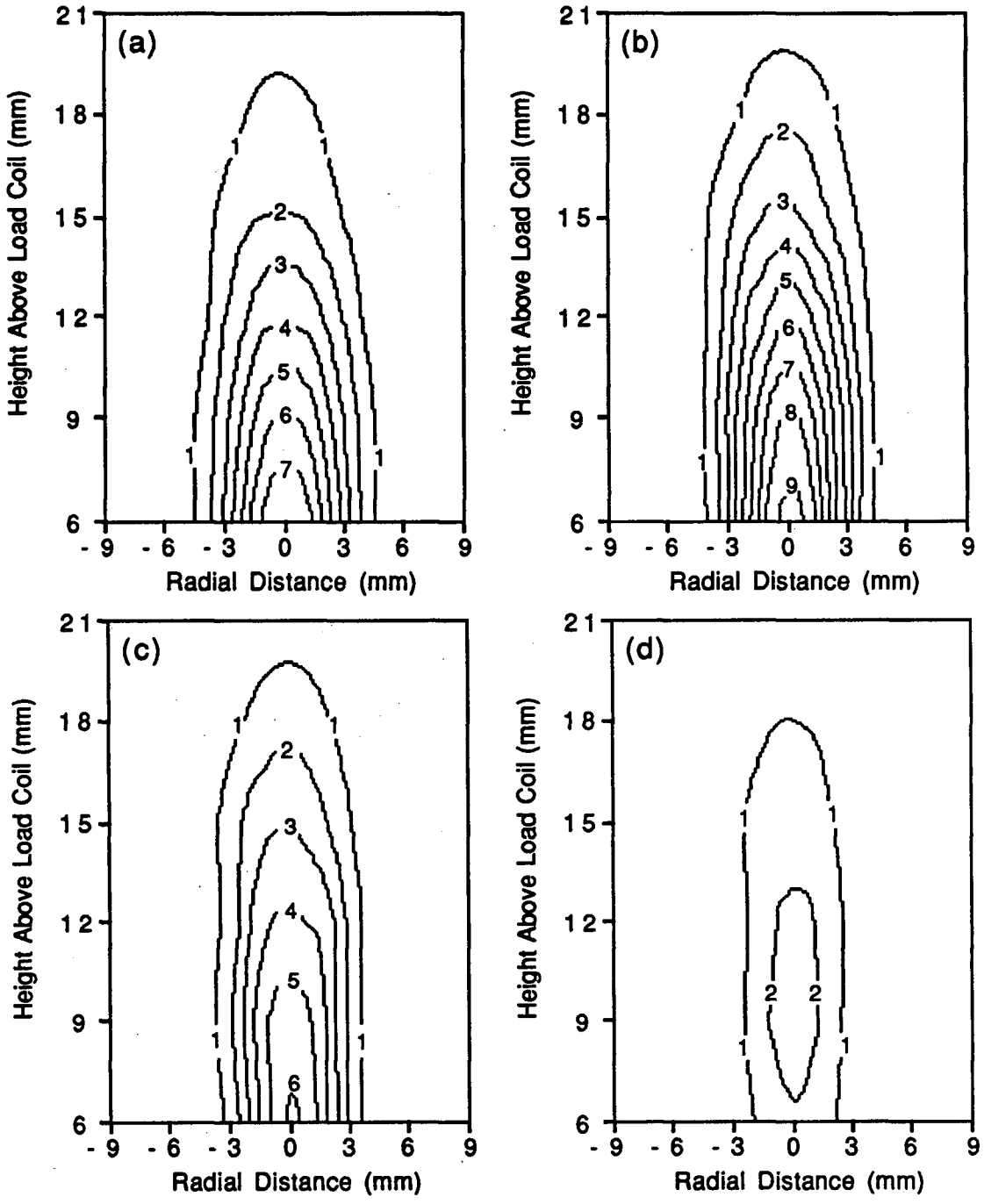

Figure 6.16 Contour plots of the spatially resolved intensity of the Cd I 228.8 nm spectral line at sheath gas flow rates of (a) 0.0, (b) 0.2, (c) 0.4 and (d) 0.6 L/min. The contour lines are labeled in arbitrary units (but are consistent with those of figure 6.17).

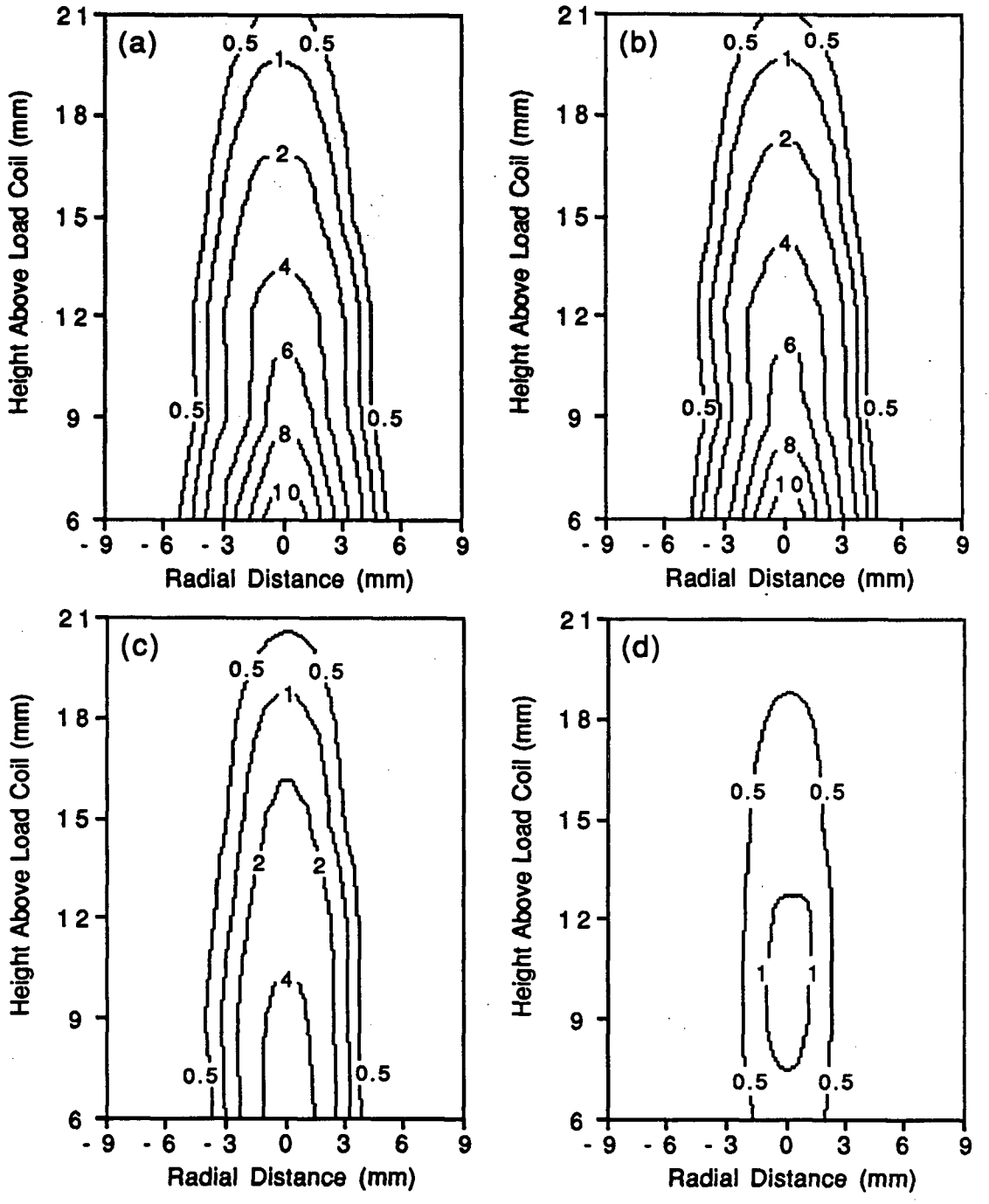

Figure 6.17 Contour plots of the spatially resolved intensity of the Cd II 226.5 nm spectral line at sheath gas flow rates of (a) 0.0, (b) 0.2, (c) 0.4 and (d) 0.6 L/min. The contour lines are labeled in arbitrary units (but are consistent with those of figure 6.16).

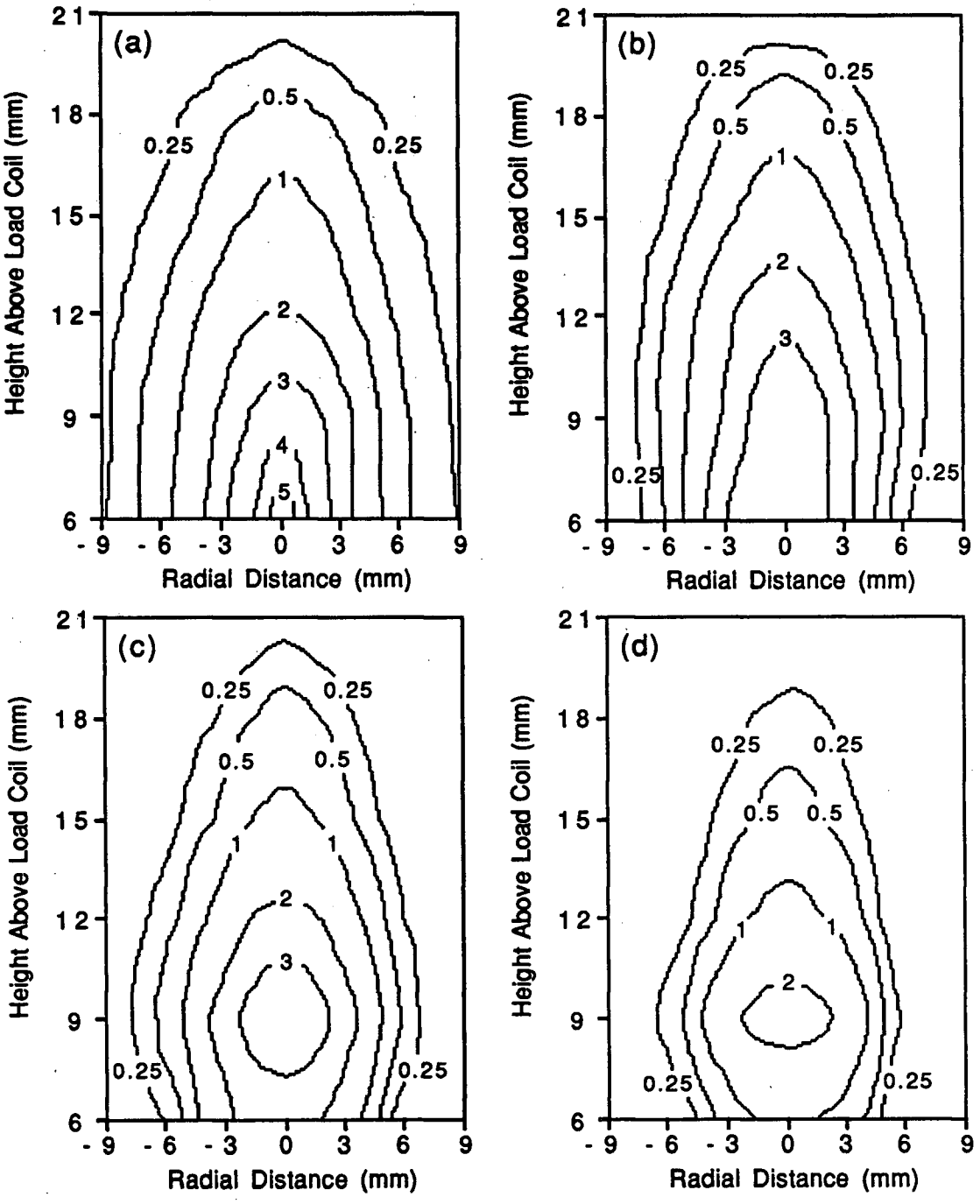

Figure 6.18 Contour plots of the spatially resolved intensity of the Zn I 213.9 nm spectral line at sheath gas flow rates of (a) 0.0, (b) 0.2, (c) 0.4 and (d) 0.6 L/min. The contour lines are labeled in arbitrary units (but are consistent with those of figure 6.19).

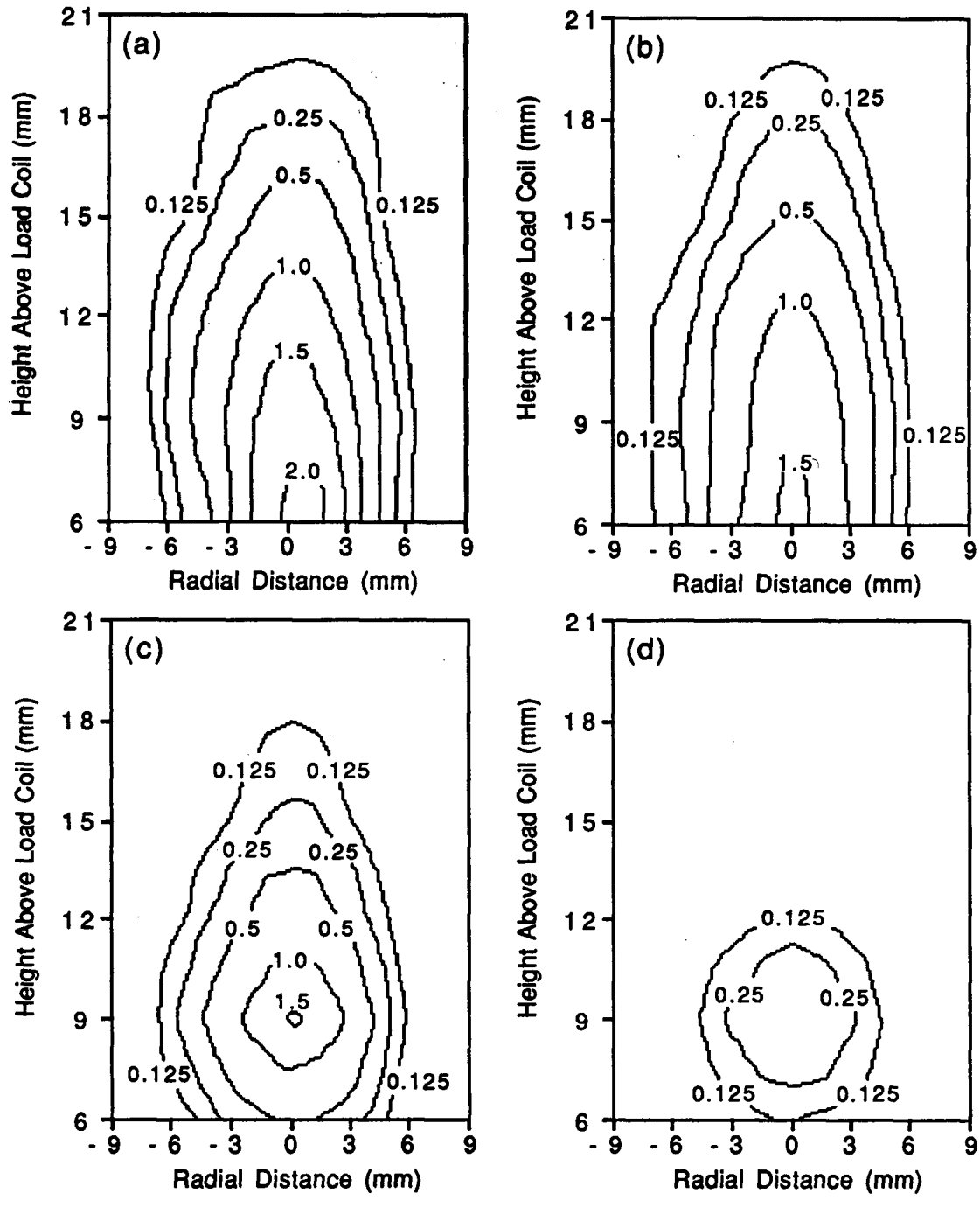

Figure 6.19 Contour plots of the spatially resolved intensity of the Zn II 202.5 nm spectral line at sheath gas flow rates of (a) 0.0, (b) 0.2, (c) 0.4 and (d) 0.6 L/min. The contour lines are labeled in arbitrary units (but are consistent with those of figure 6.18).

this one would expect the following: (1) that because the excitation energy of the level from which the Zn I transition originates is larger than that for strontium I (5.80 vs. 2.69 eV) the intensity of the zinc line would decrease more rapidly with increasing radial distance (and thus decreasing temperature), and (2) that because the total relative amount of strontium atomic species increases rapidly with a decrease in the electron density while that for zinc does not [34] (due to the higher ionization energy of zinc), that the intensity of the zinc line would fall even more rapidly than that of strontium with a decrease in the electron density. In fact this is not the case: the intensity of the zinc line drops more slowly.

At this flow rate of 0.0 L/min and a height of 6 mm alc the ionic zinc spectral line also extends to larger radial positions than does that of the strontium ionic line. This is also surprising: one would expect that as the electron density falls the intensity of the ionic zinc line would fall more rapidly than that for strontium (due to the higher excitation energy of the level from which the zinc transition originates). In addition the total number of zinc ions falls with decreasing electron density while the number of strontium ions is almost constant. It seems as if the total transport of zinc to these large radial distances is perhaps different than that for strontium and calcium; no reason for this is apparent.

As the sheath gas flow rate is increased the maximum intensity of both the Zn I and the Zn II spectral lines decreases. This is as expected: as the flow rate is increased the electron density decreases, thus the intensities of these lines decrease. One does not see the initial increase in atomic emission (as for strontium and

calcium) because the effect of the degree of ionization on the total atom density for zinc is much less significant (due to its high ionization energy) than for strontium or calcium.

The cadmium behaviour (figures 6.18 and 6.19) is similar to that of zinc; this is not surprising since they both lie in the same group of the periodic table. The most significant difference is that the emission profiles for cadmium do not extend to quite as large radial positions as for zinc. For the cadmium atomic emission there is a (small) increase in the maximum intensity for the flow rate of 0.2 L/min as compared to 0.0 L/min; this is presumably because, even though the electron density has decreased, the decrease in the degree of ionization (i.e. the increase in the total atom density) offsets the decrease in atom excitation (from the Boltzmann distribution).

Spatially resolved (i.e. Abel inverted) data were also collected, for a height of 10 mm above the load coil only, for the Ba I 553.6 nm and the Ba II 455.4 nm spectral lines for sheath gas flow rates of 0.0, 0.1, 0.2, 0.3, 0.4, 0.5 and 0.6 L/min (the rf power was left unchanged at 1.0 kW). Figure 6.20 shows plots of the intensities of these two spectral lines, at a radial position of 0 mm, as a function of the sheath gas flow rate. Unfortunately, due to its low intensity, it was not possible to measure the barium atomic line for sheath gas flow rates less than 0.5 L/min. These results are also surprising: Ite calculations (taking the contribution of doubly ionized barium into account) indicate that the intensities of both the atomic and ionic barium lines should decrease with an increase in the flow rate (with its corresponding decrease in the

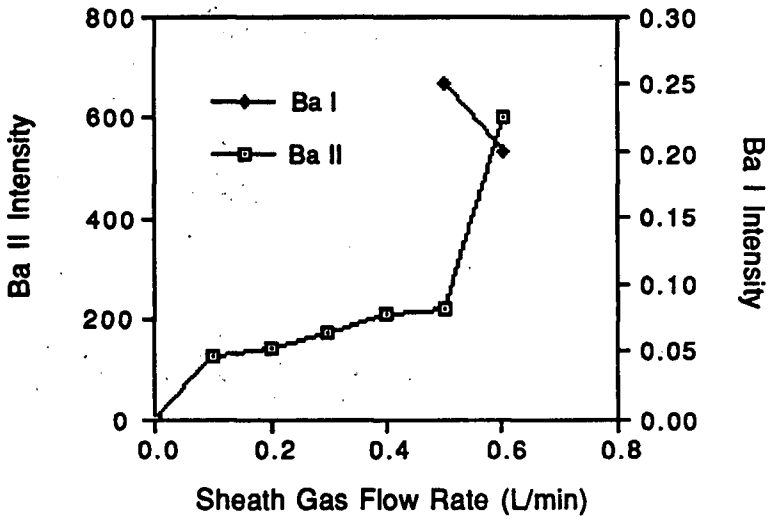

Figure 6.20 Plots of the intensities of the Ba I 553.6 nm and the Ba II 455.4 nm spectral lines (taken at radial positions of 0 mm and a height of 10 mm alc), as a function of the sheath gas flow rate.

electron density). Instead, one sees the intensity of the atomic barium line increase at a sheath gas flow rate of 0.5 L/min (however the magnitude of the increase is unclear since the intensity of the line at a flow rate of 0.4 L/min was just a little to low to be measured, while at 0.5 L/min it was just intense enough to measure). The ionic barium line increased by a factor of about 75 in going from a sheath gas flow rate of 0.0 to 0.1 L/min, and then continued to increase steadily (these results were all very reproducible).

A tentative explanation for this is the following: because the first two ionization potentials of barium are very low (5.212 eV for the first and 10.004 eV for the second), a large proportion of the barium will exist in the doubly ionized state (for an electron density of 4.5×10^{15} cm^{-3} lte calculations indicate that about 65 % of the

barium would exist as Ba^{2+}). For the sheath gas flow rate of 0.0 L/min, due to the relatively effective mixing between the sample introduction gas and the hot plasma gas, a very large fraction of the barium will exist as Ba^{2+} at vertical heights below 6 mm alc. It is possible that even at a height of 10 mm alc the Ba^{2+} will not have had sufficient time to recombine to give Ba^{+} - the intensity of whose emission lines will thus be low. As the sheath gas flow is increased and an aerosol channel forms, there will be less mixing between these gases and therefore less of the barium will exist as Ba^{2+} - it is thus plausible that the intensity of the Ba^{2+} line will increase.

6.3.4 Results for Aqueous Iron and Ferrocene Vapour

Spatial contour maps, at sheath gas flow rates of 0.0, 0.2, 0.4 and 0.6 L/min, were also acquired for the Fe I 372.0 nm and the Fe II 275.6 nm spectral lines with iron introduced into the plasma in two different ways: as an aerosol (using conventional nebulization) and as a vapour from the vapour pressure of ferrocene. The experimental set-up used to introduce the ferrocene vapour was described in the experimental section of this chapter. As was mentioned there the usual 0.6 L/min nebulizer argon flow was still present, but the sample intake tube was pinched so that no water (or air) entered the plasma. Figures 6.21, 6.22, 6.23 and 6.24 present spatially resolved contour maps for atomic iron emission with aqueous sample introduction, ionic emission with aqueous introduction, atomic emission using ferrocene introduction, and ionic emission using ferrocene introduction (respectively). The

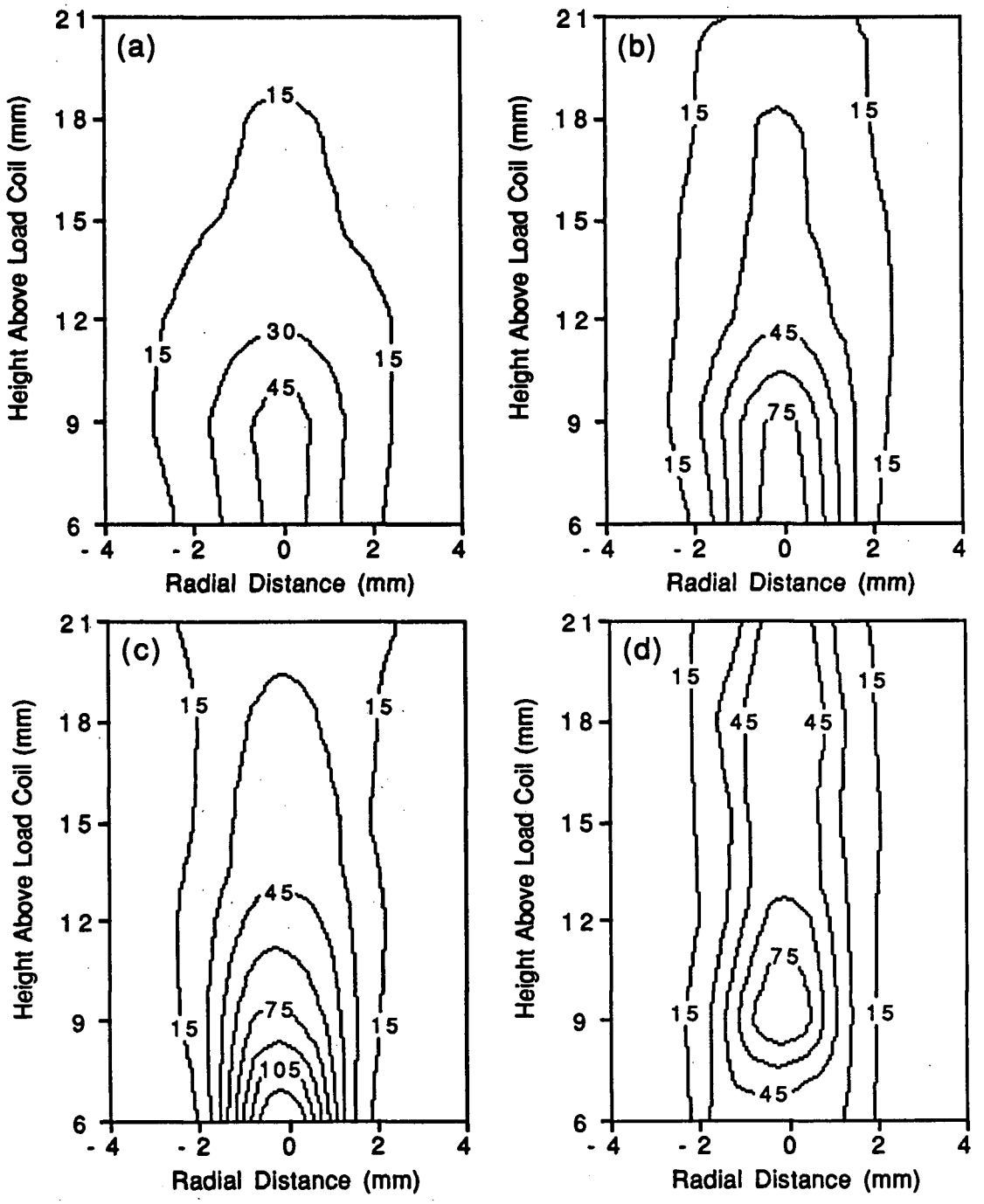

Figure 6.21 Contour plots of the spatially resolved intensity of the Fe I 372.0 nm spectral line using aqueous sample introduction at sheath gas flow rates of (a) 0.0, (b) 0.2, (c) 0.4 and (d) 0.6 L/min. The contour lines are labeled in arbitrary units (but are consistent with those of figures 6.22 to 6.24).

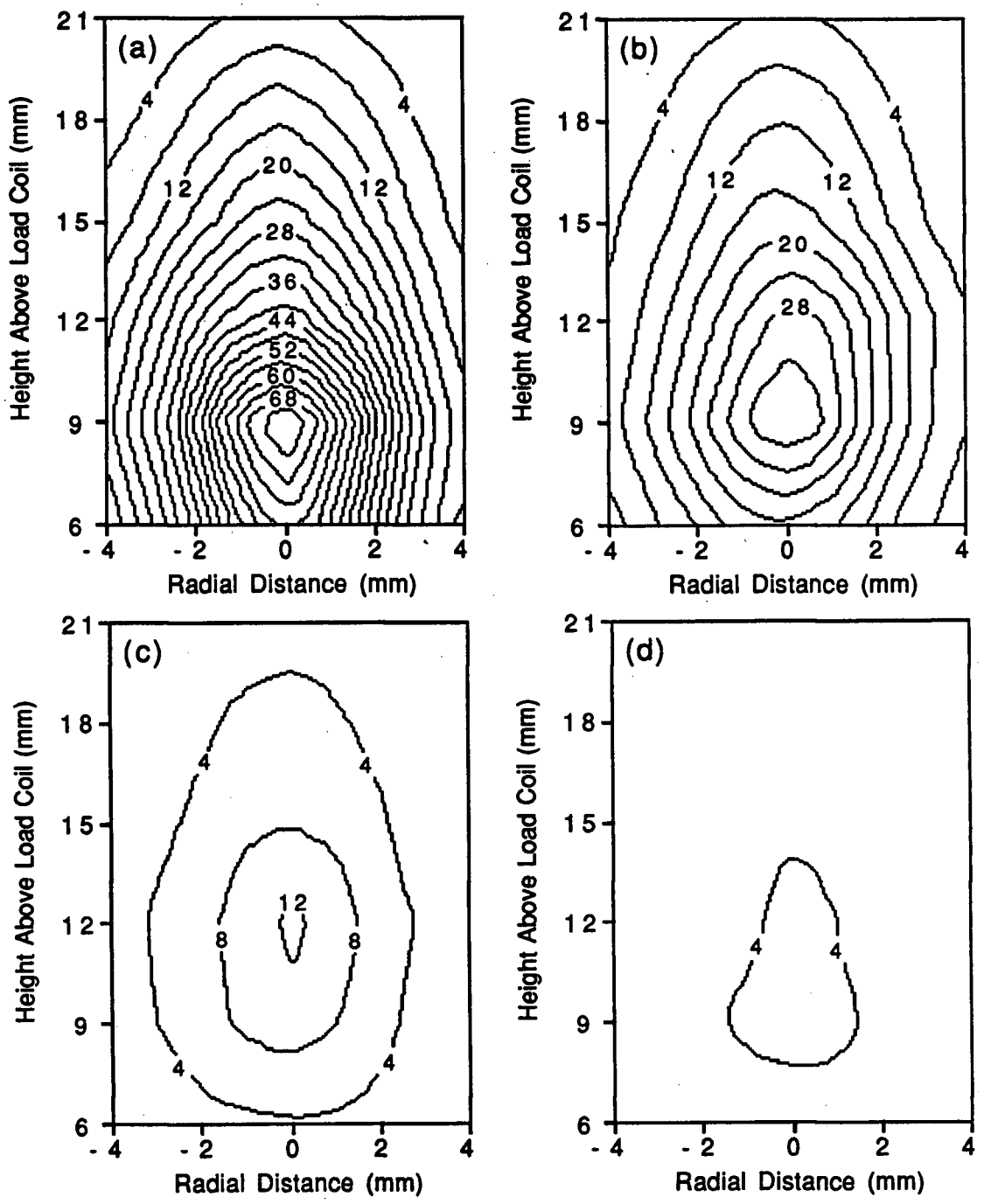

Figure 6.22 Contour plots of the spatially resolved intensity of the Fe II 275.6 nm spectral line using aqueous sample introduction at sheath gas flow rates of (a) 0.0, (b) 0.2, (c) 0.4 and (d) 0.6 L/min. The contour lines are labeled in arbitrary units (but are consistent with those of figures 6.21, 6.23 and 6.24).

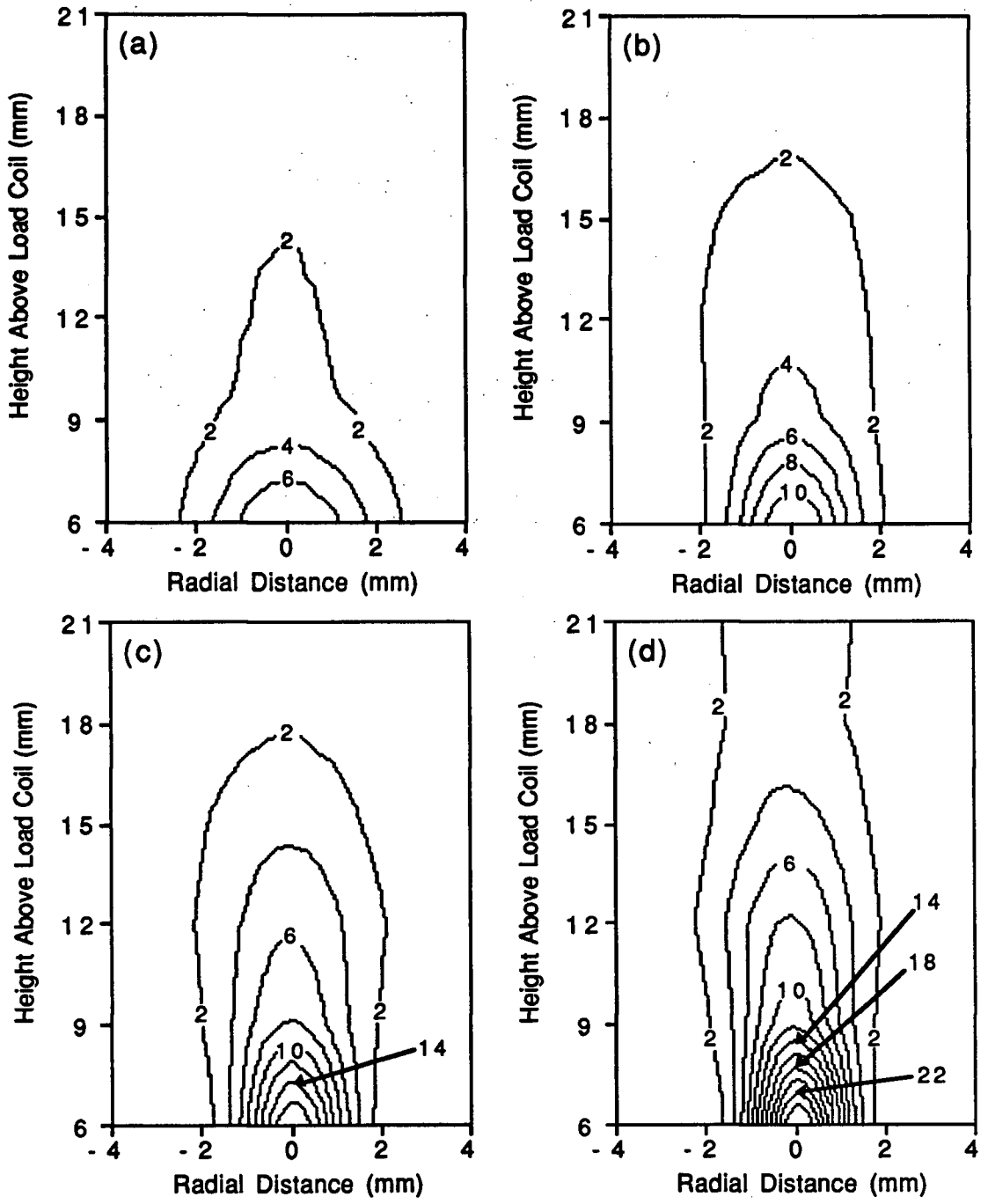

Figure 6.23 Contour plots of the spatially resolved intensity of the Fe I 372.0 nm spectral line using ferrocene sample introduction at sheath gas flow rates of (a) 0.0, (b) 0.2, (c) 0.4 and (d) 0.6 L/min. The contour lines are labeled in arbitrary units (but are consistent with those of figures 6.21, 6.22 and 6.24).

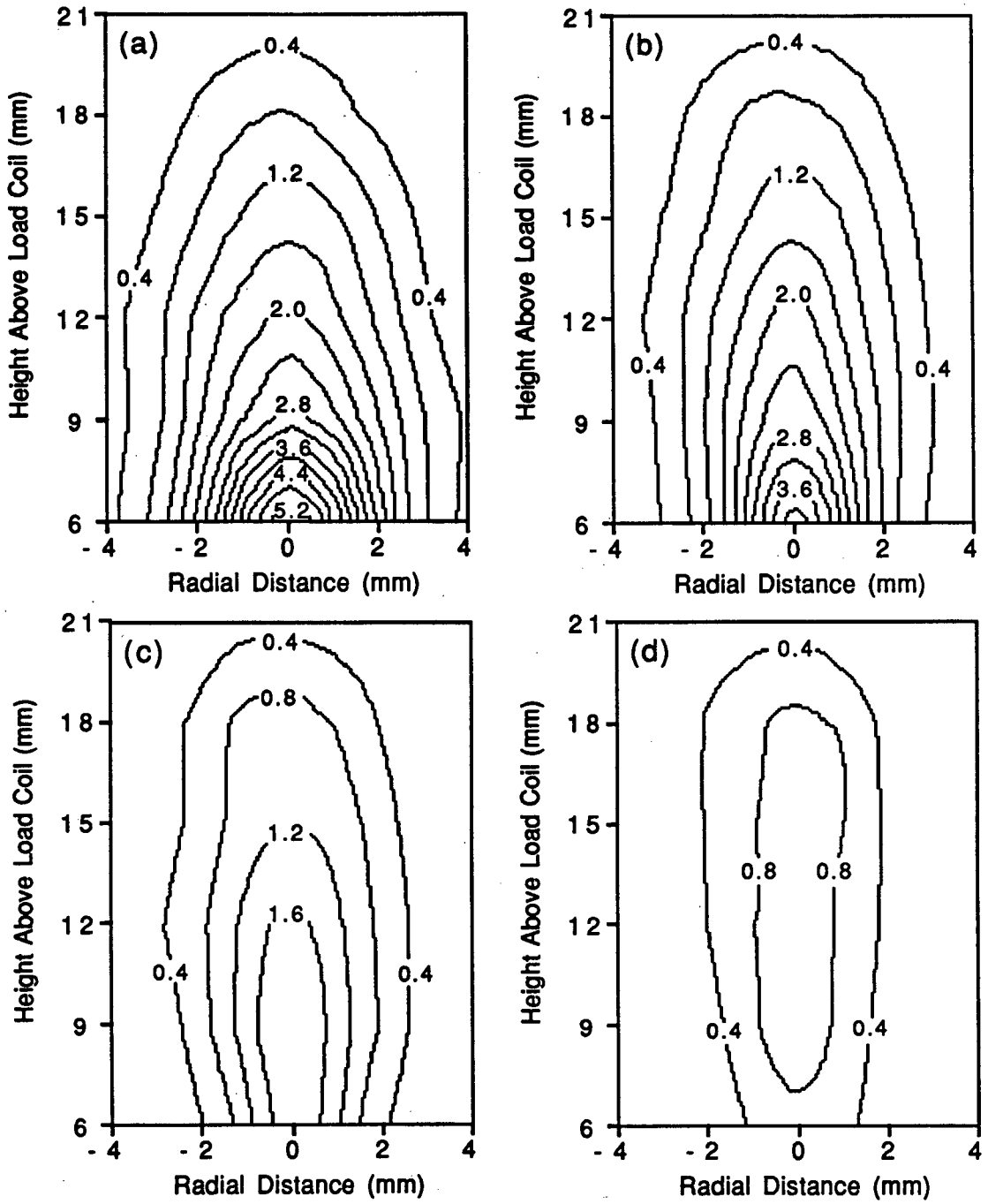

Figure 6.24 Contour plots of the spatially resolved intensity of the Fe II 275.6 nm spectral line using ferrocene sample introduction at sheath gas flow rates of (a) 0.0, (b) 0.2, (c) 0.4 and (d) 0.6 L/min. The contour lines are labeled in arbitrary units (but are consistent with those of figures 6.21 to 6.23).

sheath gas flow rates used are listed in the figure captions (note that for these plots the "Radial Distance" axis extends to only ±4 mm, not ±9 mm as for the other contour maps presented in this chapter).

Comparing figures 6.21 and 6.22 to 6.9 and 6.10 (for strontium) one can see that iron and strontium show similar behaviour. The maximum intensity of the atomic iron spectral line increases with an increase in the sheath gas flow rate from 0.0 to 0.2 and from 0.2 to 0.4 L/min; it then decreases at 0.6 L/min. With the exception of the flow rate of 0.6 L/min the maximum intensity occurs at a radial position of 0 mm and a height above the load coil of 6 mm. This is the same general behaviour shown by atomic strontium; the only essential difference between their behaviour is that, due to its low ionization potential, the maximum intensity of the atomic strontium spectral line increases rapidly with an increase in the sheath gas flow rate (from 0.0 to 0.4 L/min), while that for iron increases more slowly. The ionic lines of both iron and strontium both show a steady decrease in maximum intensity as the flow rate is increased, as well as the usual confinement to the aerosol channel.

Of more interest is the comparison of the contour maps of atomic and ionic iron emission using conventional nebulization and the ferrocene sample introduction technique: on the whole, the differences in iron excitation between the two sample introduction techniques were quite small. It should be pointed out that the spatial distribution of the electron density should not be significantly affected by the fact that, in the case of the ferrocene introduction, there was no water vapour introduced into the plasma:

Caughlin and Blades [33] have found that when water was removed from the aerosol gas "the spatial distribution of electron density remained the same".

Comparing figures 6.21 and 6.23 (of the atomic emission) one can immediately notice the extreme similarity in the shape of the contour plots for the two sample introduction techniques at sheath gas flow rates of 0.0, 0.2 and 0.4 L/min. In each case, for these flow rates, the maximum intensity obtained using conventional nebulization was a factor of 6 to 8 times that obtained using the ferrocene sample introduction technique. Since the concentration of the aqueous iron solution was 5000 ppm, the concentration of iron in the plasma when using ferrocene (heated to a temperature of 50 °C) was thus roughly equivalent to that of a 700 ppm aqueous solution. At a sheath gas flow rate of 0.6 L/min the atomic emission intensity from the iron introduced aqueously has decreased in maximum intensity from its value at the flow of 0.4 L/min; in addition the position of maximum intensity has increased from 6 mm alc to 9 mm. The iron introduced from the vapour pressure of ferrocene, on the other hand, has increased in intensity from its value at the flow of 0.4 L/min and still peaks at 6 mm alc. It is possible that the data for aqueous iron at a height of 6 mm is in error.

Comparing figures 6.22 and 6.24 one can see that the spatial contour maps for the ionic emission intensity of iron are quite similar for the two cases. The only significant difference is that the emission intensity for the iron introduced using ferrocene peaked at a height of 6 mm alc for sheath gas flow rates of 0.0 and

0.2 L/min and at 9 mm for 0.4 L/min; for the iron introduced aqueously this was not the case: it peaked at a height of 9 mm alc for flow rates of 0.0 and 0.2 L/min and 12 mm alc for 0.4 L/min (3 mm higher in each case). One possible reason for this may be the following: in reference [33] it was found that when water vapour was introduced into the plasma the increase in molar volume which it undergoes upon heating seems to lift the plasma so that the bottom of the discharge is farther from the torch. If the position of maximum ion emission intensity using ferrocene occurs at 6 mm alc (and not below) this could explain why the position of maximum intensity is about 3 mm higher in the case of aqueous sample introduction (this would not necessarily be the case for the atomic emission since it may peak below 6 mm alc).

6.4 Summary

As mentioned previously, one of the advantages of the sheath gas flow is that it allows one to study the effect of the sample introduction flow rate on plasma conditions, while keeping the total amounts of both analyte and solvent reaching the plasma constant. The electron density was found to both decrease steadily and to have its position of maximum concentration shift off-axis with an increase in the sheath gas flow rate. It appears that at low values of this flow, the mixing between the cool sample introduction gas and the much hotter plasma gas is reasonably complete, whereas at higher values there is relatively little mixing. It was shown that even a small excess volume of sample introduction gas can significantly alter the electron density. It was also found that there

is a very strong correlation between the populations of excited hydrogen and (especially) excited argon with the electron density.

Strontium atomic emission was found to increase with an increase in sheath gas flow rate from 0.0 to 0.2 and from 0.2 to 0.4 L/min; it then drops somewhat (and the position of maximum intensity shifts higher in the plasma) at a flow rate of 0.6 L/min. Strontium ionic emission both decreases steadily and shifts higher in the plasma with an increase in flow rate. The b_r values for strontium were found to be less than unity at all spatial positions - this is due to radiative decay competing with electron impact processes, and was discussed in detail in chapter three. Other elements (with the exception of barium) behaved in a similar fashion; differences were mainly due to the differing excitation potentials of the element.

Ionic barium, in particular, showed unusual behaviour. Its emission intensity increased by a factor of 75 in going from a sheath gas flow rate of 0.0 to 0.1 L/min - it then continued to increase with an increase in the flow rate (the reverse of what one would expect on the basis of lte arguments). It is believed that this potentially very useful analytical result is due to the recombination of Ba^{2+} with an electron.

Mermet's research group has stressed the importance of the "residence time" of analyte in the plasma on its excitation behaviour [94, 106, 107]. Thanks to the spatially resolved electron densities presented in this chapter, it seems more useful, in general, to think of analyte behaviour as being more or less determined by the electron density. The electron density itself is a function of, not so

much the residence time, but rather of the efficiency of mixing between the sample introduction and plasma gases (as well as the volume of sample introduction gas).

By introducing iron into the plasma, both as a standard aqueous aerosol and directly as a vapour (from the vapour pressure of ferrocene), it was found that, on the whole, the differences in iron excitation between the two sample introduction methods were quite small. This is an interesting result - not only does it mean that the introduction of water into the plasma has a limited effect on sample excitation, but also that the processes of desolvation, vaporization and dissociation which an aerosol droplet must undergo are of limited importance to the overall excitation of analyte. This finding is contrary to the speculations of Murillo and Mermet [106] that the residence time must be large in order for these processes to be efficient.

Chapter 7
Influence of Instrumental Broadening on Lineshapes Detected by PMT and LPDA Detectors

7.1 Introduction

Because the inductively coupled plasma is a relatively high temperature analytical source (as compared with flames, etc.) most samples will emit relatively line-rich spectra, thus giving rise to spectral line overlaps with analysis lines. Both direct overlaps (when the wavelength separation between an analysis line and an interfering line is less than the resolving power of the instrument) and line-wing overlaps (when the separation is greater than the resolving power) will significantly increase detection limits and worsen the accuracy of an analytical determination. In order to mitigate the effects of these overlaps, an understanding of the instrumental lineshapes generated by grating spectrometers and the resulting detected lineshapes is necessary for anyone who must make analytical lines selection or devise background correction strategies for icp-oes.

In a previous publication [31] the possibility of using computer simulated analyte emission spectra as an aid in line selection for icp-oes was investigated. In that work, a Gaussian instrumental lineshape was assumed, which led to the absence of any significant line-wings. It was suspected that the line-wings would have been more prominent if a more realistic instrumental lineshape (to be described in this chapter) had been used.

The next chapter will describe this computer simulation work (concentrating on more recent efforts using the instrumental lineshape described below), while the purpose of this present chapter is to show how the instrumentally broadened line profile comes about, and how it gives rise to the detected profile for two different radiation detectors: a scanned exit slit photomultiplier tube combination and a linear photodiode array. Theoretically calculated instrumentally broadened line profiles, and the resulting detected lineshapes, are presented for entrance slit widths on the monochromator of 10, 30, and 50 μm; these were found to be in good agreement with experimentally acquired spectra. The material in this chapter has been previously published in reference [30].

7.2 Theory

We will consider the case of a spectroscopic source imaged onto the rectangular entrance slit of a monochromator. For simplicity (since for medium resolution instruments the detected line profile is given almost entirely by instrumental broadening) the source will be considered to be monochromatic. In addition, it will be assumed that the electromagnetic waves reaching the focal plane of the monochromator have random phase (the so-called incoherent case). Incoherent illumination is actually a special case of the more general theory of partially coherent illumination; however, for the instrumental conditions of interest for icp-oes, Mielenz [100] has shown that assuming incoherent illumination leads to results extremely close to those obtained in the partially coherent case.

For any element of length across the entrance slit, diffraction by the grating will lead to the characteristic sinc squared diffraction pattern in the exit focal plane. If these diffraction patterns are integrated across the width of the slit it can be shown [129] that the intensity in the focal plane, as a function of distance, can be written:

$$I(x) = C \int_{u-v}^{u+v} \frac{\sin^2 t}{t^2} \, dt \qquad (7.1)$$

with

$$u = \pi x D/f'\lambda, \text{ and } v = \pi s D/2f\lambda, \qquad (7.2)$$

where C is a constant, x is the distance from the line centre in the focal plane, D is the monochromator aperture width (often the grating width), f' is the focal length of the collimating lens or mirror, λ is the wavelength, s is the entrance slit width, and f is the focal length of the focusing lens or mirror.

In later plots it will be shown that I(x) is a rectangular-like function with a width of roughly s (i.e. an image of the entrance slit), possessing wings which can exist for a significant distance from the line centre. If information about line-wings is desired it is clearly not possible to approximate I(x) by a straight rectangular function.

The detected intensity for a scanning pmt is simply given as the convolution of the instrumental profile, I(x), with the pmt response function [50, 71]. For a response function, R(x), of unity across an

exit slit of width s' and zero elsewhere the detected intensity is given by:

$$I_{pmt}(x) = N \int_{-s'/2}^{s'/2} I(x-t)\, dt \qquad (7.3)$$

where N is a normalization constant; it is worth noting that N is independent of slit width.

The form of the response function for the photodiode array is somewhat more complicated than for the pmt case. A typical photodiode array consists of an n-type semiconductor substrate with embedded "islands" of p-type semiconductor (which form the diodes); for the 4096 pixel lpda described in chapter two, the p-type diode regions are 7 μm wide with a centre to centre separation between these regions of 15 μm. The response function [117] for three adjacent diodes of the 4096 element array is shown in the figure below. The response across the physical width of the

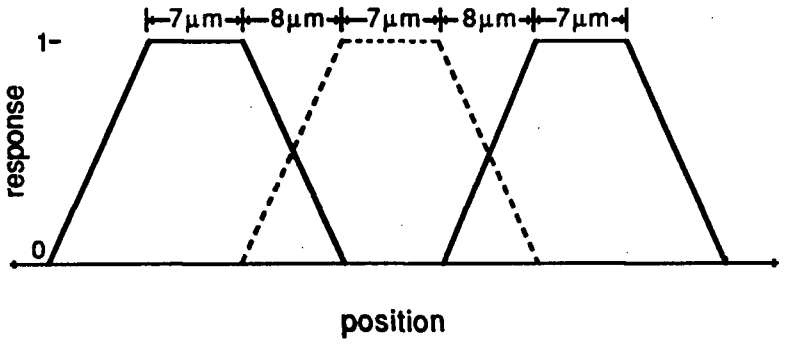

Figure 7.1 Response function (shown for three adjacent diodes) of the 4096 pixel photodiode array.

photodiodes is constant and is equal to unity, whereas between photodiodes the response falls off linearly from one to zero. Since all electron-hole pairs produced between diodes will migrate to one of the two diodes [85], the sum of the response functions in this region is equal to unity.

As pointed out in reference [85], the fact that lpda's respond to all of the light incident upon them gives them a considerable advantage over some other charge coupled devices (ccd's), such as gate-side illuminated ccd's, which can give severely aliased signals [127]. The characteristics of lpda's have been discussed in several recent publications [73, 74, 86, 126, 127].

In the frame of reference in which the exact centre of one particular photodiode (called the zero'th diode) is taken to be zero, the intensity for the n'th diode (n positive if the diode is to the right of the reference diode) is given by:

$$I_n = N \int_{c_n-11.5\mu m}^{c_n+11.5\mu m} I(t)R(t)\,dt \qquad (7.4)$$

where $c_n = (15\,\mu m)\cdot n$, is the centre position of the n'th diode and N is again a normalization constant. In order to numerically integrate the equation it is convenient to express the integral as a sum over each of the three separate parts of the diode response function:

$$I_n = N' \left(\frac{1}{8\ \mu m}\right) \left\{ \int_{c_n-11.5\mu m}^{c_n-3.5\mu m} I(t)(t-c_n+11.5\mu m)\ dt + \int_{c_n+3.5\mu m}^{c_n+11.5\mu m} I(t)(c_n+11.5\mu m-t)\ dt \right\} + \int_{c_n-3.5\mu m}^{c_n+3.5\mu m} I(t)\ dt \qquad (7.5)$$

where N' is another normalization constant. The above equation was obtained from the previous one by writing R(t) as an explicit function of position.

Theoretical pmt and lpda lineshapes have been calculated for a variety of entrance slit widths and are given in the results section below. In addition, the effect on the detected lineshapes of translating the centre of the instrumental profile in relation to the diodes has been investigated.

7.3 Experimental

The theoretical line profile plots shown below were generated on a Corona PC (Westlake Village, CA), an IBM PC compatible machine. A BASIC program was written to evaluate I(x) for 121 equally spaced points from x = -120 μm to x = 120 μm. In all cases, unless specified otherwise, λ was taken as 500.0 nm. The pmt detected response was calculated from equation (7.3), using exit and entrance slits of equal width. The photodiode array detected response was calculated from equation (7.5) for nine diodes across the width of the instrumentally broadened line, whose centre could be made to vary with respect to the photodiodes.

The monochromator (as well as the lpda detection system) is described in chapter two of this thesis; it had f = f' = 1 m and D = 140 mm. The pmt detection system consisted of a Hamamatsu (Middlesex, NJ) model R 955 photomultiplier tube, a McPherson (Acton, MA) model EU-42A high voltage power supply, and a Keithley (Cleveland, OH) model 427 current amplifier. The spectroscopic source chosen was the 546.07 nm line from a low pressure mercury discharge lamp.

7.4 Results

Figure 7.2 shows lineshape plots for the instrumental response function, I(x), for entrance slit widths of 10 μm (7.2a), 30 μm (7.2b), and 50 μm (7.2c). For the same slit widths, figure 7.3 shows the calculated pmt response, figure 7.4 a scale-expanded version of figure 7.3 showing the line-wings, figure 7.5 the calculated lpda response, figure 7.6 the experimental pmt response, and figure 7.7 the experimental lpda response. All plots are normalized to the 10 μm slit width case. For the lpda plots the centre of the instrumentally broadened profile was chosen to fall at the centre of the zero'th diode.

It can be seen that the instrumental profile plots in figure 7.2 all have half widths roughly equal to the entrance slit width, and that all have approximately the same maximum intensity. Essentially the collimating and focusing lens or mirror serves to form an image of the entrance slit in the focal plane, the line-wings coming from diffraction by the grating.

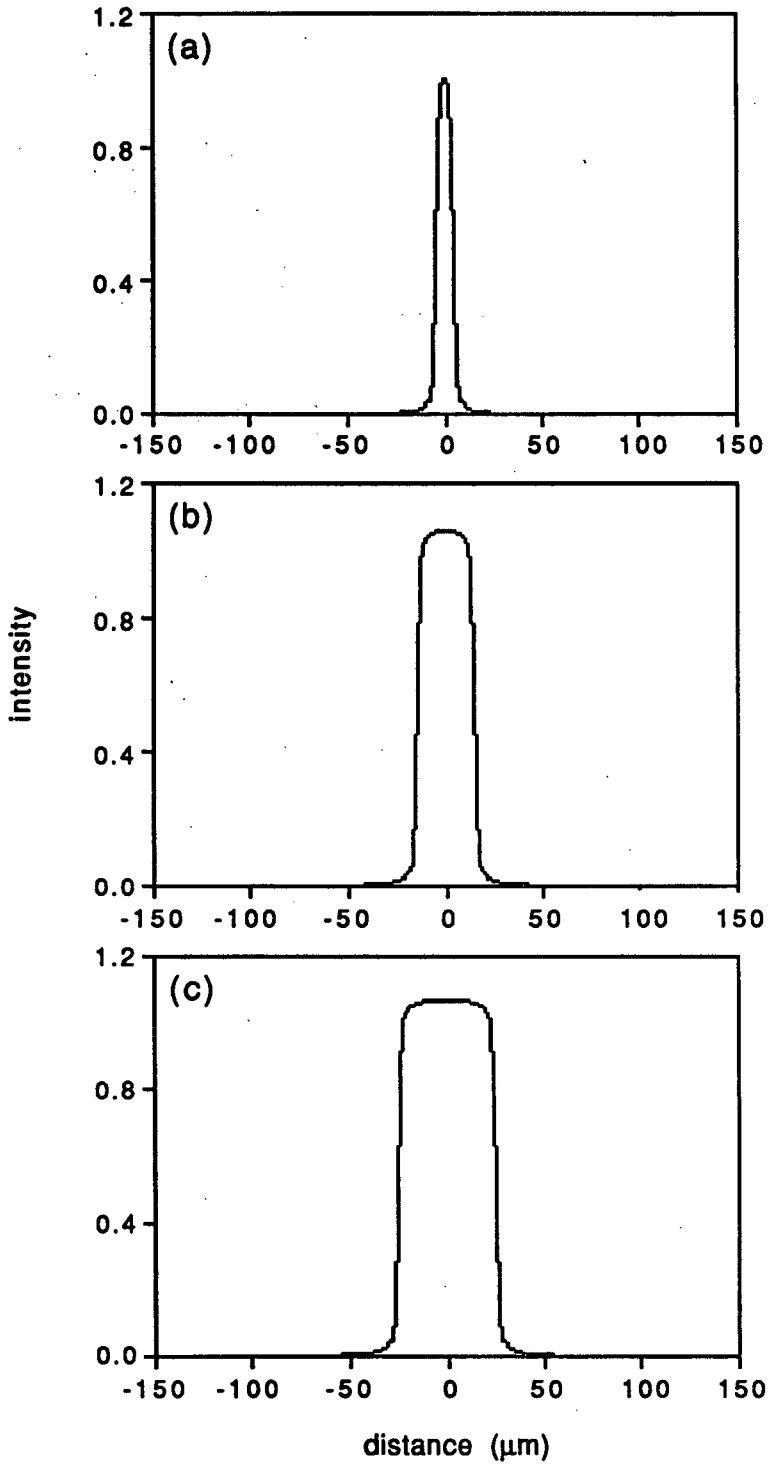

Figure 7.2 Calculated instrumental profile, I(x), for entrance slit widths of (a) 10 μm, (b) 30 μm, and (c) 50 μm.

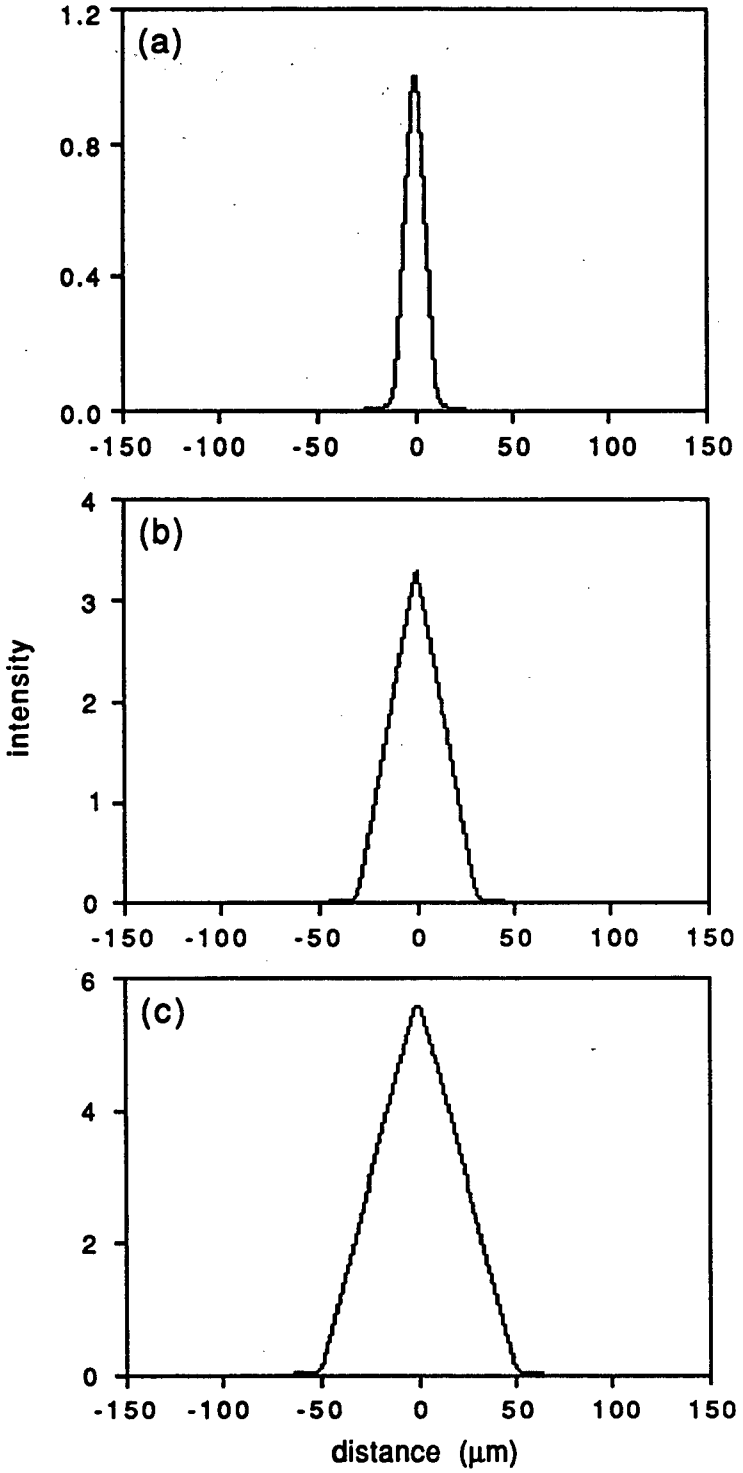

Figure 7.3 Calculated scanned pmt response for equal entrance and exit slit widths of (a) 10 μm, (b) 30 μm, and (c) 50 μm.

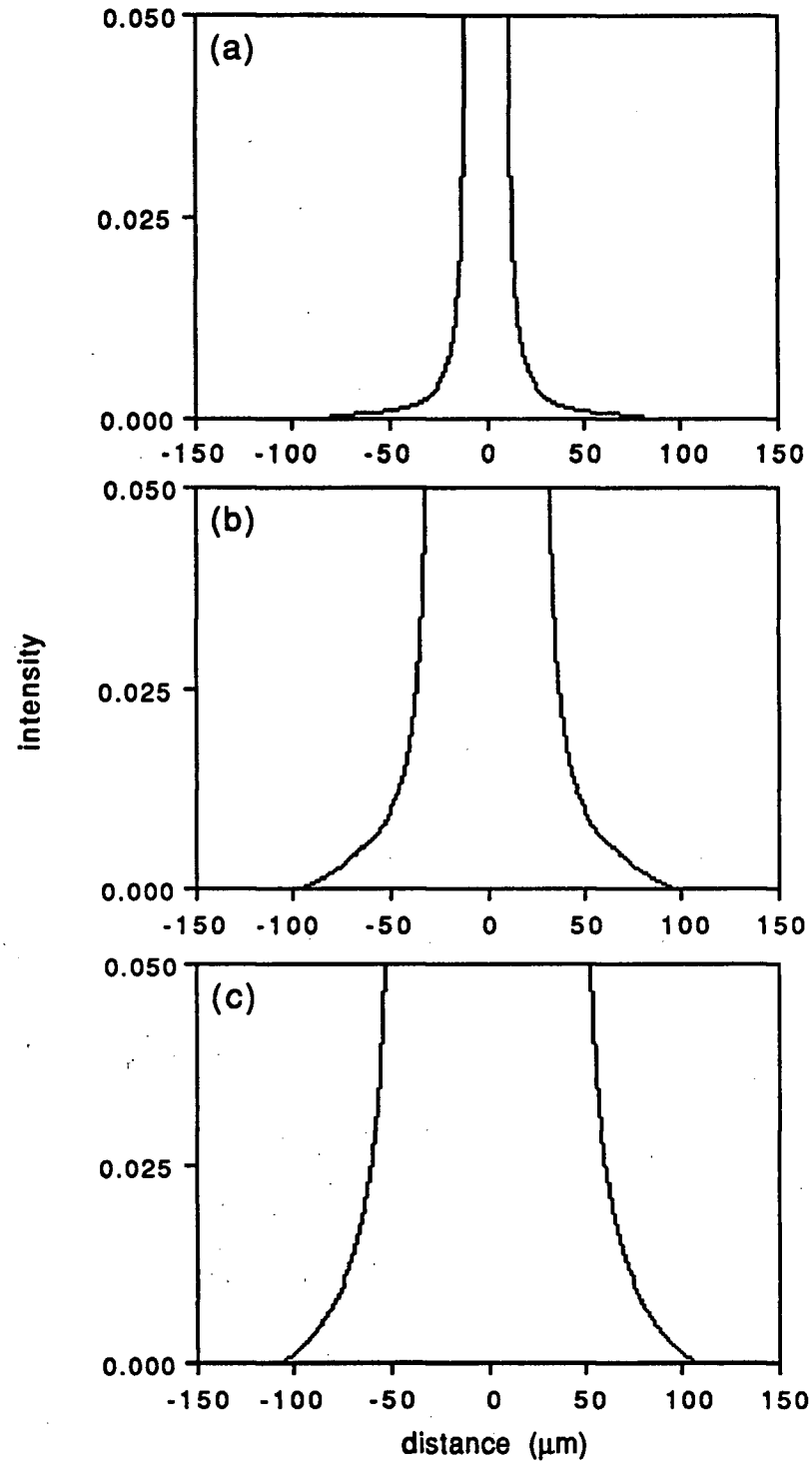

Figure 7.4 Calculated scanned pmt response, with an expanded intensity scale, for equal entrance and exit slit widths of (a) 10 μm, (b) 30 μm, and (c) 50 μm.

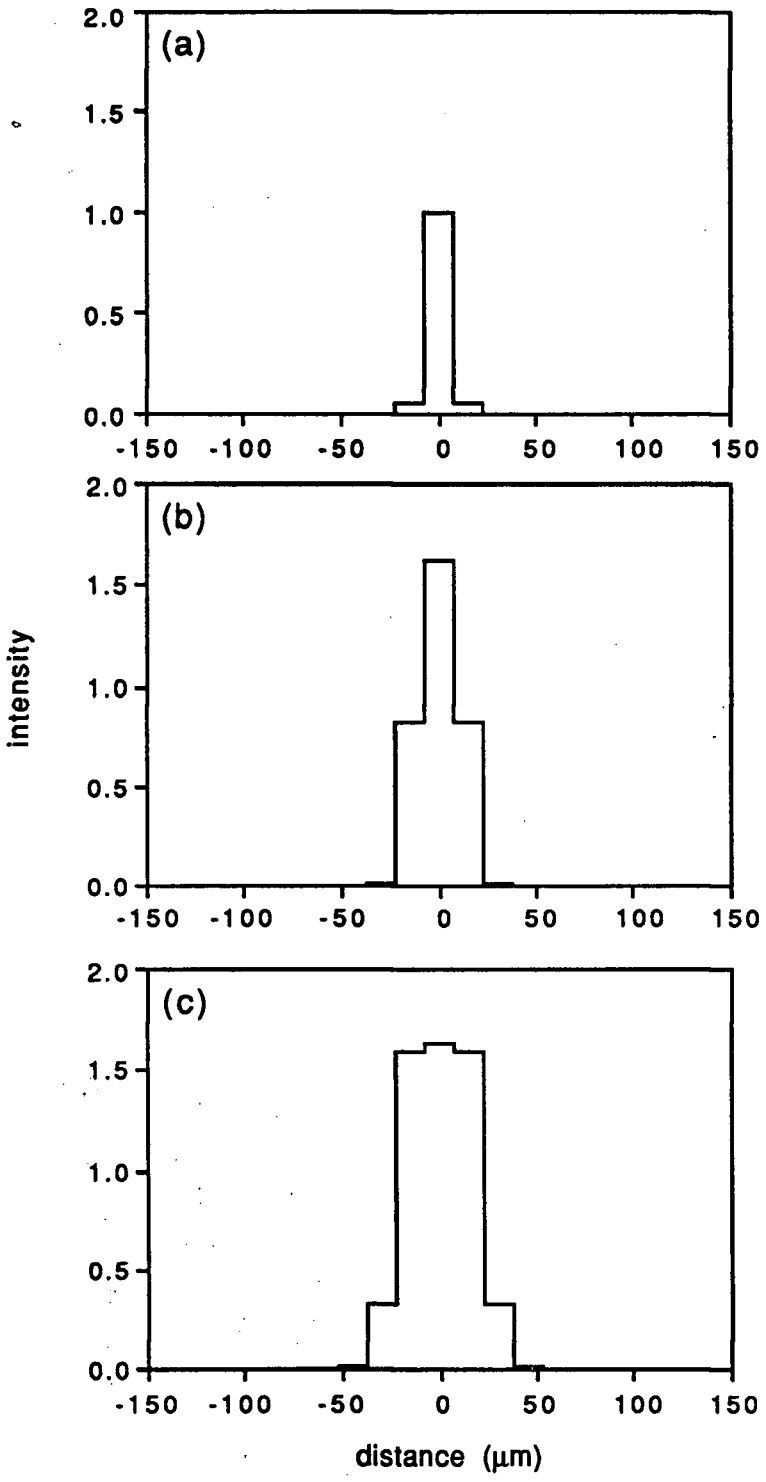

Figure 7.5 Calculated lpda response for entrance slit widths of (a) 10 μm, (b) 30 μm, and (c) 50 μm.

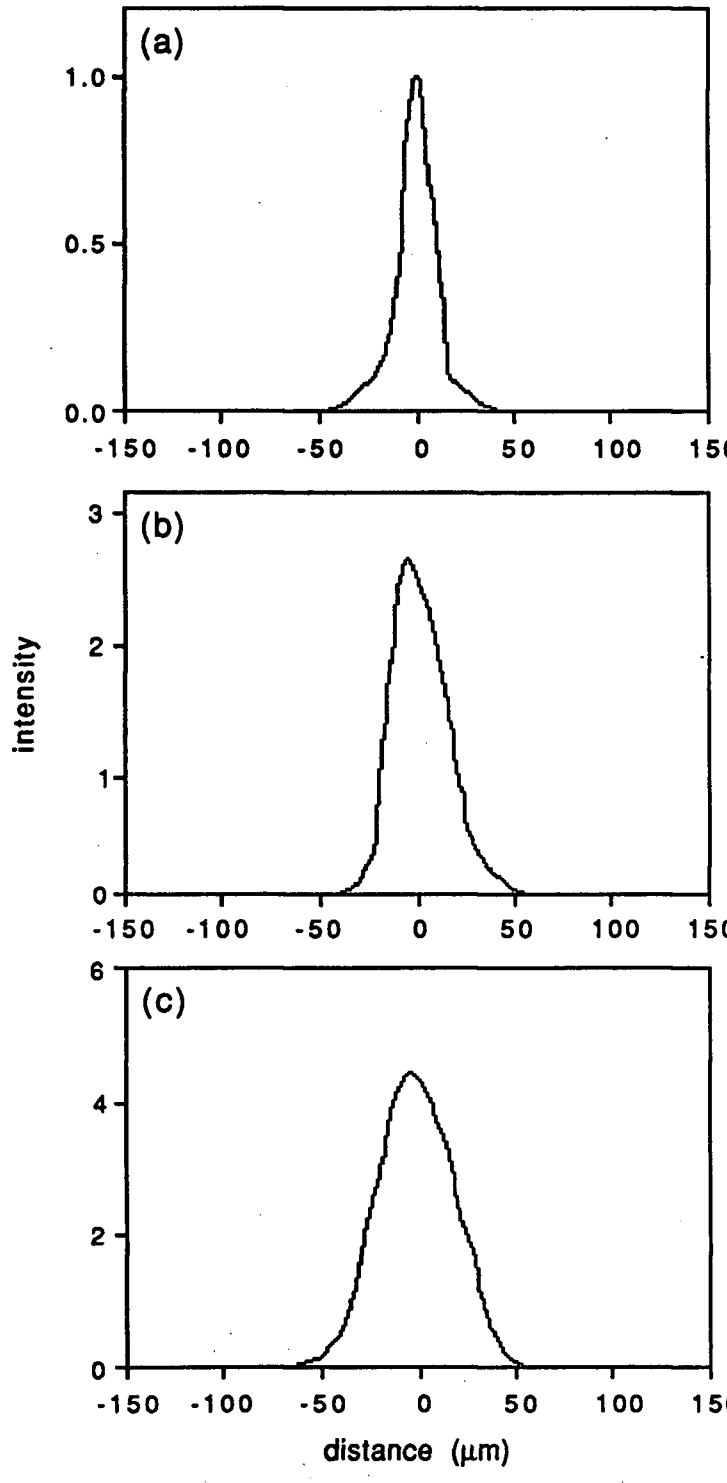

Figure 7.6 Experimental scanned pmt relative response for equal entrance and exit slit widths of (a) 10 μm, (b) 30 μm, and (c) 50 μm.

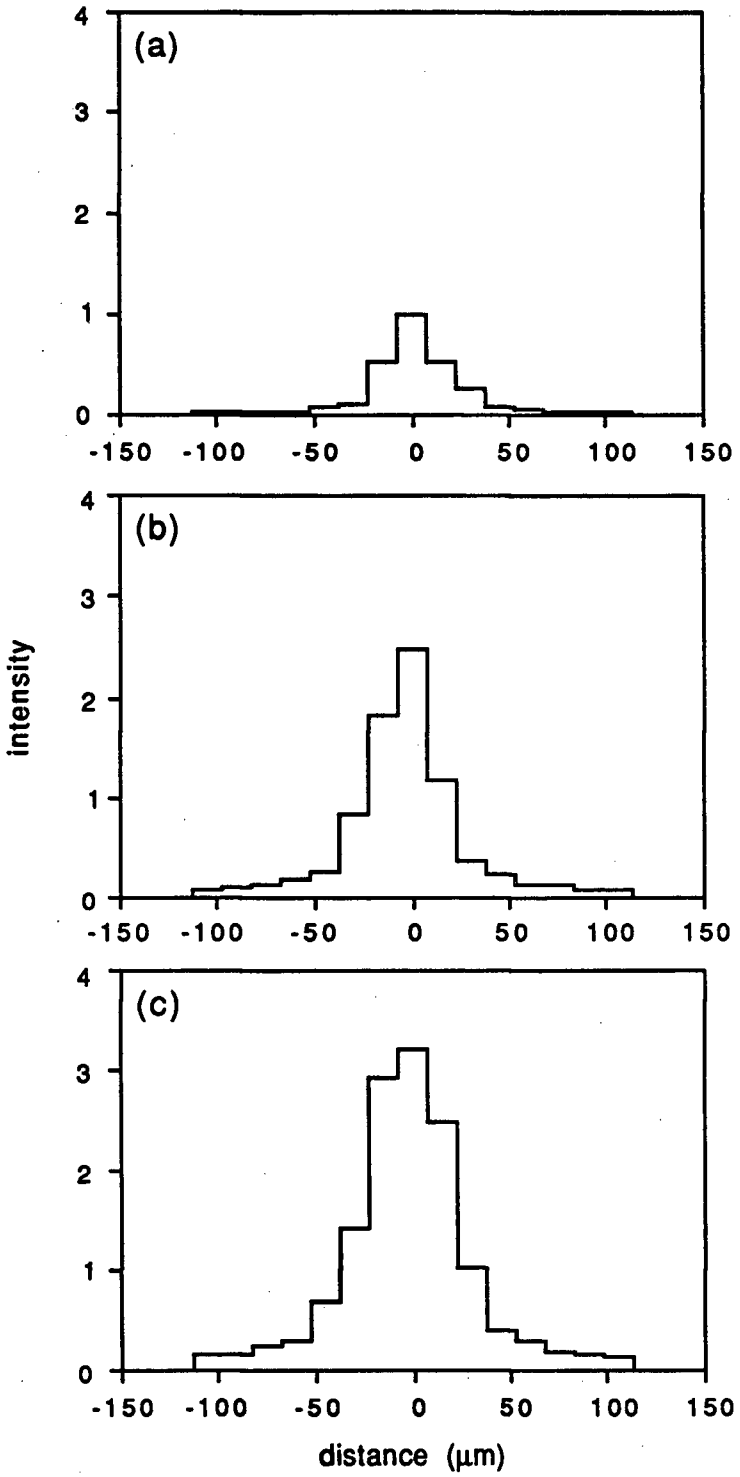

Figure 7.7 Experimental Ipda relative response for entrance slit widths of (a) 10 μm, (b) 30 μm, and (c) 50 μm.

The calculated pmt scans in figure 7.3 are all triangular, as would be expected by convoluting the rectangular pmt response function with the rectangular-like instrumental profile. The scale-expanded pmt response in figure 7.4 shows that if one had an intense spectral line in near overlap with a weaker one, then the line-wing contribution as a result of diffraction could be significant, depending on the exact wavelength difference.

One obvious difference between the calculated lpda (figure 7.5) and the scanned pmt cases (figure 7.3) is that for the scanned cases the intensity increased roughly linearly with the slit width. This is due to the fact that the exit slit was taken to be equal in width to the entrance slit; if a narrower exit slit had been used the resulting profiles would have been less intense, and would probably have been flat on top. In contrast, for the lpda case, the centre diode gradually increased in intensity as the slit width was increased until the relatively flat portion of the instrumental profile became equal to the total width integrated by a diode (23 μm).

For the lpda case the response of the centre diode will be a maximum when its centre coincides with the centre of the instrumental profile, and a minimum when the centre of the instrumental profile lies halfway between diodes. If there is a significant difference between these two responses it would be difficult to compare the relative intensities of two spectral lines.

Figure 7.8 (a) shows the effect of translating the instrumental profile 3.75 μm (one fourth the width of a diode) for an entrance slit width of 10 μm and figure 7.8 (b) shows a translation of 7.5 μm (half the width of a diode). Figure 7.9 shows the effect of

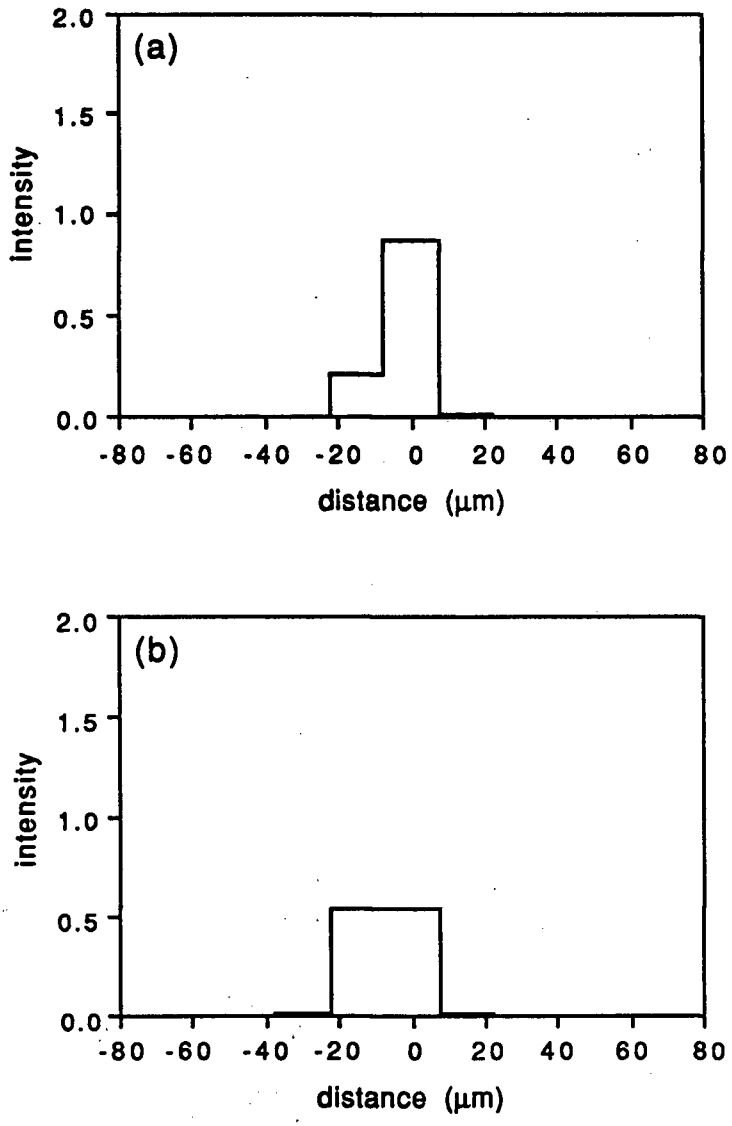

Figure 7.8 Effect of translating the calculated instrumental profile across the Ipda for an entrance slit width of 10 μm; (a) a translation of 3.75 μm, (b) a translation of 7.5 μm.

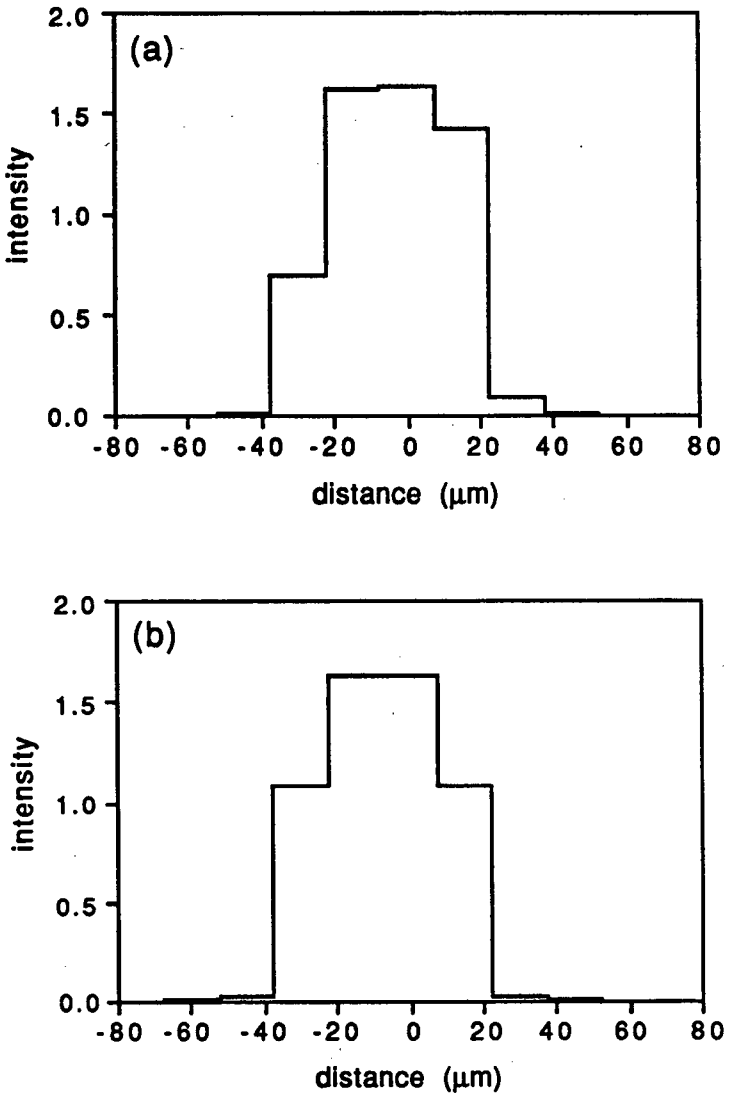

Figure 7.9 Effect of translating the calculated instrumental profile across the lpda for an entrance slit width of 50 μm; (a) a translation of 3.75 μm, (b) a translation of 7.5 μm.

identical translations for an entrance slit width of 50 μm. It can be seen that, as expected, the minimum intensity occurred when the centre of the instrumental profile was halfway between diodes. This result has recently been experimentally observed [140].

In figure 7.10 is plotted the percent of the maximum intensity when the centre of the instrumental profile lies halfway between diodes. It can be seen that the entrance slit should be at least 40 μm wide in order that the peak intensity of a spectral line remain constant regardless of where it falls on the lpda. This result of 40 μm is in agreement with our experimental result of about 45 μm. One possible way around this limitation, so that smaller slit widths may be used, is to sum the intensities from two or more adjacent diodes [140]. Effectively, rather than determining peak

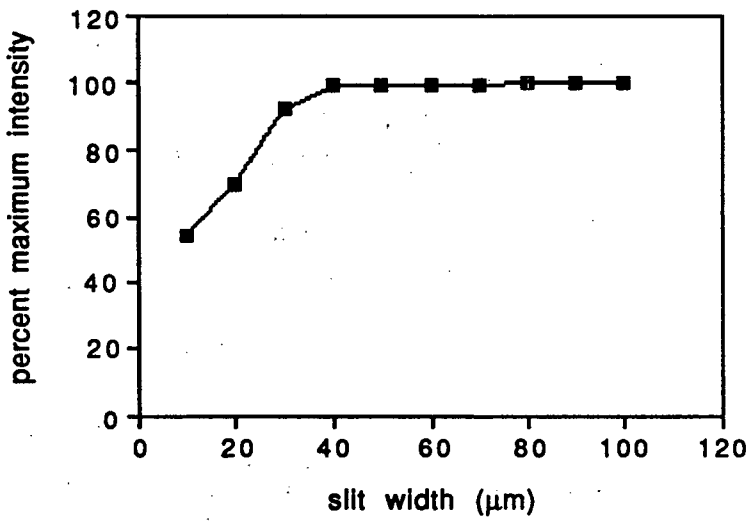

Figure 7.10 Plot of the percent maximum intensity when the calculated instrumental profile is displaced by one half of the diode width (7.5 μm) as a function of the entrance slit width.

intensities, this amounts to determining peak areas. As shown in reference [140] the area will remain constant for a given entrance slit width, regardless of where the centre of the instrumental profile falls on the lpda (this must be true because the lpda integrates all light that is incident upon it). However, diode summing suffers from the problem that it will often reduce the signal-to-noise ratio.

Experimental pmt scans and lpda data were acquired for the 546.07 nm line of mercury. Recalling the wavelength dependence of equation 7.2 one can see that there will be an error induced by carrying out the simulation at 500.0 nm. However, it was calculated that for the slit width where the error was the greatest (10 μm) the intensity of the central diode would differ by less than 0.8 %.

In figure 7.6 experimental pmt scans for the different slit widths are plotted. Except for the 10 μm case the actual intensities were almost identical to the theoretical ones: a plot of the theoretical versus experimental intensities, for slit widths of 10 to 100 μm in steps of 10 μm, gave a straight line with a correlation co-efficient of 0.9997. For the majority of slit widths the experimental scans were essentially triangular, like the calculated ones. However, for the 50 μm slit width the experimental scan was rounded on top, unlike the calculated one. This was probably due to slightly unequal entrance and exit slit widths.

Experimental lpda acquisitions for the different entrance slit widths are shown in figure 7.7. When collecting these spectra it

was attempted to make the centre of the instrumentally broadened profile fall on the centre of a diode; however the resolution of the scan controller made this difficult. By comparing the calculated and experimental lpda scans it can be seen that for the central diodes the calculated lineshapes are in qualitative agreement with the experimental ones. It can also be seen that the experimental lineshapes tended to have larger line-wings than the calculated ones. The most likely explanation for this fact is probably a lack of perfect focus onto the lpda, or perhaps to reflections off the quartz window in front of the lpda.

7.5 Summary

The instrumentally broadened profile of an atomic emission line has been used to calculate detected line profiles for two different radiation detectors: a scanned exit slit pmt combination and an lpda, for slit widths of 10, 30, and 50 μm. The instrumental profile was essentially an image of the entrance slit, with line-wing contributions coming from diffraction by the grating. The experimental pmt scans agreed quite well with the calculated profiles, and the experimental lpda acquisitions agreed with the calculated ones, at least for the central diodes. The effect of translating the instrumental profile across the lpda was investigated; it was found that for entrance slit widths less than about 40 μm the peak intensity would fluctuate considerably.

As will be seen in the next chapter, the method presented here of using the calculated instrumental line profile to derive the detected lineshape for the scanned and lpda cases will find as its major

application the spectral simulation of realistic lineshapes for complex mixtures representing real samples. As pointed out in reference [31] it is possible to simulate an emission spectrum for a given analytical line and all of its potential overlaps, based on estimated elemental composition, to aid in analytical line selection and background and inter-element correction strategies. Use of the equations presented in this chapter enables the calculation of realistic line-wing contributions to the emission spectrum which arise as a result of grating diffraction effects.

Chapter 8
Computer Simulation of Spectral Interferences In the ICP

8.1 Introduction

In recent years the optical spectra emitted by analyte atoms and ions excited in the icp have been the subject of detailed study [21-27, 88, 139]. One of the motivations for these studies is the development of effective methods for both analytical line selection and for the management of spectral line overlaps during the analysis of samples having complex composition. Spectral line overlaps can cause the analyst numerous problems; they can significantly increase detection limits and degrade the accuracy of an analytical determination. Therefore, when complex mixtures are analyzed, one must be aware of potential spectral overlaps - both direct and those due to line wings. Thus Boumans and Vrakking [27] stress that the trace and ultra-trace analysis of samples which emit line-rich spectra continues to be a major challenge in icp spectroscopy.

To provide the analyst with spectroscopic data which can be used to enable the judicious choice of analytical lines and background correction strategies, several authors have published spectral line sensitivity and spectral line coincidence tables [5, 19, 47, 111], and reproductions of actual spectral scans [141, 142]. The line coincidence tables of Boumans [19], for example, list 896 of the prominent analytical lines for 67 elements and identify potential spectral overlaps for each line. These overlaps are quantitatively expressed by a "critical concentration ratio" which is listed for a

variety of spectral bandpass values covering the range 0.01 to 0.04 nm. The listings of lines in these tables was based on the prominent lines published by Winge et al. [143] and line interference information derived from the NBS tables of Meggers et al. [92]. Boumans applied a series of "transfer factors" to convert lines sensitivities from the NBS tables to values more consistent with icp excitation conditions.

An alternative spectral data base for the icp has been provided by Winge et al. [141]. This publication contains 232 individual, experimentally obtained, wavelength scans for 70 elements. While the empirical approach used for that work can be expected to provide more "realistic" data for the icp, complete compilations are a near impossibility because of the almost infinite variety of operating conditions and sample types.

The method for generating spectral line intensity and spectral line overlap information reported in this chapter is based on an a priori approach. The information published in spectral line tables can be used to assess potential spectral overlaps, however, in many cases, it would be useful to have a visual picture of a spectral region surrounding an analytical line. In situations where the amount of sample is limited, or when the analyst would like to evaluate a number of analytical lines to allow a judicious choice for the determination, it is not always feasible to acquire actual experimental data. In these cases it would be useful to approximate icp spectra using a model; to this end we have developed a method which will simulate reasonably realistic icp emission spectra. Initially spectral simulation software developed at the NASA Ames

Research Centre [6] was used to produce synthetic analyte emission spectra. However, as will be described below, this software was found to be unsatisfactory and our own program was written.

The method of simulating icp spectra described here combines the results of icp fundamental studies [15, 16, 34-36, 131], that is to say information regarding the physical properties of the icp, with fundamental atomic and ionic data such as oscillator strengths, partition functions, etc. In developing this approach the intent was to make the method sufficiently flexible so that synthetic spectra could be generated for any combination of the instrumental operating conditions and sample composition - a major advantage over spectral coincidence tables.

The purpose of this chapter is to describe the simulation program and to show how it can be used to study spectral overlaps in complex multi-element mixtures. As an example, the problem of analyzing for silver in two representative sample types (a soil type sample and coal fly ash) is examined. The material in this chapter has been previously published in references [29] and [31].

8.2 Method

In a previous publication [31] on computer simulation of analyte emission spectra, a computer program written by Arnold et al. [6] was used. This program allowed the use of a Gaussian instrumental lineshape; however this resulted in a lack of any significant line wings. For the majority of the work presented in this chapter we have developed our own program which has a much more realistic instrumental profile (described in detail in the previous chapter), is

more appropriate for the simulation of icp spectra, is more "user friendly", and allows for a greater ease of use.

A flowchart showing the logical flow of the simulation program is provided in figure 8.1. Each step will be briefly described below. The first step is to decide which elements are present in the sample to be simulated, and their likely concentrations. For the results presented in this chapter of a "typical" silver rich soil sample the concentrations were loosely taken from Levinson [81], and for the NBS coal fly ash (NBS-1633a) they were taken from the NBS catalogue [122]. For an actual analysis of an unknown sample the analyst would have to estimate concentrations based upon knowledge of the potential composition of such a sample. Even though the concentrations would only be approximations they would likely be good enough to allow the simulation to predict which analytical line would give the best detection limit.

Once the concentrations were decided upon and a particular analytical line was chosen, the spectral line coincidence tables of Boumans [19] were used to obtain a list of the spectral lines which could cause spectral interferences. For each of these lines the following data was then entered into the program:

(1) Total species concentration (atom or ion) in plasma (n_I or n_{II})

(2) Atomic weight of species (AW)

(3) Wavelength of the transition (λ)

(4) Excitation energy of the transition (E)

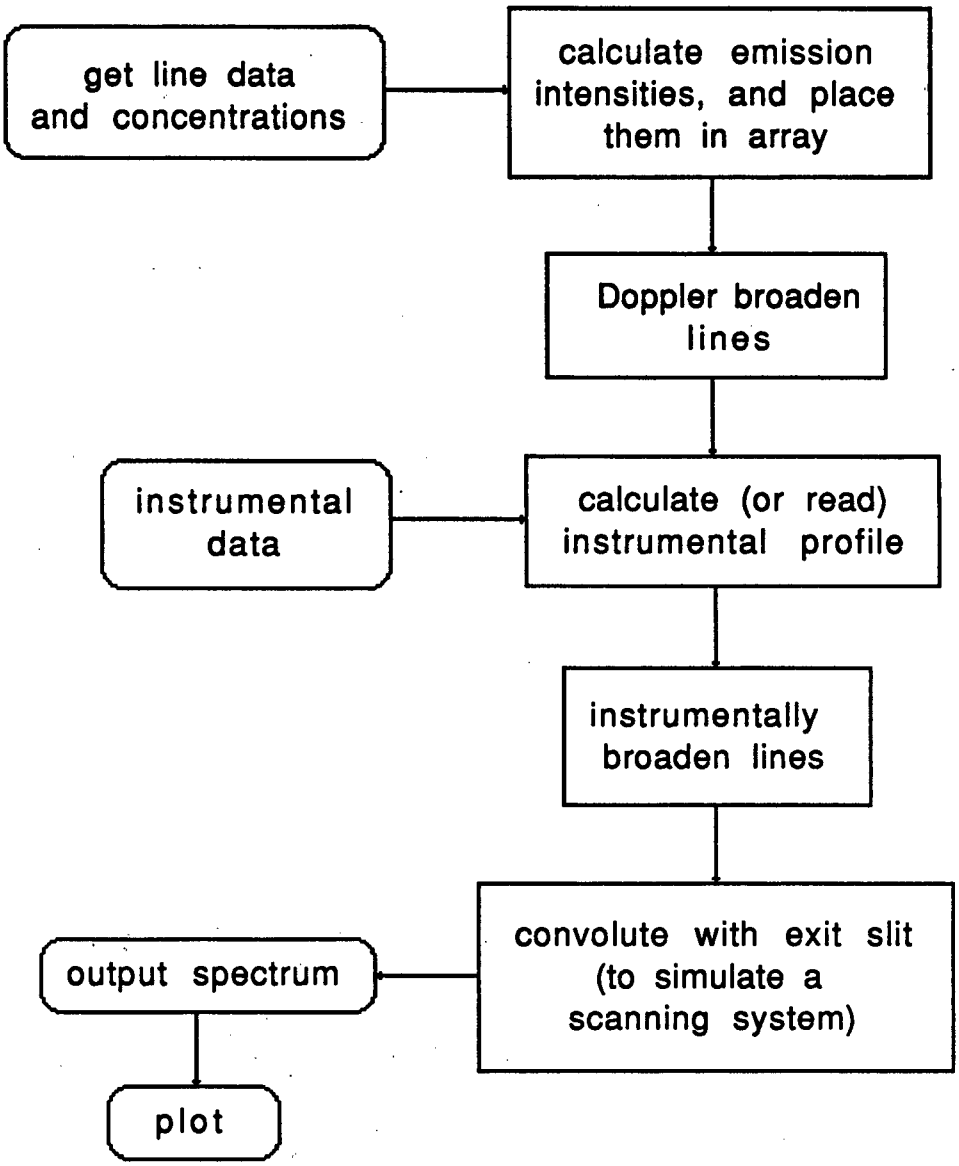

Figure 8.1 Flowchart showing the logic of the spectral simulation program.

(5) Degeneracy weighted transition probability of the transition (gA)

(6) Temperature (T=7500 K)

(7) Partition function of species (Q(T)).

The total species concentration in the plasma is calculated from:

$$n_I \alpha\ C(1-\gamma)/AW \qquad (8.1)$$

$$n_{II} \alpha\ C\gamma/AW \qquad (8.2)$$

where C is the solution concentration (in μg/mL) and γ is the degree of ionization, based on the empirical measurements of Caughlin and Blades [34]. These authors measured the functional dependence of γ on the ionization energy of a variety of analyte elements. From this data it has been found that γ can be estimated with reasonable accuracy for any element with an ionization potential between 5 and 9.5 eV.

The wavelengths are listed in the line coincidence tables [19], and E and gA were determined from Corliss and Bozman [38]. However, the gA values for some transitions were not listed in this reference. In these cases, since all of the lines in the line coincidence tables are tabulated in the *NBS Tables of Spectral Line Intensities* [92], we used the tabulated intensity for lines whose transition probability we did know to estimate one. For each element for which a transition probability was needed, a Boltzmann plot of ln (Iλ/gA) against E (where I is intensity) was constructed for those lines for which transition probabilities were tabulated; this gave a straight line (since the NBS source was in local

thermodynamic equilibrium). From this plot we could estimate unknown gA values since I, λ, and E (all in reference [92]) were known.

The partition functions for the main group elements were computed from the polynomial functions published by de Galan et al. [49], and for the lanthanide elements from the extension by Faggetter et al. [45]. Since a complete set of energy levels were not available for the actinide elements the partition functions for these elements were calculated from the limited energy level tabulation in reference [113].

Referring back to figure 8.1 the next step was to calculate the emission intensity for each line according to:

$$I \alpha \frac{gA}{\lambda \cdot Q(T)} e^{-E/kT} \qquad (8.3)$$

where k is the Boltzmann constant. Since the icp discharge is not in local thermodynamic equilibrium, equation (8.3) is not strictly valid. Since the deviation of level populations from lte values is only known for a few elements it was not practical at this time to take them into account*. However, since the degree of ionization is based on experimental measurements at the chosen temperature of 7500 K, the use of equation (8.3) should not result in excessively large errors. After the wavelength interval for the simulation was entered, the intensities were put into an array and Doppler broadened.

* This was true at the time reference [29] was published; see chapters three and four for a discussion of this.

The instrumental data input into the program was:

(1) the entrance and exit slit widths (s and s')

(2) the monochromator aperture width (D)

(3) the monochromator focal length (f)

(4) the reciprocal linear dispersion of the monochromator ($d\lambda/dx$).

For the simulations presented in the next section f = 1 m, $d\lambda/dx$ = 0.833 nm/mm, D =140 mm were chosen and s and s' were varied to change the spectral bandpass, keeping s = s'. These values are typical of a one-metre monochromator with a 1200 grove/mm grating installed. From this data the instrumental profile was calculated as described in the previous chapter and the Doppler broadened spectral lines were convoluted with the instrumental profile.

The difference between a Gaussian line profile and the diffraction limited line profile (described in detail in the previous chapter) is outlined in figure 8.2. Figure 8.2 (a) is a Gaussian profile and figure 8.2 (b) is the "diffraction" profile used for the simulations reported in this chapter. The inner plots show the profiles with no scale expansion, and the outer ones are with an expansion of 10 000 times. One can see that at positions near the line centre the Gaussian profile approximates the diffraction profile quite well. However, at positions farther away from the line centre the Gaussian profile has almost no line wings, whereas the diffraction profile has significant line wings.

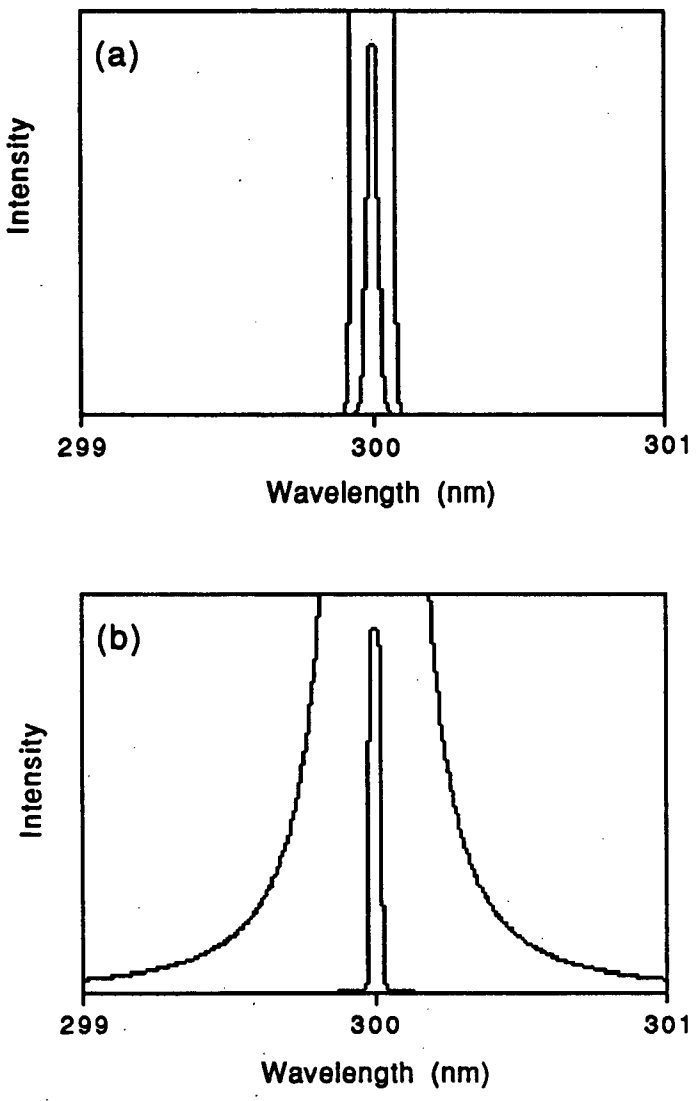

Figure 8.2 Comparison of Gaussian (a) and "diffraction" (b) instrumental profiles. The inner plots are with no scale expansion, and the outer ones are with a scale expansion of 10 000 times.

In the above discussion it was assumed that only Doppler and instrumental broadening contribute to any significant extent to the detected line shape. This is true for medium resolution spectrometers such as we were interested in, but is not the case for high resolution spectrometers, where the physical lineshapes must be taken into account.

In the final step of the program the spectrum was convoluted with the exit slit, as described in the previous chapter, and plotted.

8.3 Experimental

Preliminary computations using the NASA program were performed on a Compupro (Viasyn, Hayward, CA) System 816 computer equipped with a 68000 CPU, 1 MByte RAM, a 1.2 MByte 8 inch floppy disk drive and a 40 MByte Winchester disk drive.

All other spectral simulation computations (using our own program) were performed on a Telex (Tulsa, OK) 1280 (IBM-AT compatible) computer equipped with 1.1 MByte RAM, a 20 MByte hard disk drive, and dual 5 inch floppy disk drives. The simulation program was written in Borland's (Scotts Valley, CA) Turbo Pascal version 3.01A. The compiled program occupies about 41 KBytes of memory and the total execution time is about 2 minutes when using a previously stored instrumental profile. The resulting spectra were then transferred to an Apple (Cupertino, CA) Macintosh$^+$ and plotted using Wavemetrics' (Lake Oswego, OR) "Igor" - a data analysis and plotting program.

The experimental set-up used for the collection of the experimental wavelength scans presented in this chapter is

described in detail in chapter two of this thesis. The gas flows used were: plasma gas - 12 L/min, intermediate gas - 0 L/min, and aerosol gas - 0.9 L /min. The observation height was 14 mm above the load coil and the rf power used was 1.25 kW.

8.4 Results

8.4.1 Simulation of Single Element Spectra - Iron

In order to test the accuracy of simulating the spectrum of a single element emitting over a relatively broad spectral region, iron was chosen as a test element. Over this broad spectral range, the fact that the NASA program gave unrealistic line wings was not important (since we were not interested in observing the effects of line wing interferences), and thus the original results using this program are presented here. To generate simulated iron spectra, all of the Fe I and Fe II lines listed by Corliss and Bozman [38] in the 240 - 280 nm and the 360 - 400 nm spectral regions were used as input to the program. This listing was used because it contains the most comprehensive single listing of gA values for Fe I and Fe II available. The degree of ionization was set at 0.930. For the 240 - 280 nm simulation an equilibrium temperature of 7500 K was used. This value is consistent with the measurements of Walker and Blades [131] since the majority of the emission lines in this region originate from Fe II and high energy Fe I species. For the 360 - 400 nm simulation an equilibrium temperature of 5500 K was used. This value is also consistent with the measurements of Walker and Blades since the majority of emission lines in this spectral region originate from low energy Fe I levels. These conditions are

representative of an icp operating at 1.25 kW with an aerosol gas flow of 0.9 L/min viewed at 14 mm above the load coil.

The plot shown in figure 8.3 (a) is a simulated iron emission spectrum over the wavelength range 240 - 280 nm, while that shown in figure 8.3 (b) is over the range 360 - 400 nm. The transition wavelengths are tabulated directly on the figure. An advantage of simulated spectra over actual recorded spectra is that the identification of lines is unambiguous. The wavelength of each transition is input directly to the program and confusing spectral overlaps can be deconvoluted by selectively removing lines from the simulation. In addition, the spectrum of each ionization stage can be generated independently so that a "pure" Fe I or Fe II spectrum can be studied. In contrast, it is not possible to experimentally acquire a "pure" Fe I or Fe II spectrum. This makes line identification on a comparative basis a relatively simple matter.

In order to test the accuracy of the simulation an actual Fe emission spectrum was recorded using the photodiode array spectrometer. In figure 8.4 (a) is presented the simulation from 240 - 280 nm (without the wavelength tabulation) and in figure 8.4 (b) the experimental spectrum over the same wavelength range. The majority of the lines in figure 8.4 are due to Fe II emission, although there is a group of weak lines of Fe I between 242 and 255 nm. A comparison of the simulated spectrum with the experimental one clearly demonstrates that, on the whole, the simulation is reasonably accurate. The spectral patterns are quite similar both with respect to wavelength and relative intensity. For the most part the relative intensities between analogous peaks are

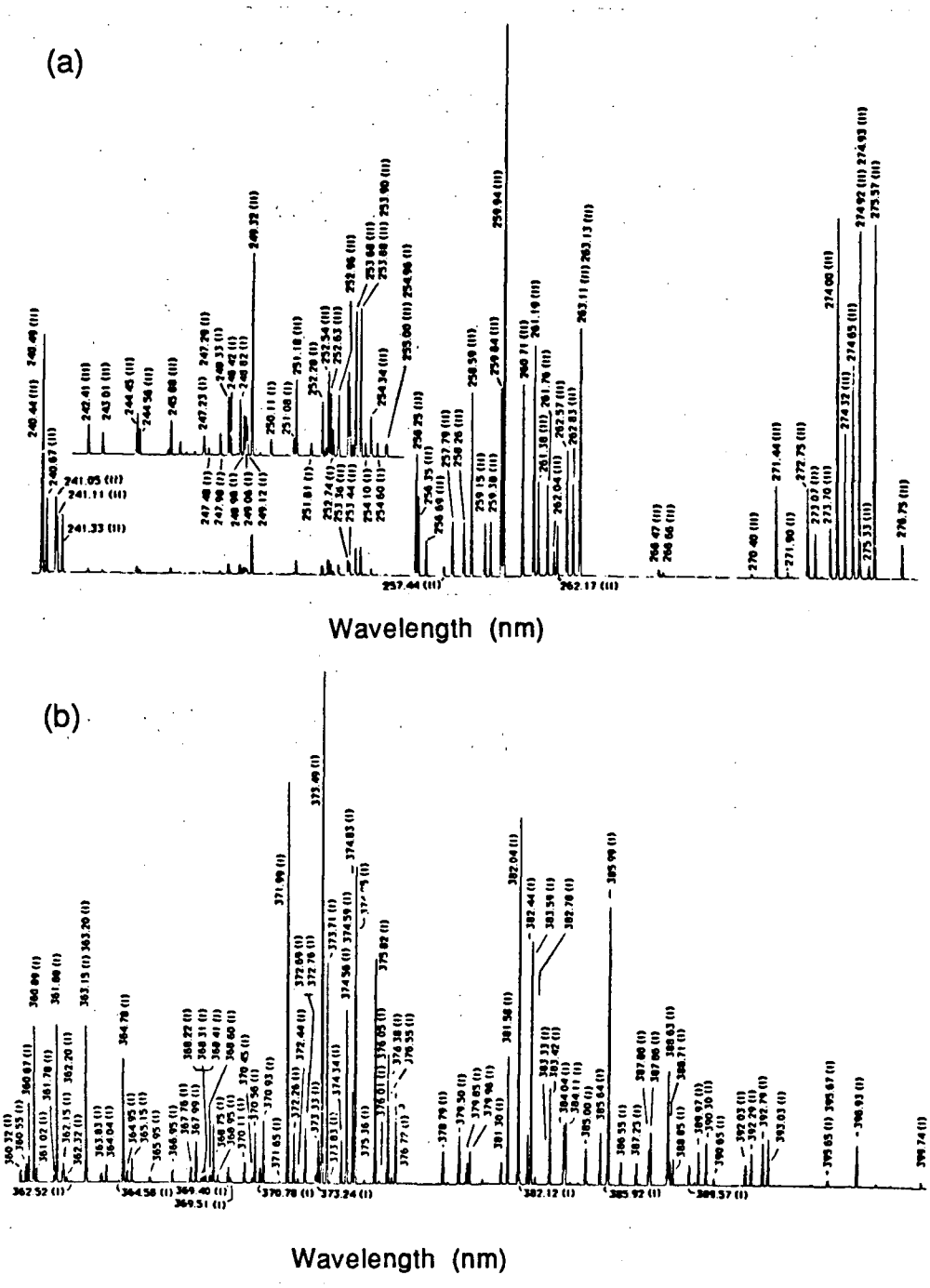

Figure 8.3 Computer simulated iron emission spectra; (a) over the wavelength range 240 to 280 nm, (b) 360 to 400 nm. Wavelengths are tabulated in nm. Inset from 242 to 255 nm was recorded at five times the gain as the remainder of the spectrum.

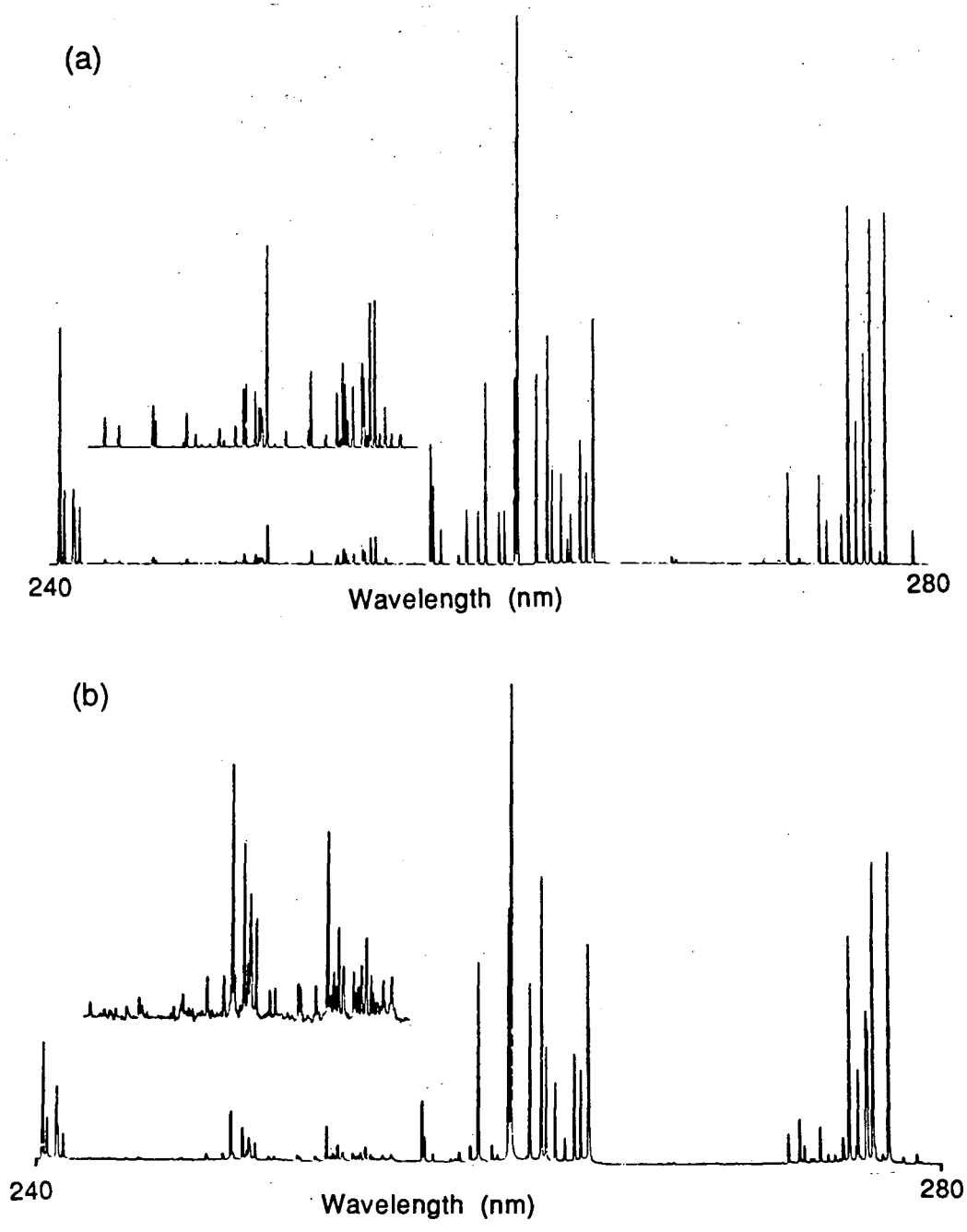

Figure 8.4 A comparison between a simulated iron spectrum over the wavelength range 240 to 280 nm (a) and an experimental spectrum over the same range (b). The insets from 242 to 255 nm were recorded at five times the gain as the remainder of the spectra.

within a factor of five. It is felt that these differences are probably due to inaccuracies in the gA values used for the simulation. It should be possible to improve the simulation by adjusting the gA values for lines for which the gA value is known to be of low accuracy to bring the simulation in line with experimental intensities by referencing to the intensities for lines which have gA values which are more accurate. The simulation could then be tested at a variety of temperatures and compared to experimental results at a variety of rf powers to optimize the fit.

A comparison of the relative intensities of the Fe I lines to those of the Fe II lines indicates that the degree of ionization used for the simulation (0.930) probably over-estimates the actual degree of ionization slightly. For example, the intense Fe I triplet at 249 nm is about a factor of four lower than the 249.32 nm Fe II line in the simulation. In contrast, the lines are approximately the same intensity in the experimental spectrum.

The plot provided in figure 8.5 shows a comparison between a simulated iron emission spectrum over the wavelength range 360 - 400 nm (a) and an experimental iron spectrum over the same wavelength range (b). All of the strong transitions in this region are due to Fe I species. The agreement between the line intensities in figures 8.5 (a) and (b) is very good indeed for both the intense and the weak lines.

8.4.2 Spectral Simulation of Complex Mixtures - Ag Analysis

Table V lists the elements and their concentration which are potential overlaps for the 338.29 nm line of silver in a "typical"

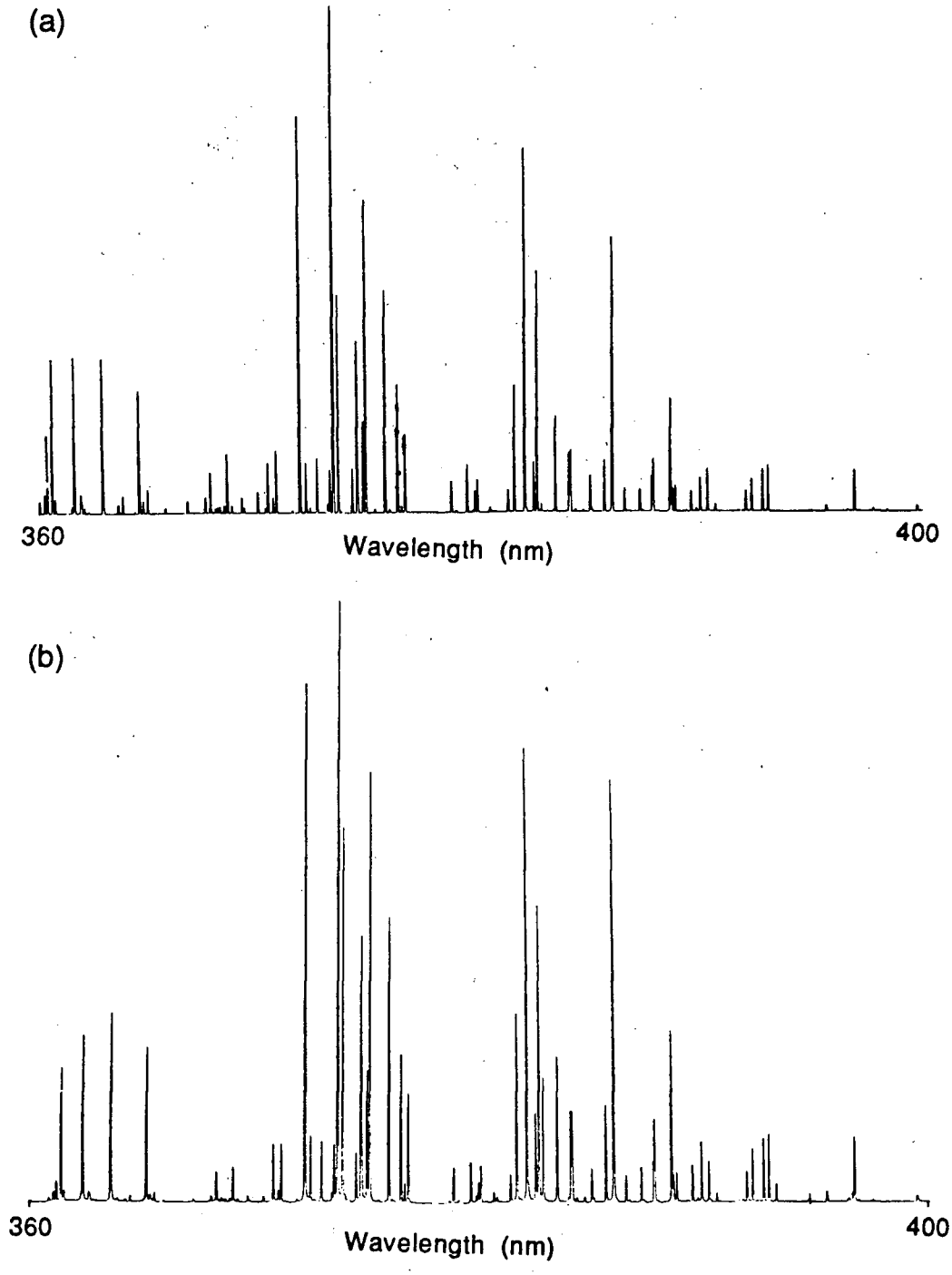

Figure 8.5 A comparison between a simulated iron spectrum over the wavelength range 360 to 400 nm (a) and an experimental spectrum over the same range (b).

Table V: Solution concentrations, wavelengths, partition functions, upper energy levels, transition probabilities, and degrees of ionization for the spectral lines occurring in the simulation of the 338.29 nm line of silver in the geochemical matrix.

	Element	Conc. (μg/mL)	Wavelength (nm)	Partition Function	Energy (1/cm)	gA (10^8/s)	γ (%)
a	Ni II	50	338.06	35	32982	6.1	99.4
b	Sr II	500	338.07	2.7	53286	1.4	99.6
c	La II	10	338.09	40.4	32161	2.6	99.7
d	Mo I	2	338.23	16	41012	0.61	97.0
e	Ti I	5000	338.23	49.2	38160	4.1	97.6
f	Mo I	2	338.25	16	40699	2.8	97.0
g	Cr II	25	338.27	10.3	49352	14	97.6
h	Ag I	varies	338.29	2	29552	1.3	94.6
i	Sb I	5	338.31	5.9	45945	1.0	88.2
j	Ti II	5000	338.38	68.4	29544	9.2	97.6
k	Fe I	50000	338.40	39	47093	9.1	93.0
l	Hf II	0.5	338.41	20.1	43901	3.9	97.3
m	Mo I	2	338.46	16.2	41396	2.0	97.0
n	Hf II	0.5	338.47	20.1	33181	0.30	97.3
o	Co I	10	338.52	44.9	33674	1.7	93.0

silver rich geochemical matrix. The concentrations were estimated from the work of Levinson [81]. The table also provides the wavelengths, upper energies, and transition probabilities for each interfering line, along with the partition function and degree of ionization (γ) for the elements. The temperature used in calculating the partition functions and in evaluating the spectral intensity from equation (8.3) was 7500 K. This temperature along with the degree of ionization used in equations (8.1) and (8.2) apply to the analytical zone (12 to 16 mm above the load coil) for an icp operating at 1.25 kW.

Figure 8.6 shows a simulation using a spectral bandpass of 0.04 nm and the NASA spectral simulation program. Figure 8.6 (a) is plotted with a linear intensity scale and figure 8.6 (b) is plotted with a logarithmic intensity scale. It can be seen that the lack of any significant line wings (especially for the intense lines) in these plots, due to the fact that a Gaussian instrumental profile was used, causes the accuracy of the simulation to be questionable. For all other spectral simulations presented in this chapter, with the exception of figure 8.7, our own program (with the instrumental lineshape described in the previous chapter) will be used.

In order to investigate the accuracy of the simulation, actual emission spectra were acquired for Mo, Ag, Hf, and Co in the same concentration ratios as those listed in Table V. Figure 8.7 (a) is the synthetic spectrum and figure 8.7 (b) is the experimental spectrum. A comparison of the relative intensities of the lines in figure 8.7 shows that the agreement is within a factor of five for all of the lines. The intensities of the molybdenum lines relative to each

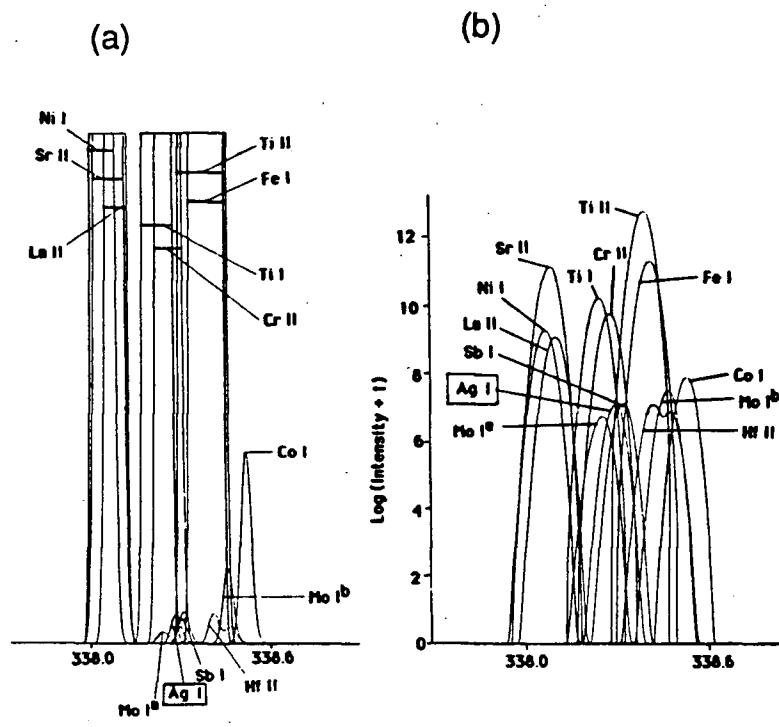

Figure 8.6 Computer simulation of a multi-element mixture. Wavelength range is 338.0 to 338.6 nm at a spectral bandpass of 0.04 nm; (a) linear scale, (b) logarithmic scale. The spectral lines used are given in Table V.

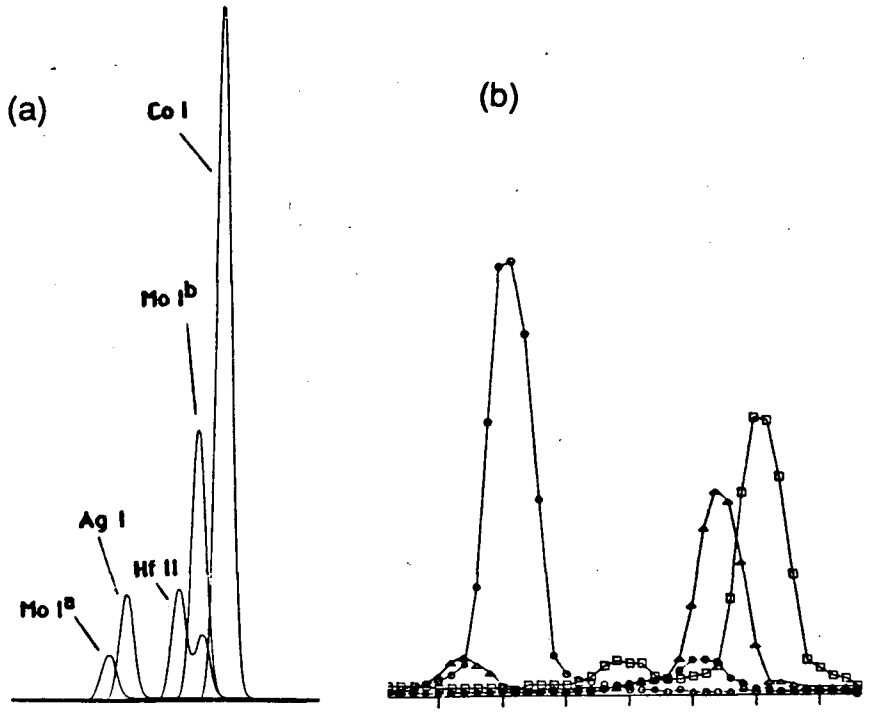

Figure 8.7 Computer simulation (a) and experimental spectrum (b) of Ag (o), Co (□), Mo(Δ), and Hf(●) in the wavelength range 338.0 to 338.6 nm. The spectral lines used are given in Table V.

other are quite accurate. The silver line appears to be too intense relative to the cobalt line; however the ratio of cobalt to molybdenum is close. The small peak at 338.4 nm is due to an impurity in the cobalt solution and is probably either the 338.376 nm Ti II line or the 338.398 nm Fe I line or both. We expect that the simulation could be made considerably more exact if there was a better understanding of how the degree of ionization varies for the different elements in the icp. When elements are as highly ionized as they are in the icp small changes in the degree of ionization can cause major changes to the atom line intensities. In addition, for these weak lines, the gA values are not known to a high degree of accuracy.

Figures 8.8 and 8.9 are the results for a series of simulations of the silver 338.29 nm line based on the data in Table V showing the effect of instrumental bandpass (using our own spectral simulation program). In each of these plots the silver is at a concentration of 10 parts per million (by weight). Figure 8.8 (a) is the spectrum obtained with no instrumental broadening, figure 8.8 (b) is for an instrumental bandpass of 0.005 nm, figure 8.9 (a) is for a bandpass of 0.01 nm, and figure 8.9 (b) is for a bandpass of 0.04 nm. In this and all subsequent plots the maximum intensity is equal to 1.0 arbitrary units.

From figure 8.8 (a) one can see that lines from Ti I, Cr II, Ti II, and Fe I will be the major interferents of the silver line. Since the intensity scale in the figure runs from 0 to 0.001 it can be seen that one of the lines (Fe I 338.40 nm) has an intensity of more than 1000 times that of the silver line. In figure 8.8 (b) the silver line

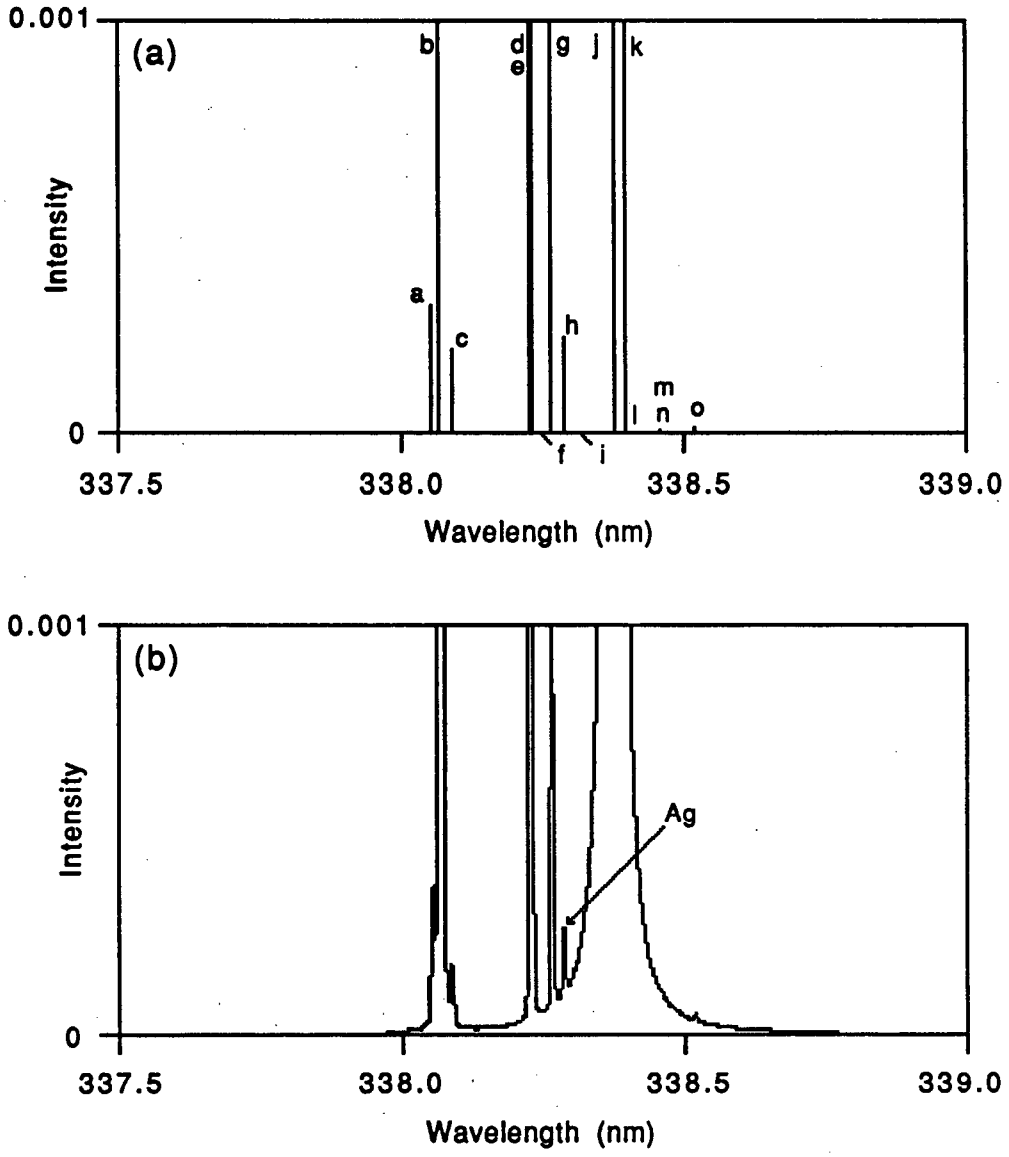

Figure 8.8 Simulation of the silver 338.92 nm line at a concentration of 10 ppm in a silver rich geochemical matrix showing the effect of instrumental bandpass; (a) with no instrumental broadening, and (b) with a 0.005 nm spectral bandpass. The lines are identified by the letters given in Table V.

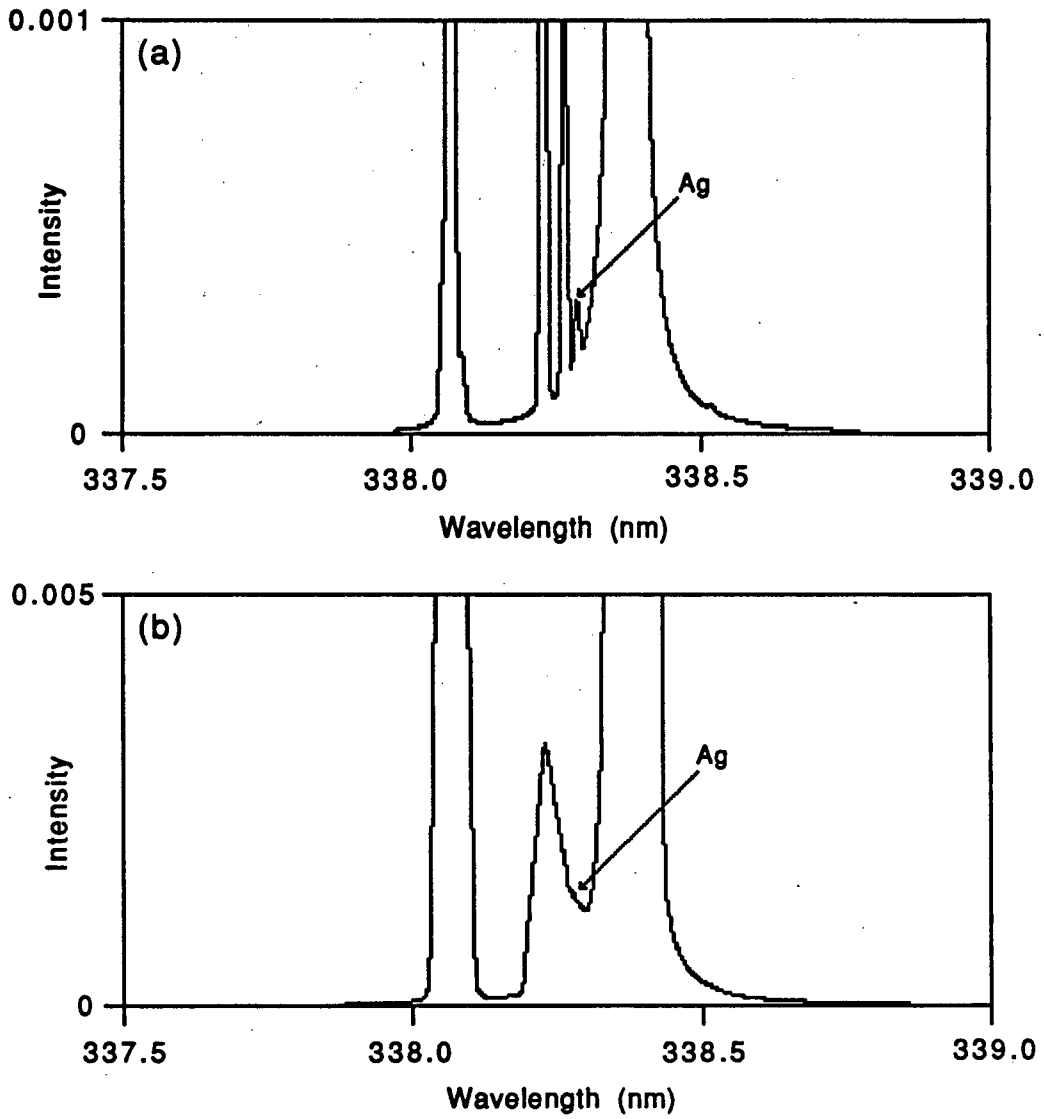

Figure 8.9 Simulation of the silver 338.92 nm line at a concentration of 10 ppm in a silver rich geochemical matrix showing the effect of instrumental bandpass; (a) with a 0.01 nm spectral bandpass, and (b) with a 0.04 nm spectral bandpass.

appears to be reasonably well resolved from the interfering lines, and in figure 8.9 (a) the silver line is just resolved. In figure 8.9 (b) it can be seen that the silver line is not resolved at all. The simulation has told us that in this ideal case with no noise, for this particular matrix, with a silver concentration of 10 ppm, we would need a spectral bandpass of at most about 0.01 nm (which corresponds to an entrance slit width of 12 μm for our one metre spectrometer) to achieve reasonable resolution of this line from the matrix lines. This points out one other use of the simulation program - to compare spectrometers with different focal lengths, dispersions, and aperture sizes with each other with respect to their ability to resolve spectral lines.

The next simulations are concerned with a silver determination in NBS coal fly ash. This matrix was chosen due to its complex nature and silver was chosen as the test element since there are only two commonly used analytical lines of silver, and there are enough data to simulate them both.

Table VI lists the elements and their concentrations which are potential overlaps of the 338.29 nm line of silver in NBS coal fly ash, and Table VII lists the potential overlaps of the 328.07 nm line. The tables also show the wavelengths, upper energies, transition probabilities, partition functions, and degrees of ionization (γ) input into the simulation program.

Figures 8.10 and 8.11 consist of a series of simulations of the 338.29 nm line of silver, based on the data in Table VI, for a spectral bandpass of 0.01 nm. Figure 8.10 (a) is the spectrum with no instrumental broadening. From this plot one can see the large

Table VI: Solution concentrations, wavelengths, partition functions, upper energy levels, transition probabilities, and degrees of ionization for the spectral lines occurring in the simulation of the 338.29 nm line of silver in NBS coal fly ash.

	Element	Conc. (μg/mL)	Wavelength (nm)	Partition Function	Energy (1/cm)	gA (10^8/s)	γ (%)
a	Ni II	127	338.06	35	32982	6.1	94.5
b	Sr II	830.	338.07	2.7	53286	1.4	99.7
c	Th II	24.7	338.13	59	44890	1.9	99.3
d	Th I	24.7	338.14	59	39151	0.93	99.3
e	Ce II	11	338.15	339.2	36202	2.3	99.8
f	U II	10.2	338.19	106	29569	0.14	99.4
g	Mo I	29	338.23	16	41012	0.61	96.8
h	Ti I	0.8%	338.23	49.2	38160	4.1	97.7
i	Mo I	29	338.25	16	40699	2.8	96.8
j	Cr II	196	338.27	10.3	49352	14	97.9
k	U II	10.2	338.27	106	30469	0.063	99.4
l	Ag I	varies	338.29	2.0	29552	1.3	94.8
m	Sb I	7	338.31	5.9	45945	1.0	88.6
n	Th II	24.7	338.31	59.4	6368	5.2	99.3
o	Ce II	11	338.37	339.2	33811	2.4	99.8
p	Ti II	0.8%	338.38	68.4	29544	9.2	97.7
q	Fe I	9.4%	338.40	39	47093	9.1	93.3
r	Hf II	7.6	338.41	20.1	43901	3.9	98.2
s	Mo I	29	338.46	16.2	41396	2.0	96.8
t	Hf II	7.6	338.47	20.1	33181	0.30	98.2
u	Co I	46	338.52	344.9	3674	1.7	93.4

Table VII: Solution concentrations, wavelengths, partition functions, upper energy levels, transition probabilities, and degrees of ionization for the spectral lines occurring in the simulation of the 328.07 nm line of silver in NBS coal fly ash.

Element	Conc. (μg/mL)	Wavelength (nm)	Partition Function	Energy (1/cm)	gA (10^8/s)	γ (%)
Ti II	0.8%	327.83	68.4	40426	6.8	97.7
Ti II	0.8%	327.89	68.4	39233	6.3	97.7
Cu I	118	327.98	3.0	43726	0.13	94.1
Ce II	180	327.98	339.2	32863	1.8	99.8
V II	45.2	327.98	60.2	49593	58	97.9
Hf II	7.6	328.00	20.1	34124	0.44	98.2
U II	10.2	328.00	106	31393	0.21	99.4
Th II	24.7	328.04	59	38494	1.8	99.3
Ce II	180.	328.05	339.2	34934	1.2	99.8
Ag I	varies	328.07	2.0	30473	3.3	94.8
Ce II	180.	328.11	339.2	37531	1.4	99.8
Ti II	0.8%	328.23	68.4	40330	7.0	97.7
V II	300.	328.25	60.2	49568	29	97.9

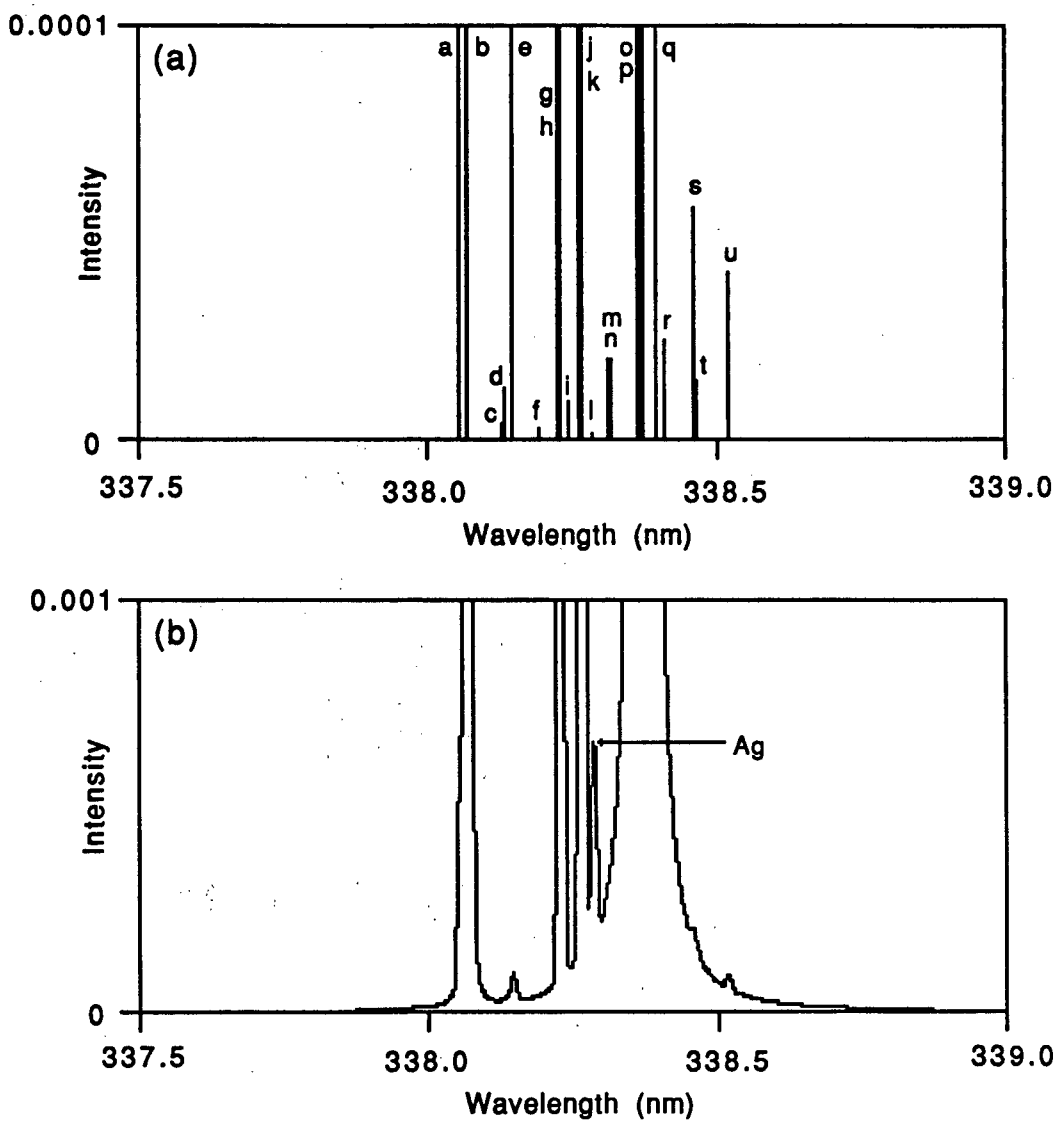

Figure 8.10 Simulation of the silver 338.92 nm line in NBS coal fly ash at a 0.01 nm instrumental bandpass showing the effect of the silver concentration; (a) with no instrumental broadening and 10 ppm silver, and (b) with 50 ppm silver. The lines are identified by the letters given in Table VI.

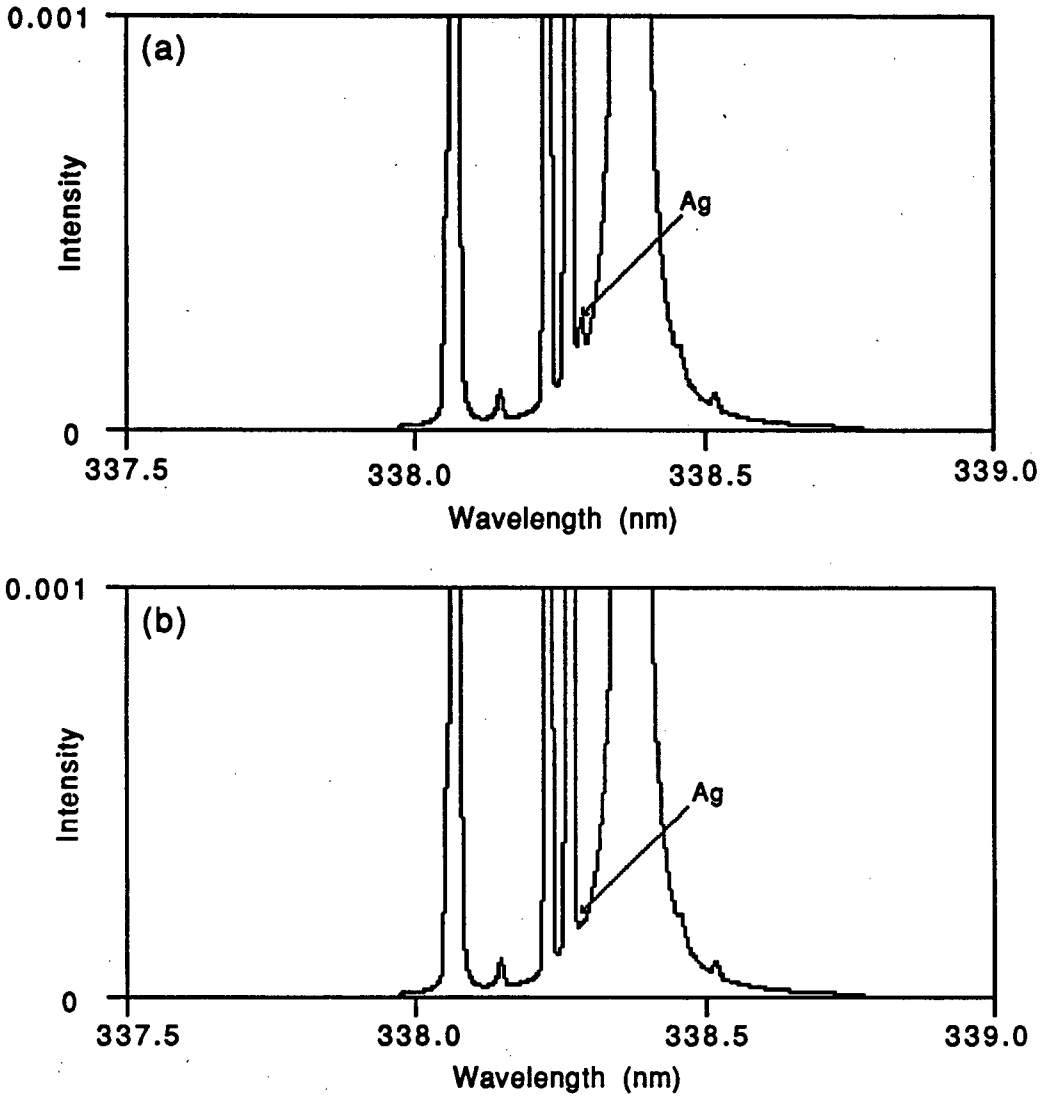

Figure 8.11 Simulation of the silver 338.92 nm line in NBS coal fly ash at a 0.01 nm instrumental bandpass showing the effect of the silver concentration; (a) with 10 ppm silver, and (b) with 1 ppm silver.

number of interfering lines and their close proximity to the silver line, and from the intensity scale one can see that the most intense line (Fe I 338.40 nm) is more than ten thousand times as intense as the silver line. Figure 8.10 (b) corresponds to a silver concentration of 50 ppm, figure 8.11 (a) 10 ppm, and figure 8.11 (b) 1 ppm. For this bandpass at concentrations greater than about 10 ppm the silver line can be resolved from its interferents, but not at concentrations lower than about 1 to 5 ppm. This value is considerably greater than the tabulated detection limit of 8.7 ppb listed in reference [19], and shows that detection limits published for matrices different from that under consideration are of limited use.

Figures 8.12 and 8.13 are similar to 8.10 and 8.11, except that they consist of a series of simulations for the 328.07 nm line of silver based on the data in Table VII. Figure 8.12 (a) is the spectrum without instrumental broadening, figure 8.12 (b) corresponds to a silver concentration of 10 ppm, figure 8.13 (a) 1 ppm, and figure 8.13 (b) 0.1 ppm. At this value of the spectral bandpass the silver line can be resolved at concentrations greater than approximately 0.5 ppm. This is about 100 times greater than the detection limit of 4.7 ppb listed in reference [19].

By comparing figures 8.10 and 8.11 to figures 8.12 and 8.13, it is clear that in such a coal fly ash matrix the 328.07 nm silver line would give lower detection limits over the 338.29 nm line by a factor of approximately 20, and would hence be the analytical line of choice in this matrix.

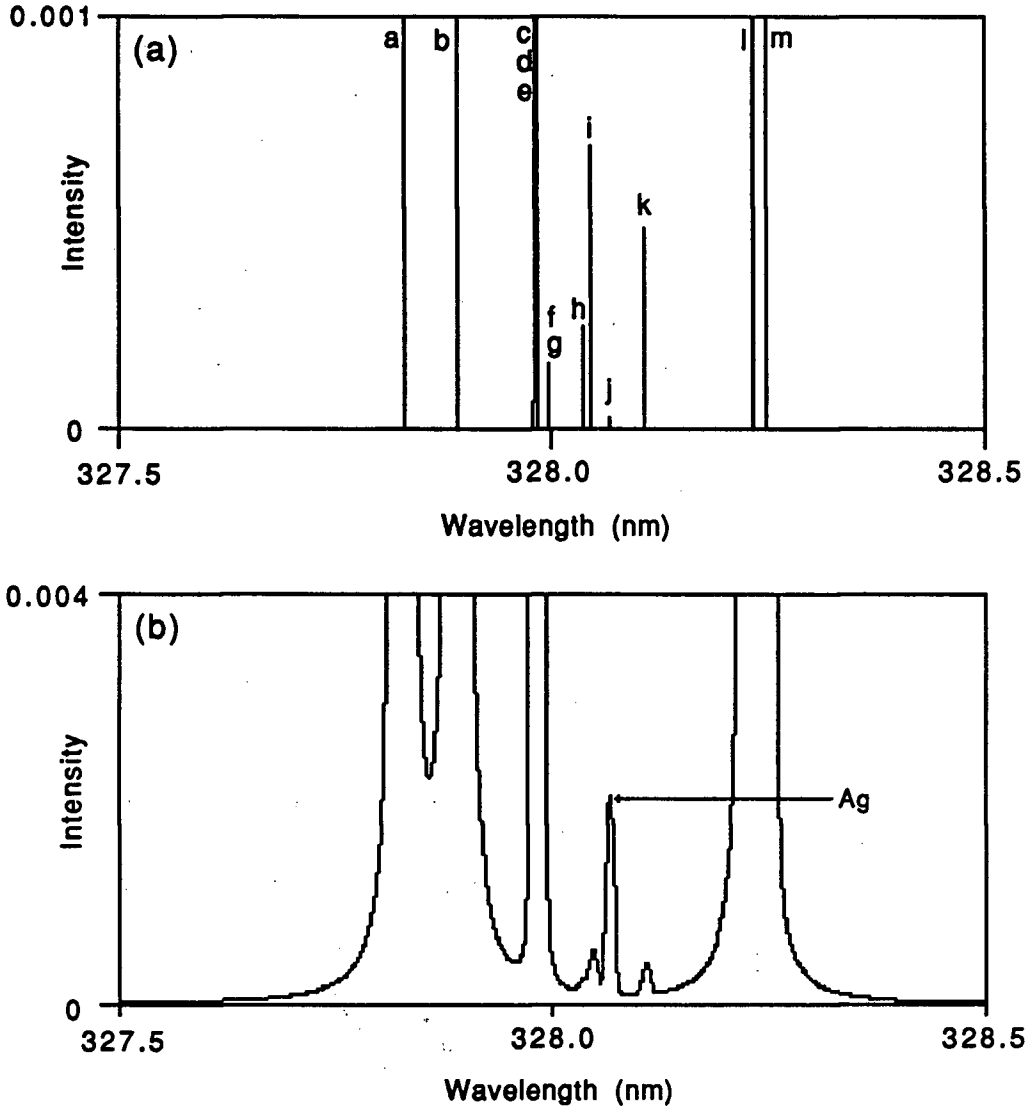

Figure 8.12 Simulation of the silver 328.07 nm line in NBS coal fly ash at a 0.01 nm instrumental bandpass showing the effect of the silver concentration; (a) with no instrumental broadening and 10 ppm silver, and (b) with 10 ppm silver. The lines are identified by the letters given in Table VII.

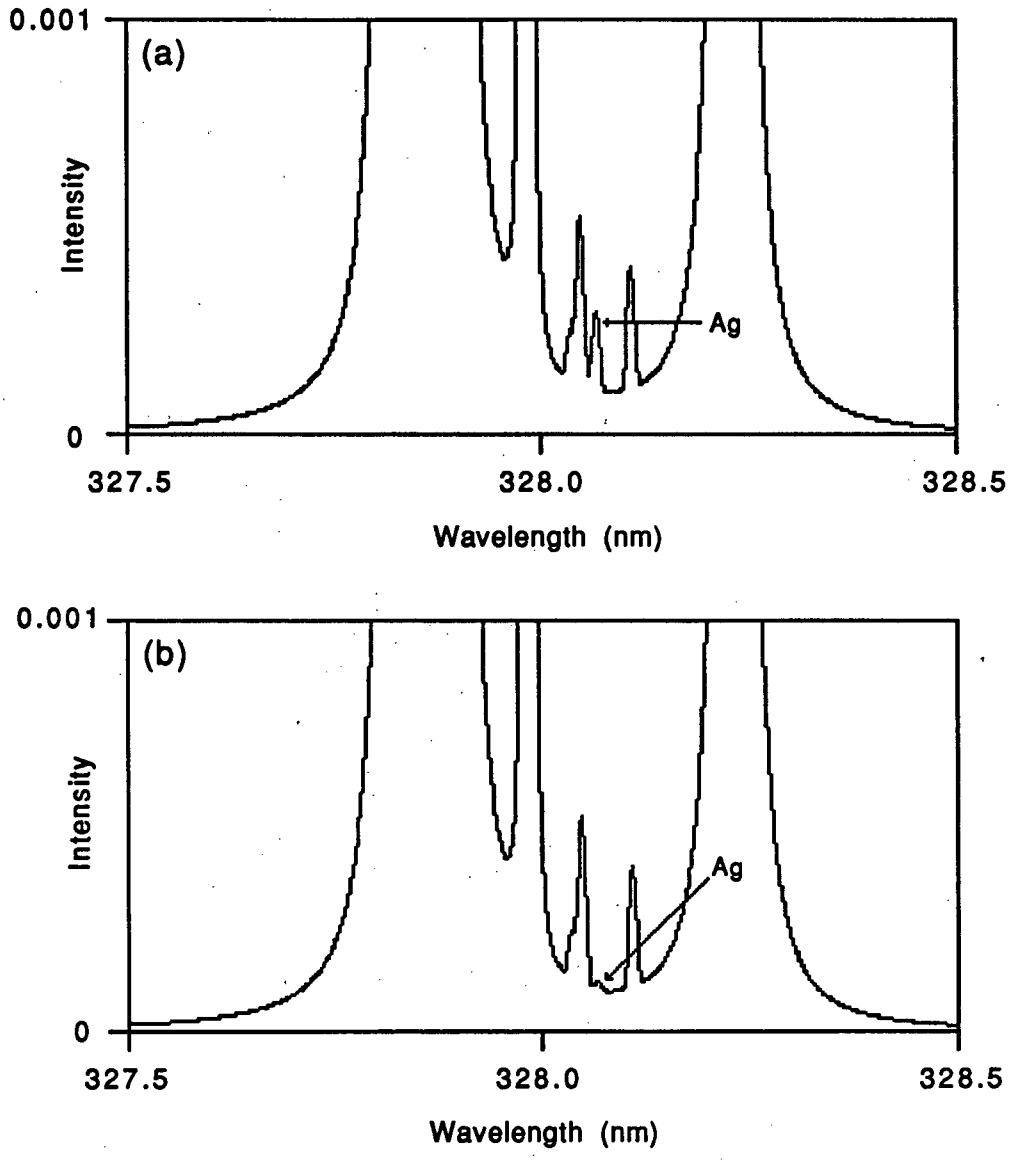

Figure 8.13 Simulation of the silver 328.07 nm line in NBS coal fly ash at a 0.01 nm instrumental bandpass showing the effect of the silver concentration; (a) with 1 ppm silver, and (b) with 0.1 ppm silver.

Figure 8.14 shows the effect of adding random noise to the spectrum presented in figure 8.8 (b) (with a bandpass of 0.005 nm and a silver concentration of 10 ppm in the geochemical matrix). In figure 8.14 (a) it is assumed that there is a constant background of 0.001 with 1 % random noise and in figure 8.14 (b) it is assumed that there is a constant background of 0.01, also with 1 % random noise (equivalent to a background of 0.001 with 10 % noise).

The detection limit (i.e. that concentration which will give a signal three times the standard deviation of the background) of silver for figure 8.14 (a) can be easily calculated to be 1.8 ppm; thus at the concentration of 10 ppm in the figure the silver is well above the detection limit (as can be seen visually from the figure). The detection limit of silver for figure 8.14 (b) is about 18 ppm; thus at the concentration of 10 ppm in the figure the silver is below the detection limit, and thus, as can also be seen from the figure, could not be analyzed for (in this matrix with this spectral bandpass).

8.5 Summary

From the results presented in this chapter it is clear that the simulation of emission spectra could one day be a viable method for providing a computerized data base for plasma spectroscopy. In addition the method shows great promise as a tool to study spectral line overlaps, particularly for mixtures having complex composition. The advantage that this method has over both line coincidence tables and actual spectral scans is that spectra for an almost infinite

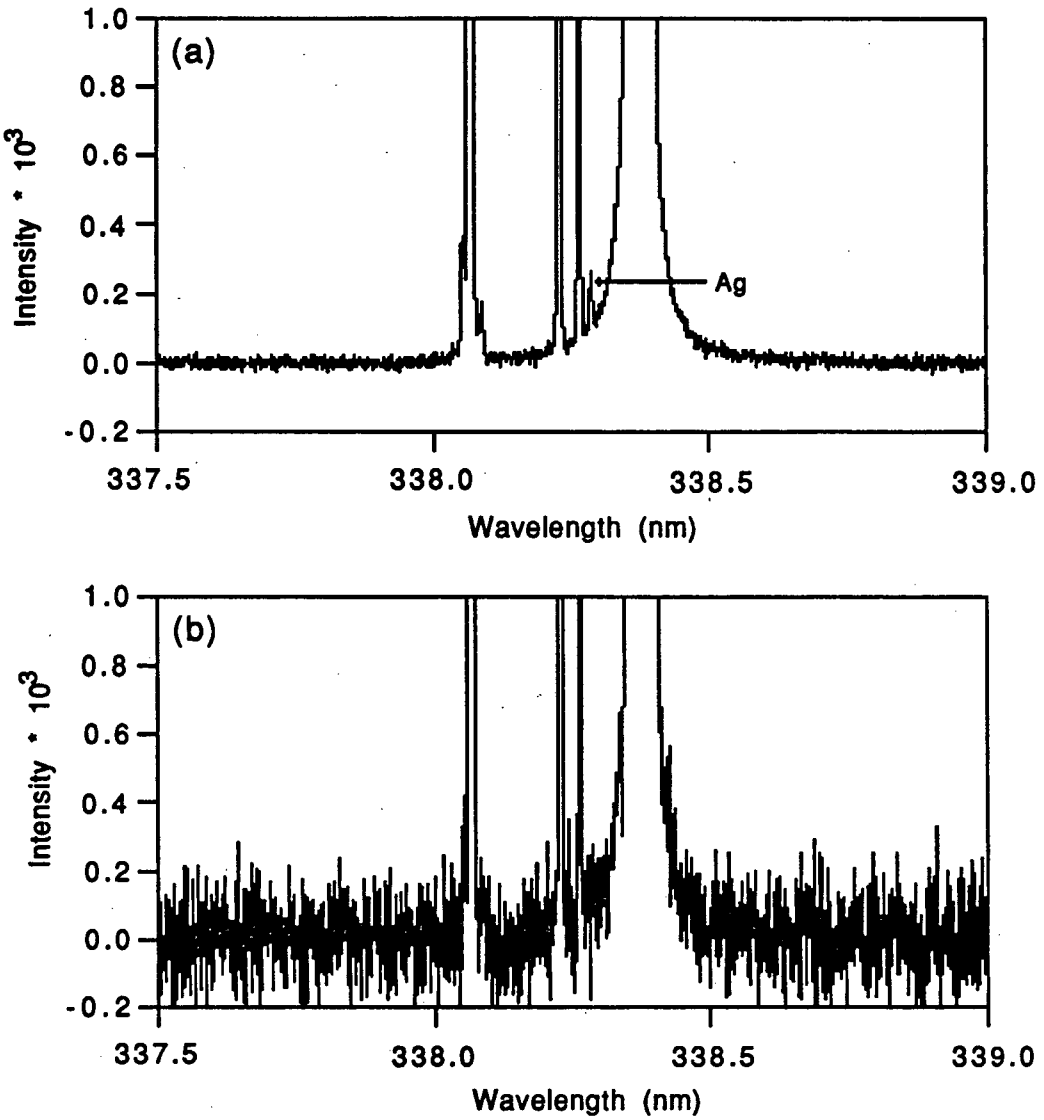

Figure 8.14 Simulation of the silver 338.92 nm line in the geochemical matrix at a 0.005 nm instrumental bandpass showing the effect of adding random noise to the spectrum presented in figure 8.8 (b); (a) with a constant background of 0.001 with 1 % random noise, (b) with a constant background of 0.01 with 1 % random noise.

variety of operating conditions can be generated using a relatively modest stored data base.

There are currently two major limitations which restrict the utility of the method. Firstly, the approach is limited by both the lack of accuracy and the limited availability of transition probabilities for all of the elements. The simulated spectra are only as complete and accurate as the gA values used to generate them. This is currently the major limitation to the successful application of spectral simulations to analytical problem solving. Hopefully this limitation will become less severe as listings of gA values become more comprehensive and accurate.

Secondly, the approach is limited by our understanding of the physical properties of the icp discharge and how these properties are affected by changes in instrumental operating conditions. This was particularly true at the time references [29] and [31] were published, however (as was seen in chapters three and four), a fair amount of progress has been made in predicting deviations from local thermodynamic equilibrium in the icp. Ideally the simulation program should be coupled to the simple rate model presented in chapter three, which can calculate level populations (for most elements) from an experimentally determined electron density - which can be related back to icp settings.

We feel that spectral simulations of the type described in this chapter will be important in the long-term development of "better" icp instrumentation. Currently the analyst must use the available tables and knowledge of the potential composition of an unknown sample to make appropriate line selections [87]. The successful

implementation of spectral simulation software could shift part of the burden from the analyst to the instrument computer, since it could provide the icp instrument with sufficient information to make an intelligent decision which would allow an automated choice of appropriate instrument settings, analytical lines and background correction strategies for an optimized solution to the particular problem at hand. This could be particularly useful for sequential icp spectrometers where line selections can be made at the moment of analysis.

Chapter 9
Conclusions

As mentioned in the introduction to this thesis, the primary goal of this work was to improve the understanding of the inductively coupled plasma from a fundamental point of view - in particular to understand why and how deviations of analyte level populations from local thermodynamic equilibrium come about. The following summary shows how this goal was achieved.

In chapter three of this work it was shown that significant departures of analyte level populations from lte could be attributed to the fact that radiative decay was not balanced by its inverse process of absorption, and thus competed with collisional de-excitation by electron impact as a level depopulating mechanism. In addition, using a simple two-level rate model approach, these deviations could be accurately estimated, at least for those elements studied which did not undergo a charge transfer reaction with the argon support gas.

It is not clear at this time if the simple two-level rate model is capable of accurately estimating these deviations for elements other than those studied (iron, chromium, and barium). Experimental Boltzmann plots need to be gathered for other elements in order to ascertain this.

It was shown in chapter four that charge transfer between argon ions and ground state magnesium atoms caused ionic magnesium energy levels to be overpopulated (with respect to the two-level rate model calculations, taking the contribution of radiative decay

into account). It seemed that the more highly energetic ionic levels were excited by electron impact from the charge transfer levels of magnesium, whereas the lower energy ionic levels were excited by electron impact from the ground state ion. It was also shown that three-body recombination of magnesium ions with electrons was likely of major importance at high electron densities, but not at lower ones.

Charge transfer in the icp is still poorly understood. For example, at the present time, there seems to be no way to a priori predict which elements will be subject to charge transfer with the argon support gas. Other elements need to be studied in detail to elucidate the nature of charge transfer.

In addition, it appeared that due to the high density of argon atoms in the icp, self-absorption was very appreciable so that, for argon, radiative decay was balanced by absorption, resulting in little or no overpopulation of the ground state atom.

Chapter five showed that for electron densities greater than about 2×10^{15} cm^{-3} the lte temperature (as calculated from the electron density) was well within the estimated experimental uncertainty of the electron temperature. At lower electron densities the calculated value of the electron temperature was higher than the lte temperature. Unfortunately, the accuracy of the electron temperature determination, at these low values of the electron density, did not allow for a definitive conclusion as to whether or not the electron temperature was actually higher.

In order to measure electron temperatures in the central channel of the icp by the method used in this work (from the ratio of the

intensity of the 430 nm spectral line of argon to that of the adjacent recombination continuum), water must be excluded from the plasma. This presents the difficulty that the electron density cannot then be measured from the Stark broadening of hydrogen lines. This could be circumvented by measuring the electron density from the Stark broadening of argon lines, as described in reference [33].

In chapter six an extra argon flow, known as the sheath gas flow, which was added to the aerosol gas was described. This allowed one to study the effect of the sample introduction flow rate on plasma conditions, while keeping the total amounts of both analyte and solvent reaching the plasma constant. The electron density was found to both decrease steadily and to have its position of maximum concentration shift off-axis with an increase in the sheath gas flow rate. It appeared that at low values of this flow the mixing between the cool sample introduction gas and the much hotter plasma gas was reasonably complete, whereas at higher values there was relatively little mixing. It was also shown that even a small excess volume of sample introduction gas can significantly alter the electron density.

Ionic barium showed unusual behaviour as a function of the sheath gas flow rate. Its emission intensity increased by a factor of 75 in going from a sheath gas flow rate of 0.0 to 0.1 L/min - it then continued to increase with an increase in the flow rate (the reverse of what one would expect on the basis of lte arguments). It is believed that this potentially very useful analytical result is due to the recombination of Ba^{2+} with an electron.

By introducing iron into the plasma, both as a standard aqueous aerosol and directly as a vapour (from the vapour pressure of ferrocene), it was found that, on the whole, the differences in iron excitation between the two sample introduction methods were quite small. This was a very interesting result - not only did this mean that the introduction of water into the plasma had a limited effect on sample excitation, but also that the processes of desolvation, vaporization and dissociation which an aerosol droplet must undergo were of limited importance to the overall excitation of analyte.

In addition to developing a better fundamental understanding of the icp discharge, the other goal of this work was to put such an understanding as currently existed to practical use. This was accomplished through the spectral simulation program described in chapter eight.

By combining the results of icp fundamental studies, basic atomic and ionic data (such as oscillator strengths, etc.), and the realistic instrumental profile described in detail in chapter seven, it was shown that it is possible to generate reasonably accurate spectral simulations. The method shows promise as a tool to study spectral line overlaps, particularly for mixtures having complex composition.

There were two main limitations to the method. The first was the lack of accuracy and the limited availability of transition probabilities. The second was the limited understanding of how level populations in the icp deviated from their lte values. This was particularly true as the material in chapter eight was written before the development of the simple two-level rate model. Ideally,

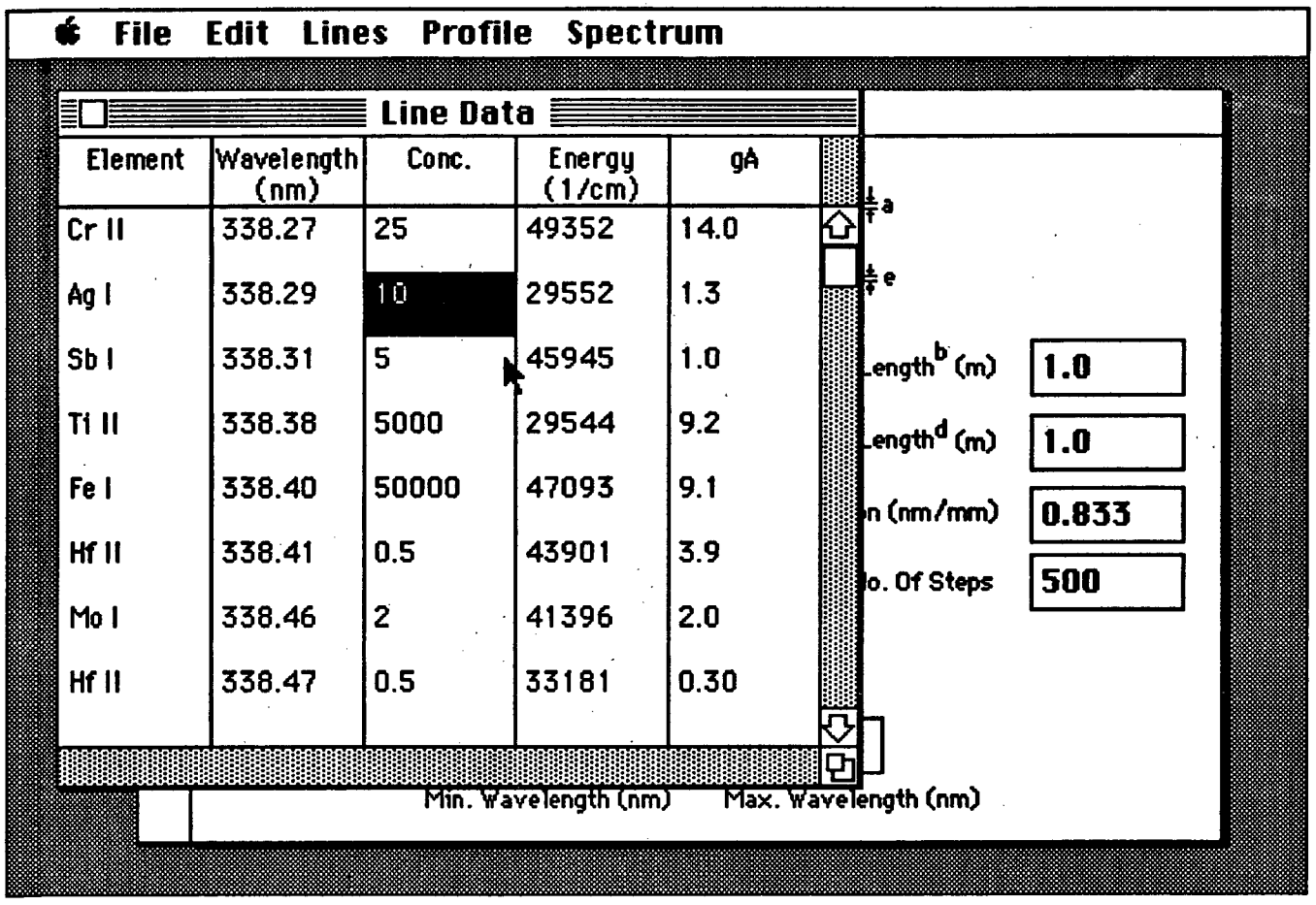

Figure 9.1: A screen dump of the "Line Data" prompt window of the preliminary spectral simulation program written for the Macintosh computer.

the simulation program should be coupled to this model. Preliminary work in this direction was started by writing a much more user-friendly version of the simulation program, to be run on a Macintosh computer. An example of a screen dump of this program is presented in figure 9.1. For each commonly used analytical line, the intention was to include an on-line data base of the wavelengths, excitation energies, and transition probabilities for each potential interfering spectral line. Unfortunately, time constraints did not allow for the completion of this project.

In summary, the objectives of this thesis have been met. An improved understanding of the icp has resulted, along with a practical application (spectral simulation) of that understanding.

References

1. F. Aeschbach, *Spectrochim. Acta* **37B**, 987 (1982).

2. J. F. Alder, R. M. Bombelka and G. F. Kirkbright, *Spectrochim. Acta* **35B**, 163 (1980).

3. C. Th. J. Alkemade and J. M. W. Milatz, *J. Opt. Soc. Am.* **45**, 583 (1955).

4 C. Th. J. Alkemade and J. M. W. Milatz, *Appl. Sci. Res.* **B4**, 289 (1955).

5. T. A. Anderson, A. R. Forster and M. L. Parsons, *Appl. Spectrosc.* **36**, 504 (1982).

6. J. O. Arnold, E. E. Whiting and G. C. Lyle, *J. Quant. Spectrosc. Radiat. Transfer* **9**, 775 (1969).

7. G. I. Babat, *J. Inst. Elec. Engrs.* **94**, 27 (1947).

8. P. Baessler and M. Kock, *J. Phys. B: Atom. Molec. Phys.* **13**, 1351 (1980).

9. R. M. Barnes, *CRC Crit. Rev. in Chemistry* **203**, Sept. (1978).

10. Glenn J. Bastiaans and Raymond A. Mangold, *Spectrochim. Acta* **40B**, 885 (1985).

11. A. Batal, J. Jarosz and J. M. Mermet, *Spectrochim. Acta* **36B**, 983 (1981).

12. G. Bekefi, C. Deutsch and B. Yaakobi, "Spectroscopic Diagnostics of Laser Plasmas" in *Principles of Laser Plasmas,* p. 549, G. Bekefi (ed.), John Wiley and Sons, New York (1976).

13. M. W. Blades, "Excitation Mechanisms and Discharge Characteristics-Recent Developments" in *Inductively Coupled Plasma Emission Spectroscopy, Part II: Applications and Fundamentals,* p. 387, P. W. J. M. Boumans (ed.), John Wiley and Sons, New York (1987).

14. M. W. Blades, *Appl. Spectrosc.* **37**, 371 (1983).

15. M. W. Blades and B. L. Caughlin, *Spectrochim. Acta* **40B**, 579 (1985).

16. M. W. Blades, B. L. Caughlin, Z. H. Walker and L. L. Burton, *Prog. Anal. Spectrosc.* **10**, 57 (1987).

17. M. Borsier and G. Labarraque, *Spectrochim. Acta* **41B**, 115 (1986).

18. P. W. J. M. Boumans (ed.), *Inductively Coupled Plasma Emission Spectroscopy,* Wiley-Interscience, New York (1987).

19. P. W. J. M. Boumans, *Line Coincidence Tables for Inductively Coupled Plasma Emission Spectrometry,* Pergamon Press, Oxford (1980); second revised edn. (1984).

20. P. W. J. M. Boumans and F. J. DeBoer, *Spectrochim. Acta* **32B**, 365 (1977).

21. P. W. J. M. Boumans and J. J. A. M. Vrakking, *Spectrochim. Acta* **40B**, 1437 (1985).

22. P. W. J. M. Boumans and J. J. A. M. Vrakking, *Spectrochim. Acta* **40B**, 1423 (1985).

23. P. W. J. M. Boumans and J. J. A. M. Vrakking, *Spectrochim. Acta* **40B**, 1107 (1985).

24. P. W. J. M. Boumans and J. J. A. M. Vrakking, *Spectrochim. Acta* **40B**, 1085 (1985).

25. P. W. J. M. Boumans and J. J. A. M. Vrakking, *Spectrochim. Acta* **39B**, 1291 (1984).

26. P. W. J. M. Boumans and J. J. A. M. Vrakking, *Spectrochim. Acta* **39B**, 1261 (1984).

27. P. W. J. M. Boumans and J. J. A. M. Vrakking, *Spectrochim. Acta* **39B**, 1239 (1984).

28. L. L. Burton and M. W. Blades, Spectrochim. Acta 45B, 139 (1990).

29. L. L. Burton and M. W. Blades, *Spectrochim. Acta* **43B**, 305 (1988).

30. L. L. Burton and M. W. Blades, *Spectrochim. Acta* **42B**, 513 (1987).

31. L. L. Burton and M. W. Blades, *Spectrochim. Acta* **41B**, 1063 (1986).

32. B. L. Caughlin, Ph. D. Dissertation, University of British Columbia, (1986).

33. B. L. Caughlin and M. W. Blades, *Spectrochim. Acta* **42B**, 353 (1987).

34. B. L. Caughlin and M. W. Blades, *Spectrochim. Acta* **40B**, 1539 (1985).

35. B. L. Caughlin and M. W. Blades, *Spectrochim. Acta* **40B**, 987 (1985).

36. B. L. Caughlin and M. W. Blades, *Spectrochim. Acta* **39B**, 1583 (1984).

37. Francis F. Chen, *Introduction to Plasma Physics,* Plenum, New York (1974).

38. C. H. Corliss and W. R. Bozman, NBS Monograph **53**, U. S. Government Printing Office, Washington DC (1962).

39. C. J. Cremers and R. C. Birkebak, *Appl. Opt.* **5**, 1057 (1966).

40. J. A. B. Daigle, Ph. D. Dissertation, University of British Columbia, (1990).

41. H. W. Drawin, "Validity Criteria for LTE" in *Progress in Plasmas and Gas Electronics, vol. 1,* p. 593, R. Rompe and M. Steenbeck (eds.), Akademie-Verlag, Berlin (1975).

42. H. W. Drawin, *High Press.-High Temp.* **2**, 359 (1970).

43. H. U. Eckert and A. Danielsson, *Spectrochim. Acta* **38B**, 15 (1983).

44. R. C. Elton, "Atomic Processes" in *Methods of Experimental Physics, vol. 9 - part A,* p. 115, Hans R. Griem and Ralph H. Lovberg (eds.), Academic Press, New York (1970).

45. B. Faggetter, G. Heisz and M. W. Blades, *Spectrochim. Acta* **42B**, 1235 (1987).

46. Velmer A. Fassel, *Spectrochim. Acta* **40B**, 1281 (1985).

47. A. R. Forster, T. A. Anderson and M. L. Parsons, *Appl. Spectrosc.* **36**, 499 (1982).

48. L. de Galan, *Spectrochim. Acta* **39B**, 537 (1984).

49. L. de Galan, R. Smith and J. D. Winefordner, *Spectrochim. Acta* **23B**, 521 (1968).

50. L. de Galan and J. D. Winefordner, *Spectrochim. Acta* **23B**, 277 (1968).

51. A. Goldwasser and J. M. Mermet, *Spectrochim. Acta* **41B**, 725 (1986).

52. D. V. Gravelle, M. Beaulieu, M. I. Boulos and A. Gleizes, *J. Phys. D: Appl. Phys.* **22**, 1471 (1989).

53. J. M. Green and C. E. Webb, *J. Phys. B: Atom. Molec. Phys.* **7**, 1698 (1974).

54. S. Greenfield, I. L. Jones and C. T. Berry, *Analyst* **89**, 713 (1964).

55. Hans R. Griem, "Stark Broadening" in *Advances in Atomic and Molecular Physics, vol. 11,* p. 331, D. R. Bates and Benjamin Bederson (eds.), Academic Press, New York (1975).

56. Hans R. Griem, *Plasma Spectroscopy,* McGraw-Hill, New York (1964).

57. H. R. Griem, *Phys. Rev.* **128**, 515 (1962).

58. H. R. Griem, M. Baranger, A. C. Kolb and G. K. Oertel, *Phys. Rev.* **125**, 177 (1962).

59. H. R. Griem, A. C. Kolb and K. Y. Shen, *Phys. Rev.* **116**, 4 (1959).

60. M. Gryzinski, *Phys. Rev.* **138**, A336 (1965).

61. Tetsuya Hasegawa and Hiroki Haraguchi, "Fundamental Properties of Inductively Coupled Plasmas" in *Inductively Coupled Plasmas in Analytical Atomic Spectrometry,* p. 267, Akbar Montaser and D. W. Golightly (eds.), VCH Publishers, New York (1987).

62. Tetsuya Hasegawa and Hiroki Haraguchi, *Anal. Chem.* **59**, 2789 (1987).

63. Tetsuya Hasegawa and Hiroki Haraguchi, *Spectrochim. Acta* **40B**, 1505 (1985).

64. Tetsuya Hasegawa and Hiroki Haraguchi, *Spectrochim. Acta* **40B**, 1067 (1985).

65. J. B. Hasted, *Physics of Atomic Collisions,* Butterworths, London (1972).

66. T. D. Hettipathirana, M. Sc. Dissertation, University of British Columbia, (1989).

67. G. M. Hieftje, G. D. Rayson and J. W. Olesik, *Spectrochim. Acta* **40B**, 167 (1985).

68. Mao Huang and Gary M. Hieftje, *Spectrochim. Acta* **44B**, 739 (1989).

69. Mao Huang and Gary M. Hieftje, *Spectrochim. Acta* **40B**, 1387 (1985).

70. M. Huang, P. Y. Yang, D. S. Hanselman, C. A. Monnig and G. M. Hieftje, *Spectrochim. Acta* **45B**, 511 (1990).

71. P. A. Jannson, *Deconvolution with Applications in Spectroscopy,* Academic Press, New York (1984).

72. J. Jarosz, J. M. Mermet and J. P. Robin, *Spectrochim. Acta* **33B**, 55 (1978).

73. D. G. Jones, *Anal. Chem.* **57**, 1207A (1985).

74. D. G. Jones, *Anal. Chem.* **57**, 1057A (1985).

75. D. J. Kalnicky, V. A. Fassel and R. N. Kniseley, *Appl. Spectrosc.* **31**, 137 (1977).

76. P. Kepple and H. R. Griem, *Phys. Rev.* **173**, 317 (1968).

77. G. Kirchhoff and R. Bunsen, *Pogg. Ann. Phys. Chem.* **110**, 161 (1860).

78. G. R. Kornblum and L. de Galan, *Spectrochim. Acta* **32B**, 71 (1977).

79. G. Kreuning and F. J. M. J. Maessen, *Spectrochim. Acta* **44B**, 367 (1989).

80. G. Kreuning and F. J. M. J. Maessen, *Spectrochim. Acta* **42B**, 677 (1987).

81. A. A. Levinson, *Introduction to Exploration Geochemistry,* second edn., Applied Publishing (1974).

82. K. P. Li, M. Dowling, T. Fogg, T. Yu, K. S. Yeah, J. D. Hwang and J. D. Winefordner, *Anal. Chem.* **60**, 1590 (1988).

83. R. J. Lovett, *Spectrochim. Acta* **37B**, 969 (1982).

84. R. J. Lovett, personal communication.

85. S. W. McGeorge and E. D. Salin, *Spectrochim. Acta* **41B**, 327 (1986).

86. S. W. McGeorge and E. D. Salin, *Spectrochim. Acta* **40B**, 435 (1985).

87. J. W. McLaren and S. S. Berman, *Spectrochim. Acta* **40B**, 217 (1985).

88. J. W. McLaren and J. M. Mermet, *Spectrochim. Acta* **39B**, 1307 (1984).

89. R. W. P. McWhirter, "Spectral Intensities" in *Plasma Diagnostic Techniques,* p. 201, R. H. Huddlestone and S. L. Leonard (eds.), Academic Press, New York (1965).

90 Marthe Marichy, Monique Mermet and Jean-Michel Mermet, *J. Anal. At. Spectrom.* **2**, 561 (1987).

91. Kim A. Marshall and Gary M. Hieftje, *J. Anal. At. Spectrom.* **2**, 567 (1987).

92. W. F. Meggers, C. H. Corliss and B. F. Schribner, *Tables of Spectral-Line Intensities: Part I, arranged by elements; Part II, arranged by wavelength,* NBS Monograph **145**, U. S. Government Printing Office, Washington, DC (1975).

93. Carl F. Melius, *J. Phys. B: Atom. Molec. Phys.* **7**, 1692 (1974).

94. J. M. Mermet, *Spectrochim. Acta* **44B**, 1109 (1989).

95. J. M. Mermet, "Spectroscopic Diagnostics: Basic Concepts" in *Inductively Coupled Plasma Emission Spectroscopy, Part II: Applications and Fundamentals,* p. 353, P. W. J. M. Boumans (ed.), John Wiley and Sons, New York (1987)

96. J. M. Mermet, *Spectrochim. Acta* **30B**, 383 (1975).

97. J. M. Mermet and J. Jarosz, *J. Quant. Spectrosc. Radiat. Transfer* **17**, 237 (1977).

98. J. M. Mermet, E. Pehlivanian and J. Robin, "Analysis of Blood Serum by ICP-AES" in *Developments in Atomic Plasma Spectrochemical Analysis,* p. 718, Ramon M. Barnes (ed.), Heyden and Son, London (1981).

99. Gerhard A. Meyer, *Anal. Chem.* **59**, 1345A (1987).

100. K. D. Mielenz, *J. Opt. Soc. Am.* **57**, 66 (1967).

101. M. Mitchner and Charles H. Kruger, Jr., *Partially Ionized Gases,* John Wiley and Sons, New York (1973).

102. Akbar Montaser and D. W. Golightly (eds.), *Inductively Coupled Plasmas in Analytical Atomic Spectrometry,* VCH Publishers, New York (1987).

103. J. J. A. M. van der Mullen, Ph. D. Dissertation, De Technische Hogeshool Eindhoven, (1986).

104. J. A. M. van der Mullen, I. J. M. Raaijmakers, A. C. A. P. van Lammeren, D. C. Schram, B. van der Sijde and H. J. W. Schenkelaars, *Spectrochim. Acta* **42B**, 1039 (1987).

105. J. J. A. M. van der Mullen, B. van der Sijde and D. C. Schram, *Phys. Lett.* **79A**, 51 (1980).

106. M. Murillo and J. M. Mermet, *Spectrochim. Acta* **44B**, 359 (1989).

107. M. Murillo and J. M. Mermet, *Spectrochim. Acta* **42B**, 1151 (1987).

108. O. H. Nestor and H. N. Olsen, *SIAM Rev.* **2**, 200 (1960).

109. S. Nowak, J. A. M. van der Mullen, B. van der Sijde and D. C. Schram, *J. Quant. Spectrosc. Radiat. Transfer* **41**, 177 (1989).

110. J. E. Osher, "Particle Measurements" in *Plasma Diagnostic Techniques,* p. 517, R. H. Huddlestone and S. L. Leonard (eds.), Academic Press, New York (1965).

111. M. L. Parsons, A. R. Forster and D. Anderson, *An Atlas of Spectral Interferences in ICP Spectroscopy,* Plenum Press, New York (1980).

112. I. J. M. M. Raaijmakers, P. W. J. M. Boumans, B. van der Sijde and D. C. Schram, *Spectrochim. Acta* **38B**, 697 (1983).

113. A. A. Radzig and B. M. Smirnov, *Reference Data on Atoms, Molecules and Ions,* Springer, Berlin (1985).

114. T. B. Reed, *J. Appl. Phys.* **34**, 2266 (1963).

115. T. B. Reed, *J. Appl. Phys.* **32**, 821 (1961).

116. H. van Regemorter, *Astrophys. J.* **136**, 906 (1962).

117. E. G. & G. Reticon, product information on RL-4096 solid state line scanners, Sunnyvale CA (1983).

118. A. Savitzky and M. J. E. Golay, *Anal. Chem.* **36**, 1627 (1964).

119. D. C. Schram, I. J. M. M. Raaijmakers, B. van der Sijde, J. J. W. Schenkelaars and P. W. J. M. Boumans, *Spectrochim. Acta* **38B**, 1545 (1983).

120. M. J. Seaton, "The Theory of Excitation and Ionization by Electron Impact" in *Atomic and Molecular Processes*, p. 374, D. R. Bates (ed.), Academic Press, New York (1962).

121. M. J. Seaton, *Month. Not. Roy. Astr. Soc.* **119**, 90 (1959).

122. R. W. Seward, NBS Special Publication **260**, U. S. Dept. of Commerce, National Bureau of Standards, Gaithersburg, MD (1986-87).

123. S. L. Simons, Jr., *Byte Magazine* (Nov.), 487 (1983).

124. M. Sperling and W. Dannecker, *Z. Anal. Chem.* **328**, 455 (1987).

125. R. Stair, W. E. Schneider and J. K. Jackson, *Appl. Opt.* **2**, 1151 (1963).

126. Y. Talmi, *Appl. Spectrosc.* **36**, 1 (1982).

127. Y. Talmi and R. W. Simpson, *Appl. Opt.* **19**, 1401 (1980).

128. C. R. Vidal, J. Cooper and E. W. Smith, *J. Quant. Spectrosc. Radiat. Transfer* **11**, 263 (1971).

129. F. L. O. Wadsworth, *Phil. Mag.* **43**, 317 (1897).

130. Z. H. Walker, M. Sc. Dissertation, University of British Columbia, (1986).

131. Z. Walker and M. W. Blades, *Spectrochim. Acta* **41B**, 761 (1986).

132. Z. Walker and M. W. Blades, *Spectrochim. Acta* **42B**, 1077 (1987).

133. A. Walsh, *Spectrochim. Acta* **7**, 108 (1955).

134. Robert C. Weast (ed.) and Melvin J. Astle (assoc. ed.), *CRC Handbook of Chemistry and Physics: 60th edition,* CRC Press, Boca Raton, Florida (1980).

135. D. G. J. Weir and M. W. Blades, *Spectrochim. Acta* **45B**, 615 (1990).

136. R. H. Wendt and V. A. Fassel, *Anal. Chem.* **37**, 920 (1964).

137. W. L. Wiese, "Line Broadening" in *Plasma Diagnostic Techniques,* p. 201, R. H. Huddlestone and S. L. Leonard (eds.), Academic Press, New York (1965).

138. W. L. Wiese and G. A. Martin, "Wavelengths and Transition Probabilities for Atoms and Atomic Ions", Part II, NSRDS-NBS **68**, Washington DC (1980).

139. R. K. Winge, E. L. DeKalb and V. A. Fassel, *Appl. Spectrosc.* **39**, 673 (1985).

140. R. K. Winge, V. A. Fassel and D. E. Eckels, *Appl. Spectrosc.* **40**, 461 (1986).

141. R. K. Winge, V. A. Fassel, V. J. Peterson and M. A. Floyd, *Inductively Coupled Plasma-Atomic Emission Spectroscopy: An Atlas of Spectral Information,* Elsevier, Amsterdam (1984).

142. R. K. Winge, V. A. Fassel, V. J. Peterson and M. A. Floyd, *Appl. Spectrosc.* **36**, 210 (1982).

143. R. K. Winge, V. J. Peterson and V. A. Fassel, *Appl. Spectrosc.* **33**, 206 (1979).